UNIVERSITY OF CALIFORNIA, SAN DIEGO

Modeling the Hydroclimate of the San Francisco Bay-Delta Estuary and Watershed

A dissertation submitted in partial satisfaction of the

requirements for the degree Doctor of Philosophy in

Oceanography

by

Noah Knowles

Committee in charge:

Dan Cayan, Chair
Kosta Georgakakos
Ken Melville
David Peterson
Richard Somerville
Mark Thiemens
Clint Winant

2000

The dissertation of Noah Knowles is approved, and it is acceptable in quality and form for publication on microfilm:

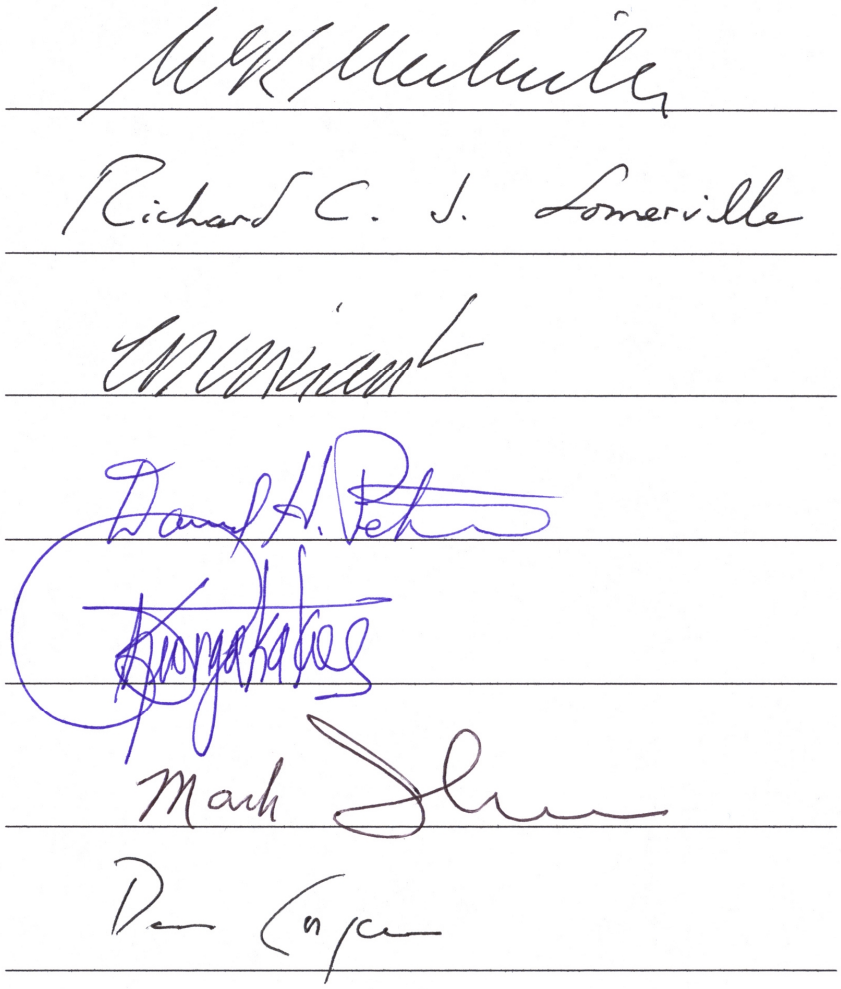

Chair

University of California, San Diego

2000

Table of Contents

LIST OF FIGURES

LIST OF TABLES

Acknowledgements

In the course of this work, I have had the pleasure of working with many fine people. I am lucky enough to have made the acquaintance early on of Dave Peterson at the USGS in Menlo Park, CA. His contributions to the work, ongoing encouragement, and sense of humor have kept my attitude positive, and my seriousness in check. Other members of the Menlo Park and Sacramento Survey groups have contributed ideas and friendship, including Larry Schemel, Rich Smith, and the Grizzly Bay team. I would also like to thank Reg Uncles of the Plymouth Marine Laboratory for his help and for lending me his estuarine model, which has been at the center of much of this work.

More locally, I have been fortunate enough to encounter several excellent scientists who were down to Earth enough that I was able to progress through graduate school without losing myself. Richard Somerville provided my first introduction to Scripps, and in his easygoing way, he helped me keep things in perspective. I was also fortunate to be guided through the initially unfamiliar terrain of hydrology by Kosta Georgakakos and others at the Hydrologic Research Center in Del Mar, CA. Kosta's enthusiasm for hydrology is contagious. Without his input and friendly guidance, this would have been a much poorer piece of work. In addition, Dmitris Tsintikidis, Jason Sperfslage and Alex Guetter of HRC helped generate some of the code which I used, and assisted me in retrieving meteorological data from HRC's database. Many other people have taken time out of their schedules to help me along the way. I would like to thank all the members of the Climate Research Division at SIO for their help. Thanks also to my many friends at SIO. Without them I would never be writing this.

Dan Cayan has been my advisor for 6 years, though he would probably prefer the term “confidant”. His friendly and non-authoritarian approach has allowed me to find my own way though graduate school even as I was being guided. I could not have asked for a better confidant.

Vita

1991	B.S., University of Illinois, Urbana-Champaign
1993	M.S., University of Illinois, Urbana-Champaign
1996	M.S., University of California, San Diego
2000	Ph.D., University of California, San Diego

ABSTRACT OF THE DISSERTATION

Modeling the Hydroclimate
of the San Francisco Bay-Delta
Estuary and Watershed

by

Noah Knowles

Doctor of Philosophy in Oceanography

University of California, San Diego, 2000

Daniel R. Cayan, Chair

The San Francisco Bay-Delta estuary has been the subject of intense scientific scrutiny in recent decades, stimulated largely by concerns of ecosystem degradation. This dissertation examines the variability of the estuary and its upstream watershed at seasonal to interdecadal scales resulting from natural and human-induced forcing. The emphasis is on the use of models to perform the analysis. A physically based hydrologic model of the watershed is developed and applied in conjunction with an already-developed estuarine model to investigate the causes behind observed variability of the system.

An overview of the problem in Chapter 1 addresses the environmental problems threatening the health of the estuary, the nature of variability in California's

freshwater cycle, and relevant research. The U-P estuarine model is used in Chapter 2 to reconstruct the long-term behavior of Baywide salinity, revealing strong interannual variability linked to forcing of the watershed by atmospheric circulation patterns. Trends in magnitude and timing of the annual salinity cycle are shown to result from intraannual shifts in inflow timing.

In Chapter 3, streamflow is analyzed to reveal that while interannual variability is shared throughout the watershed, clear differences emerge at the seasonal scale. Management has a significant impact on flow patterns, partially masking "natural" signals. In Chapter 4, reconstructions of unmanaged flows are used to simulate unimpaired salinity. Management effects are strongly dependent on natural variability, though in extreme years these effects are small compared to the natural signal. Chapters 5-6 present the physical data and the model formulation which together are used to simulate watershed hydrology. This involves the development of new techniques of parameterizing hydrologic behavior and representing heterogeneity in the watershed.

The combined estuary/watershed model is used in Chapter 7 to examine the hydrologic mechanisms underlying long-term variability. Differing regional effects of snowpack are shown to contribute to interannual outflow variability. Patterns of climate variability coincide with these regional differences, with the result that climate forcing affects estuarine variability. Both naturally forced and human-induced variability are responsible for long-term trends in the estuary/watershed system, though the propagation of these signals has surprisingly nonlinear characteristics.

1 Introduction to the San Francisco Bay-Delta Estuary and Watershed

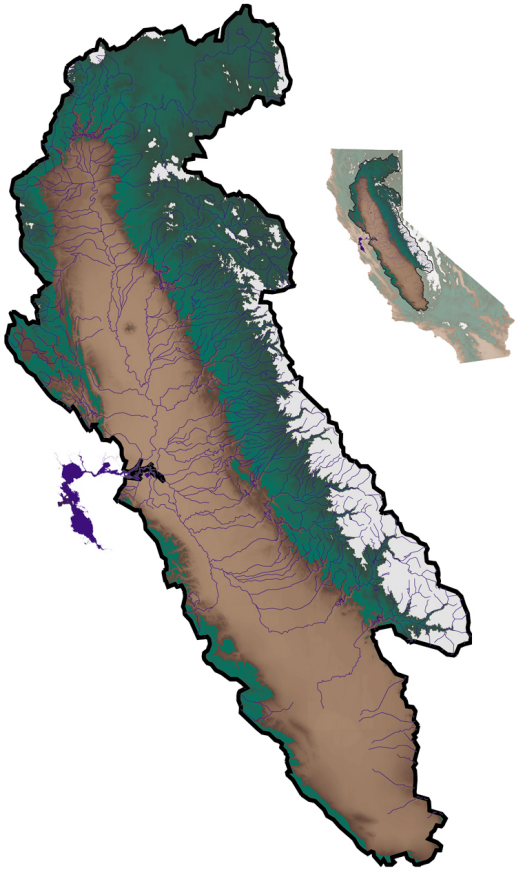

Figure 1.1 The San Francisco Bay-Delta estuary and watershed.

1.1 Overview

An estuary, defined as a body of water where fresh river water and salty ocean water meet, is by nature a very dynamic place. Where river and sea come together, a unique environment is created, since the amount of salt in water affects the dynamics, chemistry and biology in and around it. As the ocean supplies salt, the

rivers and streams which bring the freshwater into the estuary also bring nutrients and a supply of sediment, as well as contaminants. The interaction of river inflows with the seawater creates the constantly changing estuarine environment.

Twice daily, ocean tides cause seawater to rush in and out of the estuary. As this happens, salt is mixed into the estuarine waters (Figure 1.2). This acts in balanced opposition to the river flows, which tend to drive salt out of the estuary, replacing it with freshwater.

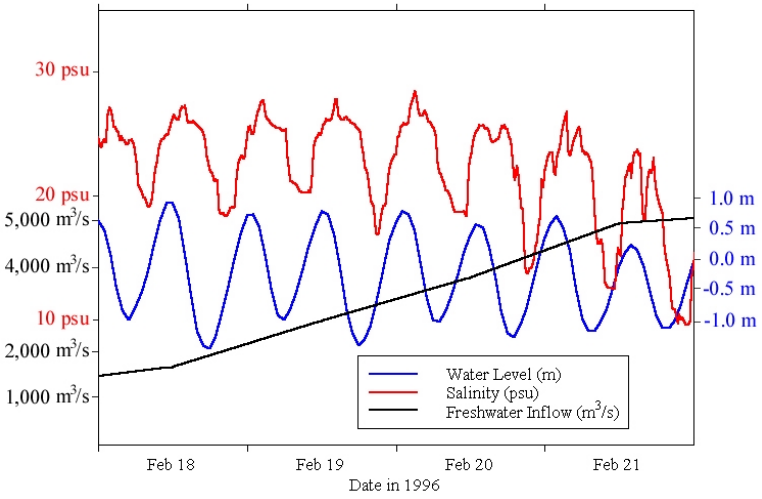

Figure 1.2 The tides, manifested as changes in the water level (blue) at the Golden Gate Bridge, force salty ocean water in and out of the estuary, as shown by the salinity value at the Bridge (red). The rate of freshwater flow into the Bay is shown in black. The longer-term evolution of all 3 values is shown in Figure 1.3.

While the daily to-and-fro of the tides maintains this balance in the short term, changes in the rivers cause a longer-term shifting of conditions in the estuary, resulting in the estuary's annual cycle (Figure 1.3). These changes are driven by conditions in the upstream watershed.

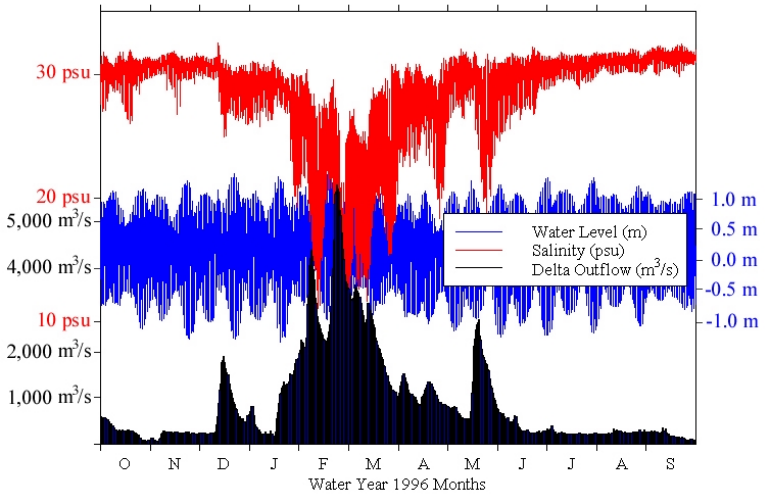

Figure 1.3 At the yearly time scale, changes in freshwater inflows drive salinity variability in the estuary. Compare to the shorter time scale shown in Figure 1.2, where tidal forcing drives the salinity variations.

An estuary's watershed is that area of land over which rainfall and snowmelt generate the streamflows which eventually reach the estuary. A watershed is typically much bigger than its estuary; the Bay-Delta's watershed (Figure 1.1) occupies about 140,000 km^2, nearly half of California's area. The river network in the watershed leads everywhere downstream towards the estuary.

Rivers such as California's have an inherent annual rhythm, with high flows during the part of the year when rain and snowmelt feed water into the river channels, and lower flows as these subside, leaving only deep groundwater to feed the streams. Ultimately, it is the generation of rain and snowmelt and their interaction with the soils and rivers of the watershed, combined with evaporative losses, which shape the estuary's annual freshwater flow curve, called the annual inflow *hydrograph*, such as the example shown in Figure 1.3. The hydrograph, in turn, drives the estuary, with the

changing supply of freshwater pushing against the relatively constant forcing of the tides. The result of this interplay is a steady annual shifting of estuarine conditions from salty to fresh and back again. Against the backdrop of this seasonal cycle is set the rich procession of the estuarine ecosystem: phytoplankton bloom, benthic clams graze, cordgrass grows, anadromous fish swim upstream to spawn, migratory waterfowl stop over, and a whole range of ecosystems, from riparian to marine, carry on in rhythm to the annual pulse of the rivers and estuary.

Once again, however, variety is the hallmark of the estuarine environment. This annual hydrograph, the pulse of the estuary and watershed, is not regular from year to year. Instead, it undergoes sometimes large swings in strength and timing, caused primarily by changes in the atmosphere. Some years, the atmosphere brings a great deal of moisture into the watershed, causing high flows and freshening the estuary. Other years are much drier, the low flows allowing the tides to mix salt far up into the estuary. The air temperatures in the mountains may stay quite cold well into the spring, preventing the snowpack from melting until early summer, this late runoff keeping the estuary fresh longer than usual. Conversely, a very warm spring could prevent the snowpack from accumulating very much; the resulting early runoff causing a large, peaked hydrograph which quickly flushes salt from the estuary but allows it to return as soon as the runoff subsides. Figure 1.4 shows some examples of this year-to-year variability.

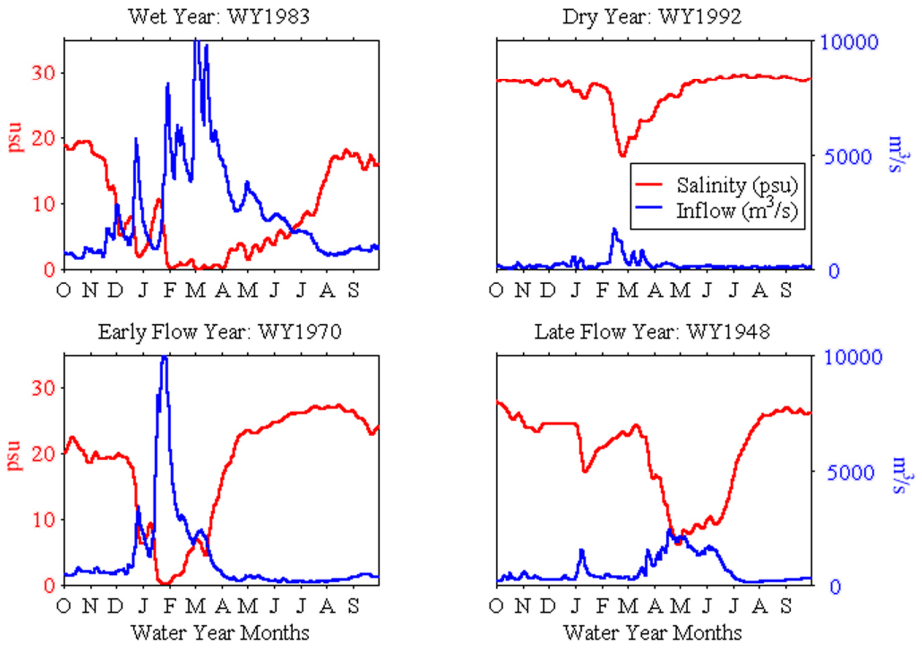

Figure 1.4 Examples of differences in annual runoff and salinity patterns. Salinity is in San Pablo Bay.

These dramatic year-to-year changes have repercussions throughout the ecosystem, most of which are just beginning to be understood (*e.g.*, Peterson, Cayan *et al.* 1995; Hollibaugh 1996). To what degree these effects may be viewed as a natural part of the ecosystem's functioning is a very complicated question, especially considering the degree to which the "natural" ecosystem has been disturbed by human activities. Such variations in the timing and amount of the freshwater supply can also have significant social and economic impact in California. Excessive rainfall in a short period can overflow reservoirs and cause severe flooding, as in the storms of January, 1997. Conversely, low total precipitation during a given rainy season can lead to freshwater shortages later in the year, potentially leading to water rationing, losses of agricultural and hydroelectric power commodities and other Statewide impacts. Low freshwater flow due to drought and excessive upstream diversions can lead to

unnaturally high salinities in the Bay-Delta estuary, potentially contaminating freshwater supplies and adversely impacting the health of the estuarine ecosystem (*e.g.*, Jassby, Kimmerer *et al.* 1995). Interannual to interdecadal variations are also of strong significance. Multi-year events such as the drought of 1987-1992 have cumulative effects on economies and ecosystems. Recently, a slow rise in winter temperatures since the 1940's has been identified which has led to earlier snowmelt runoff (Dettinger and Cayan 1995), effectively decreasing natural freshwater storage in the Sierra on the interdecadal time scale.

It is such year-to-year variations in conditions in and over the San Francisco Bay-Delta watershed, and their effect on the estuary, which are the subject of this dissertation. The interannual changes, as well as longer-term events such as multi-year droughts and interdecadal trends, are referred to as climate variability. Some of the questions which motivated the research presented here are:

1) What is the interannual and longer-term variability of salinity in the estuary? In what manner do atmospheric forcing and hydrologic response contribute to this variability?

2) How much of the freshwater which the atmosphere brings to the Bay-Delta watershed is stored as snowpack, how much is lost as evapotranspiration, and how much runs directly into the river network? Also, how does this apportionment vary from year to year and how does this affect the estuary?

3) What are the impacts of human intervention (*e.g.*, reservoirs) on river flows and conditions in the estuary, and how do these relate to natural variability?

Much of the work contained herein is aimed at the development of a combined estuary/watershed computer model which permits the investigation of hydrologic and estuarine behavior in the Bay-Delta system at a level of detail and accuracy sufficient to address the above questions. The estuarine component of the model, developed by Uncles and Peterson (Uncles and Peterson 1995) and refined by Knowles (Knowles, Cayan *et al.* 1995), is introduced in Chapter 2, where it is used to study estuarine behavior over the past seventy years, helping to answer question #1 above. In Chapter 3, observed and reconstructed flow data are used to characterize the hydrologic behavior of the watershed's individual river basins and the watershed as a whole. The Uncles-Peterson model is again employed in Chapter 4 to examine the impact of the watershed's reservoirs and freshwater diversions on conditions in the estuary (question #3). Chapters 5-6 pertain to the development and application of the hydrologic component of the combined model. It is important for the intended application of hydroclimate investigations that the model be physically-based (rather than based on calibrations), and the data needed to develop and run such a model is introduced in Chapter 5. Detailed examination of this data provides a thorough look at the properties of the watershed, and to some extent the atmosphere above it, which determine its hydrologic character. The data is aggregated to a grid to make it suitable for use in the new model. New techniques for aggregation of hydrologic processes are presented, and differing interpolation methods for meteorological data are compared. Chapter 6 presents the details concerning development and implementation of the watershed hydrologic model. Common methodologies are discussed, and a new approach

appropriate to the studies at hand is described. The incorporation of the data presented in Chapter 5 into the new model is also discussed. Finally, in Chapter 7 the new watershed model is applied to the research questions posed above, offering new insights into the hydroclimatic behavior of the estuary/watershed system.

The remainder of the present chapter offers an introduction to the San Francisco Bay-Delta estuary and watershed—its history, hydrologic cycle and physical characteristics, as well as some relevant recent research.

1.2 A Brief History

San Francisco Bay, like California itself, has been a vanguard in society's struggle to co-exist with the natural environment. As with many urbanized estuaries, demands placed on the Bay by a rapidly increasing population have pushed the ecosystem to its limits. Surrounding communities tap its resources for municipal and industrial uses, and waste waters flow in return. Bay waters support fisheries, and sustain commerce via shipping channels. A large portion of the Bay's freshwater supply is dammed or diverted to support agriculture in the Central Valley and to provide water for much of the state. The result of these combined stresses has been a steady decrease in the overall health of the estuary, indicated by severe declines of Bay fish and wildlife resources.

In 1775, the first Spanish ships sailed into San Francisco Bay and found a flourishing native culture which had existed there for over 3,000 years (Hedgpeth 1979). The flow of settlers into the area remained a trickle until the discovery of gold

near Coloma, California in 1848. The ensuing population boom embroiled the area and its finite natural resources in a tug-of-war among the varied interests of those who came to call this "land of opportunity" their home. In an effort to extract gold from the land more quickly, miners began to use high-pressure streams of water to blast apart the landscape. This method released huge amounts of sediment into local streams which was carried toward the ocean. The Bay began to silt up at an alarming rate, though it was not a concern for looming environmental disaster which ultimately ended the practice of hydraulic mining in 1884. Farmers, who had diked and leveed much of the low-lying Delta marshland, complained that the irrigation water was becoming too muddy to use (Atwater, Conard *et al.* 1979).

With the coming of the Industrial Revolution, factories began springing up around the Bay, particularly in the northern reach where freshwater arrives from the Central Valley. Bay water was used in manufacturing processes, and industrial effluent was discharged. A less obvious threat to the Bay developed as California's population steadily grew, and the demands placed on the State's finite water supply increased with it. The supply of freshwater which flowed from the western slopes of the Sierra-Nevada through the Sacramento and San Joaquin valleys to the Delta and on to the ocean, flushing out salt and contaminants as it went, was being tapped for municipal and agricultural uses before it could reach its natural destination. As the demand increased, so did the ambition of the planners. The State Water Project, the Central Valley Project, and numerous dams, reservoirs and canals collectively represent the largest civil engineering project in the world. This ability to control the

flow of California's most precious resource has transformed arid Central Valley into the country's most bountiful agricultural region and allowed civilization to thrive in the desert climate of the Southwest (Kahrl, California Office of Planning and Research *et al.* 1979). The management of water has provided the state with the level of prosperity it enjoys today.

Only in the last few decades has concern with the environmental consequences of such actions become a factor. The natural destination of the freshwater endowment, the Bay-Delta estuary, became a focus of scientific inquiry. Researchers began studying the estuary in detail, accumulating knowledge and monitoring conditions. After some years, long-term trends became evident. Salinity in the Bay, naturally a highly variable quantity, exhibited a long-term rise which was linked to the increasing diversions of freshwater. Adverse population trends were also detected and linked to salinity changes, and several species unique to San Francisco Bay's estuarine environment were nearing or had already achieved endangered status (Jassby, Kimmerer *et al.* 1995).

To address these problems, the State and federal governments have endeavored to establish standards of water quality which would ensure the Bay's future health and still allow humans to draw upon this vital resource. Under the guidance of the Environmental Protection Agency, the California Water Resources Control Board adopted a set of criteria intended to strike this balance (Herbold 1995; US Environmental Protection Agency 1995). A key component of these standards is that surface salinities at North bay monitoring sites (Figure 1.8) not exceed 2 *psu* for more

than the specified number of days during the "management period" February 1 through June 1. These standards have been satisfied primarily by an appropriate management of dam releases and controlled freshwater diversions upstream of the Bay. Such tactics are also used to repel salt water from freshwater pumping stations (Figure 1.8) which supply drinking water for much of California.

Recent years have seen continued attempts to reconcile the various demands placed upon the State's freshwater. The Bay-Delta and its upstream rivers have become the focus of "the largest and most comprehensive ecosystem restoration and water management program in the world" (http://www.governor.ca.gov/briefing/pressreleases/jun00/pr0014569.html). It is imperative that the continued attempts to understand the Bay-Delta estuary include the effects of climate variability on the freshwater supply. Large year-to-year swings, multi-year episodes of drought and abundance, and interdecadal changes are an inevitable part of the estuary/watershed system, and both management and restoration efforts must take this into account if they are to succeed.

1.3 California's Hydrologic Cycle

1.3.1 Ocean and Atmosphere

The amount of moisture which ultimately reaches the Bay-Delta watershed is determined most directly by atmospheric conditions over the eastern portion of the Northern Pacific Ocean. Meridional variations in ocean heating by the Sun are the primary factors driving the atmospheric patterns. California summers are typically dry

because a high pressure cell which forms over the eastern North Pacific deflects storms to the north. During the winter this cell migrates south and loses intensity, while the Alaskan-Aleutian low pressure center strengthens. As latitudinal temperature and pressure gradients grow, more storms pass across the Pacific. When the Alaskan-Aleutian low forms close to the west coast of North America, these storms may pass over California and yield significant precipitation. However, if the low forms further to the west, an anomalous high pressure cell may develop near the west coast and divert the winter storms to the north, resulting in a drier than average year.

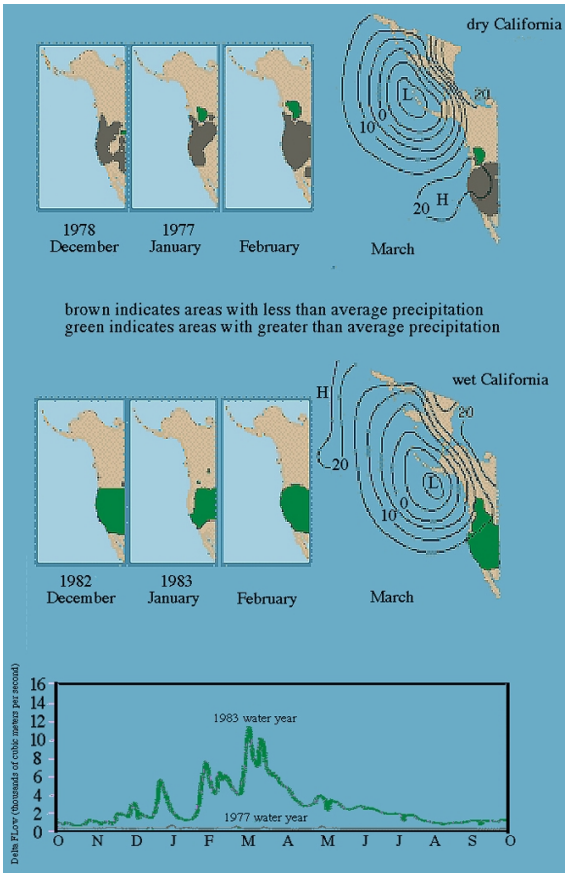

Figure 1.5 Typical atmospheric circulation patterns for wet and dry years, with associated Delta outflow rates (from Peterson *et al.*, 1995).

Figure 1.5 shows the characteristic atmospheric circulation patterns associated with particularly wet and dry years (Peterson, Cayan *et al.* 1995). This year-to-year variability is reflected in San Francisco Bay's freshwater inflows and salinity. The influence of these large-scale atmospheric systems links global climate patterns to the variability of California's freshwater supply and estuarine water quality. A combined estuary/watershed model would supply a needed link between estuarine behavior, watershed-scale hydrology and existing global and mesoscale atmospheric models, providing a tool for investigation of these connections.

1.3.2 Land

1.3.2.1 The Freshwater Endowment

California receives an annual average of nearly 250 cubic kilometers of freshwater in the form of rain and snow. Of this, about 40% ultimately becomes streamflow in the State's river network (Kahrl, California Office of Planning and Research *et al.* 1979), which culminates at the Delta of the Sacramento and San Joaquin rivers at the head of San Francisco Bay (Figure 1.1). This freshwater supply is highly managed to ensure adequate supplies throughout the year. While most of this water originates in the northern third of California, a substantial portion is collected in artificial reservoirs during the rainy season for later conveyance to the areas of greatest demand in Central and Southern California. Controlled releases of stored freshwater are also used to flush saltwater from the Delta region and San Francisco Bay,

protecting freshwater supply stations and maintaining the health of the Bay-Delta ecosystem.

1.3.2.2 Description of the Watershed

The generation of precipitation over the watershed of Figure 1.1 is best understood by examining an east-west cross-section (Figure 1.6). Most of California's precipitation is orographic in origin as the moist air from the Pacific is forced to rise over the Sierra.

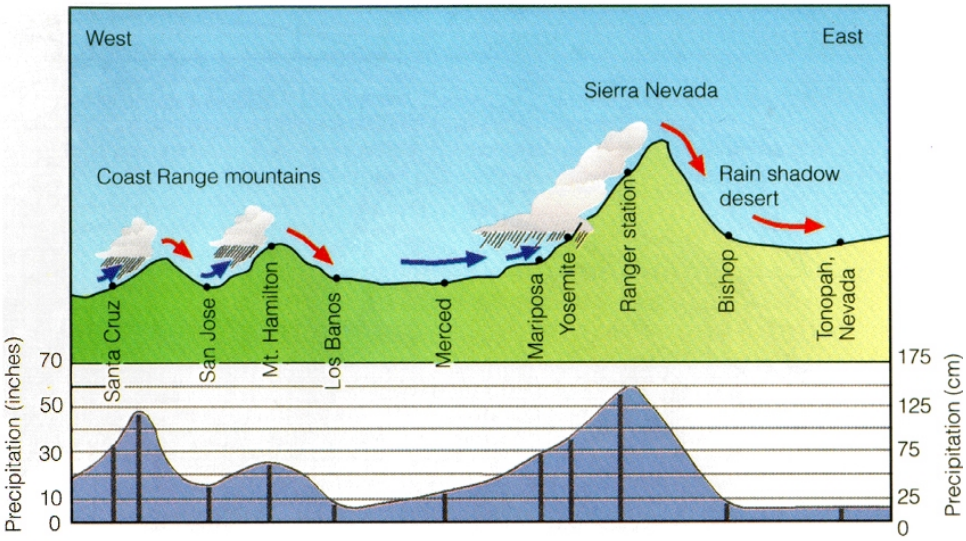

Figure 1.6 Typical orographic forcing of winter storms on an east-west cross-section of the watershed. Nearly all Coast range precipitation falls outside the watershed. Orographic forcing by the Sierra generates most of the Bay's freshwater (from Ahrens 1994).

This water, along with precipitation from throughout the watershed, has the Bay as its natural destination. Runoff from winter storms collects over the watershed's approximately 140,000 square kilometers, an area comprising nearly 40% of the state of California (Conomos, Smith *et al.* 1985). This water eventually flows into the major

valley river systems which terminate in the Delta of the Sacramento and San Joaquin rivers at the head of San Francisco Bay.

The network of rivers which feeds the Bay-Delta estuary is visible in Figure 1.1. These rivers carry water from the western slopes of the Sierra-Nevada mountains to artificial reservoirs in the Sierra foothills, where it is stored as reservoir capacity permits. Also, the Sierra-Nevada mountains, particularly the high-altitude Southern Sierra, provide natural freshwater storage in the form of snowpack. Although most of the precipitation occurs during the late winter and early spring, this natural storage typically delays about 40% of the total streamflow until the months April-July (Roos 1989), an advantageous effect for meeting summer and autumn freshwater demands. The combined natural and artificial storage make it possible for rainy season freshwater endowment to last throughout the year, though dependence on the freshwater management system also creates vulnerability to natural variability of the freshwater supply.

The hydrology of individual river basins varies dramatically across the watershed. Sacramento River flow is dominated by direct runoff from storms over the western slopes of the northern Sierra, while San Joaquin River flow is primarily due to the melting of accumulated snowpack in the southern Sierra (see, *e.g.*, Dettinger and Cayan 1995). This leads to a difference in the timing of the peak flow in the two rivers as shown in Figure 1.7 (upper plot), which shows the typical annual hydrology of the basin. Since the peak in the Sacramento River flow is associated with direct runoff from storms, it coincides with the winter/spring rainy season (Cayan and Peterson

1993). The greater elevations of the southern Sierra mean that much of the precipitation there is retained as snowpack until temperatures rise enough for melting to occur, usually in late spring and early summer. The combined effect of these natural flows is represented in Figure 1.7 by the "eight-rivers index" (green line), a value intended to represent the total available freshwater flowing into the basin.

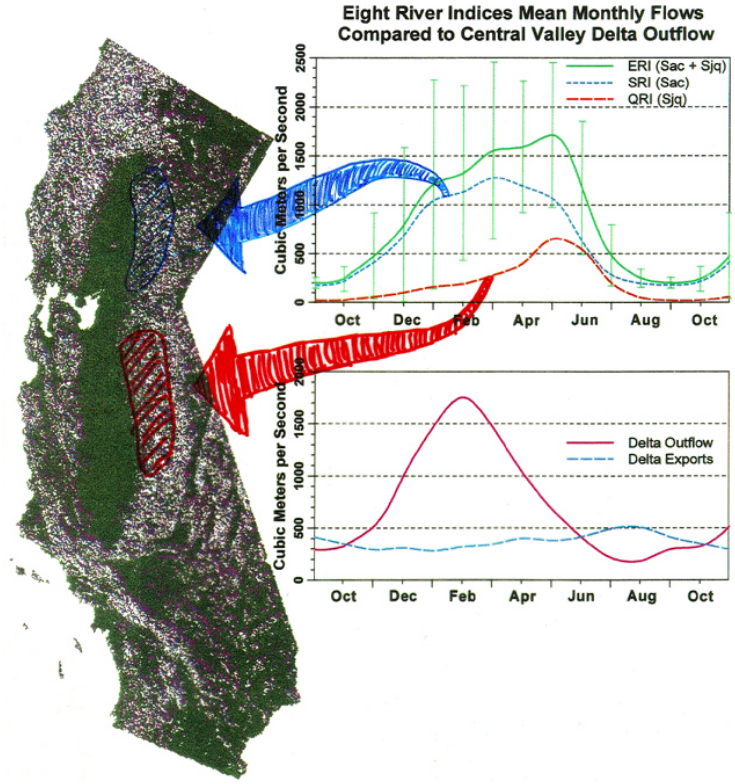

Figure 1.7 Upper plot shows regional contributions to flow; lower plot shows how much reaches the Bay and how much is diverted (plots are by Larry Riddle, SIO).

As this freshwater flows through the valleys, some is lost to seepage into underground reservoirs, some to evaporation, and a large portion is dammed and used for municipal supplies and irrigation. When the remaining flow reaches the Sacramento/San Joaquin Delta, it is subject to further reduction by the State Water Project which pumps freshwater from the Delta to supply Southern California with

much of its water, the Central Valley Project which supplies water primarily for irrigation, and several local canals which provide supplies for the Delta region (see Figure 1.8) (Kahrl, California Office of Planning and Research *et al.* 1979). These combined diversions are represented as "Delta exports" in Figure 1.7 (lower plot). The remaining flow which actually reaches San Francisco Bay typically resembles the "Delta outflow", also shown in this figure. The typical annual Delta outflow is about 20 billion cubic meters, compared to the Bay's total volume of about 6.7 billion cubic meters (Conomos, Smith *et al.* 1985).

1.3.3 Estuary

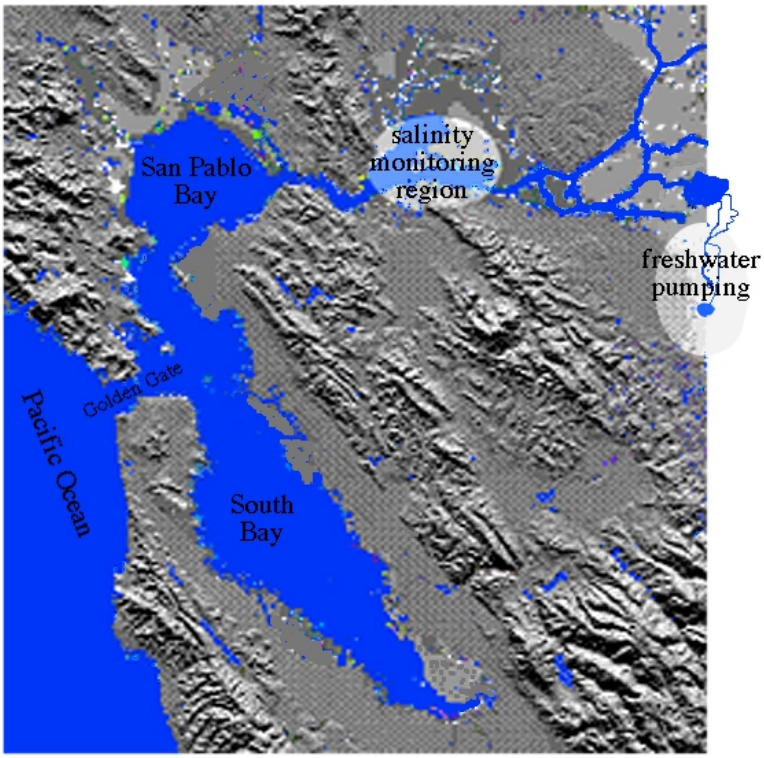

Figure 1.8 The San Francisco Bay-Delta estuary, with key management areas highlighted.

San Francisco Bay and the Sacramento/San Joaquin Delta region comprise one of the world's most significant estuarine systems. With a surface area of about 1000 km^2 and a length of over 100 *km*, it is the largest estuary on the West coast of the United States. The Bay's sole connection with the open ocean is through the Golden Gate, where relatively fresh water flows seaward near the surface and the more saline waters of the Pacific flow landward through a deep (~100 *m*) channel. Semidiurnal tides cause sea surface elevations to vary as much as 2 *m* at the Golden Gate, forcing tidal waves which propagate throughout the estuary (Conomos, American Society of Limnology and Oceanography *et al.* 1979). Most of the energy for mixing saltwater into the estuary comes from these tidal motions. The other main contributor to the landward salt flux is the estuarine circulation, a density-driven flow in which horizontal salinity gradients drive saline bottom waters up the estuary. Counteracting these salinifying effects is the freshwater inflow from the Delta, resulting in an along-estuary salinity gradient from freshwater in the Delta to near-ocean salinities at the Golden Gate. At weekly and longer time scales, the tidal mixing effect is relatively constant, so the longitudinal salinity profile depends primarily on variations in inflow. When flows are at their peak, the freshwater signal overrides the up-estuary salt flux and the entire northern reach rapidly becomes fresher. As flows subside, tidal mixing and estuarine circulation begin to dominate, slowly pushing the more saline water up the estuary. An example of the extent of these changes on seasonal and interannual scales is shown in Figure 1.9. Note that the freshest distribution of 1994 (Figure 1.9,

middle) is nearly as saline as the typical dry-season distribution (left), while 1995 shows strong freshening throughout the Bay (right).

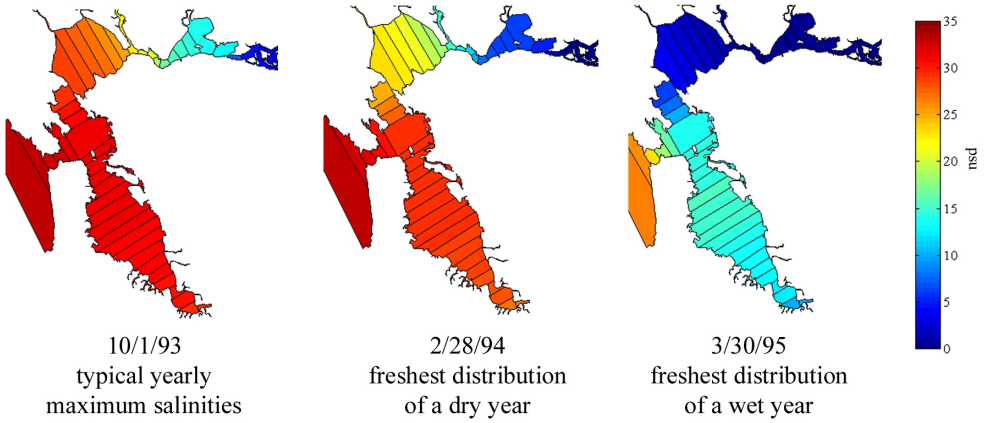

Figure 1.9 Samples demonstrating seasonal and interannual salinity variations. The left plot is typical of a year's most saline, dry-season distribution. The middle is the freshest distribution from a dry year, 1994, and on the right is the freshest distribution of the wet year 1995.

This strong response to variations in freshwater inflow affects physical and biological processes throughout the Bay, linking the estuary's behavior to the hydrologic and atmospheric variability and upstream management which drive the Delta outflow.

1.4 Prior Research Linking Climate Variability to the Bay-Delta Estuary and Watershed

The relationship between global and regional climate patterns and behavior of the estuary and watershed is a topic which, in the last few decades, has moved from the fringes of science to the mainstream, now beginning to enter into policy considerations.

One of the first climate-related subjects to enter the spotlight was global warming. As awareness of this concept grew, its implications for water supplies became a subject of concern, particularly in California where the limited water supply is extremely important. Impacts of global warming scenarios on runoff timing and amounts were estimated using a variety of methods (Gleick 1986; Roos 1989; Lettenmaier and Gan 1990). These were among the first studies to employ computer models to assess the potential impacts of climate change in California. They provided quantitative estimates of the timing and magnitude of impacts of warming on streamflow. These studies were typically limited to individual river basins within the Bay-Delta watershed.

Though global warming was among the first climate-scale events to gain widespread attention and continues to be the subject of intensive investigation (*e.g.*, Knox 1991; Wilkinson and Rounds 1998), hydroclimatology has rapidly grown into a rich and varied field of research in which global warming is one of many topics of interest. In California, precipitation, snowpack, streamflow and estuarine water quality have all been linked to intraannual and interannual variations in climate.

For example, variability in total annual precipitation have been linked to specific patterns of winter-spring atmospheric circulation associated with climate variability (Schonher and Nicholson 1989; Redmond and Koch 1991; Dettinger, Cayan *et al.* 1998; Cayan, Redmond *et al.* 1999). Studies such as these forge a direct link between climate variability such as the El Niño/Southern Oscillation and events of human and ecological importance such as flooding. Also, the seasonal influence of

precipitation and temperature on streamflow has been shown to vary significantly for different basins of the Sierra-Nevada (Aguado, Cayan *et al.* 1992; Cayan, Riddle *et al.* 1993), demonstrating directly the link between meteorological patterns and hydrologic variability within the Bay-Delta watershed.

The watershed itself has been shown to respond directly to interannual to interdecadal climate forcings. The relationship between interannual variations in precipitation and temperature and streamflow contributions from snowpack throughout the West have been clearly demonstrated and quantified, revealing large, coherent patterns of variability (Cayan 1996). Snowmelt in the Sierra-Nevada has been shown to undergo a transition each year, typically marked by a runoff "pulse". This pulse is correlated with similar signals in streams throughout the west, marking the onset of higher streamflow conditions triggered by large-scale atmospheric patterns across this region (Cayan 1999; Peterson, Smith *et al.* 2000). Longer-term but similarly widespread trends have been observed in snowpack which reveal that yearly snowmelt occurred progressively earlier from the 1940's through the 1990's, resulting from trends in atmospheric forcing (Roos 1987; Roos 1989; Dettinger and Cayan 1995). Such studies show that the watershed is intimately linked to global-scale patterns of climate variability.

Several studies have extended the analysis of hydroclimate variability in the Bay-Delta watershed downstream to the estuary. The relative contributions of the major Sierra rivers to the net inflow to San Francisco Bay have been found to show a marked seasonal dependency, and this variability across the watershed shapes the

annual salinity cycle at the Golden Gate (Dettinger 2000). Simulations of Bay salinity have been used to examine the relationship between salinity extremes, freshwater inflows, and atmospheric patterns, revealing that the link between climate and watershed clearly extends into the estuary (Peterson, Cayan *et al.* 1995). Further, studies of estuarine and watershed variability have recently been extended to paleoclimate time scales, demonstrating that these relationships have been an ongoing feature of the estuary and watershed throughout its history (Ingram, Ingle *et al.* 1996; Wells, Goman *et al.* 1997).

The connection between estuarine behavior and climate variability is not unique to the San Francisco Bay-Delta, nor are the many controversial issues surrounding the estuary. Since the behavior of an estuary is linked to the coastal ocean and to the inland rivers, understanding the behavior of any given estuary entails the study of atmospheric conditions which lead to precipitation over its watershed, as well as the processes which affect snow accumulation and melting where applicable. Also important are the hydrologic processes in which topography and soil moisture affect the water's flow through the estuary's watershed. The complex interaction of the ocean, atmosphere and land processes which drive estuarine behavior means every estuary is unique and may be understood only as a product of its total environment. The work which follows is an attempt to extend the current understanding of the way in which the Bay-Delta estuary and its watershed respond physically to changes in their environment at seasonal to interdecadal time scales.

2 Large-Scale Dynamics and Long-Term Variability In San Francisco Bay Estuary

Figure 2.1 1999 LANDSAT image of the Bay and surroundings.

2.1 Why Study Estuarine Variability at Large Scales?

The San Francisco Bay-Delta estuary is renowned for its natural beauty and its importance as a major port, the “Golden Gateway” to and from the Pacific. It is perhaps even more significant as a unique ecosystem, offering the third largest estuary in the U.S. as habitat for a wide variety of flora and fauna, including many endangered species. In the last few decades, the Bay-Delta has come under intense scientific

scrutiny, stimulated largely by concerns about destruction of natural habitat, contamination of the rivers and estuary, and declines in aquatic species populations.

Like all estuaries, behavior of the Bay-Delta estuary is linked to the coastal ocean and to the inland rivers, resulting in high variability at many scales. Observational and modeling studies of hydrodynamical, biological and chemical processes have greatly increased understanding of the estuary's inner workings at subestuary/seasonal and smaller scales (*e.g.*, Conomos, American Society of Limnology and Oceanography *et al.* 1979; Cloern and Nichols 1985; Hollibaugh 1996). Recently, increasing attention has been given to variability at larger scales, with an emphasis on long-term (10-100 years) trends, primarily in the upstream watershed (Roos 1991; Cayan and Peterson 1993; Dettinger and Cayan 1995; Peterson, Cayan *et al.* 1995). In this chapter, reconstructed Bay variability over the past 69 years will be used to examine the long-term, large-scale behavior of the estuary.

To study the estuary at these scales means examining behavior across the major subestuaries (South, Central and the northern Bays) at time scales from weeks to decades. A broad spatial perspective is useful because it acknowledges the interconnectedness of the parts of the estuary and provides the macroscale context within which the finer scale processes occur. Considering the estuary's behavior on time scales from weeks to decades allows the influence of climate variability to be included in the study. Climate variability, both "natural" and human-induced, is an inevitable part of the estuarine ecosystem, determining the range of conditions which form the year-to-year, decade-to-decade physical context of the estuary. Studying the

estuary at these spatial and temporal scales helps to better understand this large-scale context and to begin to assess the implications for the estuarine ecosystem and all its parts.

2.2 Method of Study

To examine the estuary's behavior over the past seven decades, a model capable of simulating such a long period (without excessive computational demands) while still accurately representing the macroscale behavior of the entire Bay is essential. The Uncles-Peterson (hereafter U-P) numerical water quality model (Uncles and Peterson, 1995) simulates the intertidal width-averaged salinity and along-axis current fields at a daily time scale. Dividing the Bay into 50 horizontal segments of 2 vertical layers each (Figure 2.2), the U-P model uses a box model approach, enforcing salinity conservation on a framework of theoretically determined flows. Using only five inputs (discussed in detail later), the model calculates the combined effect of tidally-induced mixing, density gradient-driven flows and river inflow forcing on the salinity and current fields for each simulated day. Intratidal processes, including tidal mixing effects, have been parameterized for the Bay using results from a higher resolution intratidal numerical model (Uncles 1991). This provides the model with its key strengths—ease of use and speed—with little loss of accuracy. It has been applied in several previous studies of the Bay and has been shown to accurately reproduce salinities at weekly to interannual time scales over a wide range of flow regimes (*e.g.*, Peterson, Cayan *et al.* 1995; Knowles, Cayan *et al.* 1997; Knowles, Cayan *et al.*

1998). A detailed description of the model's structure and performance was given by Knowles (Knowles 1996). A brief summary of that discussion follows.

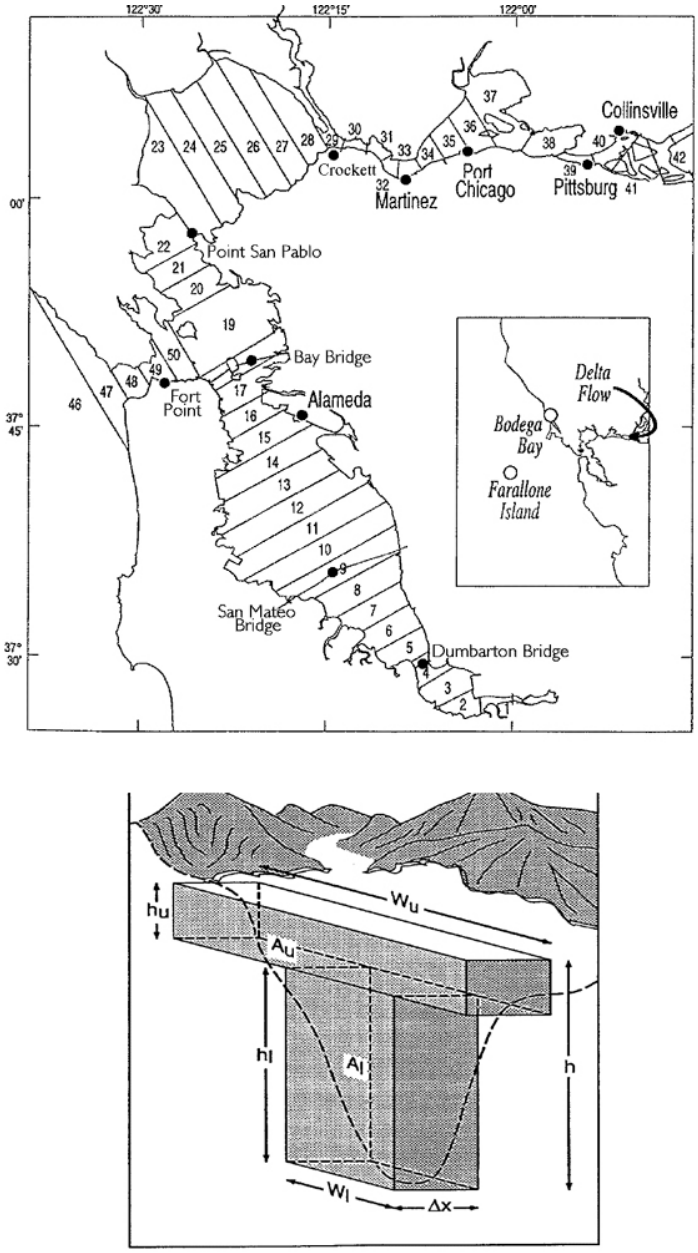

Figure 2.2 Uncles-Peterson model schematic. The upper plot shows the model's segmentation along the estuary, and the lower plot shows the division of each segment into two vertical layers.

The basic equation governing the salinity balance in the U-P model assumes the rate of change of salinity S is determined by along-estuary (x) and vertical (z) advective and diffusive fluxes in a laterally-averaged system:

$$\frac{\partial}{\partial t}(BS) = -\frac{\partial}{\partial x}(BUS) - \frac{\partial}{\partial z}(BWS) + \frac{\partial}{\partial x}(BD\frac{\partial S}{\partial x}) + \frac{\partial}{\partial z}(BK\frac{\partial S}{\partial z}) \quad 2.1$$

where U and W are laterally- and tidally-averaged longitudinal and vertical current velocities, K is the vertical eddy diffusivity, D is the longitudinal (x-direction) dispersion coefficient and B is the estuary's width. This equation is solved for each day of the simulation. With a time step of one day, the model cannot resolve tidal motions; instead it simulates residual (tidally-averaged) salinity distributions and current velocities. Daily forcing inputs are local precipitation and evaporation, salinity at the mouth of the estuary, freshwater inflow rates and tidal state which varies with the spring-neap cycle. Using these inputs along with the previous day's values for residual currents and salinities, the four terms in the salt balance (Equation 2.1) are calculated for each of the model's 100 boxes. These calculations are described in the following paragraphs, in which formulae are omitted for brevity. For a full discussion, see Knowles (Knowles 1996).

The longitudinal diffusivity D is calculated based on established formulae for estuarine dispersion (*e.g.*, Fischer, List *et al.* 1979) and using parameterized results from a high-resolution intratidal model (Uncles 1991) to estimate current velocities throughout the Bay based on tidal state. Vertical diffusivity K is estimated based on vertical salinity and velocity gradients from the previous time step using formulations

due to Uncles and Joint (Uncles and Joint 1983) and Munk and Anderson (Munk and Anderson 1948).

Along-estuary current speed, U, is calculated in each layer using expressions derived from basic principles of the balance between the pressure gradient force and the vertical gradient in turbulent stress, in addition to forcing due to inflows. Vertical currents are calculated based on conservation of mass after inflows, local precipitation and evaporation, horizontal and vertical mixing, and horizontal advection are taken into account.

With all quantities in Equation 2.1 established, the resulting inverse problem for salinity conservation is solved using a least squares method to provide the updated salinities and residual currents. The entire process is repeated for the next simulated day, and the evolution of the daily- and laterally-averaged salinity and velocity fields is obtained.

Sample model output at six locations throughout the Bay are shown, along with observations of surface salinities, in Figure 2.3. It is remarkable that the U-P box-model approach, based on a few principal theories of estuarine dynamics, manages to capture variability over the entire dynamically diverse Bay. Root-mean-square errors are under 1.6 *psu* for all stations shown, considerably less for most. Correlations are quite high, greater than 0.90 for all stations except Point San Pablo, where r=0.81. A greater discrepancy between simulation and station data is expected in this wide embayment, as the sensor is on the southeast shore while the model output represents an average across the width of the Bay.

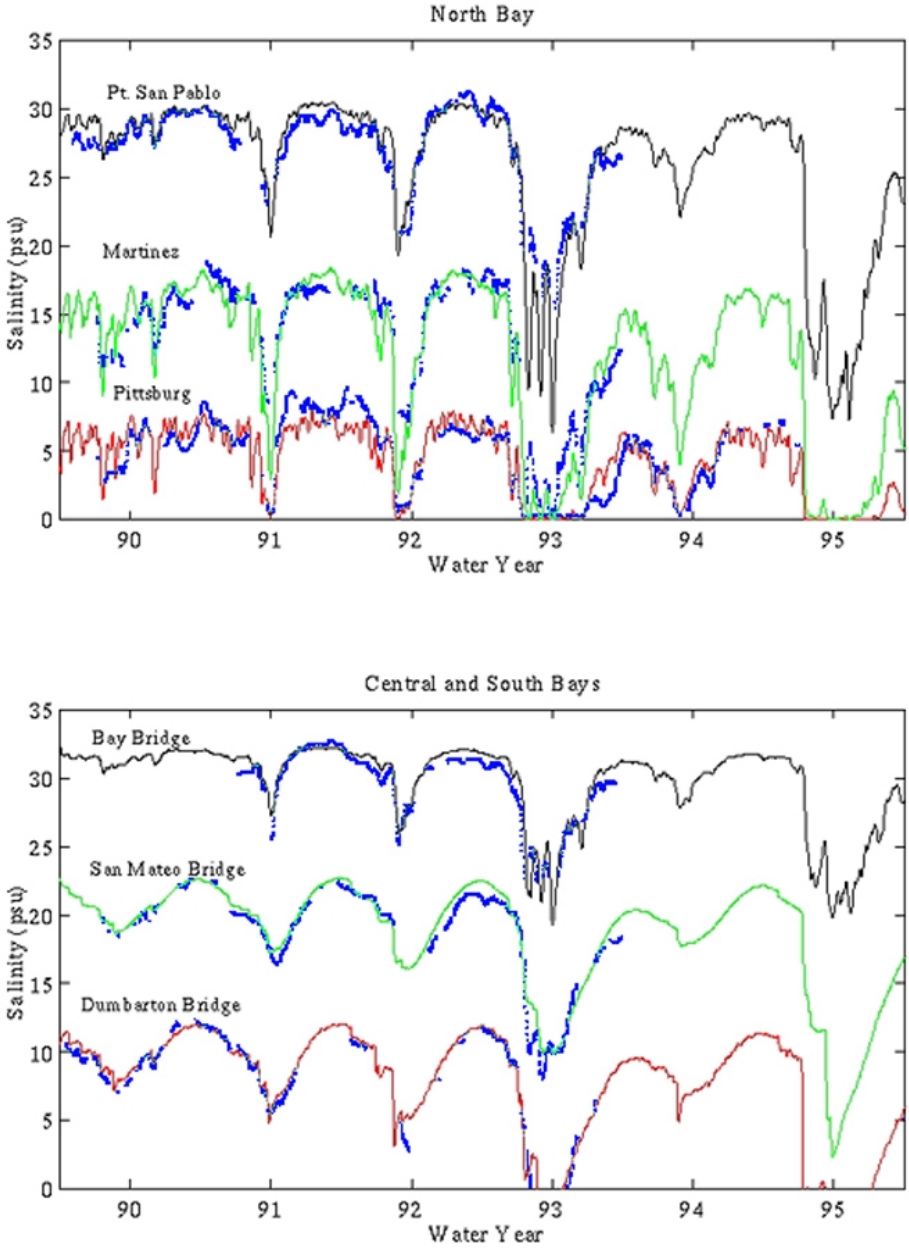

Figure 2.3 Simulated salinities (solid lines) and observations (blue dots) from several stations throughout the Bay. Observations at San Mateo and Dumbarton Bridges are offset by –10 *psu* and –15 *psu*, respectively.

For the present study, estimates of daily Delta outflow rates from 10/1/29 through 9/30/98 (California Department of Water Resources 1999), along with tidal

hindcasts, were used to drive the U-P model. This yielded estimates of daily-averaged salinity throughout the Bay for this 69-year period. This work examines the long-term variability of the salinity field at the surface of the estuary along its length. For examples of lateral and intratidal salinity variability, see Smith and Cheng (Smith and Cheng 1987). For a detailed treatment of stratification effects using this model, see Uncles and Peterson (Uncles and Peterson 1996).

The simulated salinities were examined using extended empirical orthogonal function (E-EOF) analysis (Weare and Nasstrom 1982). The E-EOF method is a variant of empirical orthogonal function (EOF) analysis. EOF analysis is a useful tool for analyzing spatially- and temporally varying fields because it describes orthogonal "modes" of variability representing simultaneously correlated (positively or negatively) behavior across the spatial domain, with modal amplitudes varying in time.

To illustrate, an example (not shown in figures) is an EOF analysis of seasonally-averaged (*i.e*, OND, JFM, AMJ, JAS) salinity data at all segments of the U-P model (Figure 2.2). Such an analysis would yield several spatial modes, each mode consisting of a single value (a "loading factor") for each model segment, representing the tendency of salinity in the different segments to vary with or in opposition to each other as the seasons progress. Each mode would have an associated amplitude value for every season (3-month period) of the record, indicating whether the behavior of the salinity field associated with the mode was positive or negative,

and how strongly, for that particular season. Each combination of a spatial mode and its time series amplitude would explain part of the overall variance in the salinity field.

The E-EOF variant incorporates a portion of the temporal variability into each mode by considering all data across the spatial domain and within a certain time interval to be one vector in the analysis. Translating the EOF example to the E-EOF method applied in the present study, the basic unit of the analysis is no longer the set of salinity values for all segments for a given 3 month period, but all four such sets within each water year (WY)[*]. The resulting modes each consist of four sets of spatially-distributed loading factors, one for each segment and each season. Now the modes represent not only the tendency of salinity at different points in the Bay to be correlated, but also the tendency of salinity to be correlated (positively or negatively) across the seasons of the water year. Each modal amplitude now has only one value per year, corresponding to the magnitude of the location-to-location and season-to-season behavior represented by the mode for that particular water year.

This method offers insight into both the geographic and the seasonal salinity variability. Also, it inherently removes the mean annual cycle of seasonally-averaged salinities from the analysis. The resulting seasonal/spatial modes reveal prevalent patterns of season-to-season Baywide surface salinity variability, as well as the relative importance of the modes for each water year of the 69-year record.

[*] A water year begins on October first of the previous year. For example, water year 1999 (WY1999) began on October 1st, 1998 and ended on September 30th, 1999.

2.3 Interpretation of the E-EOF Modes

In this discussion, only the first two E-EOF modes will be considered, as they capture most of the variability of the interseasonal Bay-wide salinity field. The spatial loading factors for these modes are shown in Figure 2.4 along with their corresponding amplitude series for the entire 69-year record. To illustrate the real effects on salinity which these modes represent, consider water year 1998 in San Pablo Bay. The first mode has an amplitude of ~-12 in this year. San Pablo Bay has a loading factor of ~+1 in the winter and spring, less in other seasons. Multiplying the loading factor by –12 reveals that this mode represents a freshening of San Pablo Bay in winter and spring of WY 98 by about 12 *psu* over the long-term averages for these seasons. The other seasons have much smaller, though still positive loading factors, so this mode represents a much smaller freshening in those seasons. The other mode works similarly, and when added together these two modes explain 88% of the total variance—a large portion of the Bay's salinity variability.

2.4 Modes Reflect Different Aspects of the System

The E-EOF analysis automatically yields modes which are strikingly different from one another (since they are orthogonal), though this is often only an artifact of the analysis. Nonetheless, the two modes in this case reflect distinct behaviors of the watershed/estuary system.

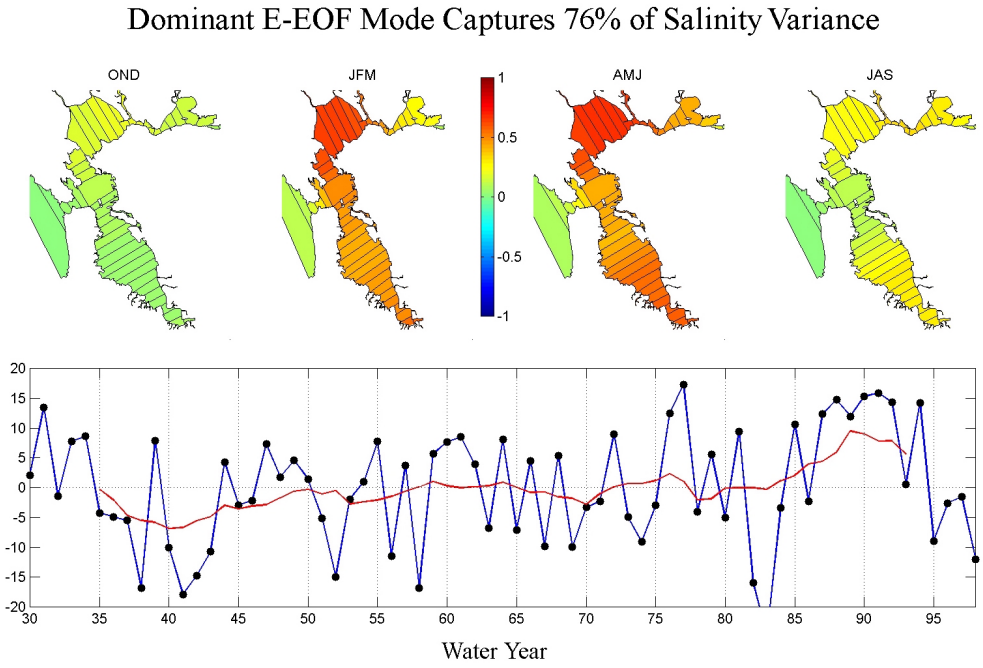

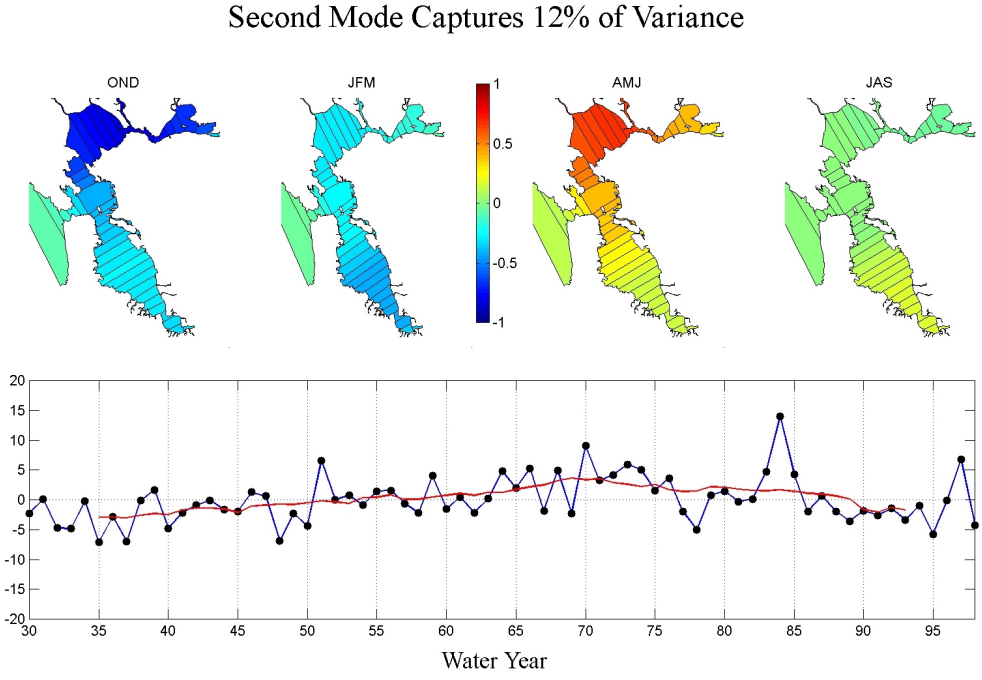

Figure 2.4 The first 2 E-EOFs with spatial loadings and temporal amplitudes. The first mode represents the magnitude of the annual salinity cycle, while the second indicates intraannual timing shifts. The red lines represent a 10-year running average of these modal amplitudes.

The first mode shows the annual cycle of salinity variability. It has high loading factors during JFM and AMJ, reflecting the naturally high variability of the Bay during these rainfall and snowmelt seasons. Note also the peak variability in San Pablo Bay due to the tendency for high salinity gradients there. The remaining seasons, OND and JAS, show very little deviation from the mean annual cycle, though JAS shows the relatively small effects in the northern reach of late-season snowmelt variability and wet-year reservoir releases. It is interesting to note the apparent long-term saline trend evident in the 10-year running average of the first mode's amplitude. This trend indicates a change of 10-15 *psu* from ~WY 40 to ~WY 90 in San Pablo Bay in winter and spring. It is important to note, however, that the early 40's were marked be several very wet years, while WY 90 was in the middle of a several-year drought, making this "trend" appear larger than it might otherwise.

The second mode represents shifts in the timing of the annual salinity cycle. When its amplitude is positive, it represents lower salinities in OND and JFM, and higher salinities in AMJ. From 1930 to 1970, there appears to be a long-term trend in this modal amplitude corresponding to a shift of freshwater inflows from AMJ to JFM. Though this trend indicates a change of up to 5 *psu* in San Pablo Bay over 40 years, it appears to have slackened since 1970, possibly reflecting a change in human effects. These long-term trends will be examined in more detail later.

Both modal amplitudes demonstrate strong interannual and multi-year variability. To begin to understand what is driving these modes' behavior, it is necessary to first examine the factors which influence the Bay's salinity.

2.5 What Factors Influence the Bay's Behavior?

Several factors influence the estuary's behavior as reflected by the salinity. These influences take on varied relative significance in different parts of the Bay and as the seasonal cycle progresses. The dominant influences on San Francisco Bay's salinity field are freshwater inflows (with significant inputs into South Bay and through the Delta), tidal mixing, near-shore ocean salinity, local precipitation and evaporation. Wind effects can be significant, but are usually a minor factor (see Smith 1987 for a relevant discussion), and wind is not included in the U-P model or in this study. Data representing the other quantities are used to drive the model, generating the daily-averaged salinity distributions as output.

2.5.1 Mean Annual Cycles of Forcing Factors

Figure 2.5 shows the mean annual cycles of the model inputs, except for the tidal state for which only a sample year's data are shown to keep the important spring/neap signal intact.

The evaporation forcing, which consists of a monthly annual cycle estimated from pan data at the San Francisco airport (Uncles and Peterson 1996), varies from 0.8 *mm/day* in the winter to 5.3 *mm/day* in summer. This amounts to removing from 10 to 65 m^3 of freshwater per second. Local precipitation is also based on measurements at the airport (Null 1995) and the mean annual cycle peaks around 3 *mm/day* in the

winter. Note the noisiness of this mean annual cycle indicating that local precipitation effects have a strong component at daily as well as seasonal time scales.

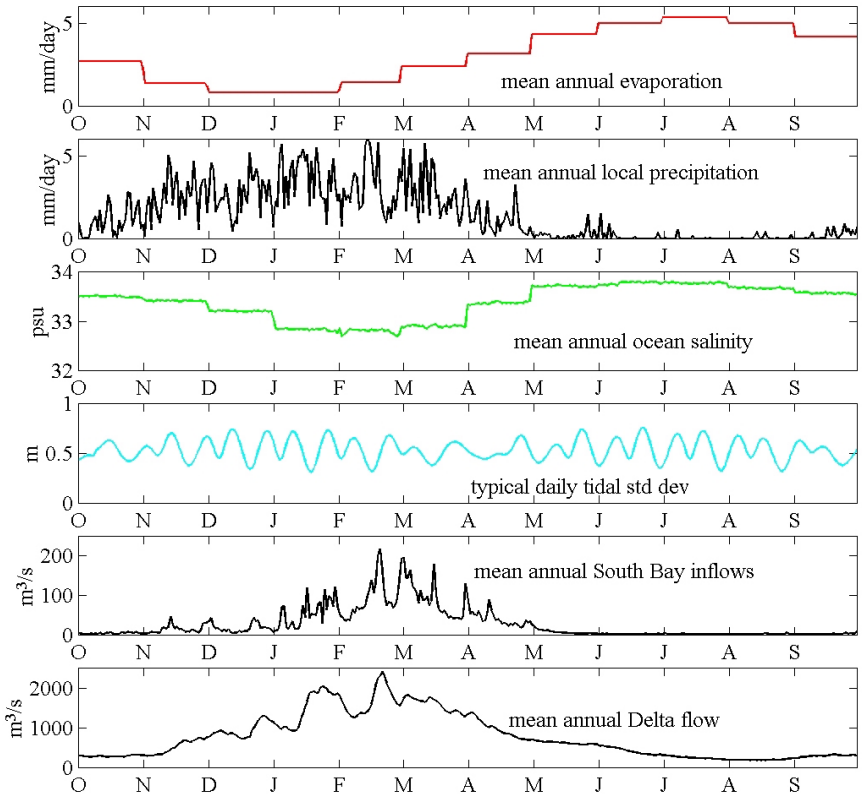

Figure 2.5 Annual behavior of model inputs. Freshwater inputs are shown in black.

The ocean salinity data, used as a boundary condition by the model, are from salinity measurements at the Farallones Islands (Cayan and Peterson 1993). The monthly steps evident in the plot are due to the use of monthly averages for the earlier part of the record (daily averages became available in 1988). Two processes are important in producing this annual cycle and deviations from it—increased upwelling of saline waters in late spring and early summer and the annual cycle in the freshwater plume leaving San Francisco Bay. The typical annual cycle in this near-shore salinity

has extremes of 32.7 *psu* in February and 33.8 *psu* in July. The maximum and minimum for the record are 34.4 *psu* and 28.8 *psu*.

Hindcast water levels at the Golden Gate Bridge at the mouth of the estuary were used to estimate the daily-averaged tidal effects (Cheng and Gartner 1984). The daily standard deviation of the water levels was calculated as an indicator of the tidal energy input to the Bay each day. This quantity shows strongest variations about its mean of 0.53 *m* at the weekly scale as spring/neap cycles cause swings of up to half a meter in the daily standard deviation.

South Bay inflows show mean peak values around 100 m^3/s in February/March, with nearly no flows in the summer and fall. The noisiness of this mean annual cycle also suggests significant variability at the daily-weekly time scale, as with the local precipitation data. In contrast, the annual cycle of Delta outflow is much larger and smoother, due to the much larger watershed sourcing Delta outflow (140,000 km^2 vs. South Bay's 4,800 km^2) (South Bay value from Larry Schemel, personal communication), as well as the much larger reservoir storage capacity in the Delta's watershed. Interannual variability in the Delta outflow signal is significant, with annual flow maxima as high as 18,000 m^3/s and as low as 400 m^3/s during the period WY 30-98.

2.5.2 Relative Significance of Forcing Factors

To determine which factors most significantly affect the estuary, and which are negligible, an assessment of the Bay's sensitivity to each input is needed. On time

scales from weeks to decades, the long-term means of these forcing factors is relatively stable. It is therefore the variability about the long-term mean which drives the Bay. To assess the relative impacts of variability in these inputs on variability of salinity, the inputs were replaced, one at a time, with their long-term means. This comparison study therefore consisted of 7 model runs, one with all model inputs unchanged as a basis for comparison, and 6 runs in which the inputs were held fixed individually. The measure of salinity variability used to assess the outcomes is the RMS change (relative to the unchanged run) in daily salinity. This measure is shown in Figure 2.6, computed throughout the Bay to illustrate the spatial dependence of salinity on the Bay's influences.

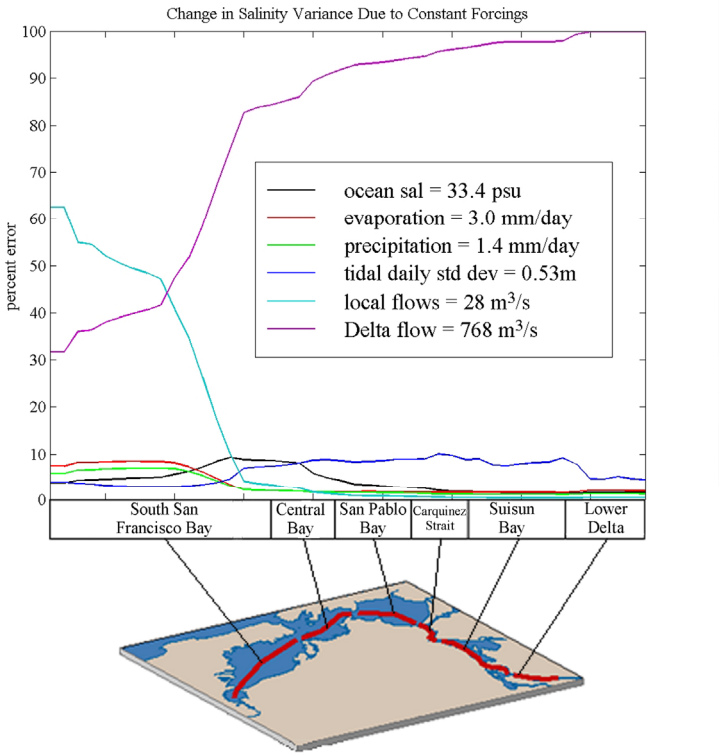

Figure 2.6 Relative RMS change in daily salinity variability due to variability in the individual forcing factors. The long-term mean of each input is given in the legend.

It is readily apparent that at time scales longer than diurnal, variability in the freshwater inflows accounts for a great deal more of the Bay's salinity variability than any of the other inputs. Similar analyses for each season showed this to be true in all seasons. The influence of Delta outflow is felt throughout the Bay, while the effects of South Bay flows reach only as far as Alameda. Delta outflow is therefore the key factor whose variability drives the Bay's salinity variability.

2.6 What Time Scales Are Important?

Since Delta outflow variability is the dominant factor affecting salinity throughout most of the Bay, it is highly pertinent to consider this factor's relative effects at different time scales. The Delta outflow's most conspicuous feature (Figure 2.5, bottom) is its large annual cycle. Deviations from this annual cycle are also quite large and tend to occur at a wide range of time scales, from the daily to weekly scale of individual storms to the seasonal scale of snowmelt runoff. As mentioned above, variability at the interannual scale is also strong.

To assess how Delta outflow's variability across multiple time scales affects the Bay, several simulations were generated in which the Delta outflow input signal was smoothed at successively longer time scales, from no smoothing (daily-averaged values) to the "infinite smoothing" represented by the long-term mean as in Figure 2.6. A 12-pole symmetric low-pass Kaylor filter was used to perform the smoothing (Kaylor 1977), with the indicated periods being the half-power points. Figure 2.7

shows the relative RMS change in salinity (relative to the unsmoothed run) throughout the Bay.

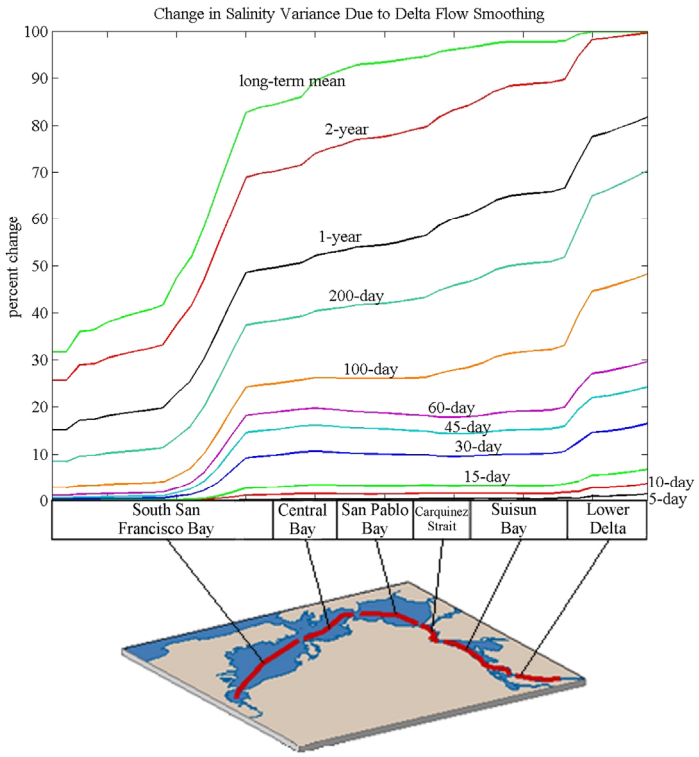

Figure 2.7 Relative RMS change in daily salinity variability due to progressively longer smoothing of Delta outflow. The low-pass filter cutoff periods are indicated.

As before, the most significant effects of changing the Delta outflow input are confined to the Central and northern Bays. For most of the Bay, there is less than a 10% change in salinity variance for a 30-day or less low-pass filtered Delta outflow signal. This represents a RMS change of well under 1 *psu* throughout the Bay. While the 30-day low pass filter allows some signal at the time scale of individual storm events to be represented, the 60-day filter represents these events much less. Still, there is under a 20% RMS change for the 60-day filtered freshwater input, for an RMS

change of less than 1.5 *psu* everywhere. For longer-period filters, the relative change increases with the cutoff frequency to over 90% for a constant input, representing RMS changes of over 7 *psu* in some parts of the Bay. Conversely, it is interesting to note that less than 20% (at the most) of salinity variance is attributable to fluctuations in Delta outflow at time scales of longer than 2 years.

This indicates that while the estuary/watershed system responds significantly at the time scale of individual storm pulses, a great deal of the Bay's variability lies in its response to seasonal, year-to-year, and to a lesser extent, longer time scales. This suggests an examination of what qualities of Delta outflow at the seasonal/annual scale are driving salinity variability.

2.7 **What Drives the Salinity Modes?**

Returning to the E-EOF analysis of salinity, it is now possible to ask what aspects of the Bay's forcing factors are driving the distinct behavior of these modes. So far, it has been shown that Delta outflow is the primary factor and that it has very strong effects at seasonal and annual time scales. For the purposes of further analysis, what is now needed is to characterize each year's Delta outflow signal as broadly as possible while still capturing its essential qualities. To reduce the information contained in each year's Delta outflow hydrograph to such basic quantities, a volume-conserving Gaussian pulse has been fit to the hydrograph for each water year of the 69-year record. This gives 3 values which coarsely represent a year's Delta outflow—pulse amplitude A, pulse width σ and pulse center X_o (Figure 2.8).

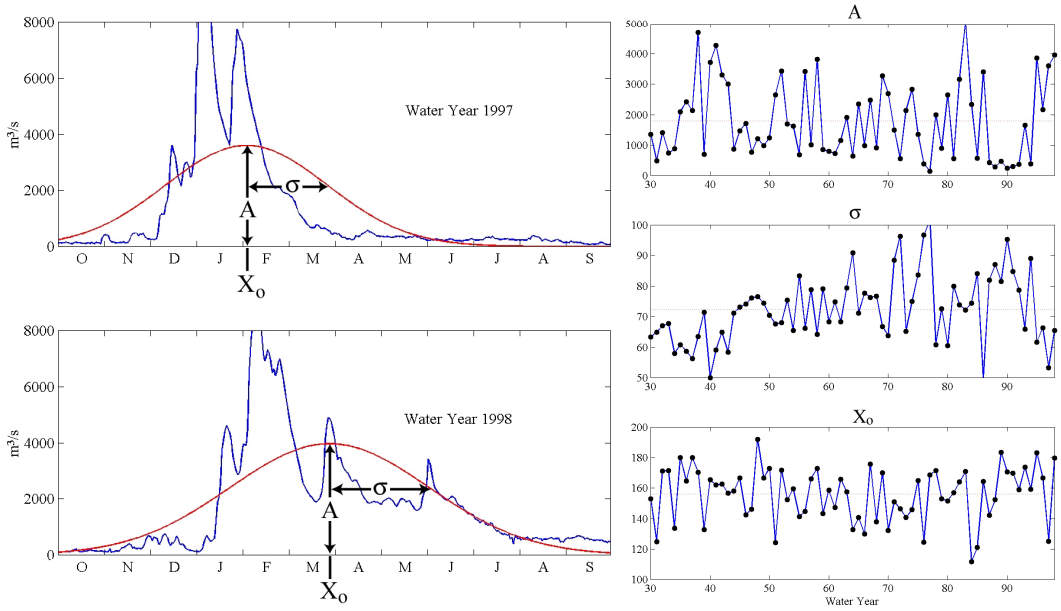

Figure 2.8 **Left:** Sample Gaussian fits with annual flow parameters for two recent Delta outflow hydrographs. **Right:** Time series for annual Gaussian hydrograph parameters.

The amplitude A represents roughly the total amount of Delta water flowing into the Bay in a given year, the width σ represents how "spread out" the flow was over the year, and the pulse center X_o gives the overall timing of the annual flow. These 3 annual hydrograph parameters provide the desired simple characterization of annual flow patterns for comparison with the amplitudes of the salinity modes. Table 2.1 shows the correlations of the modal amplitudes with the 3 Delta outflow parameters.

Table 2.1 Correlation coefficients of modal amplitudes and Delta outflow parameters. Mode 2' is the Mode 2 amplitude at a one-year lag.

	A	σ	X_o
Mode 1	**-0.94**	0.58	0.27
Mode 2	0.02	-0.24	**-0.83**
Mode 2'	0.44	0.00	0.12

These results indicate that the amplitude of Mode 1 is driven primarily by variability in the effective amplitude of the annual Delta outflow pulse (r=-0.94), while Mode 2 is driven by changes in the timing of the pulse (r=-0.83). It is quite compelling that such coarse measures of the annual flow pattern can capture so much of the seasonal salinity variability.

To take the analysis one step further, atmospheric composites corresponding to high and low 10th percentile modal amplitudes were generated for each mode (Figure 2.9-Figure 2.10). The data used were global 700 *mB* height anomalies (Trenberth and Paolino 1980). The data used are monthly from 1948-1987 and are hence somewhat limited in their applicability to the current salinity analysis which begins with 1930. To compensate for this deficiency, analogous composites were generated using sea level pressure anomaly data (Namias 1979) which covers the full record from WY 1930-1998. The results of this second analysis (not shown) concur with the results from the limited, but more appropriate to the relevant processes of moisture transport, 700 *mB* height analysis.

2.7.1 Flow Magnitudes and Atmospheric Forcing

The strong correlation of Mode 1 with the Gaussian amplitude shows that this mode reflects the overall wetness or dryness of a given water year as manifested in the Bay's salinities. The atmospheric composites for extreme values of this mode's amplitude (Figure 2.9) show that high values of mode 1, which indicate higher than average salinity in the estuary, are associated with a high pressure cell centered over

the Pacific Northwest in winter. This high deflects the storm track to the north, allowing little precipitation to reach the San Francisco Bay watershed. Conversely, low values of mode 1 which represent a fresher estuary, show no analogous high pressure cell. In such years the Alaskan-Aleutian low forms closer to North America, directing the storm track squarely into California generating much more rain and snow. The resulting high flows drive down estuarine salinities throughout the year.

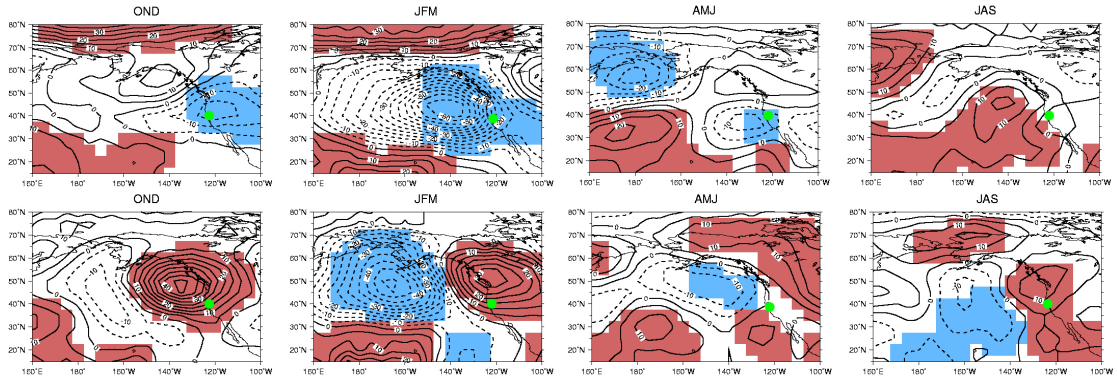

Figure 2.9 Seasonal 700 *mB* height anomaly composites for Mode 1 extreme amplitude years. Upper row corresponds to low modal amplitude values, lower row corresponds to high values. Columns correspond to fall, winter, spring and summer. The Bay-Delta estuary is highlighted in green.

These atmospheric patterns associated with wet and dry years in California have been well-established (*e.g.*, Cayan and Peterson 1993; Peterson, Cayan *et al.* 1995). They show that the large interannual swings of mode 1 are primarily linked to meteorological forcing, though the smaller long-term trend may well represent human interactions with the watershed/estuary system.

2.7.2 Flow Timing and Atmospheric Forcing

Mode 2's correlation with the timing of the Gaussian pulse show that it represents seasonal deviations of the timing of freshwater flows from the annual cycle represented by mode 1. High values of mode 2 represent earlier flows with an associated decrease in fall/winter salinities, and an increase in spring/summer salinities. Low values represent later flows and the opposite salinity shifts. The atmospheric composites for extreme mode 2 amplitudes (Figure 2.10) show that a

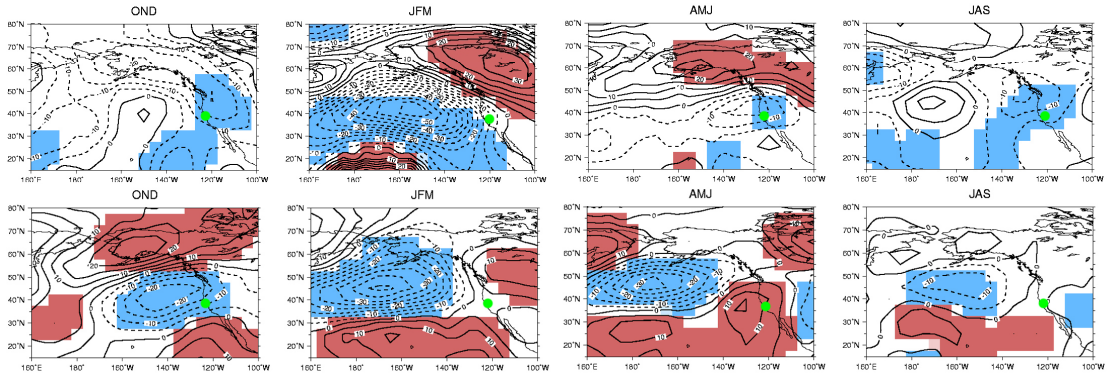

Figure 2.10 Seasonal 700 *mB* height anomaly composites for Mode 2 extreme amplitude years. Upper row corresponds to low values, lower row to high values. Columns correspond to fall, winter, spring and summer. The Bay-Delta estuary is highlighted in green.

seasonal interplay between North Pacific/North America pressure cells is the main factor behind this timing shift. For high mode 2 amplitudes (early flows), a low pressure cell feeds moisture to California in the last months of what is typically the dry season at the beginning of the water year. This behavior abates in the winter, ceasing altogether in spring as a blocking high pressure pattern migrates north from the tropics, deflecting the storm track into Canada. The result is a wet fall/winter and a dry spring/summer. Low values of mode 2, which result in the opposite timing shift, are by no means the result of mirror image atmospheric patterns as shown in Figure 2.10.

While a weak low pressure cell does influence the San Francisco Bay watershed during the fall and winter in this case, the streamlines deliver an oblique blow to the orography of the region, resulting in little moisture being released to the land below. In spring, a low pressure cell orients the streamlines nearly perpendicular to the Coastal and Sierra–Nevada mountain ranges which border the watershed, resulting in much stronger orographic forcing of precipitation. This late-season wet pattern even endures somewhat into the summer months, resulting in the lower-than-average spring/summer salinities represented by low mode 2 amplitudes.

It is also important to note the role of snowpack in the timing variability represented by mode 2. Snowpack acts to delay a significant portion of runoff for up to several months, with the prime snowmelt season being the spring, or AMJ in Figure 2.10. The temperatures during this season therefore have a direct effect on flow timing. The atmospheric composites in Figure 2.10 do in fact reveal that earlier flows correspond to higher temperatures, with a high pressure cell pulling warm air from the South. This would lead to a more rapid snowmelt and less snowpack altogether. Conversely, later flows correspond to cooler patterns and a larger and longer snowpack retention.

A secondary process represented by Mode 2 is the lagged response of the watershed/estuary system to precipitation of the previous water year. This lag effect leads to early flows in years following wet years and relatively late flows in years following dry years. Atmospheric composites of the seasons preceding years with extreme values of mode 2 amplitudes (not shown) demonstrate this, with a tendency

for wet circulation patterns before years with early flows and dry patterns before late flow years. This effect is also evidenced by the much higher correlation of mode 2 with the Gaussian amplitude when it lags the amplitude by one year (*r* increases from .02 to .44). A good example of this effect is the very high mode 2 amplitude of WY 84 (see Figure 2.4). This is due not to especially early rains that water year, but to the very wet winter and spring of WY 83. Lags in the watershed caused high flows from the strong storms of winter/spring 1983 to persist in the system, causing lower salinities in the fall and winter of WY 84. In addition to the atmospheric evidence, a reconstruction of "unimpaired" flow (*i.e*, estimates of what the flow would have been without human interference) suggests that the year-to-year carryover is both a natural hydrologic as well as an artificial reservoir lag effect.

2.8 **Interannual and Several-Year Variability**

So far it has been demonstrated how, at seasonal to annual time scales, salinity variability throughout the San Francisco Bay estuary is driven primarily by flow from the Delta, which is in turn driven by large-scale atmospheric patterns and their hydrologic interactions with the managed watershed. The next step is to take an even longer perspective to examine the combined behavior of the atmosphere/watershed/estuary system at interannual to decadal time scales.

Recall that the main components in the analysis of seasonal/annual behavior are an annual magnitude, affecting all seasons, and an interseasonal timing shift, primarily between spring and winter. The amplitude time series of the corresponding

salinity modes in Figure 2.4 suggest that there is significant interannual variability as well as record-length trends in these components. To quantify this longer-period variability at all levels of the hydrologic system, statistics were calculated using annual watershed precipitation totals (Karl and Knight 1998), annual Delta outflow totals, and annual salinity means in three San Francisco Bay subestuaries from water years 1930-1998. Analogous statistics were generated for the spring fraction of total annual precipitation and Delta outflow, and for the spring means of salinities, normalized by the yearly salinity means. Table 2.2 summarizes these statistics, showing means, coefficients of variation, and results of Kendall's-τ trend tests (Kendall 1938) for all time series.

Table 2.2 Means, coefficients of variation, and trends for annual and fractional spring values of precipitation, flow and salinity. The fractional spring values are from a time series of spring totals (means where appropriate) divided by annual totals (means) for each.

		Annual			Spring Contribution		
	μ	σ/μ	p_τ		μ	σ/μ	p_τ
P	72 cm	0.32	+0.06, 52%		0.14	0.46	-0.09, 70%
T	14.1^{O}C	0.04	+0.11, 83%		1.15	0.06	-0.04, 36%
Q	26 km^3	0.65	-0.06, 51%		0.25	0.45	-0.28, **99.9%**
S (Suis)	6.35 *psu*	0.43	+0.10, 76%		0.58	0.80	+0.26, **99.9%**
S (SPB)	20.2 *psu*	0.22	+0.13, **88%**		0.83	0.29	+0.24, **99.7%**
S (SMB)	26.9 *psu*	0.13	+0.07, 59%		0.88	0.14	+0.15**, 94%**

First, note the clear trends in spring flow and salinity indicated by high significance levels of the Kendall's-τ trend test. It particularly interesting that parts of the Bay show definite increases in annual mean salinity, while annual total Delta outflows exhibit no such trend. This suggests that the long-term interseasonal shift in flow timing is at least partially responsible for the trends in annual mean salinity. The

trends will be discussed in some detail later, as the discussion telescopes out to these longer time scales.

The coefficient of variation statistic also demonstrates the amplifying effect of the watershed at the annual scale. The coefficient of variation of Delta outflow is twice that of watershed precipitation. This is due to the fact that average annual watershed soil moisture, which is correlated with annual precipitation, determines the amount of precipitation which enters the stream network culminating in the Delta. That is, any rain or snowmelt occurring in dry years tends to be absorbed by the unsaturated soils occurring in such years. Conversely, precipitation in wet years tends to fall on wet soils and enter the streams in more abundance. This leads to a disproportionate increase or decrease in Delta outflow compared to changes in precipitation over the watershed. The opposite effect occurs as signals move from the Delta into the Bay, with coefficients of variation in salinity significantly less than that of Delta outflow. This happens because tidal diffusion and baroclinic advection work constantly in opposition to the freshening effects of Delta outflow, mixing seawater into the estuary. Consequently, the strength of the annual Delta freshwater signal as reflected by salinity diminishes significantly away from the Delta, the coefficient of variation dropping to 0.13 in southern South Bay.

Perhaps the most striking result from Table 2.2 is the amount of interannual variability present in the system—the standard deviation of annual freshwater inflow to the Bay is 65% of the mean! Clearly, such huge changes generate significant interannual variability in the Bay's behavior. This must affect not only salinity

distributions, but also estuarine dynamics, sediment fluxes, nutrient transport, phytoplankton production, and so on through all levels of the ecological web in and around the estuary (cf Cloern and Nichols 1985). Undisturbed ecosystems, having evolved under conditions of large interannual variability, incorporate this context as part of their natural condition. However, the current remnants of these original ecosystems in and around San Francisco Bay may behave much differently in response to such large year-to-year changes.

2.8.1 Interannual Persistence

In light of the large interannual variability, it is natural to consider what patterns of year-to-year salinity persistence do exist and what mechanisms may underlie the persistence. It has already been shown that atmospheric patterns in a water year may affect salinities the following water year via natural and artificial persistence effects in the watershed. The other levels at which interannual persistence could be introduced are persistence of atmospheric anomalies themselves and persistence of salinity due exclusively to processes in the estuary.

Figure 2.11 and Figure 2.12 show composite San Pablo Bay salinity and Delta outflow values for years with extreme modal amplitudes, as well as for the years immediately preceding and following them. Composites for high and low mode 1 amplitudes are shown in Figure 2.11.

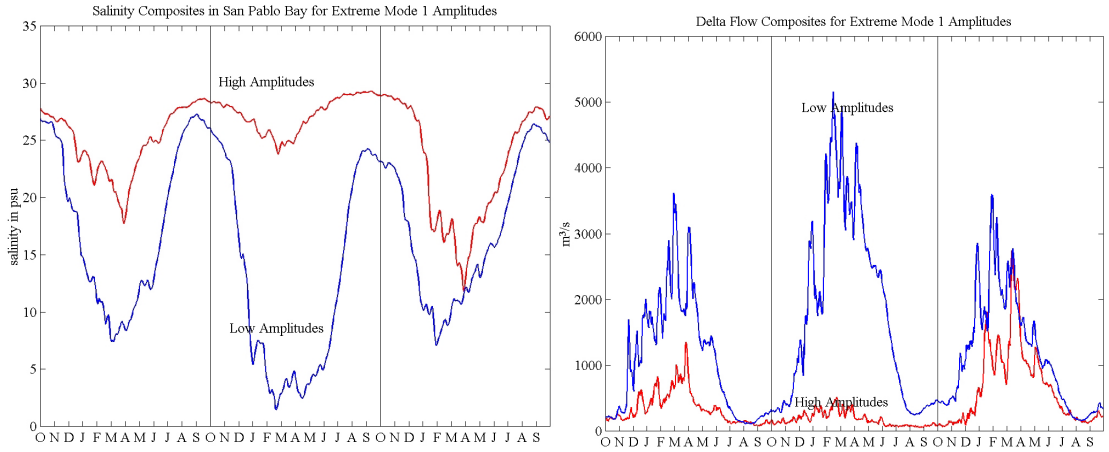

Figure 2.11 Composites of San Pablo Bay salinity and Delta outflow corresponding to extreme values (highest 10% and lowest 10%) of mode 1 ("magnitude" mode) amplitudes.

Clearly, there is significant year-to-year persistence of the salinity signal. Years before fresh or saline years tend to also be fresh or saline. In years following extreme years, the separation between composite salinity extremes is much smaller. To explain these persistence patterns, begin with the estuary and work backwards through the freshwater cycle. By the end of years preceding extreme years, the two Delta outflow composites are the same. The salinity composites are slightly different, suggesting that some year-to-year carryover exists within the estuary itself, though this effect appears to be quite small.

Most of the carryover from year to year appears in the Delta outflow signal, indicating the main source of persistence lies in the watershed and/or atmosphere. Analogous composites for 700 *mB* height anomalies (not shown) show that years before years with extremely fresh or saline estuarine conditions tend to have "wet" or "dry" atmospheric patterns, respectively. However, years following extremely fresh or saline years appear overall to have neither particularly wet nor dry. This apparent

atmospheric persistence from the year preceding the extreme year is certainly an analytical artifact rather than any indication of true atmospheric persistence. The lagged response of the watershed/estuary system to flows from the previous water year is the real persistence being represented, confirmed by the asymmetry of the artifactual atmospheric persistence.

Similar conclusions follow from Figure 2.12, the salinity composites for mode 2 extremes. While very little composite signal exists in either salinity, watershed outflow, or atmospheric anomalies in years following years with extreme mode 2 amplitudes, there is significant signal indicated at all levels in the years preceding them. Salinity, Delta outflow, and atmospheric patterns suggest that wet years precede early flow years and dry years precede late years.

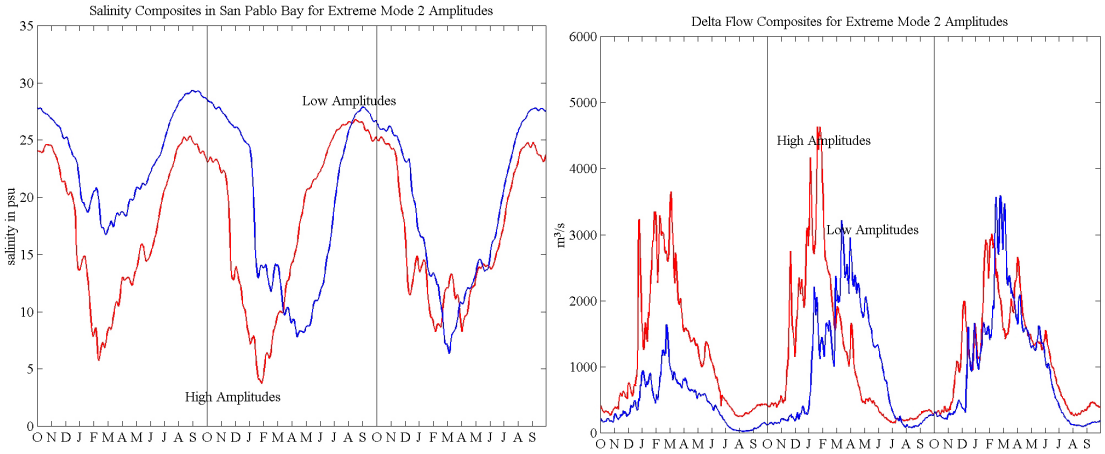

Figure 2.12 Composites of San Pablo Bay salinity and Delta outflow corresponding to extreme values (highest 10% and lowest 10%) of mode 2 ("timing" mode) amplitudes.

Since there is very little year-to-year persistence inherent in the estuary itself, and since the atmospheric composites associated with Figure 2.11 show no tendency

for meteorologically "late" or "early" years following dry or wet years, the conclusion follows that the year-to-year persistence of anomalies in the salinity cycle is due primarily to persistence at the watershed level.

2.8.2 Several-Year Events

The lack of apparent interannual persistence outside the watershed level of the hydrologic cycle is by no means an indication that multi-year episodes forced by the atmosphere do not occur. Indeed, multi-year drought and abundance episodes are among the most noteworthy of hydrologic events (*e.g.*, Stine 1994; Krannich, Keenan *et al.* 1995; Schimmelmann, Zhao *et al.* 1998; Masutani and Leetmaa 1999). The recent drought of WY 87-92 had very significant impacts in California, not the least of which were in the Bay-Delta estuary. To get a feel for the magnitude of the impacts which multi-year episodes of drought and abundance can have in the estuary, Figure 2.13 shows an example of each. This figure shows the movement of the salinity field, as represented by the position of the 2 *psu* isohaline, across four consecutive drought years (WY 87-90, red) and four consecutive abundance years (WY 40-43, blue) relative to the mean annual cycle (black). This isohaline position, measured in kilometers along the estuary from the Golden Gate Bridge, is a commonly used index in the Bay research and management communities.

The difference between drought, abundance and the climatological mean in the estuary is quite impressive. Note that the upstream movement of the field extends

beyond the model's boundary at 84 *km*. Nonetheless, it is apparent that in the dry season, all three

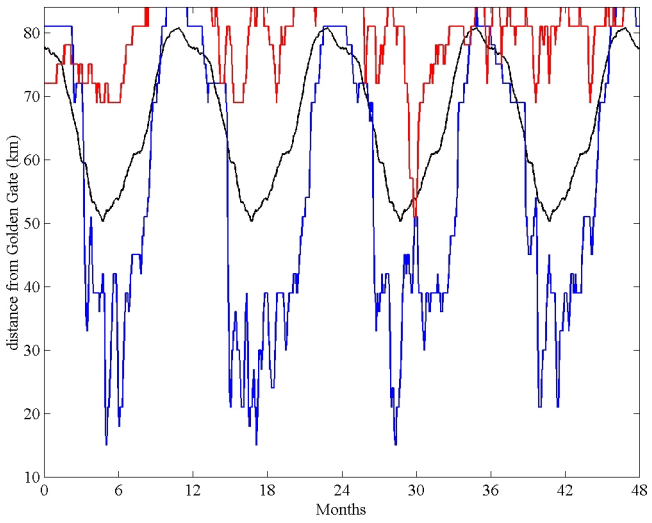

Figure 2.13 Examples of four consecutive years of drought and abundance relative to the mean annual cycle. The plot is distance of the 2 *psu* isohaline upstream from the Golden Gate Bridge. (blue: WY 40-43, red: WY 87-90, black: mean annual cycle)

cases tend to converge as the salinity moves upstream. There is clear year-to-year carryover in the drought years, resulting from the watershed-based persistence discussed above. It is also interesting to note that even in the abundance example the upstream limit of X2 is at or beyond the mean annual cycle for the entire record. This reflects the different management capabilities in effect during this particular abundance (early 40's), before Shasta reservoir was completed.

The real difference between the cases is during the wet season. In every drought year, the wet-season X2 position hovered in the lower Delta, while in the years of abundance it stayed nearly 40 *km* downstream in San Pablo Bay. As discussed previously, it is not unusual to see such differences in the estuary from one year to the

next. However, when such large shifts of the salinity field occur for several consecutive years, the cumulative effects on the estuarine ecosystems are significant (note also that the drought example actually continued for two more years!), particularly in an urbanized estuary such as San Francisco Bay.

In an undisturbed environment, the various ecosystem types would tend to migrate up or down the estuary with their preferred salinity regime. Extensive human development on the borders of the San Francisco Bay estuary hinder such adjustments, making the remaining natural preserves more sensitive to shifts in the salinity regimes. If the salinity shifts exceed the tolerance of the various estuarine/wetland ecosystems to variations in their salinity environment, such extreme conditions over a few consecutive years may lead to serious ecosystem degradation and loss (*e.g.*, Nichols, Thompson *et al.* 1990; Jassby, Kimmerer *et al.* 1995; Bay Institute 1998; San Francisco Bay Area Wetlands Ecosystem Goals Project 1999). Further, sediment cores form the estuary provide evidence for more intense droughts which lasted over 80 years (Ingram, Ingle *et al.* 1996), and tree-ring records tell of ~250 year droughts in the Bay's watershed (Stine 1994), dwarfing the present examples.

2.8.3 Record-Length Trends

Returning now to Figure 2.4 and Table 2.2, it is time to address the long trends apparent in the smoothed modal amplitudes and in the Kendall's-τ trend tests. Figure 2.4 shows both a record-length trend toward increasing salinities in the Bay (higher mode 1 amplitudes), and an overall trend towards lower winter and higher spring

salinities commensurate with earlier runoff (higher mode 2 amplitudes). These modal trends have over 90% significance levels in Kendall's-τ tests. The trend significance levels in Table 2.2 concur with these results. Higher annual mean salinities are indicated, particularly in San Pablo Bay where variance is highest and the trend has 88% significance. The mode 2 trend is supported by the nearly 100% significance levels of decreasing spring flow contribution and increasing spring salinities (relative to the yearly mean).

The real-world implications of these trends are significant changes in the annual salinity cycle. The mode 1 trend represents an increase of 10-15 *psu* over ~WY 40-90 in San Pablo Bay in winter and spring. This is an enormous signal considering that ocean salinity is only ~34 *psu*. The mode 2 trend has more subtle, but still significant implications. While over the entire record it represents only a small net change in salinity timing, taken in two parts it becomes more significant. From ~1930 to ~1970, the mode 2 trend represents a shift of freshwater inflows from AMJ to JFM. This shift indicates a change of up to 5 *psu* in San Pablo Bay in spring over 40 years, though it appears to have slackened since 1970. These two shorter trends have significance levels approaching 100%.

The causes of these long-term changes in mode 2's amplitude are likely a mix of natural and artificial effects. A long-term trend toward lower winter and higher spring salinities is evident from the 1930's until around 1970. The direct cause is made evident by comparing mode 2's amplitude (Figure 2.4) with the plot of estuary freshwater inflow seasonal contributions (Figure 2.14).

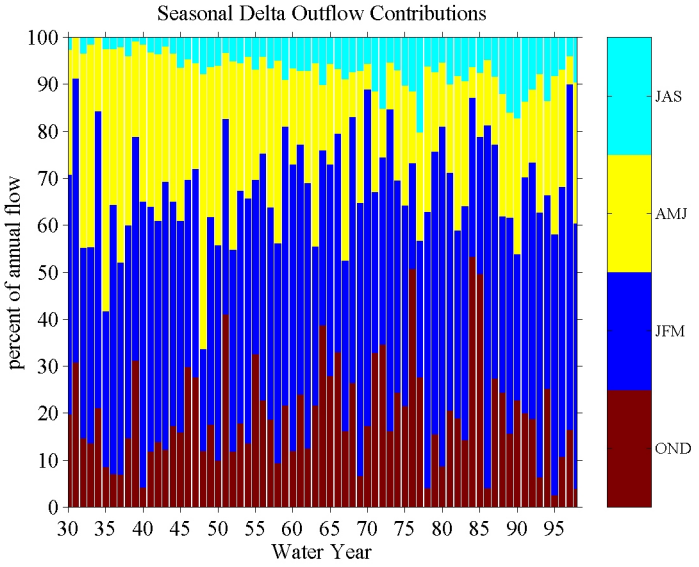

Figure 2.14 Breakdown of Delta outflow by season. Each colored bar represents the percentage of the given year's total flow which occurs during the specified season.

This figure clearly demonstrates an overall decrease, through approximately 1970, in the percent of each water year's total inflow which arrives in the spring (AMJ), resulting in higher spring salinities. Previous work has suggested that this trend is contributed to by earlier snowmelt runoff due to higher winter/spring temperatures related to climate variability (Roos 1991; Dettinger and Cayan 1995).

It is also apparent that there has been an overall increase in summer (JAS) contributions, which suggest that management also plays a strong role in long-term timing trends. The main purpose of reservoirs is to hold wet-season runoff both for flood control purposes and for use during the dry season, and the increasing summer flow contribution is the result of increasing reservoir effects. Most of the delayed flows, however, do not show up as Delta outflow, as they are diverted out of the watershed by freshwater pumps in the Delta. The net effect of reservoirs removing

water from the spring portion of the hydrograph and returning it later in the year only to have it removed by pumps is to shift flow timing *earlier* in the water year. Thus, increasing management over the last 70 years may actually contribute to the earlier average arrival of flows . This effect will be analyzed in more detail in the next chapter. But what to make of the trend abatement since the 1970's?

In fact, while the effects of reservoirs and earlier snowmelt runoff may contribute to the mode 2 timing trends, there is evidence that this "trend" and its "abatement" are also partly the estuary/watershed system's response to a decades-long oscillation in the global climate system. In Chapters 3 and 7, long-term shifts in the amount of precipitation falling as high Sierran snow will be discussed, and the suggestion of a link between flow timing and decadal climate variability will be explored.

As for mode 1, attempts to understand the causes of its long-term trend representing higher salinities reveal some interesting behavior. The trend toward higher mean annual salinities represented in the amplitude of mode 1 agrees with the trends in annual mean salinities indicated in Table 2.2. Though this mode's behavior is highly correlated with total annual Delta outflow, the trend toward higher salinities does not appear to be the result of any long-term trend in annual flow, as indicated in Table 2.2. The only trend apparent in the forcing factors is the redistribution of spring flows to other seasons. It appears that the trend in mode 1 at least partially reflects a trend in annual mean salinities which is forced by shifts within the annual flow cycle, not by any clear trend in the mean annual flow itself. This trend may therefore be

influenced by the intraannual redistribution of the hydrograph by natural variability (earlier snowmelt) and anthropogenic effects (reservoirs, Delta pumping). Note that this salinity trend is most significant in San Pablo Bay. The Bay's sensitivity to intraannual redistribution of Delta outflow will discussed further in Chapter 7.

2.9 Summary

Using a seven-decade simulation of surface salinities in the San Francisco Bay estuary, seasonal to multi-decadal variability of the estuary has been examined. An extended empirical orthogonal function analysis revealed significant interannual variability, as well as longer trends, in both the magnitude and timing of the annual salinity cycle throughout the estuary. Delta outflow was demonstrated to be the dominant factor affecting Bay salinities, with much of its influence at seasonal to annual time scales. Simple parameters coarsely representing each year's Delta outflow hydrograph were able to provide a great deal of skill in predicting the timing and magnitude of the Baywide seasonal salinity cycle. Atmospheric composites revealed how the timing and the magnitude of the salinity cycle are primarily forced by patterns of seasonally and interannually shifting pressure over the North Pacific, though lags induced hydrologically by the watershed also played a clear role.

An analysis of interannual variability showed that the atmosphere/watershed/estuary system exhibits immense year-to-year variability, with changes in precipitation being amplified greatly in the watershed by nonlinear effects. Interannual persistence of the salinity signal was found to result almost entirely from

hydrologic persistence in the watershed, with carryover from the previous year influencing both the effective timing and magnitude of the current water year's hydrograph. Examples of the effects of several years of drought versus several years of abundance were given, demonstrating the enormous impact of such events on the estuary. Possible implications of such events for existing estuarine ecosystems were discussed briefly. Finally, trends across several decades in both the timing and the magnitude of the seasonal salinity cycle were analyzed. An intraannual redistribution of the hydrograph by natural variability and anthropogenic effects appears to contribute to both trends.

The clear links of estuarine behavior to processes in the watershed and atmosphere, particularly at seasonal to interannual scales, provide impetus for a more detailed examination of these processes in relation to the estuary. In particular, the important role of the watershed flow timing and amplification of interannual and longer atmospheric variability make it an obvious subject of interest. The remaining chapters concern the effects of management in the watershed in relation to interannual variability, as well as the development of watershed modeling capabilities for more quantified studies of long-term, large-scale variability and its implications for the estuary.

3 River Flows In the Watershed

3.1 Introduction

The Bay-Delta watershed encompasses a wide variety of landscapes. There are the arid, irrigated valleys and the lush forests of the Klamath Mountains, the high volcanic peaks in the North and the even higher southern Sierra, and the abrupt Coastal and Sierra Nevada Ranges as well as the extensive Klamath and Cascade Ranges. Accordingly, the watershed displays a diversity of hydrologic behavior. The high southern Sierra retain most precipitation as snowpack until late spring and early summer. Progressing north along the Sierra Range, elevations drop gradually and average temperatures rise. More of the precipitation falls as rain, entering directly into the soils and streams of the middle and northern Sierra; consequently, the snowpack is smaller. In the valleys, almost all precipitation falls as liquid. The San Joaquin Valley is so arid that evaporation demand almost always exceeds available moisture, yielding little or no local streamflow contribution. It is the extremely varied hydrologic behavior, interacting with the effects of human intervention, that determines the amount and timing of freshwater inflows to the Bay-Delta estuary. The characterization of river flows throughout the watershed and the effects of management on these flows are the subject of this chapter.

The Bay-Delta estuary has undergone extensive human development over the past 150 years, as has its upstream watershed. Current attempts to understand and

restore the Bay-Delta's valuable ecosystems are complicated by both natural and human effects on freshwater inflows. Freshwater flow through the Delta of the Sacramento and San Joaquin Rivers (Figure 2.1, Figure 3.11) is the most significant single factor affecting water quality in the estuary, as shown in Chapter 2. These inflows flush seawater from the Bay-Delta, determining levels of salinity throughout the estuary. Salinity levels in turn determine water density and flow patterns, which affect nutrient concentrations and so on. Salinity conditions are also directly related to the survival of some plants and animals in the estuarine ecosystem (Nichols 1985).

As discussed previously, processes in and over the watershed determine the timing and amount of inflow to the Bay. Annually, an average of about 30 km^3 of freshwater enter the Bay from the watershed, with peak flows coming in early March, on average. Interannual variation in both timing and amount of these flows can be large and is due to both natural and human-induced effects.

Figure 3.1 shows locations in the watershed where human effects significantly impact flow patterns. Reservoirs with a combined capacity of over 35 km^3 (roughly equal to the Bay's total annual inflow) substantially alter the magnitude and timing of river flows throughout the watershed (California Department of Water Resources 1998). Also, freshwater is exported from the Delta region for municipal, industrial and agricultural uses. The combined effect of reservoirs and Delta exports constitute the bulk of human-induced changes in Bay freshwater inflows (other effects include return flows, groundwater pumping, river confinement and land use changes).

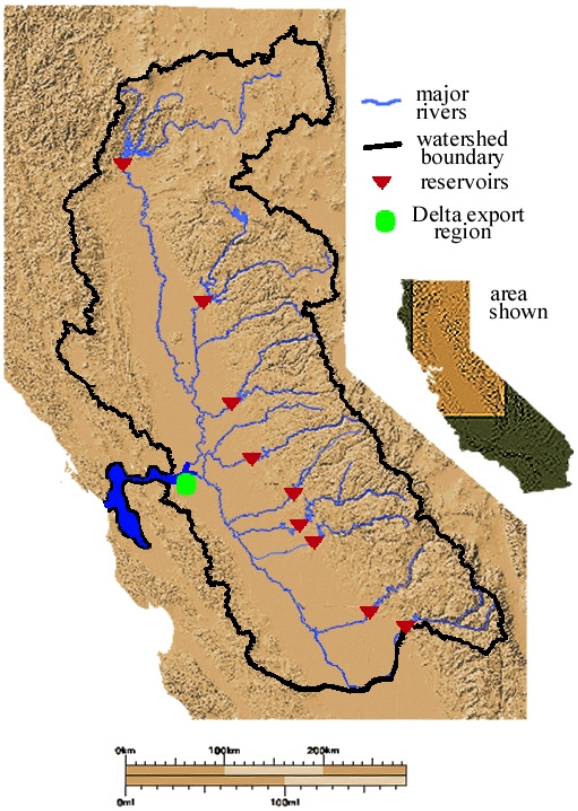

Figure 3.1 Map of the San Francisco Bay estuary and watershed, showing locations of major human influences on freshwater flows.

Subsequent use of the term “human effects” in this and the next chapter refers to the impacts of reservoirs and Delta exports on freshwater flows into the Bay, and the resulting effects on salinity in the estuary. These effects take place in the shadow of the watershed’s large natural hydrologic variability, resulting in a complex managed watershed/estuary system.

An analysis of the implications of human effects on Bay freshwater inflows, in the context of natural variability, for water quality in the estuary will be presented in the next chapter. First, however, the flow data to be used in that analysis, and later to

develop the watershed hydrology model, is presented. This data offers a first look at the river basin-scale characteristics of the watershed as reflected by river flows.

3.2 River Basins

The Bay-Delta watershed may be viewed as many different river basins linked together by the watershed-wide river network. The fifteen basin delineations used in this work are shown in Figure 3.2.

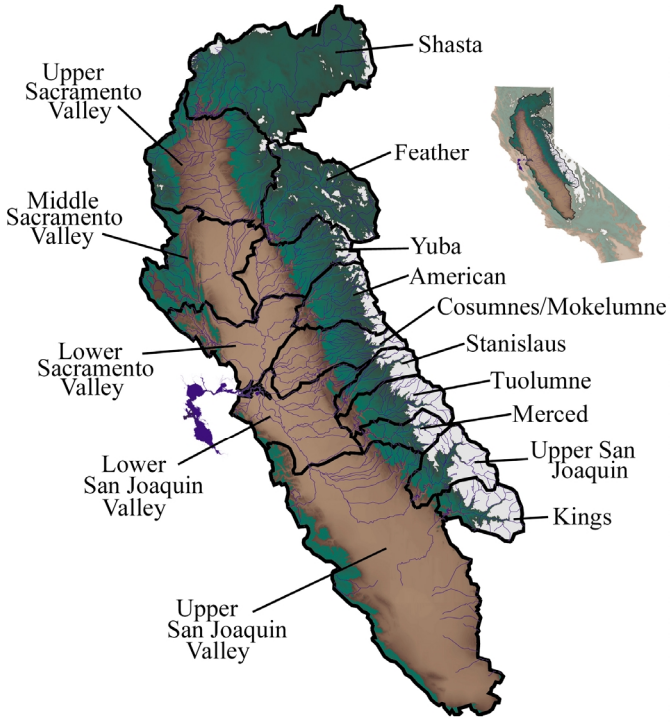

Figure 3.2 River basins of the Bay-Delta watershed, with names used in this study. Mountain basins are labeled on the right, valley basins on the left.

These basins are conglomerations *hydrologic units* determined by the USGS as the fundamental regions of hydrologic response (U.S. Geological Survey 1987). There are ten mountain basins and five valley basins. These behave individually in a self-

similar manner to the entire watershed, in that all flow generated by rainfall and snowmelt with the boundaries of each river basin eventually reaches a single outflow point for that basin. For this reason, and due to the convenient fact that most of these river basin outflow points have flow data, these 15 basins will be used in the remainder of the dissertation to evaluate model performance and to study flows throughout the Bay-Delta watershed.

3.3 Flow Gauge Data

To hydrologically characterize each of the watershed's river basins, flow data was obtained from the USGS web site (http://waterdata.usgs.gov/nwis-w/CA) after examining USGS Water Resources data reports (U.S. Geological Survey 1998). These reports contain detailed schematics of river flows, reservoirs sites, artificial diversions and bypasses, *etc*., relating gauge locations and all significant junctions for the various hydrologic regions of California. In the cases where the actual basin outflow points were ungauged, the schematics, along with hydrologic maps (U.S. Geological Survey 1987), were used to formulate estimates of basin outflows from nearby stations. The 25 flow gauges used to generate basin outflow records for the 15 basins are shown in Figure 3.3.

For reasons to be discussed later in this chapter, it was desirable to determine basin outflows for the period WY 1965 - WY 1987. In some cases, gauges were located closer to basin outflows points than the ones used here, but those records were prohibitively sparse over this period. The gauges used in their place were compared to

the unused records, and the 25 gauges shown here were deemed satisfactory for the estimation of outflows from the 15 river basins.

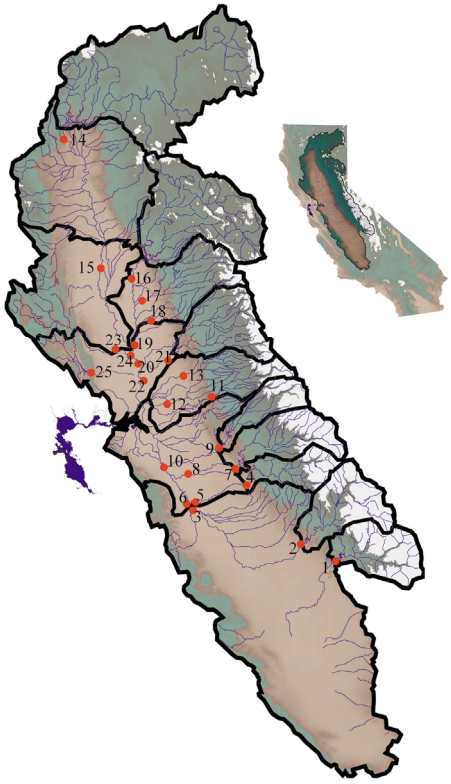

Figure 3.3 Location of flow gauges used in this study. See Appendix A for detailed gauge information.

In two cases, direct substitution of gauges was not appropriate, and proxy representations of outflow had to be established. Gauge #7, at the outflow of the Tuolumne River basin, is the ideal choice for that basin, but this gauge was not established until 1971. During the period WY 65-70, a linear regression of this gauge's available record with a downstream station, gauge #8, was used. Similarly, gauge #3 is missing data for most of the 70's, but a regression on the difference between gauge 6 and gauge 5 gave satisfactory results in its place. The resulting formulae used to determine basin outflows are shown in Table 3.1.

Table 3.1 Formulae for river basin outflows. The numbered subscripts correspond to the station designations in Figure 3.3. Basin inflows are expressed in terms of outflows, with "---" representing no inflows (headwater basins).

Basin Name (Abbreviated Code)	Outflow Formula	Inflows
Shasta (SHA)	$Q_{SHA} = Q_{14}$	---
Upper Sacramento Valley (SAC1)	$Q_{SAC1} = Q_{15}$	Q_{SHA}
Feather (FTH)	$Q_{FTH} = Q_{17} + Q_{18}$	---
Middle Sacramento Valley (SAC2)	$Q_{SAC2} = Q_{19} + Q_{24} - Q_{23}$	Q_{SAC1}
Yuba (YUB)	$Q_{YUB} = Q_{16}$	Q_{FTH}
American (AMR)	$Q_{AMR} = Q_{21}$	---
Lower Sacramento Valley (SAC3)	$Q_{SAC3} = Q_{22} + Q_{20} + Q_{25}$	$Q_{SAC2} + Q_{YUB} + Q_{AMR}$
Cosumnes/Mokelumne (MOK)	$Q_{MOK} = Q_{11} + Q_{12} + Q_{13}$	---
Stanislaus (SLS)	$Q_{SLS} = Q_{9}$	---
Lower San Joaquin Valley (SJQ2)	$Q_{SJQ2} = Q_{10}$	$Q_{SLS} + Q_{TUO} + Q_{MRC} + Q_{SJQ1}$
Tuolumne (TUO)	$Q_{TUO} = Q_{7}$ or regression on Q_{8}	---
Merced (MRC)	$Q_{MRC} = Q_{4}$	---
Upper San Joaquin (SJQ)	$Q_{SJQ} = Q_{2}$	---
Upper San Joaquin Valley (SJQ1)	$Q_{SJQ1} = 0.78(Q_{6}-Q_{5})$ (regression on Q_{3})	$Q_{SJQ} + Q_{KNG}$
Kings (KNG)	$Q_{KNG} = Q_{1}$	---

Some minor stream crossings of river basin boundaries, visible in Figure 3.3, were ignored. It should also be noted that these calculations involve no time lag to account for in-stream travel times. While such lags were estimated, using lagged correlations, as 1-2 days within most of the river basins, incorporating these values in the outflow calculations yielded little change. The intended use of the outflow data is to characterize the hydrologic behavior of the individual river basins at time scales of weeks and longer. Thus, it was deemed unnecessary to attempt a full accounting for lag effects in the flow data.

Finally, not only does each basin have an outflow, but some have inflows as well. These are also shown in Table 3.1, as functions of the calculated outflows. A basin's inflow is independent of the actual behavior of the basin, so to truly

characterize each river basin separately, the inflows must be subtracted from the outflows to yield local in-basin contributions. The resulting mean annual hydrographs of the local contribution data from WY 65-87 are shown for each of the 15 basins in Figure 3.4.

There are several reasons for the dramatic differences between the basins' hydrographs. First, there is a clear difference between the mountain basins and the valley basins. The valley basins are the only ones to have negative values in their mean annual hydrographs. This is due to the effects of irrigation in the valleys. Water is removed from the valley streams to irrigate crops, and most of it is lost to evapotranspiration or aquifer recharge before it can return to the streams. Thus, the net contribution of these basins can in fact be negative. The two San Joaquin Valley basins, in particular, have almost entirely negative hydrographs. This is due to the irrigation effect combined with the very arid conditions there. If no irrigation were occurring, these basins would have a local contribution hydrograph essentially identical to zero, since any precipitation would be lost to evaporation before it could enter the streams.

There are clear differences among the mountain basins, as well. Most evident is the shift from early to late runoff as one scans the basins from North to South. This is an effect of the higher elevations and colder temperatures in the South. Snowpack is retained until early summer in the high Southern Sierra, whereas in the lower elevation Northern Sierra, lower elevations and subsequently higher temperatures cause less snow to accumulate, and what does accumulate melts earlier.

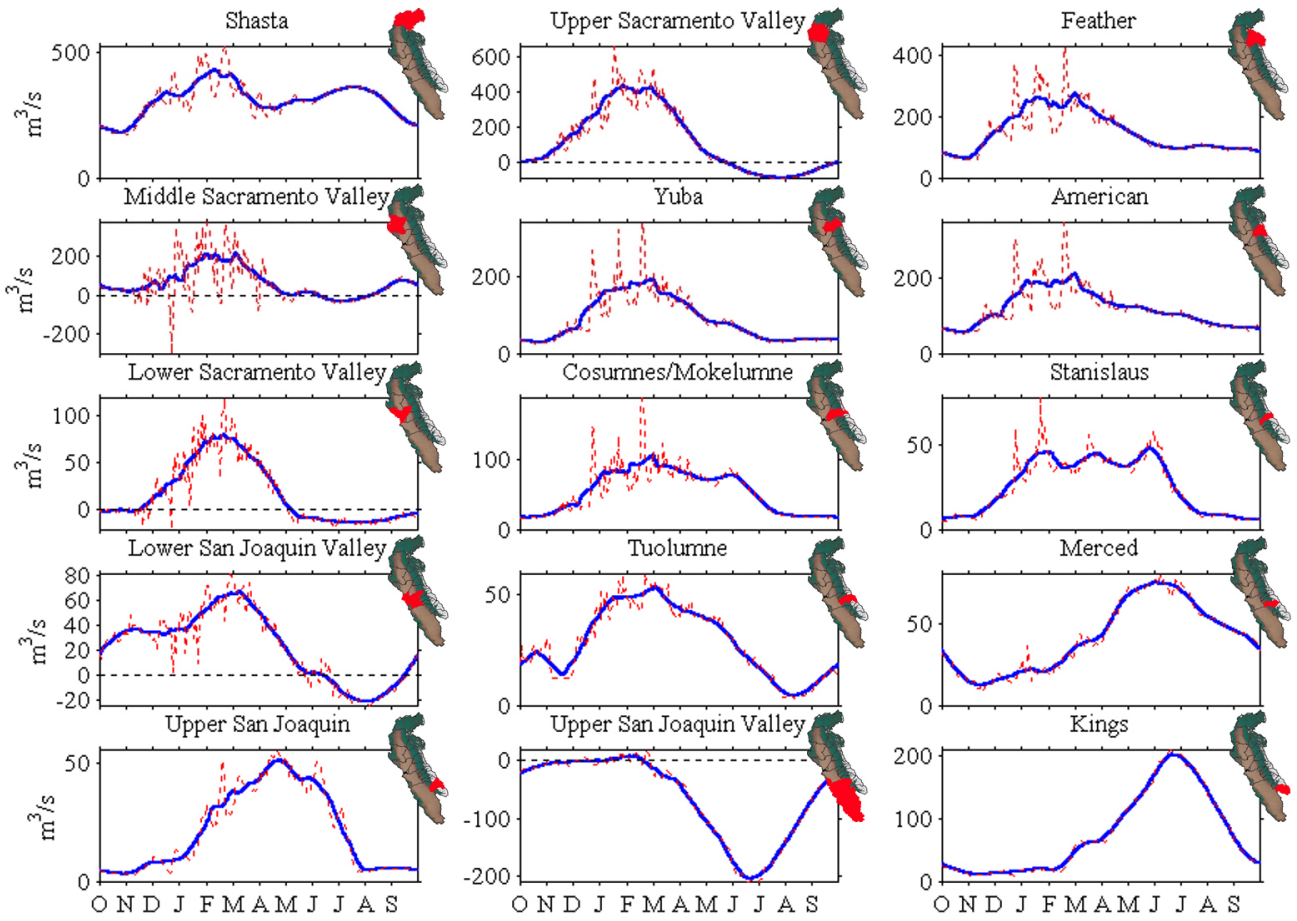

Figure 3.4 Mean annual cycles (for water years) of actual local flow contributions from the river basins. The mean of the daily data is shown in red; a 30-day smoothed version is shown in blue.

Though the hydrographs in Figure 3.4 are useful for characterizing the basins, it must be remembered that they represent highly impeded flows, the water having encountered reservoirs, canals, pumps and more along its path. It is difficult to tell the difference between artificial and natural effects in these plots. To gain a better understanding of the watershed's natural behavior, it is necessary to first address the effects of manmade impediments to river flows.

3.4 Reservoirs and Reconstructed Outflows

There are over 1,400 dams in California, with an accumulated storage capacity of around 50 km^3, compared to the 80-100 km^3 of streamflow generated, on average, Statewide. The total storage capacity of reservoirs in the Bay-Delta watershed is around 35 km^3, roughly equal to the average annual inflow to the Bay. The largest of these reservoirs are described in Table 3.2. The effect of the reservoirs is generally to limit flow peak flows to preventing downstream flooding, and also to delay a portion of river flows until the dry season, when the water is released for use. The management of reservoirs and the resulting basin outflows, though dependent on the natural variability of a river basin, represents a strong alteration of natural flow patterns. A physically-based hydrologic model to be used in hydroclimate studies, therefore, must attempt to reproduce a basin's natural variability. Reservoir management procedures may then be incorporated into the model, with the simulated natural flows as the starting point. The difficulty lies in estimating a basin's natural behavior from such reservoir-impacted flow estimates as those presented in the

previous section. The effects of reservoirs and other impediments to the natural flow must be removed from the data as much as possible. Of course, considering the number of reservoirs involved, this is a formidable task. Since the goal of this work is to characterize and simulate the basins' natural behavior at relatively long time scales (monthly and longer), it is appropriate to consider the effects of only the larger reservoirs, since the effects of the smaller ones will be averaged out as the time scale increases. A cutoff reservoir storage capacity of 1 million acre-feet* was chosen. Removing the effects of reservoirs larger than this should give an estimate of natural flow levels at monthly and longer time scales.

A common method of removing reservoir effects from impaired flow data involves adjusting the flows for storage changes in the reservoirs. Natural flow estimates determined in this manner were courteously provided by Scott Staggs of the California/Nevada River Forecast Center (http://www.wrh.noaa.gov/cnrfc/). This data was calculated at outflows from 9 major reservoirs (corresponding to all the major rivers except the Yuba) in the watershed by accounting for daily storage changes at each reservoir and at significant upstream reservoirs, as well as for diversions into manmade canals. That is, for a given reservoir, daily natural flow below the reservoir was determined as the sum of the daily storage change at that reservoir, the daily outflow at that reservoir, the sum of the daily storage changes at upstream reservoirs, and out-of-basin diversions from all reservoirs. Note that this data goes beyond the 1 million acre-feet cutoff requirement by including effects at the smaller upstream dams

* Millions of acre-feet is a preferred unit of measurement in the water resources community. 1 million acre-feet is equivalent to 1.234 km^3. SI units will be used from now on.

and canals. This reservoir storage accounting method is, however, somewhat limited in that water movement due to release flows and winds can affect instantaneous water level measurements and yield inaccurate storage values. Also, evaporation from the reservoirs can have a significant effect. This method generates estimates of unimpaired daily flow rates accurate to within about 20% (Robert Newton, CADWR, personal communication).

The CNRFC natural flow estimates had coverage at all 9 reservoirs for the full period mentioned previously, WY 1965-1987. This represents all major reservoir outflows, with two exceptions. The Mokelumne and Stanislaus river natural flows were estimated at locations elsewhere on these rivers than the major reservoirs, Camanche and New Melones. For the Stanislaus, estimates are actually at the outflow of a smaller reservoir downstream of the New Melones, the Goodwin dam. For the Mokelumne, the effects of the Camanche reservoir were not included, the estimates corresponding to the upstream location, Mokelumne Hill. This is acceptable as the Camanche has a capacity of only 0.53 km^3, considerably less than the 1.234 km^3 cutoff.

Finally, natural flow estimates were not available for one large reservoir, New Bullards on the Yuba River. The California Center for Data Exchange (http://cdec.water.ca.gov) does have some natural flow estimates for this site, but these are very sparse and do not cover a sufficient portion of the desired W65-87 period. While the New Bullards' storage capacity is below the cutoff, it is the largest reservoir

on the Yuba. When subsequently examining flow estimates for this river, the fact that they are impaired by New Bullards must be kept in mind.

Table 3.2 Largest reservoirs on the watershed's major rivers. Natural flow estimates were available for all rivers except the Yuba. The Mokelumne and Stanislaus natural flow values were not calculated at the major reservoirs; the names and relative locations of the natural flow locations are indicated.

Reservoir or Location and year of completion	River	Capacity of Largest Reservoir (km^3)	Mean Total Annual FNF (km^3)
Shasta (1945)	Upper Sacramento	5.55	7.49
Oroville (1968)	Feather	4.30	5.35
New Bullards (1970)	Yuba	1.20	2.79 (actual flow)
Folsom (1956)	American	1.23	3.48
Camanche (1963)	Mokelumne	0.53	0.91 (at Mokelumne Hill, upstream)
New Melones(1979)	Stanislaus	2.96	1.37 (at Goodwin, downstream)
Don Pedro (1971)	Tuolumne	2.51	2.13
Exchequer (1967)	Merced	1.27	1.22
Friant (1942)	Upper San Joaquin	0.64	2.21
Pine Flat (1954)	Kings	1.23	2.23

Figure 3.5 shows the mean local contribution hydrographs, adjusted for reservoir effects. The actual mean annual hydrographs from Figure 3.4 are also shown for comparison.

Reservoirs clearly have the strongest effect in the high southern Sierra. These reservoirs were designed to capture the snowmelt for delivery into the arid San Joaquin Valley to meet its agriculture's high irrigation demands, as well as for flood prevention. The Upper San Joaquin, Tuolumne and Stanislaus rivers show the strongest effects of diversions for irrigation, resulting in much larger reconstructed natural flows than the observed flows after these irrigation diversions are added back in. When reservoir effects are removed, it can be seen that these basins, on average,

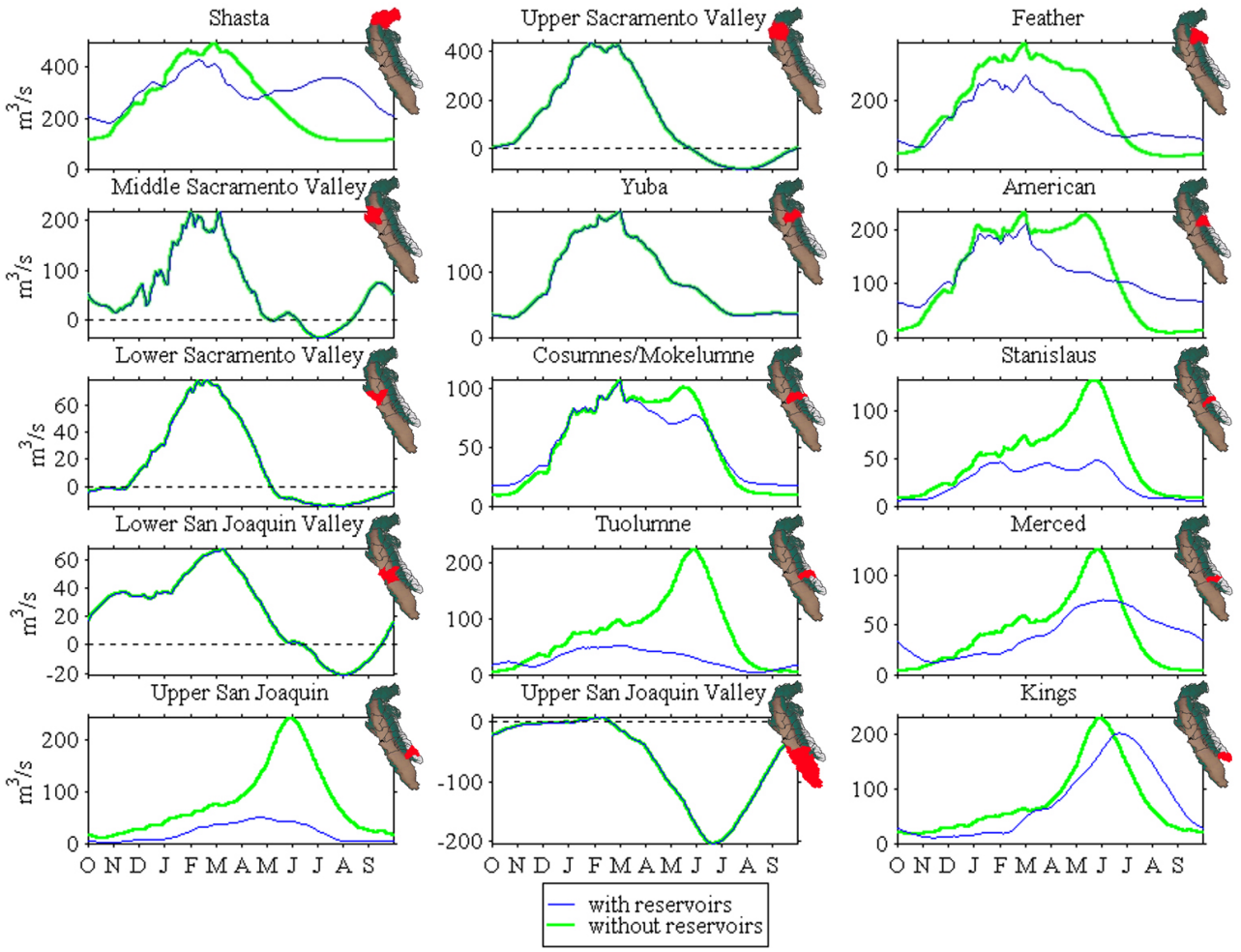

Figure 3.5 Mean annual local (in-basin) contribution hydrographs, with and without reservoir effects.

exhibit a strong natural snowmelt peak in May and June. The more northern hydrographs show a much stronger runoff signal during the rainy season centered on January, February and March, with low flows during later months, when adjusted for reservoirs. Yuba basin and the valleys, of course, show no change from Figure 3.4. It is worth noting that the Shasta basin actually shows more total flow in the actual flow hydrograph than in the reconstructed natural flows. This is due to artificial diversion of water from the Trinity reservoir in the neighboring Klamath mountains through a tunnel into the upper Sacramento River, above the gauge location.

While Figure 3.5 reveals mean hydrologic differences across the watershed, the full time series of the reconstructed natural flows (Figure 3.6) reveal watershed-wide similarities.

Only the mountain basins are shown in Figure 3.6, since the valley signals are corrupted by irrigation effects. Among these basins there are still obvious differences, such as the much wetter conditions in the northern mountains. However, year-to-year changes in the magnitude of river flows tend to be shared among all basins, indicating the large scale of atmospheric forcing at the interannual level. Prominent events spanning the watershed include the drought of 1976-77, the very wet years WY 1982-83, and the isolated storm spike of late February, 1986.

It appears that while pronounced differences exist across river basins at time scales shorter than a year, interannual and longer variability tends to be shared among the basins. At this point, it is worth examining in more detail the relative behavior of the northern and southern mountain basins. The goal is to discern the similarities and

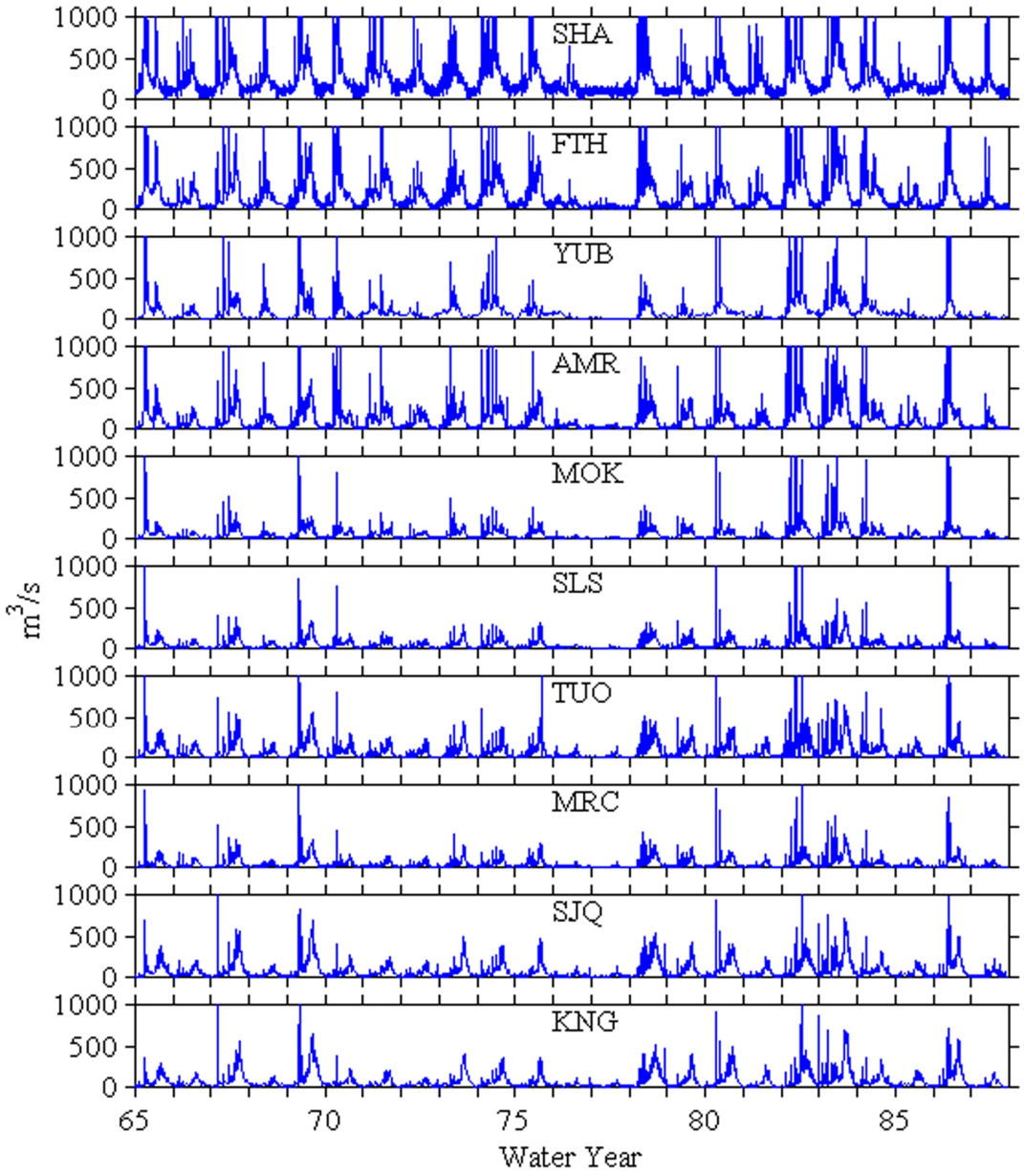

Figure 3.6 Natural flow estimates for the mountain basins for WY 65-87. The order is from north to south.

differences, at the interannual scale, in the northern and southern contributions to the Bay-Delta estuary's freshwater inflow.

3.5 Sacramento vs. San Joaquin

In order to examine the relative variability of Sacramento and San Joaquin basin flows, the unimpaired flow estimates from the headwater basins of each of these larger regions (Figure 3.7) have been summed to generate two time series (WY 65-87). The low-altitude valley basins have been excluded due to contamination of those flow signals by agricultural diversions.

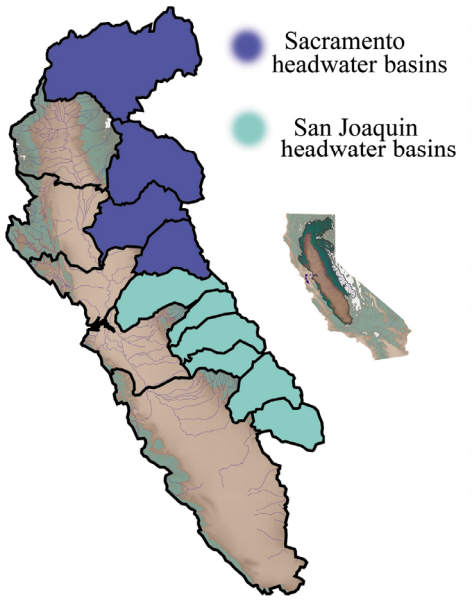

Figure 3.7 Division of watershed into Sacramento and San Joaquin headwater basins.

The mean annual hydrographs of the two time series (Figure 3.8) show the distinct signature of each region. The strong effect of the larger snowpack in the San Joaquin headwaters creates peak flows about 3 months later, on average, than Sacramento flows.

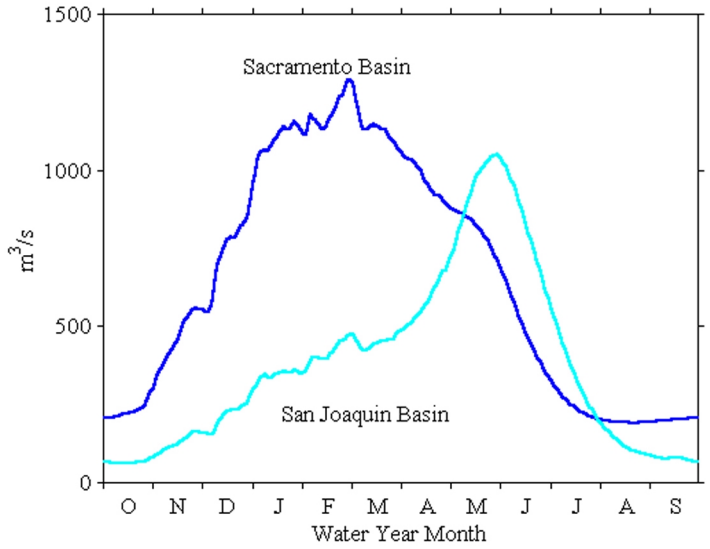

Figure 3.8 Shown above are the mean annual flow contributions from the two basins, from the original time series smoothed with a 30-day running average.

Though snow delay is a persistent feature of the Bay-Delta watershed's hydrology, the length of the delay does vary somewhat, as shown in Figure 3.9. Here, the timing is not peak flow but the date of the "center of mass" of the water year annual hydrograph. If this were a plot of peak flow, there would be much more variability in the Sacramento timing than in the San Joaquin timing. Sacramento flows are driven primarily by rainfall, and are thus subject to the more capricious timing of the precipitation process. The center of mass date, however, is closely paralleled in the two basins, with the San Joaquin coming just over a month later on average.

Though the timing of the two regional hydrographs contributes to the overall timing of unimpaired Delta freshwater inflows, another important factor is the relative amount of water which each region provides.

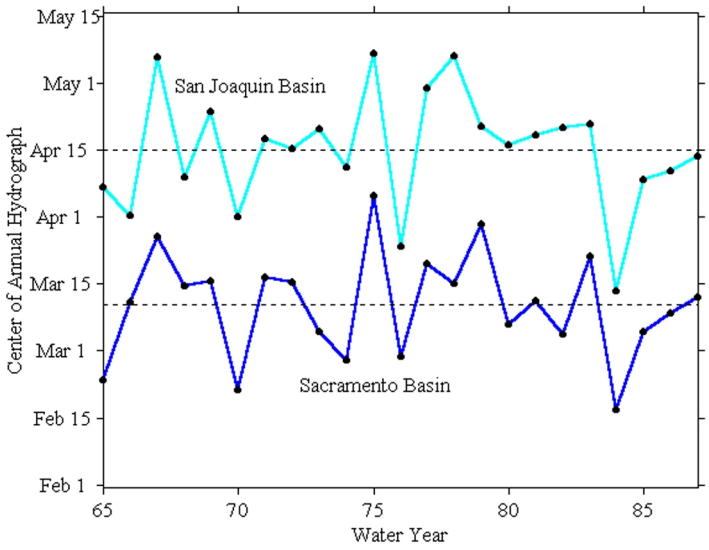

Figure 3.9 These are the dates of each water year's flow center of mass for the 2 basins.

The average hydrographs (Figure 3.8) show the much larger overall contribution of the Sacramento basin, due to its broad hydrograph. Even though the average peak flows differ by only 300 m^3/s, average annual mean flow from the Sacramento headwaters is about 190% that of the San Joaquin headwater basins. Again, these contributions vary strongly from year to year, as shown in Figure 3.10. Here the annual average flow rates for the Sacramento and San Joaquin headwaters display highly correlated interannual variability, as suggested previously in Figure 3.6. However, the relative contributions of the two regions varies strongly. Figure 3.10 reveals that although the Sacramento region's contribution is consistently larger than the San Joaquin region's, there is some intriguing behavior in the ratio of the two.

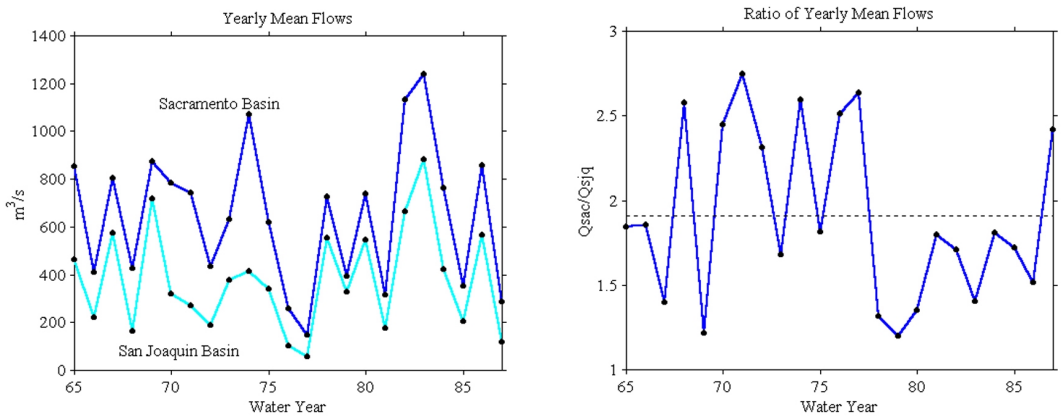

Figure 3.10 **Left:** Yearly mean flow rates for 23 water years.
Right: Ratios of each year's mean flow (Q_{SAC}/Q_{SJQ}). The mean ratio is ~2.25.

Until 1977, the ratio of unimpaired annual flow in the Sacramento region to that of the San Joaquin region was, in general, greater than 1.9. It appears as though a shift may then have occurred, as subsequently the ratio was consistently less than 1.9. This shift of flows from Sacramento to the San Joaquin regions suggests a southerly movement of the storm track. This movement has indeed been observed to have occurred, in 1976-77, resulting from changes in the ocean and atmosphere of the northern Pacific, the region which most strongly influences atmospheric behavior over the Bay-Delta watershed (*e.g.*, Dettinger, Cayan *et al.* 1998). This change in the North Pacific, in fact, appears to be part of a larger pattern of decadal oscillations in the North Pacific which has been dubbed the North Pacific Oscillation (NPO) (Latif and Barnett 1994; Latif and Barnett 1996; Mantua, Hare *et al.* 1997), suggesting an interdecadal swinging of which Figure 3.10 (right) shows only a portion.

Thus, it seems clear that the effect of the regional timing shifts of Figure 3.9 on the timing of Delta inflows are modulated by the relative amounts of precipitation in each region, north and south. The fact that this balance is very sensitive to the average

position of the storm track, which in turn depends on interdecadally-oscillating conditions in the northern Pacific, offers a tantalizing glimpse into the connections between estuary, watershed, and global climate. This subject will be addressed further in Chapter 7.

3.6 Other Human-Induced Impacts on Flow

There are four major ways in which human activities have large impacts on flows in the watershed. One, reservoirs, has already been addressed. The other three are in-basin irrigation diversions, river containment, and Delta exports. Before addressing these, however, there is one more effect worthy of mention. This is groundwater recharge and extraction.

California has a vast underground storage system of natural aquifers, with an estimated capacity of 1500 km^3, in which porous soils hold water deep in the ground (see http://capp.water.usgs.gov/gwa/ch_b/B-text3.html). This water can only be accessed through wells, and is not available to evaporative processes. It is therefore a much-relied-upon source of freshwater, particularly for irrigation during dry years, though in the past it was used as though its supplies were limitless. Groundwater availability was taken for granted until recent decades, when excessive pumping caused a severe drawdown of these underground reservoirs. When these porous soils became dry, they compacted, causing a subsidence of the land surface and resulting in a permanent loss of aquifer storage capacity (Galloway, Jones *et al.* 1999). This threatens the reliability of the resource when it is truly needed, and groundwater

extraction and recharge (purposefully letting water seep into the aquifers) have therefore become carefully monitored processes. On average, approximately 10 km^3 of water are extracted yearly from the watershed's aquifers, mostly in the arid Upper San Joaquin Valley Basin, and the same amount is recharged. Some of the recharged water comes from reservoirs and was therefore accounted for in Section 3.4; the rest is part of the "irrigation effect" seen in the valley basin hydrographs in Figure 3.5. The extracted water is largely lost to evapotranspiration, but some returns to the aquifers, and some enters the stream network. In this study, groundwater extraction will not be considered. These effects will be folded into the many human effects impacting the valley hydrographs. Only the natural recharge of groundwater will be considered, and this only during the development of the hydrologic model.

Another human-induced impact on flows is in-basin irrigation diversions, that is, the taking of water out of in-basin streams for redistribution over agricultural fields. The effect of this is mainly a net loss of water to evapotranspiration (see valley basins in Figure 3.5). An attempt to "remove" such effects from flow data, as was done for reservoirs, would require an explicit accounting of irrigation diversions throughout the watershed as well as some means of estimating return flows (irrigation water which makes its way back into the stream network). Quantifying irrigation effects and adjusting flows to account for these effects is therefore a formidable task, and one which will not be attempted in this dissertation.

The containment of rivers refers mainly to the use of levees, dikes, canals, bypasses and other artificial means of controlling flowing water to prevent rivers from

overflowing their banks. This has had a particularly strong impact in the Sacramento Valley region, where floodplain inundation was once a yearly event:

> "Under natural conditions, flood waters in the lowland Central Valley spilled over natural levees…. Enormous flood plains and natural flood basins functioned similar to reservoirs, filling and draining every year. This delayed the transmission of flood flows, reducing peak flows and velocities, and increased summer flows as the water spread out over the floodplain slowly drained back into the river later in the year." (Bay Institute 1998)

This "inland sea" clearly had a drastic impact on the shape of the annual hydrograph reaching the estuary. While it would be very interesting to attempt to re-create and understand these effects and their significance for the ecosystems involved, it is unlikely that the full "inland sea" effect will be felt again by the estuary anytime soon[*]. It is perhaps more pertinent then, not to mention feasible, to exclude river containment from the present effort to understand and quantify human impacts on flow, limiting the effort to reservoirs, addressed previously, and Delta exports.

[*] However, smaller-scale floodplain inundation projects are now planned as part of the Bay-Delta restoration effort, and their effects on the estuary in the context of hydroclimatic variability will require study.

3.7 Delta Diversions and Outflow

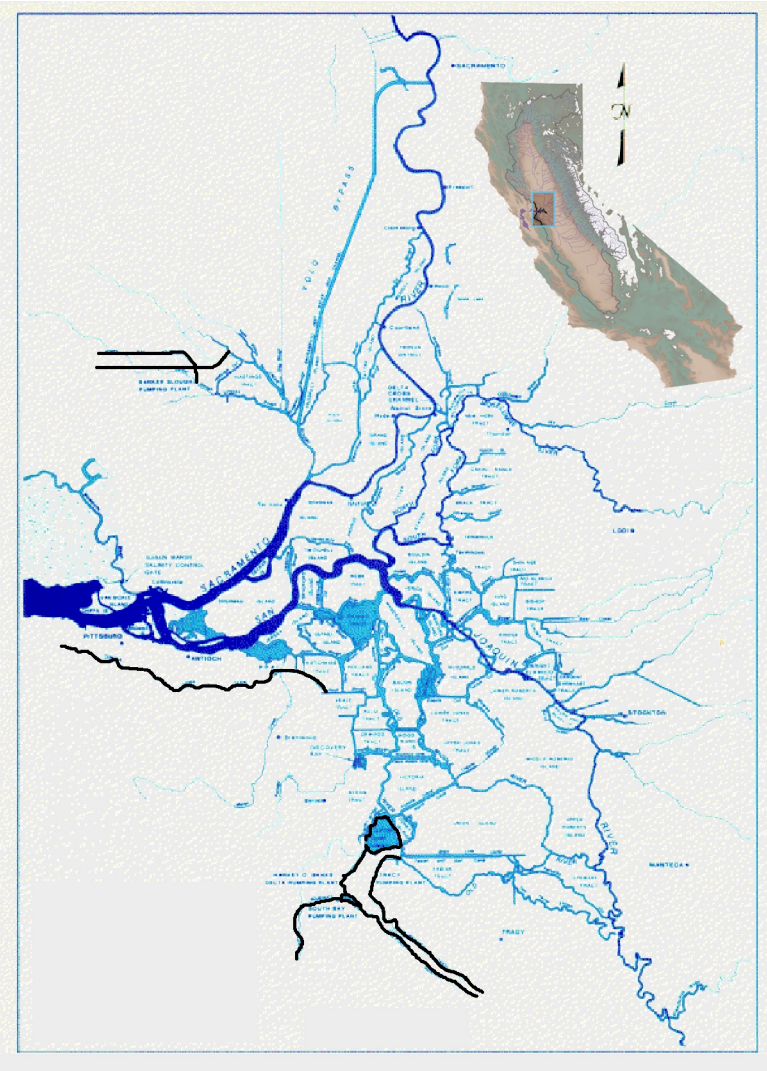

Figure 3.11 The Delta region. The Sacramento, San Joaquin and Mokelumne rivers are indicated in dark blue, lesser waterways in light blue, and major aqueducts and pumping facilities in black (from the *Delta Atlas*, http://rubicon.water.ca.gov/delta_atlas.fdr/daindex.html).

The Delta of the Sacramento and San Joaquin Rivers (Figure 3.11) is a maze of bays, islands, and meandering channels which lies to the east of San Francisco Bay and at the heart of many of California's water issues. This region is part of the Bay-

Delta estuary, containing the state's most diverse ecosystem alongside the state's most fertile farmlands. It is also another place where humans have significantly altered the natural plumbing of California. Pumping stations (Figure 3.11) extract enough freshwater from the Delta to irrigate nearly 20,000 km^2 of farmland as well as to supply two-thirds of the state's population with all or part of its water (Mount 1995). These diversions of freshwater are the last artificial changes to the Bay-Delta watershed's flow patterns before the water reaches the Bay. To understand the behavior of the estuary, the nature of these changes must be examined.

DAYFLOW is a program administered by the California Department of Water Resources (California Department of Water Resources 1999) which has provided an invaluable record of the freshwater budget in the Delta. Using a few of the data stations shown in Figure 3.3 as well as other stations in the Delta region, and estimating some effects such as local evaporation and precipitation, DAYFLOW apportions Delta freshwater into numerous components in three broad categories—total Delta inflow, net channel depletions and total Delta exports. Total Delta inflow is the same as the sum of all the local contributions from the fifteen river basins of Figure 3.2 (including reservoir effects). Channel depletions include effects such as local evaporation and precipitation. Total Delta exports are just that—the sum of all artificial diversions which remove freshwater from the Delta. Of these three, channel depletions are the smallest, with the lowest impact on flows into the Bay. The other two are examined below.

The time series for Delta inflows and exports are shown for WY 65-87 in Figure 3.12.

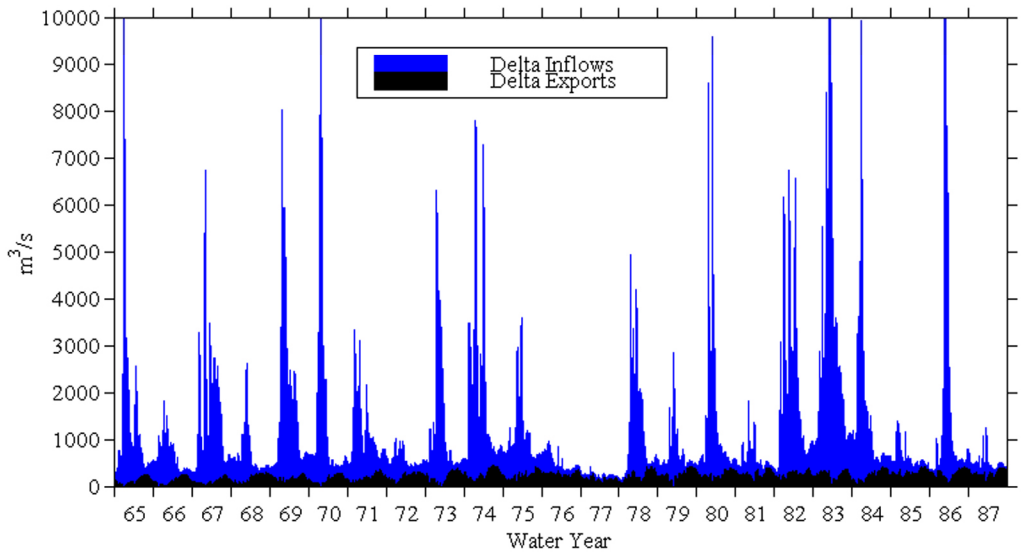

Figure 3.12 Time series of total Delta inflows and total Delta exports.

Delta inflows from WY 65-87 averaged about 33 $km^3/year$, and an average of about 5 $km^3/year$ was exported. Interannual variations in exports (Figure 3.12) are small compared to those in inflows. The relation between exports and the incoming water supply will be examined in more detail in the next chapter. For now, note that there is an annual cycling to exports (Figure 3.13), with higher diversions during the dry season when they are more needed.

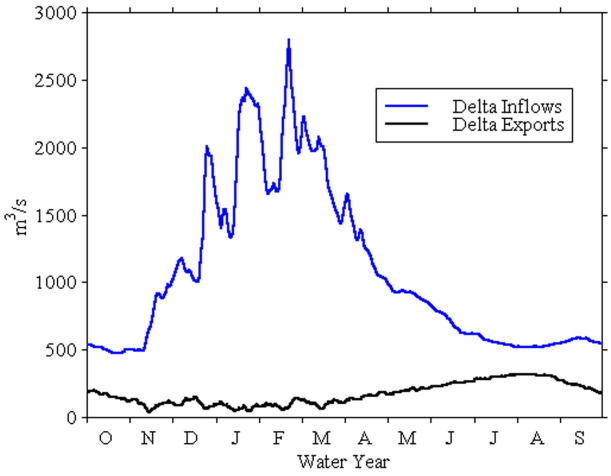

Figure 3.13 Mean annual cycles of Delta inflow and exports.

Using the export data along with the estimated reservoir effects, the influence of these human effects on Delta outflow can be reconstructed. The mean annual hydrographs of the reconstructed outflows (Figure 3.14) shows that the main effect of exports (red line relative to blue line) is to lower flows year-round, with the largest impact from May through October (commensurate with Figure 3.13).

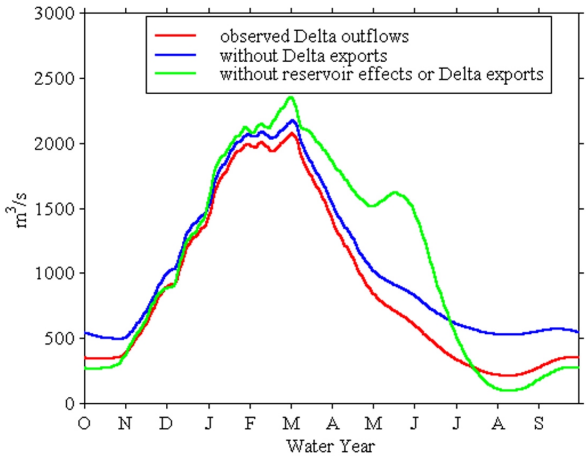

Figure 3.14 Observed and reconstructed mean annual cycles (30-day low-pass filtered) of Delta outflows corresponding to different levels of human impact.

The average effect of reservoirs (blue relative to green) on Delta outflow is a timing shift, wherein snowmelt flows (May-June) are captured by the reservoirs and returned to the rivers in the dry season (July-October). On average, the reservoirs capture a total of 11.3 km^3 of freshwater and return 7.9 km^3, for a loss of 3.5 km^3. Contributions to the reservoir effect on Delta outflow vary from north to south and from year to year. These variations will be addressed in the next chapter.

Of the ~8 km^3 which reservoirs return to the rivers, Most (~5 km^3) is exported be Delta pumps. Thus the net effect of reservoirs and Delta exports is to lower flows most strongly during April-June, with relatively small effects during the rest of the year.

The fully reconstructed flow data (with both reservoir and export signals removed) should provide a cleaner signal with which to examine the influence of atmospheric and hydrologic variability on Delta outflows. Figure 3.15 shows the interannual variability in the magnitude and timing of reconstructed Delta outflows. The strong year-to-year changes in magnitude are the most apparent feature at this time scale; Figure 3.6 showed that this is a watershed-wide phenomenon. The timing changes are more subtle, but still impressive, representing a difference of over 5 months at the extremes.

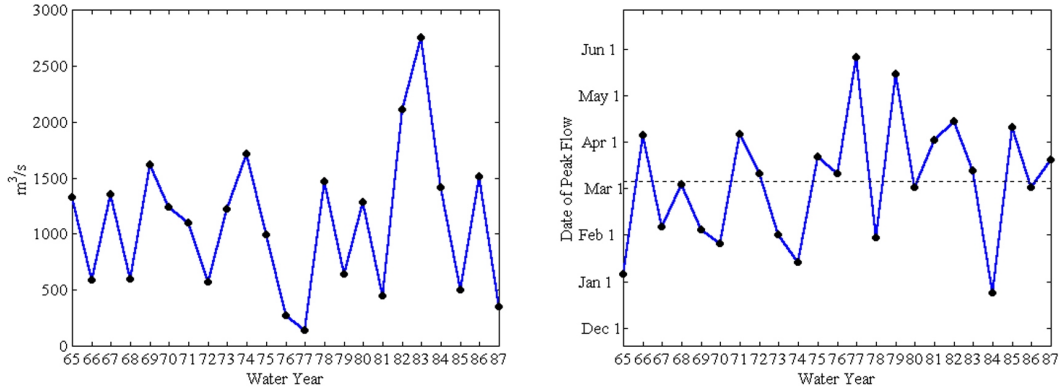

Figure 3.15 **Left:** Estimates of unimpaired annual mean Delta outflows. **Right:** Peak (30-day smoothed) annual unimpaired Delta outflow dates for WY 65-87.

Unlike the variability in magnitude, the variability in timing has a range of causes across the watershed, as seen in Section 3.5. The hypothesis presented in that section was that a shift of the storm track from north to south in 1976-77 caused relatively more snowpack to accumulate, which should lead to later Delta outflows. While no shift is clearly apparent in Figure 3.4 (right), it is true that 7 out of 11 years before 1976 have peaks earlier than the average (beginning of March), and the same proportion of flow peaks after 1976 came later than the average. Reviewing Figure 3.9, it is clear that the storm track shift is not the only factor potentially affecting flow timing, and it is expected that other factors such as variability of precipitation timing have an influence on the timing signal of Figure 3.15. Nonetheless, statistically speaking, a large-scale event such as an interdecadal shifting of the storm track might cause a signal which is still evident in the midst of such relatively stochastic effects.

Comparing the "unimpaired" Delta outflow peak timing to actual outflow timing (Figure 3.16), it is clear that there is significant corruption of the original timing signal. First, an overall shift toward earlier flow peaks can be attributed to the

fact that the net effect of management is to remove late-season snowmelt flows from the annual hydrograph. Second, the reservoirs completely change the timing in some years, with very little effect in others. Comparison with mean annual flows (Figure 3.15, left) reveals that the most significant timing changes due to reservoirs tend to occur in dry years. This suggests that natural variability may not be completely

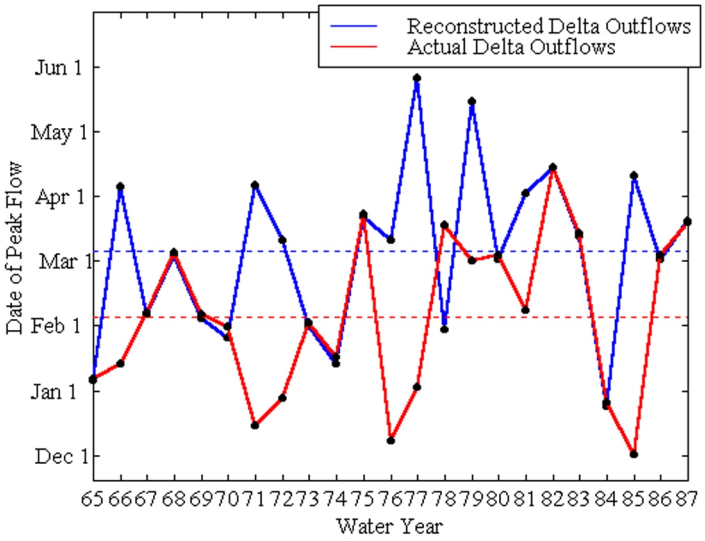

Figure 3.16 Effect of reservoirs and Delta exports on peak (30-day smoothed) flow dates.

overwhelmed by the reservoir effect. In fact, for actual Delta outflow, only 2 of 11 years before 1977 had later-than-average peak flows, with the same proportion having earlier-than-average peaks after 1977, suggesting effects such as a storm track shift may be evident even in the impaired signal, that is, in the signal which in reality drives the estuary's annual cycle.

Indeed, examination of the full DAYFLOW record appears to support this claim. The smoothed version of this time series (Figure 3.17, right) appears to show a timing shift corresponding to the storm track shift inferred from Figure 3.10. Further,

with the exception of 1957-1966, a period centered on several consecutive dry years (which may generate an added effect on flow timing), this timing shift appears to be part of a longer-term oscillation, with another major shift having occurred around 1946. This will be further investigated in Chapter 7. Less evident, though still significant, are shorter-length oscillations in the magnitude of annual flows reaching the estuary (Figure 3.17, left). Any climate variability associated with this apparent 15-year cycle in the magnitude of Bay-Delta watershed outflows has not yet been identified (Mike Dettinger, personal communication), though the signal is tantalizingly. regular.

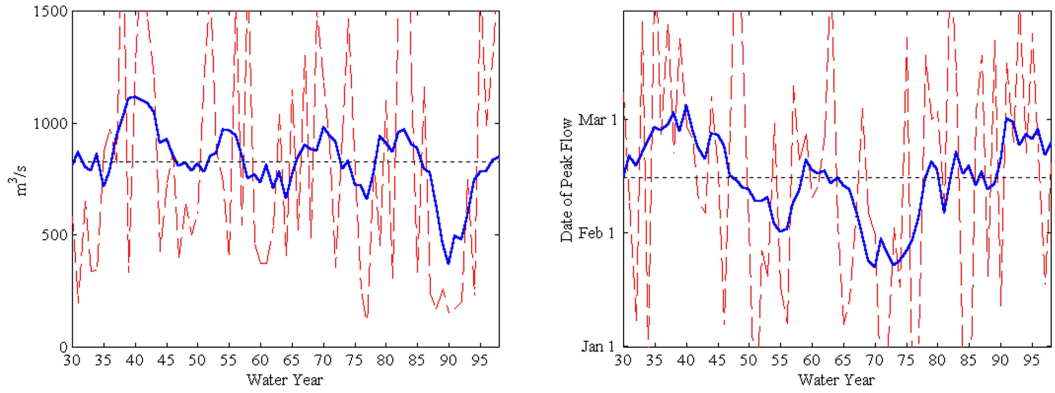

Figure 3.17 **Left:** Annual mean Delta outflows, with 10-year smoothed version. **Right:** Peak (30-day smoothed) annual Delta outflow dates, with 10-year smoothed version.

3.8 Summary

In this chapter, we have examined the behavior of river flows throughout the watershed. Differences between observed flows and reconstructed natural flows have demonstrated the strong impact of reservoirs and freshwater pumping in both the individual river basins and the watershed as a whole.

Reconstructed unimpaired flows offer estimates of the true "natural" behavior of the Bay-Delta watershed, revealing impressive differences in the hydrology of the various river basins. In particular, it has been shown that the northern Sacramento river basin exhibits an annual hydrograph which is strongly influenced by winter rainfall runoff, whereas the southern San Joaquin river basin shows a very different, snowmelt-driven hydrograph.

Despite consistent differences in hydrologic behavior, all parts of the watershed share strong interannual variability, both in the magnitude and the timing of flows. This similarity, however, masks more subtle changes in the north-south distribution of precipitation and flows, which appears to be linked to climate variability. This discovery provides a first glimpse of connections between the watershed and the global climate system, connections which will be investigated further in Chapter 7.

This chapter also demonstrated clearly that management has a significant, though not overwhelming, effect on the estuary/watershed system, causing strong deviations from "natural" behavior. Though some natural signals are evident despite these alterations, a better understanding of the relationship between natural variability and management effects, and the consequent implications for the estuary, should make the big picture even clearer.

4 Management Effects

4.1 Delta Outflow Variability and Human Effects

4.1.1 Analysis of Delta Outflow Components

To study the impacts of management on the estuary, the starting point must be the impacts of management on Delta outflow. Figure 4.1 summarizes this data, which was discussed in the previous chapter. “Unimpaired flow” is the estimate of Delta outflow with reservoir and Delta exports removed, “reservoir effect” is the contribution of reservoirs to Delta outflow, negative when reservoirs are capturing water and positive for releases, and “Delta export effect” refers to the amount of water diverted from the Delta region. The latter is primarily negative, so that all three time series represent components of actual Delta outflow, their sum being equal to actual Delta outflow.

A cursory examination of the flow component time series (Figure 4.1) reveals that year-to-year variability of both the natural signal and human effects is large, with extreme events providing notable examples. The signature of the 1976-77 drought is evident in all three signals, while years of major abundance, such as water year 1983, are reflected most clearly in the unimpaired and reservoir signals. The Delta export effect, consistently negative (other than occasional positive spikes representing in-Delta storm runoff), became noticeably stronger over the period of

record. It is also apparent that each of these signals has a strong annual cycle, though the exact timing is not clear in this figure.

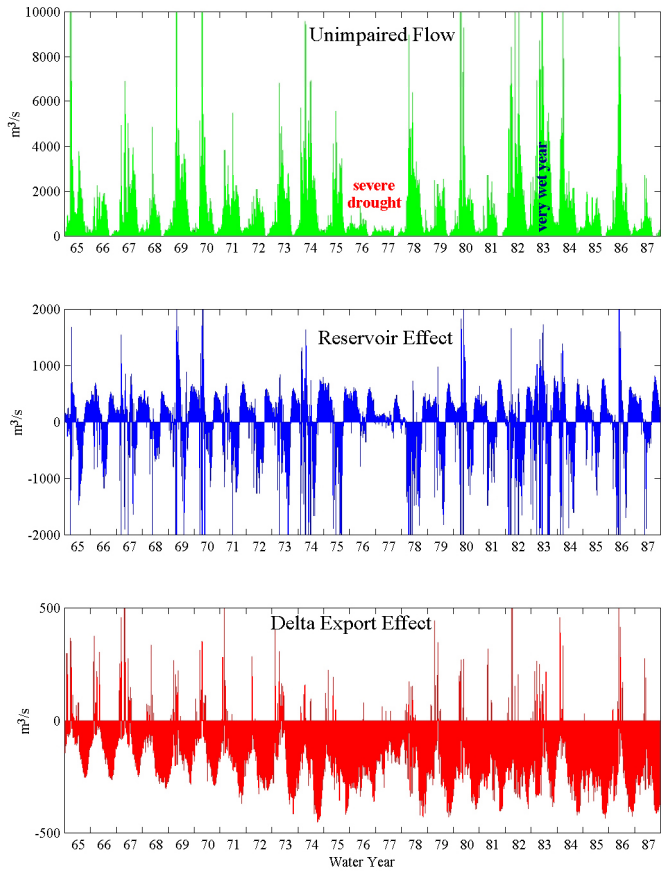

Figure 4.1 Estimates of unimpaired flows and effects of reservoirs and Delta exports Bay freshwater inputs through the Delta. Note the differing scales of the plots. Adding the 3 series yields estimates of Delta outflow.

However, a plot of the mean annual cycles (with smoothed versions for clarity) of the flow contribution time series from Figure 4.1 clearly illustrates the mean yearly timing of natural and human effects (Figure 4.2).

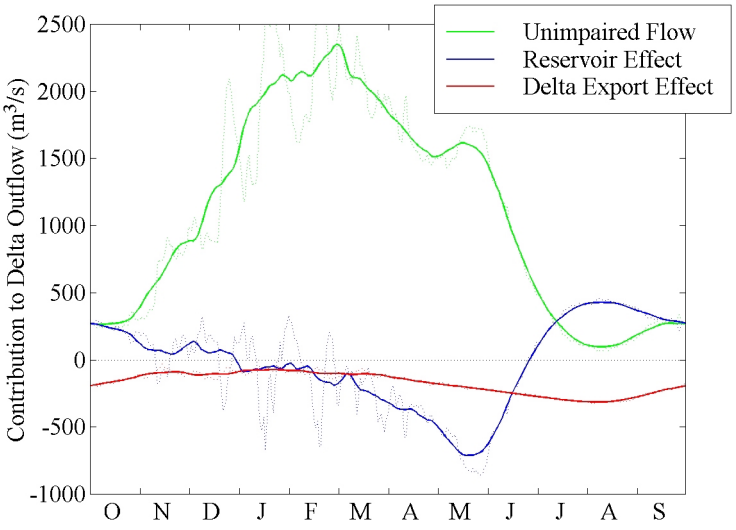

Figure 4.2 Mean annual cycles (30-day smoothed) of unimpaired, reservoir and Delta export flow contributions (unsmoothed versions are dashed lines).

Natural flows reach a peak in February-March, with the low flows of the dry season extending from July through October. On average, reservoirs effectively remove water from Delta outflow from February through early June, returning it during the dry season. The sharp peak in the negative reservoir effect in May is due primarily to reservoirs in the southern Sierra capturing snowmelt runoff. This figure also shows Delta exports to be at their maximum during June, July and August, with the lowest diversions occurring from November through May. Though these human effects are clearly related to natural variability, the year-to-year character of these connections is not apparent from Figure 4.2. An empirical orthogonal function analysis (EOF) of standardized versions (with zero mean and standard deviation equal to one) of these time series provides a more quantified representation (Figure 4.3) of the relationships between human effects and natural variability.

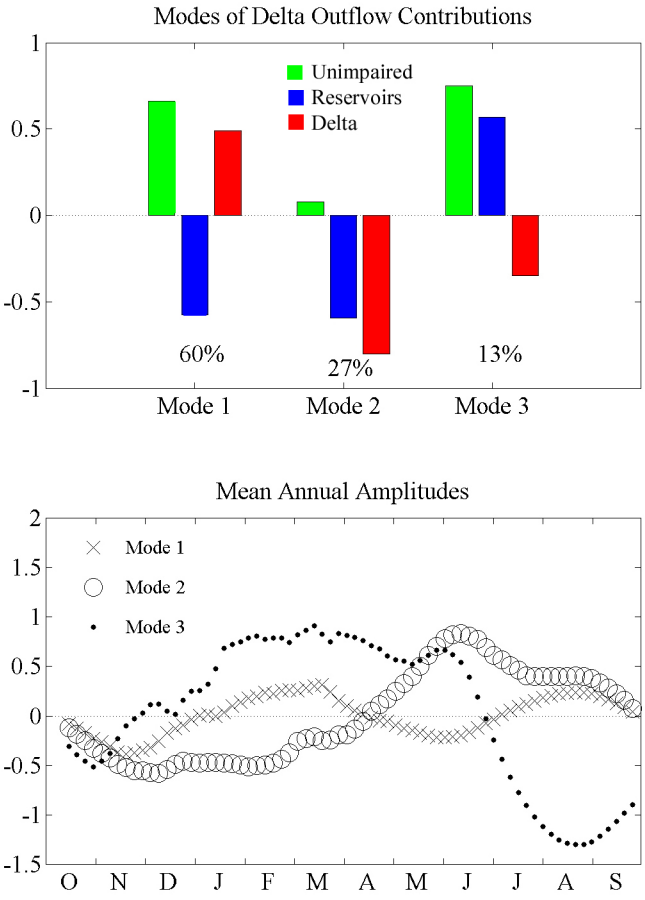

Figure 4.3 EOF Modes and their mean annual cycle amplitudes for daily Delta outflow contributions.

The EOF analysis breaks down the variability of the three standardized flow components into portions which are perfectly correlated with one another, called "modes". Thus, if all natural variability were perfectly correlated with both human effects, only one mode would result which would capture all of the Delta outflow variability. Conversely, if the three components were completely uncorrelated, the EOF analysis would yield three modes, each representing one of the original series. Here, the analysis yields three modes which explain 60%, 27% and 13% of the total variance of the standardized data. The 1st and 3rd modes represent flow variability

which is directly due to, or results from a management action correlated with, concurrent (at the daily scale) natural variability. These "nature-correlated" modes capture a total 73% the variance. The dominant mode shows that reservoir effects and Delta export effects tend to be negatively correlated. This is no surprise as non-flood related reservoir releases are primarily scheduled to meet export demands. The remaining 27% of variance captured by the 2nd mode represents human effects which are either unrelated to natural variations, or which are correlated but with a time lag. This may represent, for example, changes in demand unrelated to natural variability or management actions based on the flow history or on runoff forecasts.

Two key results of this analysis of influences on Delta outflow are that human effects are strongly dependent on the large natural variability, and that reservoir effects tend to be negatively correlated with both natural variability and Delta export effects. These will be shown to have significant implications for the Bay-Delta estuary.

4.1.2 Simulating the Estuarine Response

The next step in evaluating human impacts is to develop simulations of the salinity field's response to the reconstructed flows. The model used here is again the Uncles-Peterson model (Uncles and Peterson 1995), the advective-diffusive intertidal box model, described in Section 2.2, whose dominant inputs are tidal state (a measure of the spring-neap tidal status) and freshwater inflows. Other data used to force the model are coastal ocean salinity and local precipitation and evaporation. This model simulates San Francisco Bay's daily- and laterally-averaged salinity and current fields

with a very low computation load, making it ideal for applications requiring long-term, multiple simulations such as this study.

To explore the effects of human-induced flow changes on the estuary, three versions of reconstructed Delta outflow were used to drive the model. The flow components (Figure 4.1) were summed sequentially to generate three time series, two of which are hypothetical (Figure 4.4): unimpaired Delta outflow, Delta outflow with reservoir effects only and estimated real Delta outflow, which includes both reservoir effects and Delta exports.

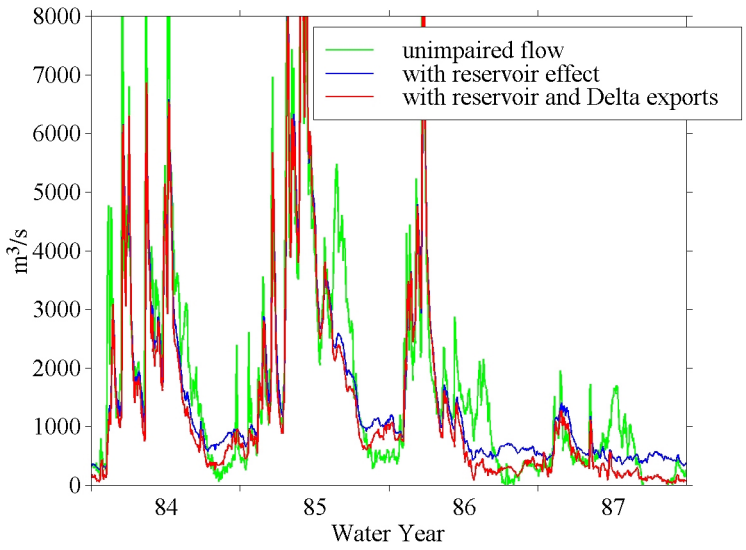

Figure 4.4 Sample daily time series for reconstructed flows with differing levels of human impacts.

These three time series were used to force the U-P model over 21 water years from October of 1966 through September of 1987 to provide estimates of salinity under the three reconstructed levels of impairment.

4.2 Impacts on Salinity

4.2.1 Long-Term Mean Response

A plot of two simple measures of the influence of reservoirs and Delta pumping on salinity throughout the estuary— the mean and standard deviation of the daily salinity field (Figure 4.5)— reveals that though the effects on the mean salinity field might seem small, the final result of all human impacts is to raise mean salinity 1-2 *psu* throughout the estuary.

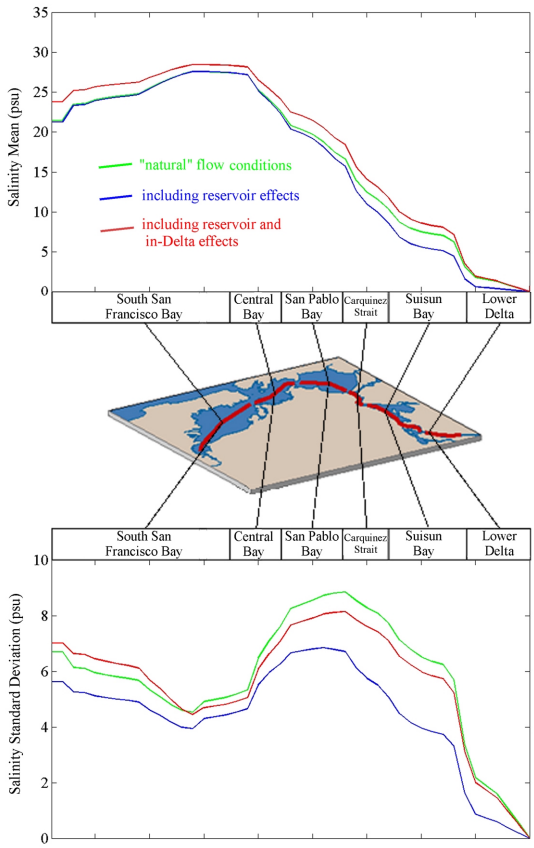

Figure 4.5 Mean (upper panel) and standard deviation (lower panel) of modeled Bay-Delta salinities over a 21-year period (10/66-9/87).

Reservoir effects alone tend to lower average salinity by up to 2 *psu* in the northern part of the Bay-Delta (from San Pablo Bay through the lower Delta), an indication of the practice of releasing water to repel salt from the export region during the dry season. Reservoir effects also reduce the variability of salinity, lowering the standard deviation by 1-2 *psu* from unimpaired levels. Delta exports have the opposite effect, restoring variability to well within 1 *psu* of unimpaired levels throughout the Bay. The competing effects of reservoirs and Delta exports on the statistics of the salinity field are a result of their negative correlation, as discussed in the results of the modal analysis (Figure 4.3). It is also worth noting that since the northern Bay is near zero *psu* in most wet seasons, human effects on salinity there are largely restricted to the dry-season months. In South Bay, on the other hand, salinity tends to reach a maximum in the dry season, and is relatively unaffected by human impacts on Delta outflow except during the wet season. It is also pertinent to remember that the relatively small South Bay inflows remain unchanged in these simulations; only impacts on Delta outflow are represented.

4.2.2 Annual Cycle and Interannual Variability

Though human effects on the long-term statistics may seem small, changes in the mean annual cycle are much more significant. Human impacts on the monthly mean annual cycle of the salinity field's position are clearly indicated by X2 (Figure 4.6), the commonly-used salinity index which is defined as the distance of the near-bottom 2 *psu* isohaline from the Golden Gate (Jassby, Kimmerer *et al.* 1995). High

values of X2 correspond to saline conditions, while low values signify fresh conditions and higher inflows.

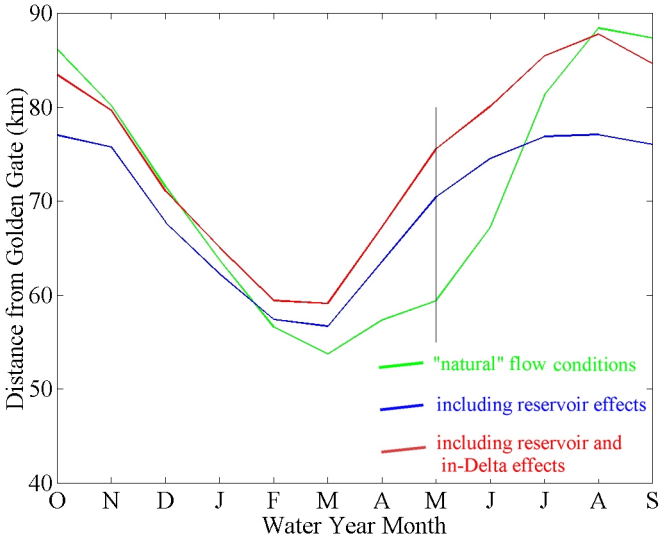

Figure 4.6 Average annual cycle of human effects on salinity. The maximum difference between "natural" and actual X2, in May, is highlighted. See Figure 4.7 for interannual variability of May effects.

Although in the long-term, reservoir and Delta export effects are negatively correlated and have competing effects on salinity relative to unimpaired conditions, Figure 4.6 shows that this is not true year-round. From February through mid-June, the two effects combine to increase monthly mean salinity levels, shifting X2 by a maximum of over 15 *km* up the estuary in May. During the dry season, on the other hand, reservoir effects move X2 as much as 10 *km* downstream relative to unimpaired conditions, while competing Delta exports increase the salinity, pushing X2 to near-unimpaired levels.

Considering the large average impact of humans in spring, it is useful to examine the year-to-year variability of these effects. Figure 4.7 shows the May effects

for each year of the record, relative to unimpaired conditions. X2 displacements due to reservoir and Delta export impacts vary hugely, particularly at 5-10 year intervals. Reservoir effects displace May X2 anywhere from 0 km to 22 *km* landward of unimpaired values. Delta export effects increase this displacement as much as 10 *km*. Despite the huge variability of these impacts over the record, reservoirs and Delta exports consistently act in concert during this time of year. Both displace X2 landward in every year of the record, the only exception being the slight seaward displacement due to reservoirs in May of 1977, the second year of an extreme two-year drought.

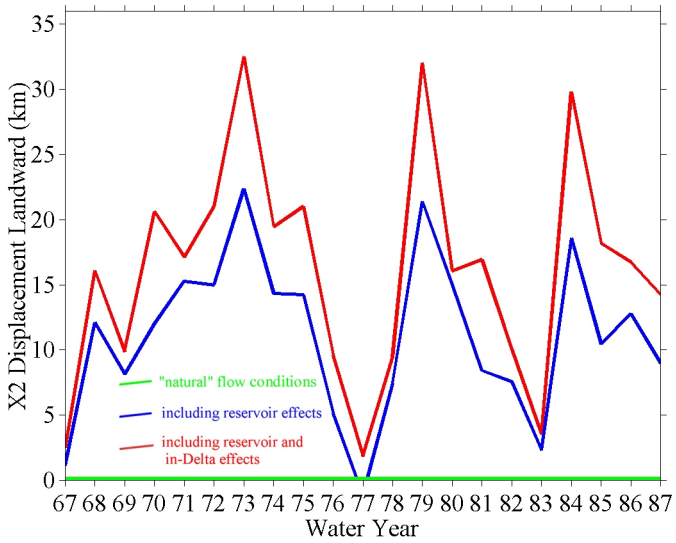

Figure 4.7 May residual management effects on salinity intrusion, relative to unimpaired conditions. See Figure 4.6.

A comparison of the X2 displacement data (Figure 4.7) and average "unimpaired" inflow rates (Figure 4.8) reveals no clear correlation at the annual scale between May management effects and natural variability, except that the largest effects tend to occur in moderate (non-extreme) flow years. Also, May is the time when the 2nd mode of the EOF analysis of Delta flow components (Figure 4.3),

representing human effects not correlated with natural variability, reaches its largest amplitude. It appears that in May, human effects on Delta outflow and Bay salinities reach not only their highest level, but also their greatest independence from concurrent natural variability.

4.2.3 Extreme Years

Having examined the long-term and year-to-year impacts of humans on salinity in the Bay-Delta, it is now interesting to consider the average effects in particular types of water years. After selecting the five wettest and driest years with respect to average annual "unimpaired" flow rates (Figure 4.8), composite mean annual cycles of X2 were generated for the different human impact levels (Figure 4.9).

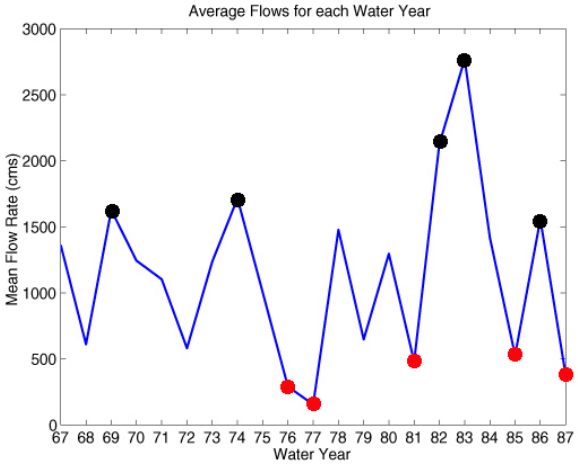

Figure 4.8 Annual average "unimpaired" Delta outflow rates, with 5 wettest and driest years indicated.

Several interesting facts emerge from a comparison of these two plots. First, with the exception of late summer, human effects on X2 (the spread between the simulated "natural" and "actual" values) are much stronger in dry years. Though this

is partially due to the greater proximity of the 2 *psu* isohaline to the Delta during dry conditions, it is largely a result of increased human effects on flow during such years. Also, though spring impacts are still the largest, during dry years the maximum human impact comes in April, one month earlier than in the mean annual cycle (Figure 4.6). Conversely, in wet years this maximum occurs later, in June.

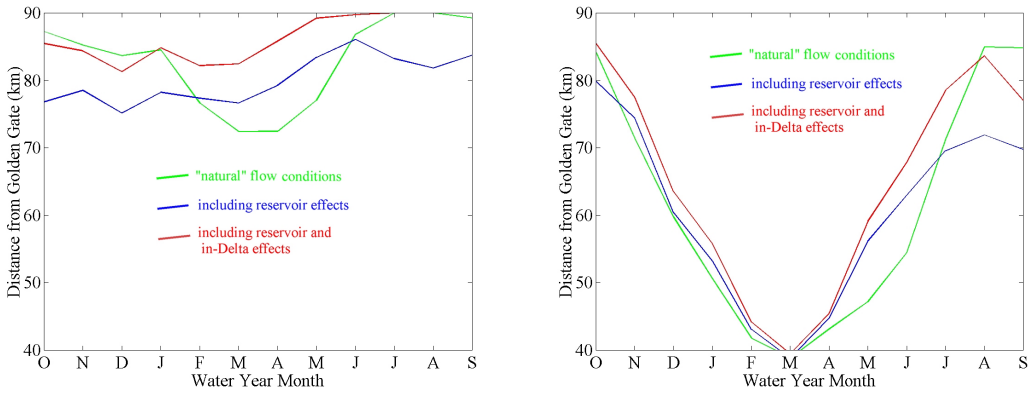

Figure 4.9 Dry- and wet-year composite annual cycles of human effects on salinity.

Note also that though it may not be obvious, the maximum human impact on X2 is slightly larger in wet years than in dry years. In both composites, it is still true that reservoir and Delta effects counter one another during the dry season. This is particularly evident during dry years and during August and September of wet years, when releases to provide flood control storage generate a large reservoir effect.

Perhaps the most noteworthy aspect of the information in Figure 4.9 is that human effects in the estuary are dwarfed during the wet season by natural differences between the wet and dry composites. Clearly, the overwhelming difference in spring X2 values between relatively wet and dry years suggests that natural variability will

often impact the estuary in ways that are not, and likely cannot be, mitigated by upstream freshwater management.

4.3 Discussion

In this study, effects of reservoirs and Delta exports on Bay-Delta salinity were estimated by using reconstructed Delta outflows to drive a numerical salinity model. Both natural and human effects exhibited large seasonal and interannual variability. The long-term mean annual cycles and a modal analysis of contributions to Delta outflow showed human effects to be strongly related to concurrent natural variability. Reservoir effects were largely negatively correlated with both natural variability and Delta export effects. This leads to competing effects of the two human influences on the mean and variance of Baywide salinities. Within a water year, the relative effects of Delta exports and reservoirs are, on average, opposite during the wet versus the dry parts of the year. During the wet season, both effects serve to raise salinities, while they tend to offset one another during the dry season. While some of these results may seem obvious considering the operating procedures of the reservoirs and the Delta pumping stations, understanding the magnitude and timing of these impacts could have important implications for the health of the estuarine ecosystem.

Spring was shown to be the period of largest human impacts in the estuary in terms of X2. This is a critical time of year for many species in the estuary (*e.g.*, Jassby, Kimmerer *et al.* 1995), though the implications of particular changes caused by altered flows are still poorly understood. The importance of spring is further

emphasized by recent research which suggests that there is usually a snowmelt-driven runoff surge from Sierra watersheds which marks the transition from winter to spring (Cayan 1999). This phenomenon spans western North America and is driven by hemispheric atmospheric patterns. The large scale of these patterns suggest that the spring snowmelt surge may be a predictable event, possibly allowing the timing and magnitude of estuarine impacts to be more accurately forecast.

Compositing mean annual X2 cycles for wet and dry years revealed several interesting differences in impacts between water year types, such as the fact that maximum human impacts occur earlier in dry years. The most interesting result, however, was that natural variability in the freshwater supply can cause large year-to-year shifts in salinity patterns which are not significantly altered by human effects. This has important implications for understanding ecosystem health. In the case of several consecutive dry years followed by several wet years, as has occurred since 1987, native and restored estuarine ecosystems must be capable of adapting to the accompanying shift in salinity regimes. Much attention has rightfully been given to the concept that "the volume and timing of freshwater flows to the Bay should reflect historical or natural conditions under which the Bayland habitats and animals developed" (San Francisco Bay Area Wetlands Ecosystem Goals Project 1999). Clearly, it is also important to consider the existing large natural variability when studying surviving and restored ecosystems, which are but remnants of the original ecosystem and must be able to adapt to inevitable natural variability.

5 Describing the Watershed: Soils, Landscape and Meteorology

Having examined in some detail the natural and managed behavior of flows in the watershed and their influence in the estuary at weekly to decadal scales, the focus now shifts to the physical details of the watershed itself. With the ultimate goal of developing a physically-based hydrologic model of the watershed, a fairly comprehensive collection of data characterizing the watershed's physical characteristics is here presented and examined. The flows studied so far are a result of the complex hydrologic interaction of the meteorology driving the watershed with the topography, landcover and soils which define its character. Each of these properties, from the time series of spatially-distributed precipitation to the depth to bedrock throughout the watershed, must be quantified and assembled into a coherent database. In bringing together such a collection of data, the first step is to establish a coordinate system appropriate to the intended uses.

5.1 Map Projections and the Data Grid

Though coordinates on the Earth's surface are most often given as a longitude and a latitude, these are not suitable coordinates for referencing data across an area as large as the Bay-Delta watershed. For example, an east-west measurement of 1° at the southern end of the watershed represents a distance which is approximately 10% longer than the same measurement at the northern end, due to poleward convergence

of the meridians (Figure 5.1). Such a distortion would cause significant errors in any calculation involving distance between two points (such as interpolation) or areal averages, which are very common in hydrology. For hydroclimate studies, it is necessary to reference all data distributed spatially over the watershed to a coordinate system in which distances and areas are minimally distorted.

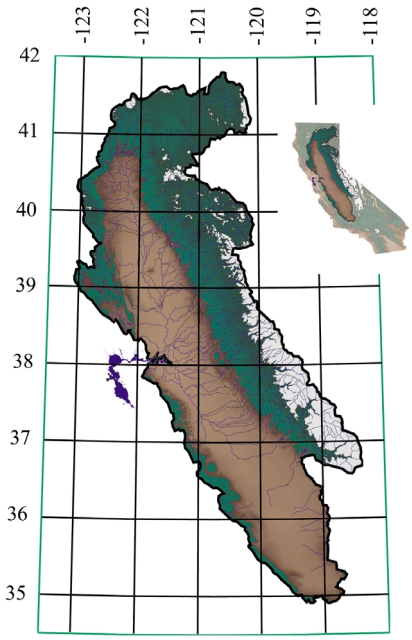

Figure 5.1 Geographic coordinates of the San Francisco Bay-Delta watershed.

The method by which data is converted from the spherical Earth to a plane is called a map projection. There are many map projections in common use, and the choice of which projection is best suited to a given application depends on which properties of the spherical surface are most important to preserve in the transformation. As mentioned, distance and area are critical elements to large hydrologic studies such as this. A suitable projection, used in this study, which

minimally distorts these quantities is the Albers equal-area conic projection (Snyder 1987).

This method is equivalent to projecting the sphere onto a cone with its apex directly over the North pole, then unrolling the cone to a flat surface. Unlike some variants of this conic method, the cone used here is not tangent to the Earth at one parallel; it is instead secant, intersecting the sphere at two parallels. Distortion of distance, area and even shape is minimal near and between these parallels of secancy, or *standard parallels*. A rule of thumb for choosing the standard parallels in the Albers equal-area conic projection is to choose latitudes $1/6^{th}$ of the north-south extent of the region of interest from its northern and southern limits (Deetz 1934). For the Bay-Delta watershed, the standard parallels were placed at 36.01°N and 40.67°N. All spatially-distributed data presented subsequently in this chapter were either interpolated or projected onto this coordinate system.*

Once a common coordinate system was selected, it was necessary to aggregate all data to a common grid. This allowed easy comparison of different data, greatly simplified calculations and was generally more conducive to model-building than having data sets with differing distributions and resolutions. The particular choice of data grid resolution was a compromise between the need to represent the heterogeneity of the watershed's hydrologic characteristics and the need to avoid prohibitively large data sets.

* These manipulations, along with much of the calculations and processing of the data, were performed with the GIS software ARC/INFO (http://www.esri.com/). Other relevant projection parameters include the datum, NAD83, and the spheroid, GRS80.

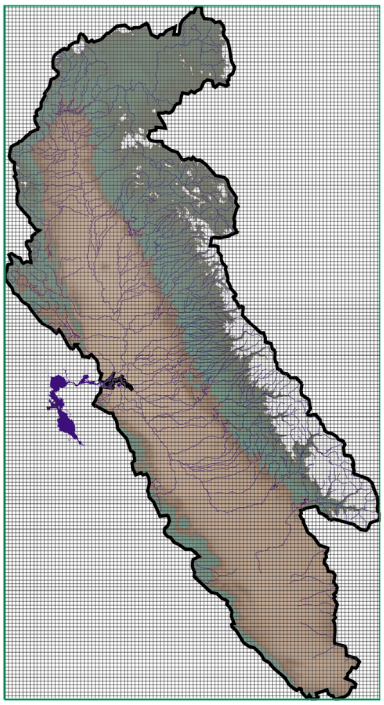

Figure 5.2 Grid used for aggregating and referencing watershed data.

A resolution of 4 *km* was chosen for the data grid (Figure 5.2). This value allowed much of the heterogeneity in land cover, soil properties and topography to be represented, while remaining coarse enough that interpolation and other calculations remained computationally feasible. In each of the subsequent sections of this chapter, data characterizing a particular aspect of the watershed will be presented, then the appropriate method of aggregating or interpolating the data to the 4 *km* data grid will be discussed. Finally, the aggregated data will be examined to shed more light on the hydrology behind the river flows.

5.2 Topography

5.2.1 Dependence of Hydrology on Topographic Parameters

One of the most basic, and yet most important, characteristics of any watershed is the spatial distribution of elevation. The connection between topography and the shape of a basin's annual hydrograph has already been alluded to, with an emphasis on the effects of high altitude snowpack. There are also many other links between the layout of the terrain and the hydrologic behavior generated therein.

While the dependence of rainfall and snow generation on elevation is the primary topographic control on hydrology, slope and aspect also affect the snowpack's evolution, the movement of liquid water after it reaches the ground, and the transition to water vapor. The local slope affects the rate at which water flows downhill, both in and on top of the soil. Slope combined with aspect determine how much of the landscape is exposed to sunlight, and how directly, at any given time of the day and within the year. This solar energy drives evaporation and snowmelt, linking the layout of the land to ablation of the snowpack and losses as water vapor.

A topographic description of the watershed is therefore essential to the process of building a hydrologic model. This is the next step in understanding how inflows to the Bay-Delta estuary are shaped.

5.2.2 Digital Elevation Models

A digital elevation model (DEM) is an array of elevation estimates, developed primarily from existing topographic maps, but with some use of aerial photographs. Using both manual and automated methods, elevation data are transferred to digital form and interpolated to a grid (http://edc.usgs.gov/glis/hyper/guide/1_dgr_dem/). The DEM data obtained for the San Francisco Bay-Delta watershed (Figure 5.3) have a horizontal resolution of 83 *m* (also called a "3 arc-second", or "1:250,000 scale" DEM).

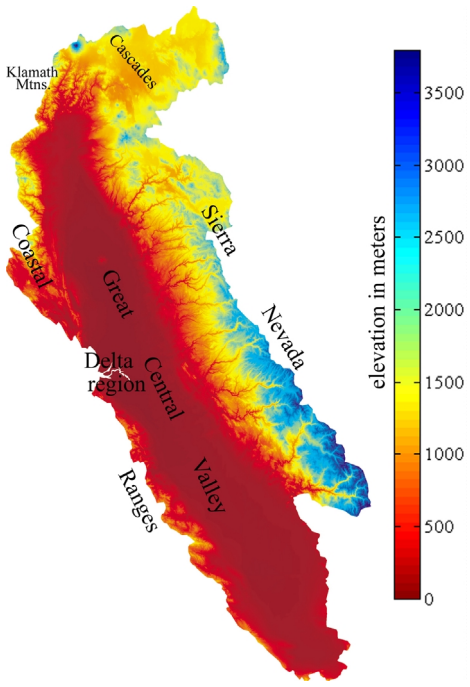

Figure 5.3 DEM elevation data for the watershed, with main geographic features indicated. Original data has a horizontal resolution of 83 *m*.

At this resolution, the major rivers with their forks are clearly visible as they wind their way into the valleys. The increasing elevation moving south along the

Sierra is also evident, as is the broad, low-lying Central Valley, culminating at its lowest point, the Sacramento-San Joaquin Delta.

5.2.3 Manipulation of DEM Data

Although the 83 *m* resolution data provides a great deal of detail about the watershed, such detail is not required for this study, and the data set used to create Figure 5.3 is too large for many of the intended applications here. Simple averaging over the 4 *km* by 4 *km* grid cells was performed to aggregate this data to the data grid (Figure 5.2). For comparison, the version of the DEM data used in this study is shown in Figure 5.4.

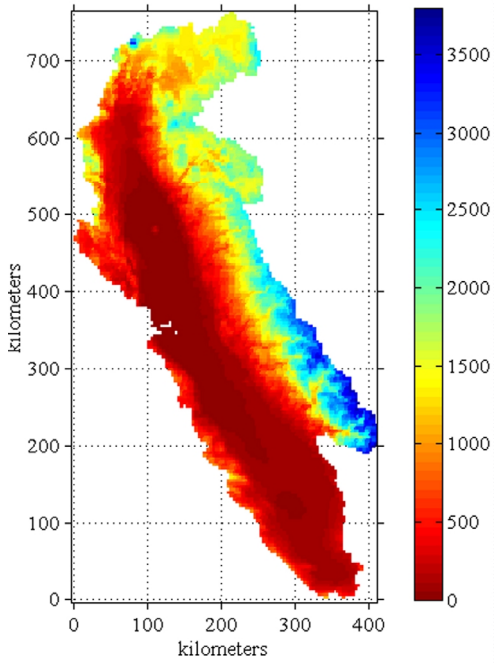

Figure 5.4 The 4 *km* resolution version of the DEM data, used in this study.

The two other topographic quantities needed to characterize the watershed, slope and aspect, were also derived from the original DEM data. Within each of the 16

km^2 grid cells, there are about 2,300 data points in the original DEM. This data was used to estimate slope and aspect at the 83 *m* resolution, which were then averaged to produce slope and aspect values at the 4 *km* resolution (Figure 5.5).

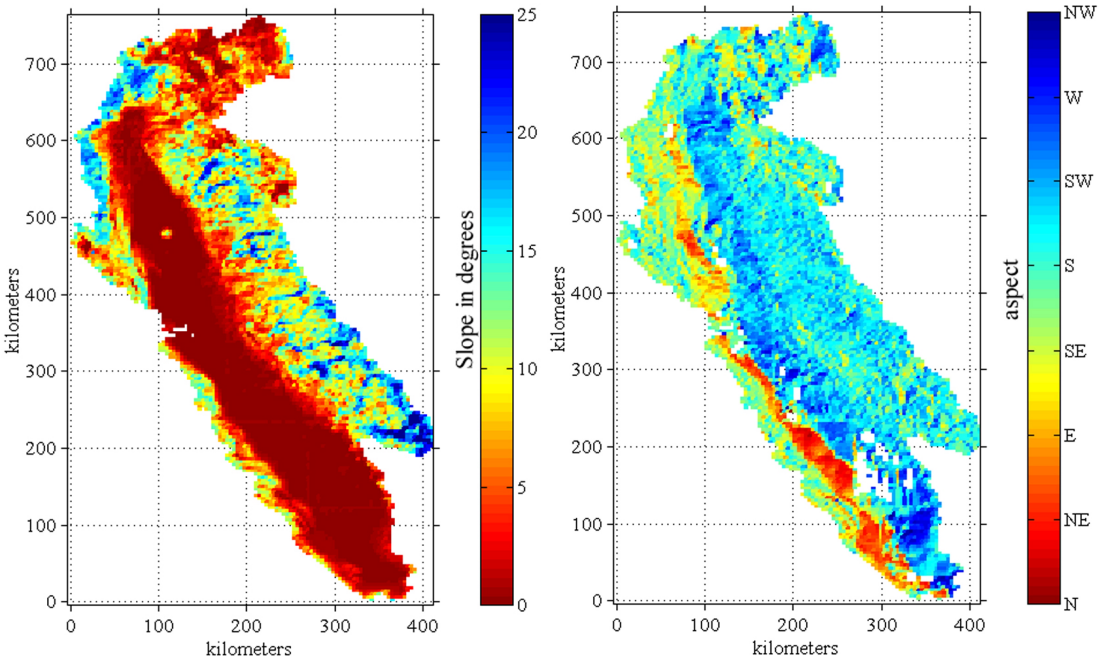

Figure 5.5 Slope (left) and aspect (right) of the watershed, averaged to a 4 *km* grid.

The use of simple averaging in the aggregation of topographic quantities is somewhat arbitrary. Other measures, such as the median, minimum or maximum values, or a weighted average within each of the 4 *km* grid cells could have been used. The use of the simple average reflects an assumption of linear dependence of all hydrologic processes on the respective topographic quantity. In the future, other aggregation methods may be evaluated to test the significance of this assumption.

5.2.4 Topographic Description of the Watershed

The most prominent topographic features of the watershed (Figure 5.3) are the Sierra Nevada and the Central Valley, followed by the Cascades, the Coastal Range and the Klamath mountains. The Tehachapi mountains border the Valley to the south, but these do not figure in the watershed's hydrology, nor do the extreme southern Sierra mountain basins south of the Kings River basin. Though these regions are technically (topologically) part of the Bay-Delta watershed, they are hydrologically isolated from the rest of the watershed and are not included in this study.

Most of the Sierra rise well above 2000 *m*, while the northern mountains are largely below 2000 *m*, though higher latitude enhances their snow-bearing tendencies. The high peak of Mount Shasta is clearly visible in the Cascades, the Klamath range barely intruding into the watershed just to the south.

The Sierra show a clear SSW exposure (Figure 5.5, right), meaning that in winter the snowpack and soil moisture there are strongly (topographically speaking) exposed to sunlight. The distinct topography of the Cascades as compared to the other mountains is highlighted by the more random distribution of aspect, as well as lower average slope of the terrain. The watershed side of the Coast Ranges have a northeasterly aspect, sheltering their relatively small amount of moisture from the Sun.

The Klamath and northern Coast ranges show a sharply-sloped (15-20°) transition to the Sacramento Valley. This could cause relatively rapid runoff of rainfall in this region. Other locales which might manifest the hydrologic effects of steep terrain are the river valleys scattered throughout the Sierra, and the very steep peaks of

the highest Southern Sierra where the 16 km^2 areally-averaged slope exceeds 30°. Topography is only one aspect of the watershed, however; the hydrologic effects of steep terrain can be strongly moderated by other factors such as landcover, snowpack and soil properties.

5.3 Soils

5.3.1 Water Movement in Soil and Relevant Parameters

The geologic origins of the rocks of the watershed, combined with the evolving hydroclimate which weathered and eroded them, produced the soils of the watershed as they are today. This natural process has shaped the watershed and distributed the soils in a self-organized system, in which the hydrology shapes the watershed and vice-versa. The movement of water through soil is at the center of traditional hydrology. Attention now turns to the hydrologic influence of the soils' physical parameters, and their distribution throughout the watershed.

One of the most hydrologically important qualities of soil, especially at the beginning of the wet season, is its capacity to take in water. The amount of water which a soil can absorb depends on its porosity (φ). This is the total amount of space between the actual soil particles, usually expressed as a fraction of total volume. The higher the porosity, the more water a soil can absorb before generating surface runoff.

Modifying this is the thickness of the soil layer. Bedrock underlies much of the watershed's soil. Vertical water movement is highly restricted by bedrock; this also

limits the soil water capacity. Other areas are underlain by deeper aquifers, relatively unconnected to the surface soil layer. Water seeping into these aquifers may remain there for a long time, unless extracted as well water.

While porosity and soil depth constrain the total amount of water which a soil can hold, the actual movement of water in the soil, both initially and after entering the soil matrix, is approximately governed by a simple equation known as the Buckingham-Darcy (B-D) Equation (*e.g.*, Hillel 1980):

$$q = -K\left(\frac{\theta}{\varphi}, z\right)\nabla H(\frac{\theta}{\varphi}, z) \qquad 5.1$$

where q is the flow rate per unit cross-sectional area of soil (*m/s*), K is the soil's *hydraulic conductivity* (*m/s*), and H is the *total hydraulic head* in the soil, expressed as energy per unit weight of water (*m*). The hydraulic head is the result of changes in water's potential energy due to gravitational head and soil moisture pressure head.

$$H = h(\frac{\theta}{\varphi}) + z \qquad 5.2$$

The soil moisture pressure head h is mainly a result of the attraction between water and the soil matrix due to electrochemical forces, and is thus often called the *matric potential*. It is negative, and the gravitational head is measured relative to an arbitrary datum, with z increasing upward.

As indicated in Equations 5.1 and 5.2, both the hydraulic conductivity and the matric potential are functions of $\frac{\theta}{\varphi}$, the volumetric soil moisture content divided by the volumetric porosity. $\frac{\theta}{\varphi}$ varies from 0 for a very dry soil, to 1 for a completely saturated soil with all pore spaces filled. The dependence of K and h on $\frac{\theta}{\varphi}$ varies

significantly from one soil type to another, but as a general rule both increase with $\frac{\theta}{\varphi}$ to some maximum value. Numerous attempts have been made to parameterize the dependence of K and h on $\frac{\theta}{\varphi}$ (Brooks and Corey 1964; Campbell 1974; Clapp and Hornberger 1978; Van Genuchten and Nielsen 1985), and the parameters thus defined have been subject to refinement using more sophisticated analysis and more soil samples (Ghosh 1980; Cosby, Hornberger *et al.* 1984). In these parameterizations of K and h, the parameter values were usually based on the USDA textural classification of the soil, a commonly-available soil descriptor (see Table 5.1). Each texture category was assigned an empirically-determined parameter value, and other quantities such as porosity have also been estimated for each texture.

The parameterizations of K and h due to Campbell and also Clapp and Hornberger have the advantages of being reasonably accurate over a wide range of soil moistures, widely-used and well-supported with data, and numerically simple, which makes them stable and efficient when incorporated into numerical simulations of soil water movement. In this study, the Van Genuchten parameterizations were also tried, but were eventually thrown out for not meeting the above criteria, particularly the latter. The Campbell/Clapp and Hornberger parameterizations are:

$$h(\tfrac{\theta}{\varphi}) = h_{sat}\left(\frac{\theta}{\varphi}\right)^{-b} \qquad 5.3$$

$$K(\tfrac{\theta}{\varphi}) = K_{sat}\left(\frac{\theta}{\varphi}\right)^{2b+3} \qquad 5.4$$

where h_{sat} and K_{sat} are the saturated values of matric potential and hydraulic conductivity, respectively, and b is a parameter which has been determined both theoretically and empirically with good agreement for all textural classes.

To summarize, characterizing the soils of the watershed and modeling the movement of water through them requires information on porosity, soil depth, saturated hydraulic conductivity (also called *coefficient of permeability* or simply *permeability*) and matric potential, and the power-law parameter b. With these parameters, and using Equations 5.1-5.4 with elevation data from the DEM, the hydrologic behavior of the watershed's soils can be estimated.

5.3.2 STATSGO Soils Data and Texturally-Based Soil Parameters

With this understanding, the next step toward modeling the watershed is to obtain the required data. The STATSGO soils data set was developed by the Natural Resources Conservation Service (formerly the Soil Conservation Service), a division of the U.S. Department of Agriculture (http://www.ftw.nrcs.usda.gov/stat_data.html). STATSGO is an extensive database providing horizontally- and vertically-distributed information on a large number of soil properties. It is derived primarily from maps based on field soil surveys and supplemented by satellite and other data.

At the time of this writing, STATSGO provides the most complete data on soils in the study region. More detailed data sets exist (SSURGO, also by NRCS), but their coverage is incomplete. The resolution of the STATSGO data is well-suited for a

study of watershed-scale hydroclimate variability. The most fundamental spatial division in the STATSGO data base is called a *map unit*. The coverage of the Bay-Delta watershed is comprised of 1,715 individual map unit areas, the delineations of which are shown in Figure 5.6.

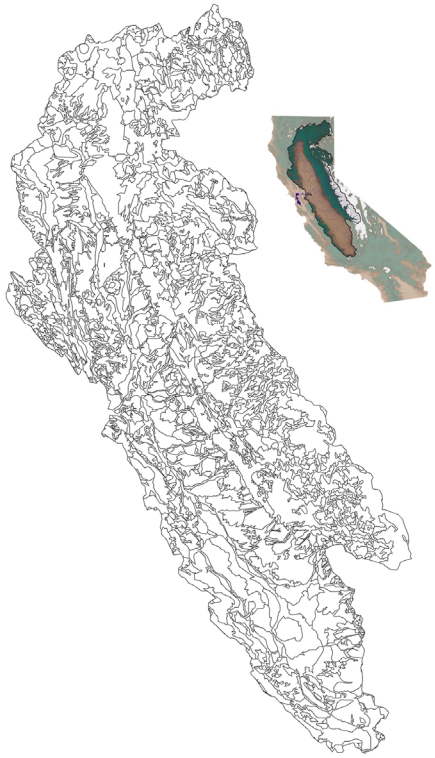

Figure 5.6 Delineations of the map units of the STATSGO soils database.

The map units are clearly fine enough to capture heterogeneity in the watershed's soils. Each map unit is further composed of up to 21 individual soil *components*, each of which has up to 6 vertical layers which combine to form a vertical soil *profile*. The spatial distribution of the components within a map unit is not known; only the area occupied by each component is defined. This seemingly vague hierarchy is a result of the methods used to derive the STATSGO data, as well as the

classification methods used by soil scientists. Certain types of soil profiles tend to occur in groups, and the assemblage of these different profiles is called a *soil series*, each profile being called a *phase*. Details of the STATSGO methodology are provided in its associated metadata summary:

> In those few areas where detailed maps did not exist, reconnaissance soil surveys were combined with data on geology, topography, vegetation, climate, and remote sensing images to delineate map units and estimate the percentages of components. The STATSGO map unit components are soil series phases, and their percent composition represents the estimated areal proportion of each within STATSGO map unit. (http://www.ftw.nrcs.usda.gov/metadata/ca.html)

The combination of field samples, satellite data and statistical inference used to derive the STATSGO data are geared toward determination of the presence of a soil series, but not enough detail is achieved to determine the exact location of each soil profile. Thus, the map unit remains the fundamental spatial unit of the soils data, but the composition of the map unit is known and provides additional information.

The actual data available for each layer of each STATSGO component is quite extensive. The layers themselves correspond to soil *horizons*, which are horizontal bands of soil with distinct physical properties. Most layers in the database are characterized by layer depth and extent, soil textural class, saturated hydraulic conductivity and bulk density, among many other properties. These few properties are the ones relevant to this study.

Bulk density is a quantity which may be used to calculate porosity, but nearly all the soil profiles in the watershed are missing at least one bulk density estimate. This is not surprising, considering the effort involved in obtaining this data. Bulk density is estimated in the field by spraying a clod of dirt with “saran-wrap” coating

and returning to lab, then oven-drying and weighing the sample (Norman Bliss, personal communication).

In fact, much of the STATSGO data is incomplete. Fortunately, estimates of K_{sat} have very good coverage in the watershed. Basic quantities such as layer depths have complete coverage, as do textural class designations. To complete the data characterization of the watershed, however, it is necessary to turn to empirically-determined values of φ, h_{sat} and b, tabulated according to textural class. STATSGO does not provide estimates of b or h_{sat}, and, as mentioned, the data needed to calculate porosity is prohibitively sparse.

Several studies have been conducted over the past 40 years to relate hydraulic soil parameters to commonly-used soil characteristics such as texture. Cosby *et al*. (Cosby, Hornberger *et al.* 1984) presented a detailed synthesis of several such studies, producing the texturally-based assignments in Table 5.1.

Table 5.1 Soil parameters by textural class (adapted from Cosby, Hornberger *et al.* 1984).

Textural Class	φ (as a fraction of total volume)	K_{sat} (*mm/day*)	h_{sat} (*mm* H_2O)	*b*
Sandy loam	0.43	452	-141	4.74
Sand	0.34	4028	-69	2.79
Loamy sand	0.42	1216	-36	4.26
Loam	0.44	292	-355	5.25
Silty loam	0.48	243	-759	5.33
Sandy clay loam	0.40	385	-135	6.77
Clay loam	0.47	211	-263	8.17
Silty clay loam	0.46	176	-617	8.72
Sandy clay	0.41	624	-98	10.73
Silty clay	0.47	116	-324	10.39
Light clay	0.47	84	-468	11.55
All classes	0.46	232	-389	7.22

Before blindly proceeding to substitute these texturally-based soil parameters in place of the missing STATSGO data for φ, h_{sat} and b, it is important to first consider the reasonableness of such an approach.

The National Soil Survey User Handbook (http://www.statlab.iastate.edu/soils/nssh/), which contains the guidelines used to collect and assemble the data used in the STATSGO database, contains the following comments regarding K_{sat}, here referred to as "permeability":

> Since measurements are difficult to make and are available for relatively few soils, estimates of permeability are based on soil properties….
>
> (1) In making estimates, the soil characteristics that exert the greatest control on permeability are evaluated first. For many soils, this soil characteristic is texture. If texture exerts the greatest control, permeability is related to texture and then the classes are modified on the basis of other observed properties.
>
> (2) The general relationships are adjusted up or down depending on structure, pore size, density, organic matter, clay mineralogy, and other observations within the soil profile, such as consistency, dry layers in wet seasons, root mats or absence of roots, and evidence of perched water levels or standing water.

So the notion of using textural class as the basis for assigning soil parameters seems supported by STATSGO methodology itself. Where possible, such as with permeability, the use of the STATSGO data directly clearly seems preferable, due to its better representation of real-world heterogeneity over the textural method.

Representation of heterogeneity is the prime benefit of using "real" physical data. If heterogeneity is adequately represented in the hydrologic model of the Bay-Delta watershed, relative differences in the hydrologic behavior of individual river basins should be captured. If these relative differences are adequately represented, any necessary adjustments to the model may be applied universally, to the fundamental

model structure, rather than resorting to calibration of the individual river basins. This allows the model to maintain its claim of being "physically-based".

To assure that (2) above is indeed a secondary effect, Figure 5.7 shows a comparison of average STATSGO K_{sat} values tabulated by textural class and the corresponding values from Table 5.1.

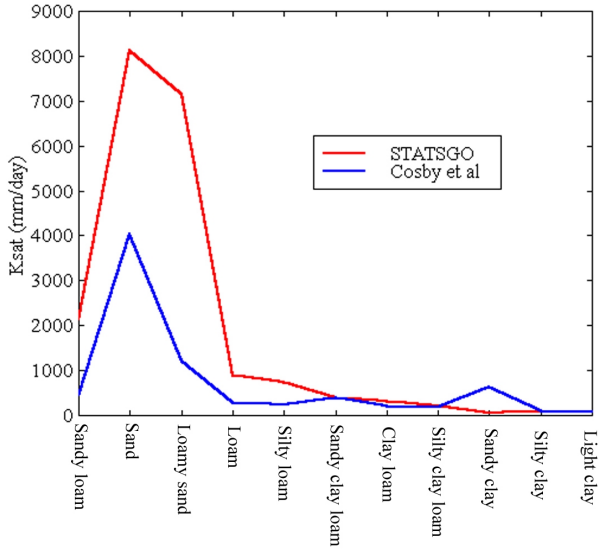

Figure 5.7 Comparison of texturally-based soil K_{sat} values.

The values covary fairly well, having a correlation of r=0.85. Notable differences are for soil with sandy content. These values are considerably larger in STATSGO than the corresponding entries in Table 5.1. This may be due to the secondary criteria listed above for estimating K_{sat} in the field. A substitution of texturally-based K_{sat} values for STATSGO data would result in an underestimation of hydraulic conductivity for these types of soils. Fortunately, STATSGO K_{sat} data has comprehensive coverage of the watershed, and such a substitution is unnecessary.

A similar comparison of STATSGO porosities inferred from bulk density estimates (where available) versus Cosby–derived porosities by textural class (Figure 5.8) shows reasonably good agreement for all textures, with a correlation of r=0.90.

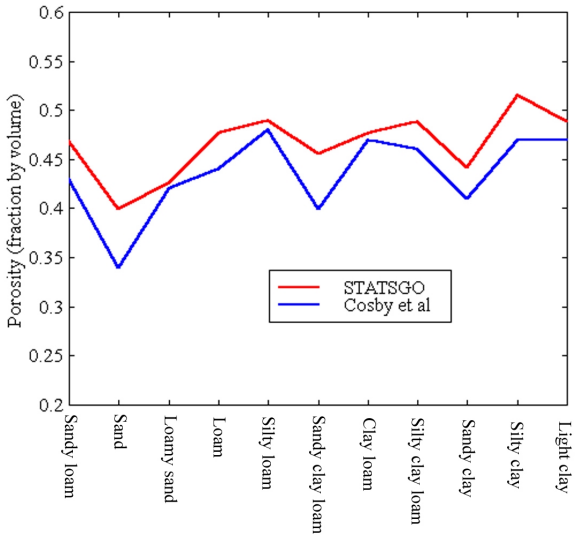

Figure 5.8 Comparison of texturally-based soil porosity values.

It therefore seems reasonable to use STATSGO textural classes with Table 5.1 porosity values to assign porosity throughout the watershed. For b and h_{sat}, there is no choice but to use the values from Table 5.1. It can only be postulated that the demonstrated correspondence of porosity bears out the reasonableness of using texturally-based soil parameters, and that most importantly, this approach should usefully approximate the hydrologic heterogeneity of the watershed.

5.3.3 Determination of Interface Depth and Soil Water Capacity

Jumping ahead somewhat, the modeling approach to be introduced in Chapter 6 will represent the watershed vertically as two homogeneous layers (for each 4 *km* by 4 *km* horizontal model element). It is therefore necessary to prepare the data in an appropriate manner, aggregating soil properties vertically into two layers and parameterizing the hydrologic behavior of the soils relative to the layer interface.

First, however, the method of choosing layer interface depth must be determined. The reason for using two vertical layers is that soil moisture tends to vary more rapidly in the upper 10-30 *cm* than in the deeper soil. The higher variability of the upper layer is due to exposure of the shallow soils to atmospheric forcing and depends on the particular climate, but its depth is modulated by landcover and soil properties. Since soil water moves roughly according to Equation 5.1, and since STATSGO permeabilities are stated to include the effects of roots (landcover), permeability seems a good proxy for inferring appropriate interface depth.

The approach taken here was to examine vertical profiles of permeability for all components in the watershed, and choose layer depths as the depth at which the maximum drop in permeability occurs. That is, the depth for which the underlying horizon's K_{sat} is maximally less than that of the overlying horizon. This corresponds to an upper layer in which soil water moves more freely and a lower layer which holds its water more tightly, with the intent that the real hydrologic change with depth is optimally represented in the 2-layer formulation. In the relatively uncommon cases where no decrease in K_{sat} with depth occurs, an arbitrary choice must be made. The

method used here was to choose the minimum of one-third the depth to bedrock and 30 *cm*. These values represent reasonable choices for the layer interface depth in the absence of further information, as they correspond to the findings of profile analysis by Guetter and Georgakakos (their Figure 3) (Guetter and Georgakakos 1996). Further, the average layer interface depth for all profiles where a valid determination could be made was approximately 30 *cm*. Some sample K_{sat} profiles and the resulting interface depths are shown in Figure 5.9.

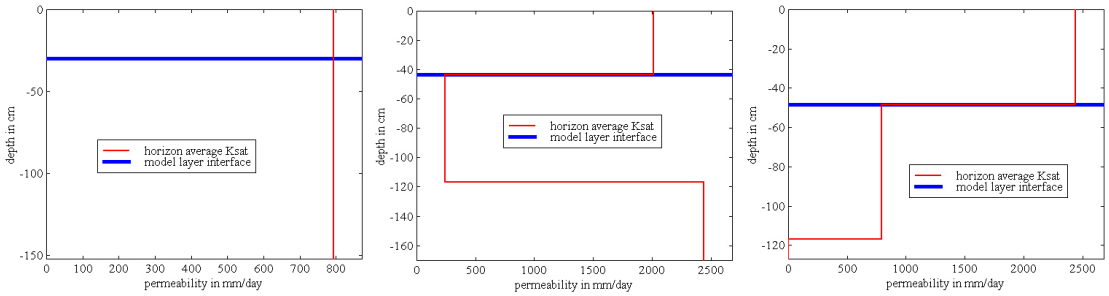

Figure 5.9 Examples of using permeability changes to determine model interface depth. See text for discussion.

Once the interface depth was determined for each STATSGO vertical profile in the watershed, it was a simple matter to calculate the total soil moisture storage capacity, Φ, for the upper and lower layers in each profile. This is equivalent to the total pore space in each layer, or the porosity of each horizon above the interface depth times the horizon's thickness, summed over all horizons above the interface, and similarly for the lower layer. Since this data is at the horizontal resolution of STATSGO components, much of the horizontal heterogeneity within the individual river basins of the watershed is captured. As an example of the differences within and between river basins, the sample cumulative distribution functions for the upper and

lower layer soil moisture capacities are shown in Figure 5.10 for the watershed's 15 river basins.

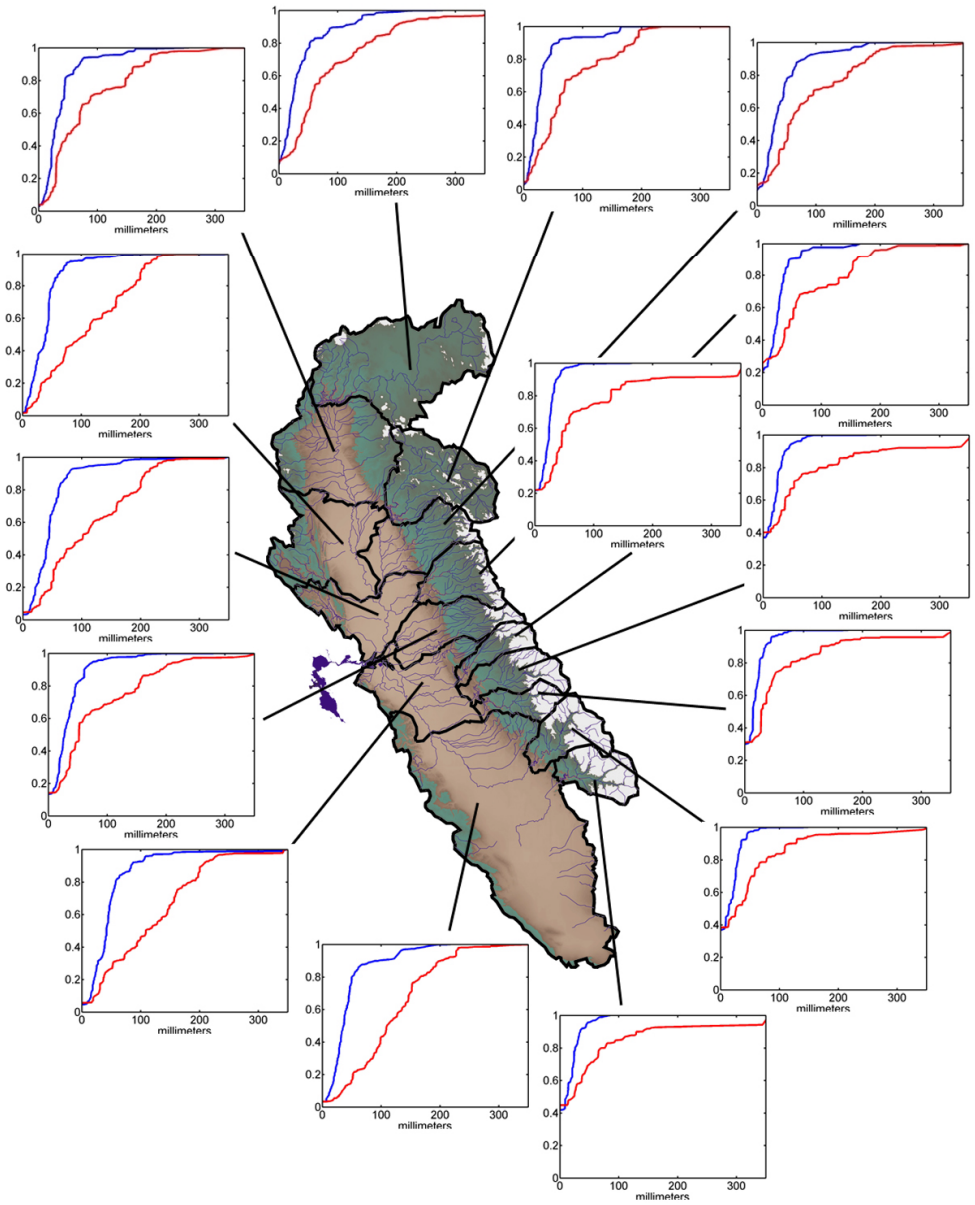

Figure 5.10 Sample distribution functions of soil moisture capacity (in mm) for river basins of the watershed. Blue lines represent upper layer capacities; red lines represent lower layer capacities.

These show a good deal of variability in the distribution of soil moisture capacity throughout the watershed, particularly in the deeper soils. The valleys show a

tendency for deep soils with large capacities, while the mountains, particularly the high Sierra, have deep soils with relatively small capacities. The high Sierra distributions also show a high proportion (up to 40%) of zero-capacity soils, representing exposed bedrock.

As a sensitivity test of the arbitrary parameters used in determination of interface depth, namely the values 1/3 and 30 *cm* ("…one-third the depth to bedrock and 30 *cm*"), these parameters were varied over an order of magnitude. Several different combinations yielded virtually no change in the soil moisture distribution functions of Figure 5.10, suggesting that the few cases where this arbitrariness enters into the calculation do not significantly affect the outcome.

5.3.4 Vertical Aggregation of Hydrologic Parameters

To represent hydrologic behavior in each of the two layers arrived at above, the soil parameters must be aggregated in a manner appropriate for representing hydrologic behavior in each layer. Porosity has already been aggregated in such a manner, yielding total soil moisture capacity values for both layers in every vertical profile of the watershed, corresponding to the STATSGO component data. This describes the amount of water each layer can hold. Now the aggregate movement of water through the layers must be described.

Here the movement of soil water is broken into two directional components, horizontal and vertical. In the horizontal, the soil is considered homogeneous and isotropic within any given horizon of a given STATSGO vertical profile (component).

Further, the soil moisture content will be considered constant within each of the two layers of the given profile. Under these conditions, the B-D Equation is simplified, and Equation 5.1 reduces to:

$$q = -K\left(\frac{\theta}{\varphi}\right)\frac{dz}{dx} \qquad 5.5$$

where the hydraulic head gradient has reduced to the average slope of the topography, assuming the soil horizons and the bedrock are generally parallel to the surface. Thus, for horizontal soil water movement, the only quantity which must be aggregated vertically is the hydraulic conductivity.

The nonlinearity of the hydraulic conductivity (Equation 5.4) means a simple average of the relevant parameters K_{sat} and b will not conserve mass through the aggregation process. Instead, to aggregate the hydraulic conductivity vertically, the curve represented by Equation 5.4 was sampled at many values of $\frac{\theta}{\varphi}$ for each horizon in a given layer, the values weighted by the horizon thicknesses, and summed to generate a new aggregate curve which was then fitted with optimal aggregate values of K_{sat} and b.

This "nonlinear averaging" process will be used again in this chapter to aggregate other hydrologic parameters, and is given here in its general form:

$$G(\underline{\alpha}') = \frac{1}{\sum h_i} \sum h_i G(\underline{\alpha}_i) \qquad 5.6$$

where $\underline{\alpha}_i$ represents the relevant hydrologic parameters for an individual horizon (in the case of hydraulic conductivity, the elements of this vector are K_{sat} and b), h_i is the horizon's thickness, and G is the functional form of the process to be aggregated (in

this case, G is given by Equation 5.4). The optimal aggregate parameter values are given by $\underline{\alpha}'$, and both sums are over all horizons in a profile (STATSGO component).

In this manner, aggregate hydraulic conductivity parameters were generated for the upper and lower layers of each component in the watershed. This "nonlinear averaging" technique conserves water mass for horizontal flows under the assumptions stated in the previous paragraph.

In the vertical dimension, Equation 5.1 becomes:

$$q = -K\left(\tfrac{\theta}{\varphi}, z\right)\left(\frac{dh(\tfrac{\theta}{\varphi}, z)}{dz} + 1\right) \qquad 5.7$$

Here, the vertical movement of soil water from the upper to the lower layer is complicated by the fact that the water is crossing soil horizons of different physical characteristics, violating the simplifying assumptions of isotropy and homogeneity. Further, the matric potential varies in the vertical due to both changes in the medium and the change in soil moisture across the layer interface. For these reasons, the aggregate representation of the movement of soil water from upper to lower layers, or *percolation*, requires a more sophisticated approach.

5.3.5 Parameterizing Percolation

5.3.5.1 Vertical Diffusion Simulations

To parameterize the vertical movement of soil water under complex conditions, it is helpful to turn to numerical simulations of soil moisture changes. The equation of continuity and the B-D equation (Equation 5.7) yield the diffusion equation for soil moisture (Richard 1931):

$$\frac{\partial\theta}{\partial t} = \frac{\partial}{\partial z}\left[K\left(\tfrac{\theta}{\varphi}, z\right)\left(\frac{dh(\tfrac{\theta}{\varphi}, z)}{dz} + 1 \right)\right] \qquad 5.8$$

or, defining the *hydraulic diffusivity* $D \equiv K\left(\tfrac{\theta}{\varphi}, z\right)\frac{dh}{d\theta}$,

$$\frac{\partial\theta}{\partial t} = \frac{\partial}{\partial z}\left[D\left(\tfrac{\theta}{\varphi}, z\right)\frac{d\theta}{dz} + K\left(\tfrac{\theta}{\varphi}, z\right)\right] \qquad 5.9$$

This is the one-dimensional vertical diffusion equation for soil moisture through a heterogeneous, variably saturated soil. Its solution over time and throughout a given soil profile permits the characterization of soil water movement downward through the profile.

Many solution algorithms for the equivalent of Equation 5.9 in one to three dimensions have been developed (*e.g.*, http://water.usgs.gov/software/). One which has been commonly used, thoroughly validated, and is well-suited to the present application is the program VS2D (Lappala, Healy *et al.* 1987; Healy 1990, http://water.usgs.gov/software/vs2di.html). This program uses fully-implicit temporal and centered spatial discretizations, along with linearization of the nonlinear terms

represented by Equations 5.3 and 5.4. As elsewhere in this study, the Campbell/Clapp and Hornberger soil property parameterizations were used. For the profiles simulated here, a 1 *cm* vertical resolution was chosen, and an adaptable time step was used. The latter feature is extremely useful for simulating soil moisture movement in a variety of soil media. Each simulation of a new soil profile involved providing the VS2D model with a description of the profile's horizons, including depth, extent, and values of K_{sat}, h_{sat}, φ and b—all derived as discussed in Section 5.3.2. The numerical experiments presented here simulate diffusion into a dry soil with a ponded surface boundary condition. The depth of the simulated soil profile was the depth to bedrock or to the deepest soil measurement.

The model output, generated every 60 time steps, included the distribution throughout the profile (at 1 *cm* intervals) of hydraulic head h, volumetric soil moisture θ, and cumulative surface inflow Q_{in}. These provide a detailed description of the percolation of water through the given soil profile. At this stage, the problem becomes how to extract useful parameterizations of the percolation process from these detailed simulations.

5.3.5.2 Holtan's Representation of Percolation

A parameterization of infiltration of rainfall into soil which may be usefully applied in the current context to the vertical percolation of water from the upper to the lower soil layers (as defined in Section 5.3.3) was originally developed by Holtan (Holtan 1961). On the basis of field experiments, Holtan found that the rate of

infiltration of water into the soil surface minus the steady-state infiltration rate varies approximately as a power of the soil moisture deficit for the soil below. Specifically,

$$f - f_c = C_p F_p^{m_p} \qquad 5.10$$

with

$$F_p = 1 - \frac{\Theta}{\Phi}$$

where

f is the rate of infiltration, a function of time,
f_c is the steady-state rate of infiltration (after a long time),
C_p and m_p are the infiltration parameters, unique for a given soil profile, and
F_p is the soil moisture deficit, a function of
Θ, the total soil water content, and
Φ, the total soil water capacity, or total pore space.

Under saturated upper layer conditions and for typical soil profiles, this formula may equivalently be applied to the percolation of soil water from the upper to the lower layer, *i.e.*,

$$f_{1\to 2} - f_{c1\to 2} = C_p \left(1 - \frac{\Theta_2}{\Phi_2}\right)^{m_p} \qquad 5.11$$

where the subscripts 1 and 2 refer to the upper and lower layers, respectively.

This parameterization of the percolation process has been used in models such as the Sacramento hydrologic model, used by the National Weather Service for river forecasts (Burnash and Ferral 1983), and its predecessor, the Stanford model (Crawford and Linsley 1966), with good results. Those models, however, rely upon calibration methods to determine the parameters C_p and m_p. The present study is

unique in that it attempts to determine these parameters on a physical basis, using results from the diffusion simulations introduced in the previous section.

To obtain Holtan-style parameterizations of upper-to-lower-layer percolation from the VS2D model outputs for a given soil profile, lower layer moisture deficit (F_p) and percolation across the layer interface ($f_{1\to 2}$) were calculated every 60 time steps for each simulation. The lower layer moisture deficit was calculated as $F_p = 1 - \frac{\Theta_2}{\Phi_2}$, where Θ_2 is the total volume of water in the lower layer, and Φ_2 is the total pore space in the lower layer. The percolation rate, $f_{1\to 2}$, was determined by mass balance, using the total inflow at the surface and the total amounts of water in the upper layer and in the lower layer.

The portion of the resulting percolation-moisture deficit curve used to determine the Holtan parameters was determined as the sequence of data falling temporally between upper layer steady state (saturation) and the first moisture reaching the lower layer's deep limit (corresponding to bedrock or the deepest measurements of soil properties). This is intended to limit the curve to that portion after the period when upper layer vertical effects are varying and when other lower-layer processes are limiting (baseflow and groundwater seepage) to the percolation process. In the few cases where moisture reached the deep extent of the lower layer before the upper layer had reached steady state, the Holtan parameters were determined by fitting to the data occurring before the deepest extent showed first moisture, and after approximately one half of that time had elapsed. This approximation was based on analysis of these unique cases, in which it was

determined that the upper layer was typically very near saturation after half the simulation time had elapsed. In all cases, the steady-state infiltration rate, $f_{c1\to 2}$, was estimated as the final infiltration rate in the selected portion of the percolation-moisture deficit curve. The final step was then to calculate the slope and intercept of a linear best fit to a plot of $\log(f_{1\to 2} - f_{c1\to 2})$ versus $1-\frac{\Theta_2}{\Phi_2}$ to estimate the Holtan percolation parameters C_p and m_p for the simulated profile.

The procedure outlined above was automated to simulate and parameterize percolation of soil moisture for all soil profiles (STATSGO components) in the San Francisco Bay-Delta watershed. The soils database for the Bay-Delta watershed contains nearly 10,000 vertical soil profiles, though among these less than 3,000 unique profiles exist as determined by the profiles' layer thicknesses, K_{sat} values and textural classifications. It was therefore necessary to consider only these unique profiles when estimating percolation parameters, which could then be redistributed over the watershed, thus completing the parameterization of percolation throughout the watershed. Before these results can be applied to model development, however, they must first be aggregated, along with the rest of the hydrologic parameters, to the data grid of Figure 5.2.

5.3.6 Horizontal Aggregation of Hydrologic Parameters

At this point, the vertical soil profiles corresponding to the components of the STATSGO database have each been divided into two layers based on their permeability profiles. Total soil moisture capacity has been determined for each layer,

and aggregate parameterizations of both horizontal and vertical soil water movement in each layer of each STATSGO component have been derived. The final step in processing the soils data is to horizontally aggregate the data corresponding to the irregularly distributed STATSGO components to the data grid presented in Section 5.1.

Each 16 km^2 grid element (Figure 5.2) may be comprised of one or more STATSGO map units, and each map unit is comprised of up to 21 components. All the aggregated data derived in the previous sections were at the component level. The portion of the 16 km^2 which each component represents is easily determined from the STATSGO data. Three of the parameters determined so far are easily aggregated to the data grid by a simple area-weighted average of the corresponding component values. These are the steady-state percolation rate ($f_{c1\to 2}$), the interface depth, and the total soil moisture capacity for the upper and lower layers. The assumption inherent in aggregating these parameters in this simple manner is that the contribution of these parameters to the hydrology is linear at the horizontal scale of the unaggregated data, that is, at the horizontal resolution of the STATSGO components. While this is clearly a simplification, the horizontal scale of the STATSGO components is sufficiently smaller than the scale of individual river basins that the role of heterogeneity of soil parameters in determining basin outflow variability should be adequately captured even given this simplifying assumption.

The parameters describing the movement of soil water, however, contribute to the hydrology in very nonlinear ways and must be aggregated accordingly in order that

the aggregation process conserves mass. The percolation process represented by the parameters C_p and m_p is aggregated horizontally in the same manner that hydraulic conductivity was aggregated vertically in Section 5.3.4, using the "nonlinear averaging" technique represented by Equation 5.6. In this case, the percolation-moisture deficit curves were sampled at many values of F_p for each component, the values weighted by the component areas (instead of horizon thicknesses), and summed to generated a new aggregate curve which was then fitted with optimal aggregate values of C_p and m_p.

The horizontal aggregation of the parameters related to horizontal soil water movement could be more complicated, in the same way that the vertical aggregation of the parameters related to vertical soil water movement was complicated by violation of the assumption of homogeneity. However, a reasonable simplifying assumption is that the stream network is dense enough that water will not, on average, flow horizontally far enough to cross into a new component before entering the stream network. Prior research supporting such an assumption has shown that stream networks have a fractal dimension of two and are therefore space-filling (Tokanaga 1978; Tarboten, Bras *et al.* 1988). Under this assumption, the values of K_{sat} and b determined by aggregating vertically in Section 5.3.4 may now be aggregated horizontally in an identical manner to that of the percolation parameters above, with the weights in the "nonlinear average" (Equation 5.6) based on each component's contributing area. This completes the aggregation of the STATSGO soils data onto a rectangular grid with each grid element represented by two vertical layers. The next

section summarizes the soils data and discusses implications for the hydrologic behavior of the Bay-Delta watershed.

5.3.7 Soil-Based Characterization of the Watershed

The Klamath mountains and the Sierra were originally formed primarily as marine sediments and some volcanic materials, metamorphosed under pressure and uplifted as a result of subduction of the Pacific plate under the North American plate. The Cascades interrupt this chain with soils of more recent volcanic origin, an extension into California of topographies more typical of the Northwest. The Central Valley is comprised primarily of relatively unaltered marine sediments (Norris and Webb 1990).

Glaciers have also played a key role in forming this landscape. During numerous glacial episodes over the past several million years, ice flows have scoured tremendous amounts of rock and sediment from the high mountains, depositing them as the ice melts at the terminus of the ice flow. This has formed many of the watershed's most impressive features, such as Yosemite Valley (Norris and Webb 1990).

In addition to their geologic origin and the effects of glacial scouring, the distribution of soils in the watershed is determined by sediment transport. The transport of weathered rocks by running water has covered about 67% of Earth's continental areas with sediment (Leopold 1994). A river's *competence*, or ability to carry sediment, tends to decrease as the slope of the river decreases along the river's

course. The result is a graded deposition of sediment materials, from heavier coarse materials to fine silt, as the river descends, flattens and widens (Mount 1995). This effect acts on a regional scale, and is responsible for determining much of a watershed's hydrologic character as defined by the distribution of soil properties. The aggregate soil properties derived in the previous sections provide a detailed look at the results of the combined effects of geologic origin, glaciers and sediment transport in shaping the Bay-Delta's watershed.

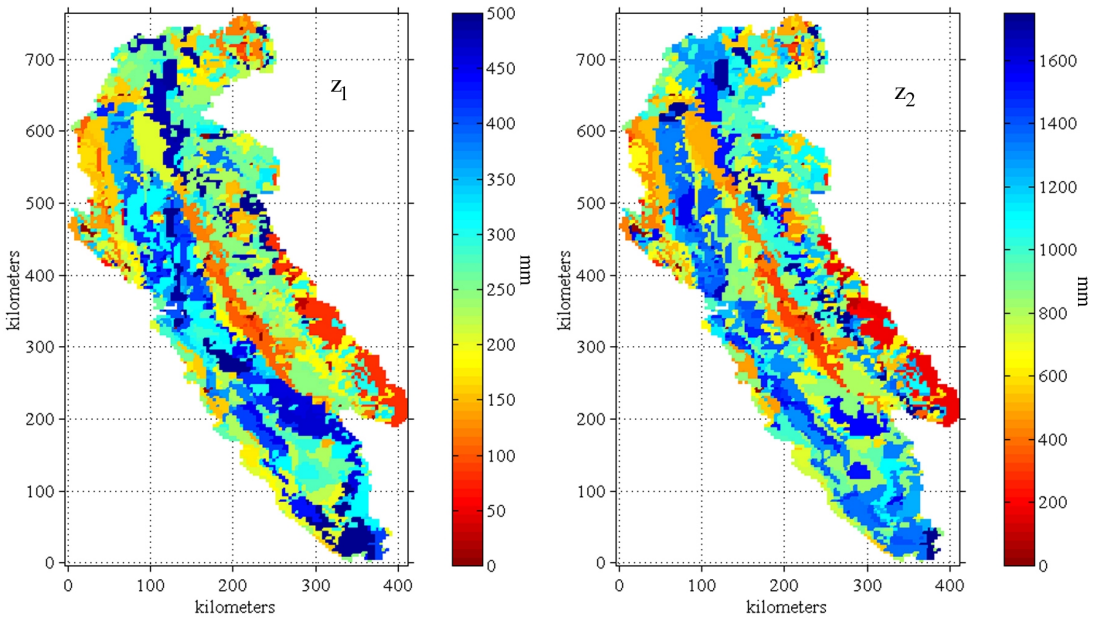

Figure 5.11 Model layer depths. Upper layer (left) was derived from permeability profiles, lower layer (right) is depth to bedrock or deepest soil measurement.

The model layer depths (Figure 5.11) show the complex organization of soils in the watershed. It is clear from the similarity of these two plots that the average depth of the active upper soil layer as determined from permeability changes is

approximately proportional to the total soil layer thickness, or depth to bedrock. Depth of the active soil layer appears to be generally about one-third of the total soil depth.

It is important to note that the total soil thickness values derived from STATSGO data (Figure 5.11, z_1+z_2) do not always represent actual depth to bedrock. In some cases, the soil is actually deeper than shown, and the indicated depth is simply the maximum depth of soil measurements. The deeper soils are important for characterizing long-term persistence of streamflow, but simulating the soil layers indicated in Figure 5.11 should capture most of the streamflow variability, and these depth values clearly portray the heterogeneity of soil layer thickness in the watershed.

Comparing Figure 5.11 with Figure 5.4, the valleys have soil depths considerably larger than the mountains, though the mountains exhibit an interesting along-range banding of depth. This banding appears to be the result of the varied geologic origin of the mountains and foothills (Norris and Webb 1990). The valley compositions of marine and alluvial sediments explain the deep soils shown here. The High Sierra have extremely shallow aggregate soil layers; in fact up to 40% of these river basins are exposed bedrock, as shown by the intercepts in the sample distributions of Φ in Figure 5.10. Runoff there would be extremely rapid, or "flashy", if not for the buffering effect of snowpacks.

The soil moisture capacities, Φ (Figure 5.12), in each of these layers show a similar structure.

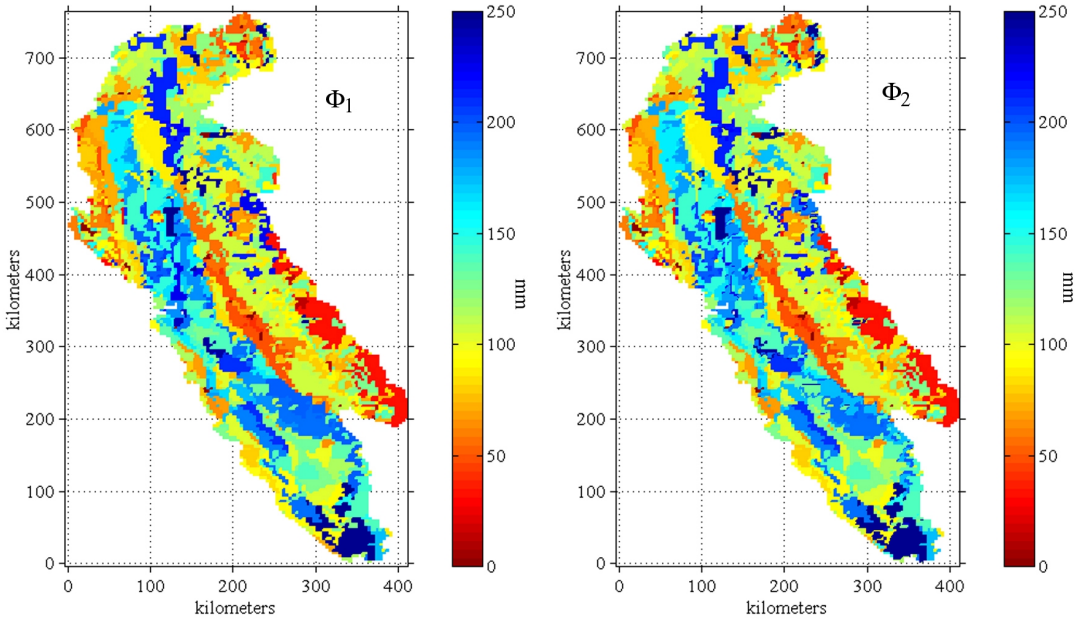

Figure 5.12 Total soil moisture capacity Φ for upper (left) and lower (right) layers.

Interestingly, the total capacity of the upper and lower layers is roughly the same even though their thicknesses differ so much. This is due to the reduced porosity of the deeper soils as a result of isolation from surface weathering effects, and compaction from the weight of the shallower soils. The mountains show much lower capacities than the thick valley soils, and the effects of geologic banding and exposed bedrock are again apparent.

The parameters representing the aggregate horizontal movement of water through the soils of the watershed (Figure 5.13-Figure 5.14) show a very different structure than the previous plots. Here, the distinction between the volcanic Cascades and the metamorphic Sierra is more evident, particularly in the exponents m_k (defined as $m_k=2b+3$) of the hydraulic conductivity parameterization. The smaller values of this

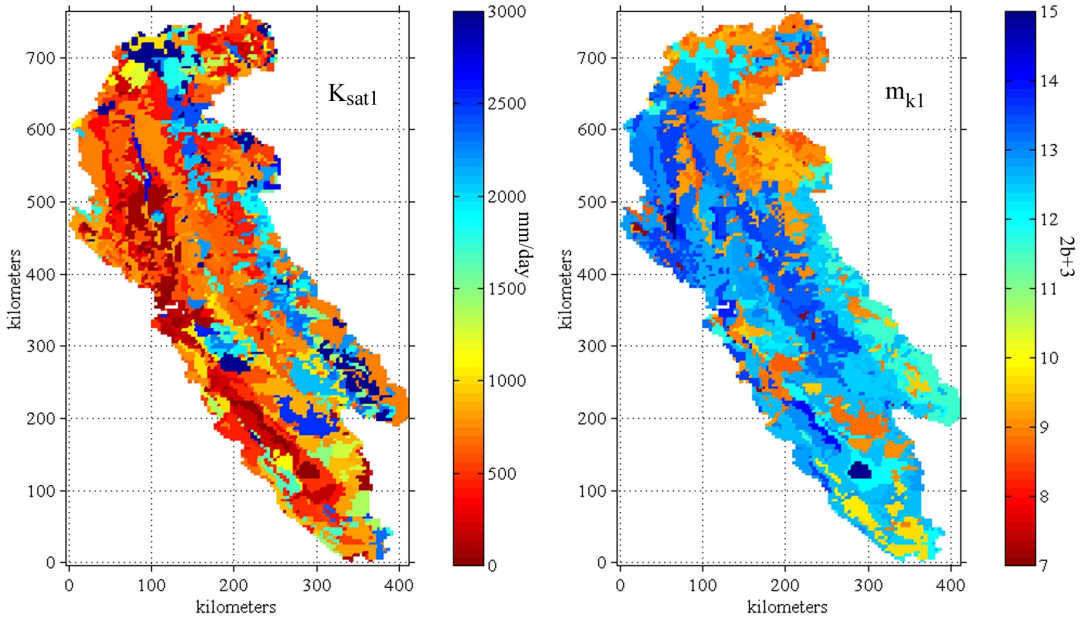

Figure 5.13 Hydraulic conductivity parameters K_{sat} (left) and m_k=2b+3 (right) for the upper layer.

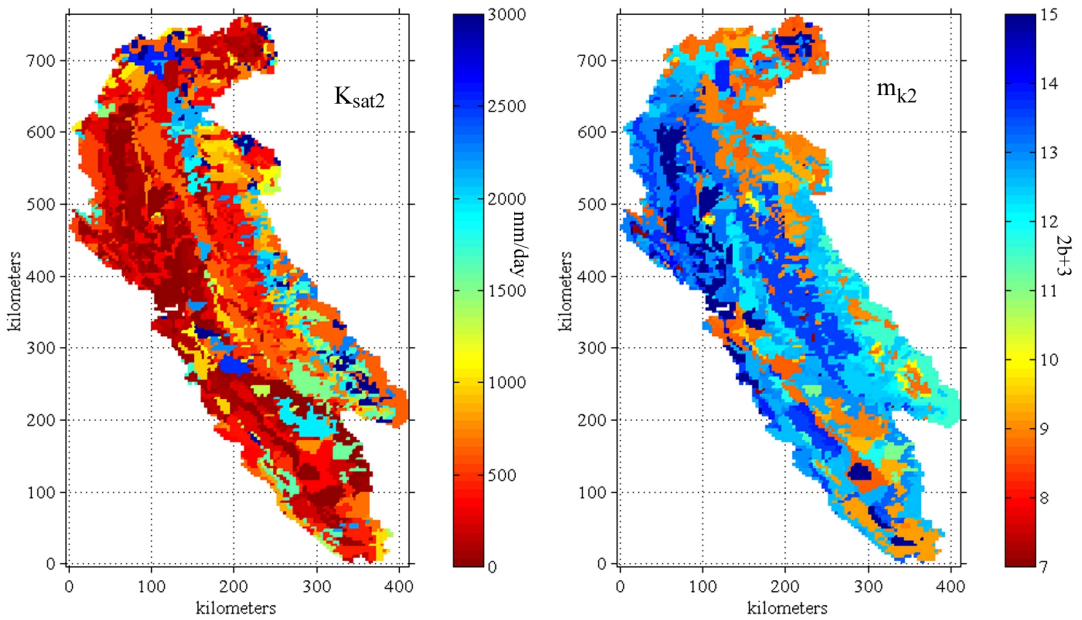

Figure 5.14 Hydraulic conductivity parameters K_{sat} (left) and m_k=2b+3 (right) for the lower layer.

exponent in the Cascades indicate less attenuation there of the hydraulic conductivity, $K\left(\frac{\Theta}{\Phi}\right)$, with decreasing soil moisture.

There is also a north-south variation of this exponent in the valleys, with a sharper attenuation of $K\left(\frac{\Theta}{\Phi}\right)$ for drier soils in the north. The values of K_{sat} in tend to be considerably lower in the valleys than the mountains for both layers, indicating the valley soils hold water more tightly.

Finally, the percolation parameters C_p, m_p and f_c (Figure 5.15) show a rich structure representing a wide variety of percolation behavior in the watershed. The multiplicative constant C_p represents the overall change in percolation over the range of wet to dry lower layers. This value is highest in regions of the Cascades, the northern Coast Range, and the Central Sierra foothills, indicating that lower layer soil moisture will have the strongest effect on percolation in those regions. The percolation exponent m_p represents the rate of decline in percolation rates with increasing lower layer soil moisture. The higher values in the Cascades, the Sierra foothills and the valleys imply that percolation there drops off more sharply for increasing lower layer soil moisture than elsewhere.

The steady-state percolation parameter f_c has the strongest overall effect on percolation rates, as it is an additive constant for all values of lower layer soil moisture. It has a rich and rapidly varying structure, with strong high and low values co-existing in all areas of the watershed with the exception of the high Sierra, where exposed bedrock makes percolation meaningless. In this case, the percolation

parameters were all assigned zero values, so that Equation 5.11 would generate zero percolation.

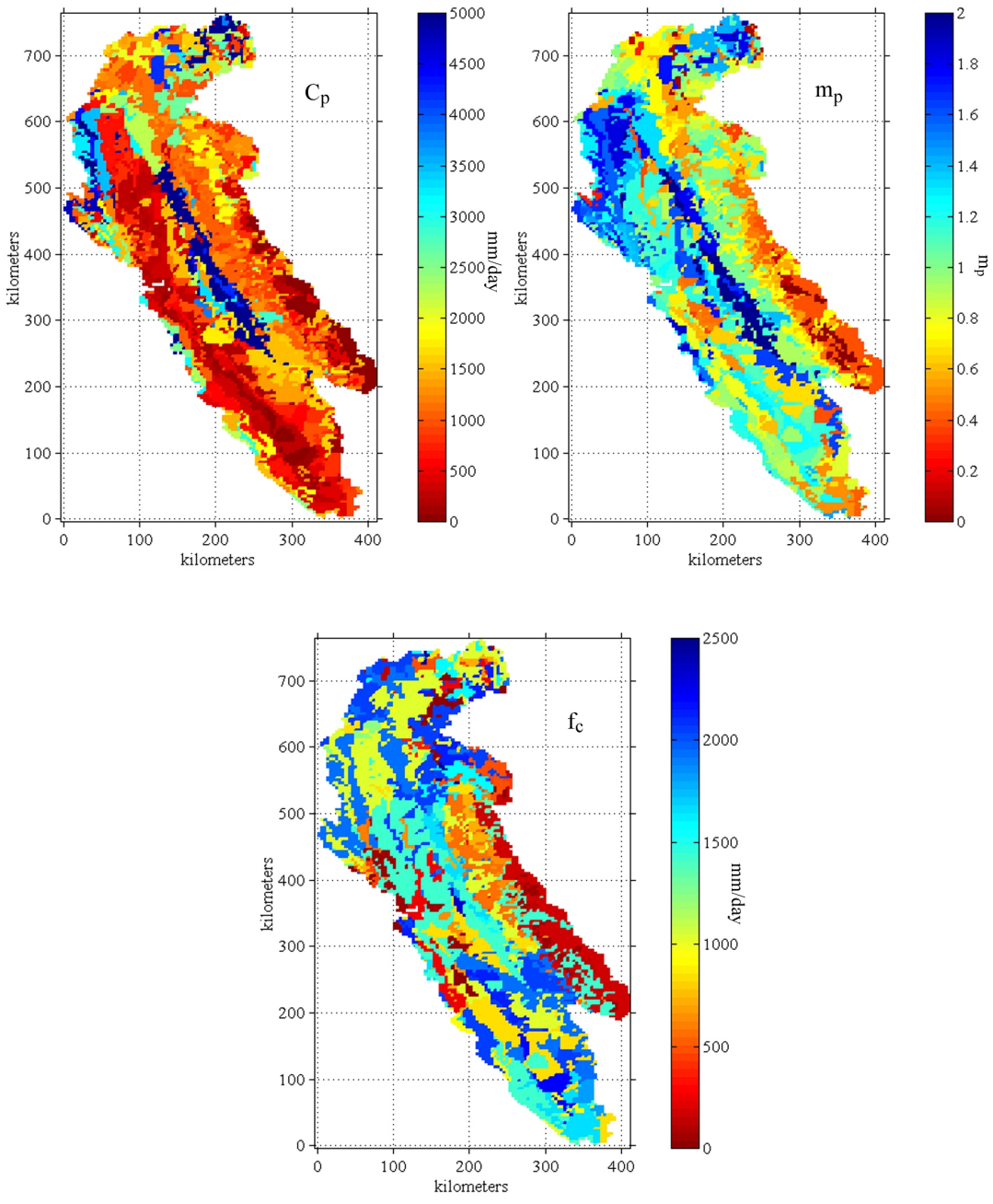

Figure 5.15 Percolation parameters C_p (upper left), m_p (upper right), and f_c (lower).

The preceding sections have yielded a great deal of information about how the hydrologic-hydraulic soil properties of the watershed regulate the flow of water. This behavior partially determines how much water can enter and leave the soil matrix, but features at the boundaries above and below the soil are critical to this process as well. Attention now turns to a quantitative description of these features and some of their implications for the hydrology of the watershed.

5.4 Features Above and Below the Soil

What covers the land surface can have a tremendous impact on water's interaction with the soil. Plants intercept varying amounts of rainfall which then evaporates, preventing it from reaching the soil. Urban areas tend to be highly impermeable, with many paved areas allowing little to no water to infiltrate into the soil. Trees not only intercept precipitation, but shade what water does reach the ground from the effects of the wind and Sun. Plants also send roots down into the soil to extract soil water for their growth and sustenance. All these effects depend strongly on the particular type of landcover at the top of the soil. Land cover data for the Bay-Delta watershed was digitized by the USGS from a USDA land-use map last updated in 1967 (U.S. Geological Survey 1967). Certainly some features have changed since that time, but the overall layout is much the same, and this data should sufficiently characterize the role of land cover in the watershed's hydrology.

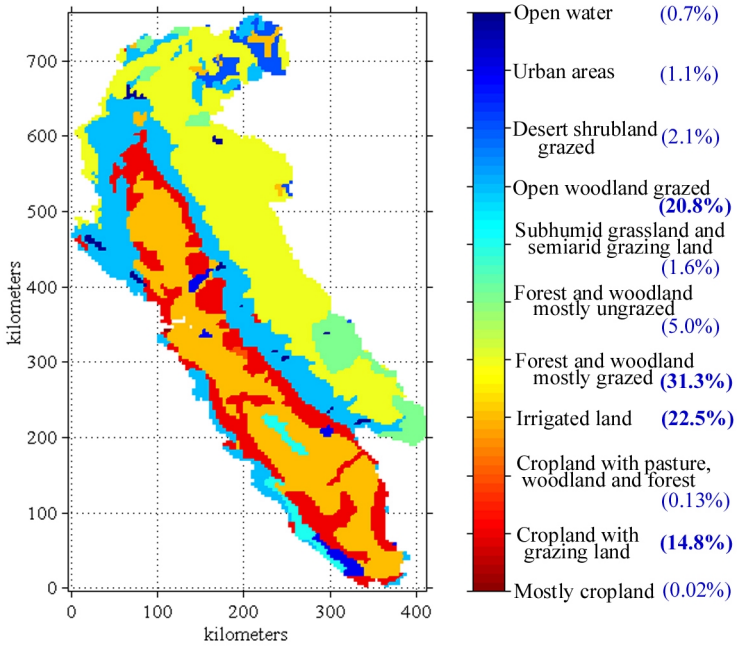

Figure 5.16 Land cover classifications of the watershed with percent area covered. The dominant categories are "cropland with grazing land", "irrigated land", "forest and woodland mostly grazed", and "open woodland grazed".

Land cover in the watershed shows a clear elevational dependence. The lowest areas of Central Valley have been developed as irrigated land, bordered by a region of cropland with grazing land. Next, the foothills of the mountain ranges are covered by open, grazed woodlands. The next highest in elevation is the dominant category, covering over 30% of the watershed's area— mostly grazed forest and woodland. Finally, in the highest elevations of the Sierra is mostly ungrazed forest and woodland.

The last two forest and woodland categories are particularly important to hydrology, first because they cover so much of the watershed, and second because trees have particularly strong interception and transpiration influences through shading and deep root penetration. To fully characterize these effects, more detailed data on

forest characteristics is required. In particular, *canopy closure* data is needed. Canopy closure, or forest density, is the percent of ground area covered by a direct downward projection of the horizontal extent of the trees in the forest. It is, in effect, the percentage of ground shaded by the forest when the Sun is directly overhead. This data, more than the land cover data representing simply the presence or absence of forest, helps to characterize the range of hydrologic impacts which different forests have.

Using satellite data, ground measurements for calibration, and statistical regression techniques, Zhu and Evans (Zhu and Evans 1994) developed a 1 *km* resolution forest density data set covering the continental U.S. (available under http://www.nohrsc.nws.gov/98/html/gisdata.htm). The portion covering the Bay-Delta watershed is shown in Figure 5.17.

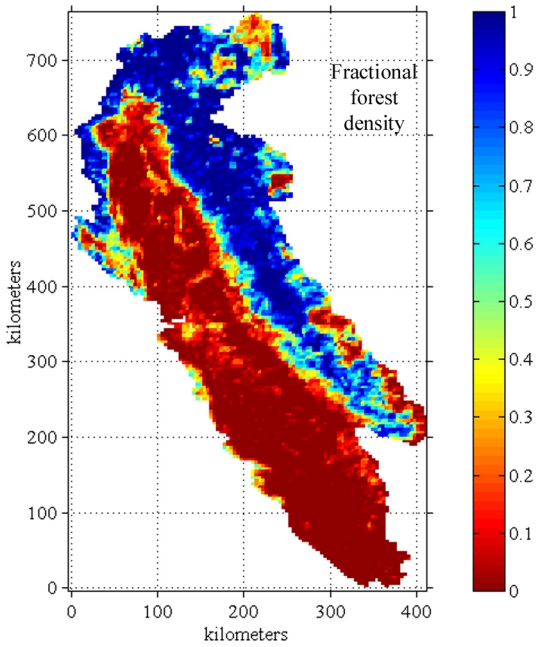

Figure 5.17 Forest density, or crown closure.

While this data corresponds well with the land cover data (Figure 5.16), it provides more useful information on the forests. Especially notable are the lower forest densities of the high Sierra. The thinner forests intercept less falling snow and provide less shade for the hydrologically important snowpack.

While land cover affects how much water enters the soil, other features at both the top and bottom of the soil layer influence water leaving the soil. At the surface, streams are not only carry the running water, but their distribution actually plays a role in generating flow. If streams are distributed very sparsely, horizontally moving water may remain in the soil for some time, whereas a dense stream network provides many exit points for the soil water.

The *stream network density*, $\mathcal{D}$, is defined as the total length of rivers and streams in a given region, divided by the total area of the region. It thus has units of 1/length, and its inverse is proportional to the average distance soil water must travel to enter the network. The EPA provides the data (http://www.epa.gov/surf3/states/CA/) necessary to calculate the network density for the individual hydrologic units of the watershed (Figure 5.18). It should be noted that such estimates of drainage density depend greatly on the map resolution used in their determination. Nonetheless, the essential goal of incorporating such data is to capture the hydrologic influence of the heterogeneity of stream network densities in the watershed, and this goal is met regardless of systematic errors in the data.

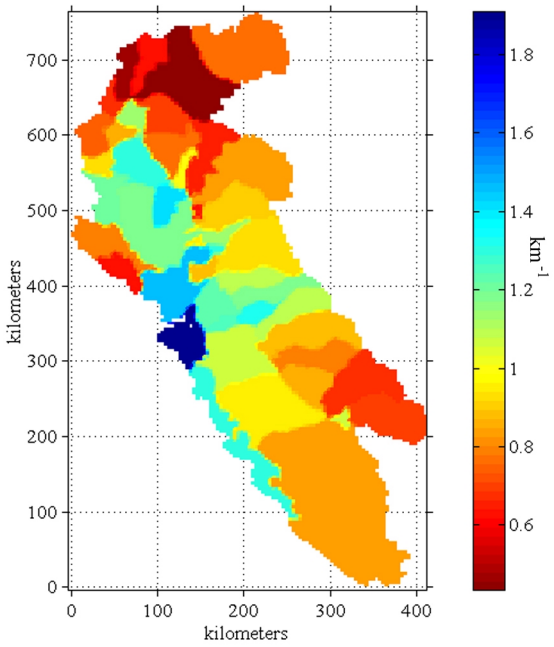

Figure 5.18 Stream network density.

The Cascades and high Sierra have sparse stream networks, implying that the distance soil water must travel to reach a stream is relatively long in these regions. However, remember that some of these mountains, particularly the high Sierra, are quite steep, a quality which would counteract the effect of low network density on soil water residence times as per Equation 5.5. Conversely, the valleys (particularly the Sacramento river valley and the Delta region) have higher stream densities but much lower slopes, again demonstrating the competing interaction between network density and slope.

Moving now to the bottom of the soil layer, the EPA also provides USGS data on aquifers. Aquifers were discussed in Section 3.6, where their effect on hydrology was briefly described. Water in the lower reaches of the soil layer may continue

leaking downward through bedrock into aquifers if they are present, preventing it from entering the stream network until it is extracted. The relative area underlain by aquifers, or conversely by impermeable bedrock, is therefore an important quantity affecting the watershed's hydrology.

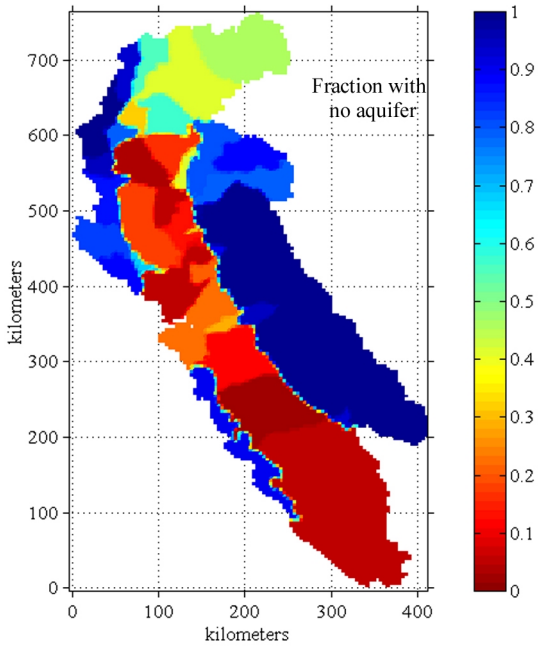

Figure 5.19 Fraction of area underlain by impermeable bedrock with no aquifer.

Figure 5.19 shows the fractional area underlain by impermeable bedrock, $\beta_{\text{no aquifer}}$, derived from the USGS aquifer data, for the Bay-Delta watershed. The geologic and erosional origins of the watershed are clearly apparent. The rocky Sierra and Coast Range have very little area with underlying aquifers, meaning that soil water not lost to evaporation will eventually enter the stream network. The volcanic Cascades are underlain by volcanic aquifers over 40-60% of their area, and the Central Valley lies almost entirely on top of aquifers formed from marine sediments. The

effects of aquifers are therefore expected to be evident in the long-term hydrologic behavior of these three regions.

The features above and below the soil layer, the physical properties of the soil layer, and the topography of the watershed all influence what naturally happens to water between the moment it reaches the land surface in the form of snow or rain and when it enters the estuary. The behavior of the atmosphere over the watershed, or the *meteorology* of the watershed, ultimately controls the amount, timing and distribution of water falling into the watershed. Meteorology also determines how much precipitation falls as snow, influences how long the snow remains before melting, and affects how much soil water and snow water re-enter the atmosphere as water vapor. Meteorology is the most important factor driving the watershed's hydrology, and it merits a comprehensive examination.

5.5 Meteorology

5.5.1 Precipitation

The precipitation process varies strongly in space and time over the watershed. Understanding this variability and the factors affecting it is essential both to a more complete description of the watershed's hydrology and to the development and application of appropriate interpolation methods to estimate precipitation over the entire watershed from the available observations.

5.5.1.1 Precipitation Data

Daily precipitation data was obtained from EarthInfo/NCDC CD-ROMs (http://www.earthinfo.com/earthinfo/) at 362 sites throughout the watershed (Figure 5.20). Spatial coverage is quite good, as is temporal (see caption). The main exceptions are the spatially sparse distributions in the valleys and high mountains. In the valleys, the existing data should suffice to characterize precipitation, as there is relatively low rainfall and a general lack of orographic diversity. This is evident in a plot of the mean precipitation at the gauges (Figure 5.21).

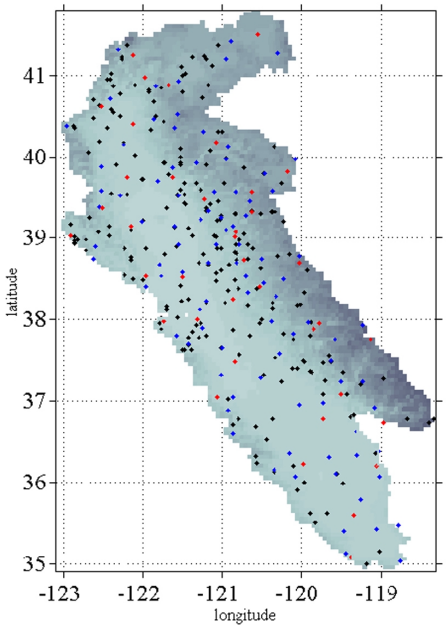

Figure 5.20 Locations of the 362 precipitation gauges used in this study. The 131 stations whose period of record included the entire period of study (WY 65-87) are shown in blue and red. The 37 stations in red were excluded from the interpolations for use in error analysis.

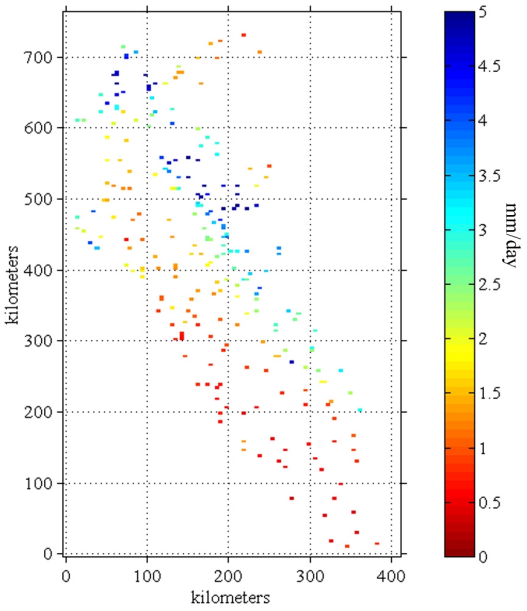

Figure 5.21 Mean daily precipitation values for the gauges shown in Figure 5.20.

The effect of topography on precipitation is clear in Figure 5.21, making the lack of high mountain stations a problem. The importance of the higher elevations is demonstrated by the strong increase of mean daily precipitation with elevation (Figure 5.22).

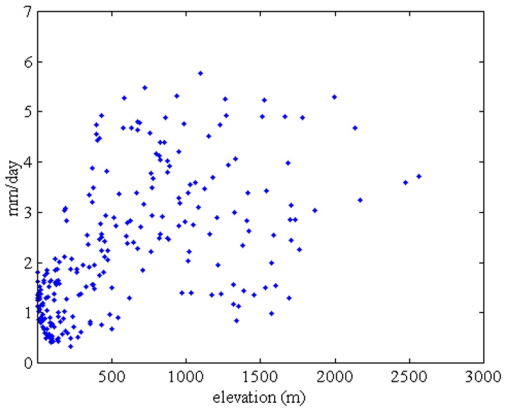

Figure 5.22 Mean daily precipitation versus gauge altitude.

The paucity of high-elevation stations is also hydrologically significant due the occurrence of snowpack in those regions. Interpolation methods need to account for the influence of topography on precipitation if snowpack is to be properly represented.

5.5.1.2 Interpolation Methods

Interpolation of precipitation from available gauge data has been highly studied, and numerous methods are currently in use. The general equation for linear interpolation of a stationary field is:

$$\hat{P}(\underline{\mathbf{x}}) = \frac{1}{\sum \lambda_i} \sum_{i=1}^{n} \lambda_i (\underline{\mathbf{x}}_i - \underline{\mathbf{x}}) P(\underline{\mathbf{x}}_i) \qquad 5.12$$

where $\hat{P}$ is the estimated precipitation at location $\underline{\mathbf{x}}$, $P(\mathbf{x}_i)$ are the gauge data from the locations $\mathbf{x}_i$, and λ_i are the interpolation weights assigned to the individual gauges. These weights are a function of the vector $\mathbf{x}_i - \mathbf{x}$ for a stationary field, and it is the method of determining the weights that differentiates various interpolation methods.

One method in common use is the *inverse-distance squared* method, where the weights are given as:

$$\lambda_i = \frac{1}{\mathbf{x}_i - \mathbf{x}^2} \qquad 5.13$$

While this method does capture the tendency for closer stations to be more strongly correlated, it represents only a rough approximation of this effect. This method also has the disadvantage of ignoring the influences of other factors, such as topography, on precipitation. This could be particularly important considering the low-elevation bias in California data gauges.

Another method which has had a great deal of exposure in hydrology is the method of *kriging*, originally developed by Matheron and others (Matheron and Huijbregts 1971; Journel and Huijbregts 1978) for use in mining applications. A definition of kriging is "a collection of generalized linear regression techniques for minimizing an estimation variance defined from a prior model for a covariance" (Olea 1991). The equation for *simple kriging* is:

$$\hat{P}(\mathbf{x}) = m + \sum_{i=1}^{n} \lambda_i (\mathbf{x}_i - \mathbf{x})\left[P(\mathbf{x}_i) - m\right] \qquad 5.14$$

where m is the mean (in space and time) of the precipitation field. It is clear from this equation that kriging generates an *unbiased* estimate. That is, the estimated field has the same mean, m, as the "real" field. The other key to kriging is that it minimizes the *estimation variance*, which, using Equation 5.14, can be expressed in terms of the covariance:

$$E\left\{\left[\hat{P}(\underline{\mathbf{x}})-P(\underline{\mathbf{x}})\right]^2\right\}=-\sum_{i=1}^{n}\lambda_i(\underline{\mathbf{x}}_i-\underline{\mathbf{x}})C\left(\underline{\mathbf{x}}_i-\underline{\mathbf{x}}\right)+C\left(\underline{0}\right) \qquad 5.15$$

where C is the covariance between two points in the field, which is a function of the difference vector between them for a stationary field. Thus, given knowledge of the first (mean) and second (covariance) order behavior of a stationary field, simple kriging provides an unbiased estimate with minimum quadratic error. Unfortunately, the true mean of the field is often unknown.

The variant of kriging used here is *ordinary kriging*, which imposes the constraint $\sum_{i=1}^{n}\lambda_i=1$ on Equation 5.14. The estimate remains unbiased, but a priori knowledge of the mean is not required. This constraint and the equations resulting from the minimization of 5.15 yield a set of equations called the *kriging system*, which may be solved using traditional matrix inversion solvers.

The main advantage of kriging is the additional, second-order information it incorporates through the covariance. The covariance structure of a field such as precipitation may be estimated by theoretical or empirical methods, then used with kriging to generate informed estimates of unknown quantities.

The main problem with simple and ordinary kriging is the assumption of the stationarity of the field being interpolated. In the case of meteorological quantities, trends in space associated with topographic trends are not represented. When such trends are present, this limitation can cause significant errors, as the kriging method assumes no trend exists. A variant of ordinary kriging is to estimate and remove such a trend before kriging, then add the trend back into the kriged result. The most important factor in this method then becomes the choice of trend such that deviations from the trend represent as stationary a field as possible. For precipitation and temperature, the most obvious choice is an elevational trend.

In what follows, the inverse-squared method, ordinary kriging, and ordinary kriging with a variety of trend choices are applied to the precipitation data of Figure 5.20. All calculations related to kriging were performed with routines from the GSLIB numerical software package (Deutsch and Journel 1998, http://www.gslib.com/). Approximately 10% of the stations are excluded from the interpolations (see Figure 5.20, caption), so they can be used to estimate error. The statistics used to characterize performance at the excluded stations are mean error, root-mean-squared error and correlation coefficient.

5.5.1.3 Kriging versus Simpler Methods

Before evaluating variants of the kriging method, it is first pertinent to assess the usefulness of kriging versus a common simpler method such as the inverse-

squared method (Equation 5.13). Is the increased complexity of the kriging method worth the extra effort involved in its use?

To answer this question, the performance of ordinary kriging with no trend will be compared with that of the inverse-squared method, also with no trend. The methods will be applied to daily data over the period WY 65-87 at the gauges indicated in Figure 5.20, excluding stations to be used in the error analysis.

The first step in developing the kriging estimates is to produce a sample semivariogram, $\gamma(\underline{\mathbf{h}})$. The semivariogram characterizes the spatial structure of the field being interpolated, treated it as a random field. It is defined as:

$$\gamma(\underline{\mathbf{h}}) = \tfrac{1}{2} E\left\{\left[P(\underline{\mathbf{x}}) - P(\underline{\mathbf{x}}')\right]^2\right\} = C(\underline{0}) - C(\underline{\mathbf{x}} - \underline{\mathbf{x}}') \qquad 5.16$$

where $\underline{\mathbf{h}} \equiv \underline{\mathbf{x}} - \underline{\mathbf{x}}'$ and C is covariance. When determining the sample semivariogram from the observed data, 5.16 becomes, in practice:

$$\gamma(\underline{\mathbf{h}}) = \frac{1}{2N(\underline{\mathbf{h}})} \sum_{i=1}^{N(\underline{\mathbf{h}})} (P_i - P_i')^2 \qquad 5.17$$

where $N(\underline{\mathbf{h}})$ is the number of pairs with separation $\underline{\mathbf{h}}$, and P_i and P_i' represent the data from each of those pairs. By dividing $\underline{\mathbf{h}}$ into bins and calculating 5.17 for each bin, the sample semivariogram, representing the covariance structure of the field, may be numerically estimated using available routines (Deutsch and Journel 1998).

As indicated by the vector notation $\underline{\mathbf{h}}$, the semivariogram may also be a function of direction. By considering only those $\underline{\mathbf{h}}$ whose direction falls in a certain

angular range, the dependence of the field's covariance structure may be calculated as a function not only of separation, but also of relative direction.

Applying these algorithms to the precipitation data in the Bay-Delta watershed yields the sample semivariograms shown normalized by the stationary variance, 28 mm^2, in Figure 5.23. The directional variograms (twice the semivariograms) were calculated by limiting the direction of **h** to a 45° range centered on a line parallel to the Sierra-Nevada (the "along-range" curve) as well as a 45° range centered on a line perpendicular to the range. The isotropic version is also shown.

Overall there is little difference among the three variograms. Due to the similarity of the variograms, isotropy will be assumed when kriging.

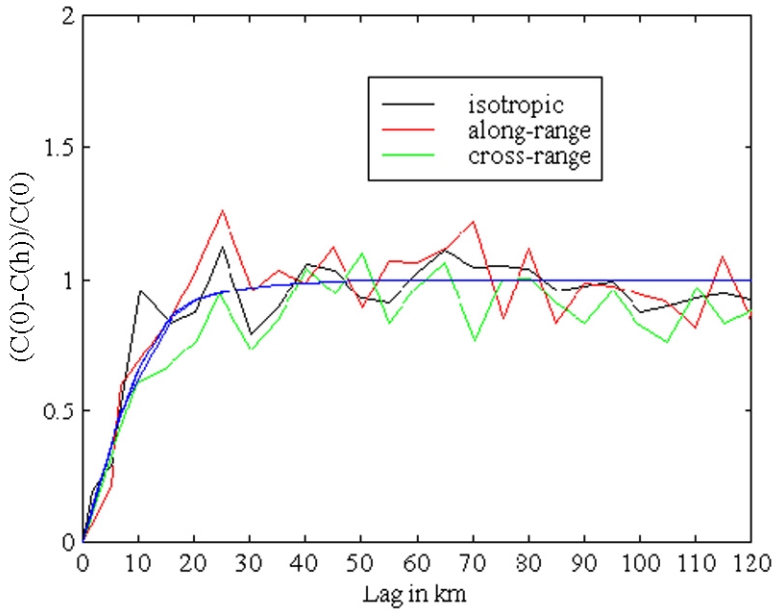

Figure 5.23 Sample variograms for the daily watershed precipitation data, normalized by the stationary variance, C(0)=28 mm^2, with a fitted variogram model shown in blue.

The sample variogram must be modeled with an analytic expression in order to use this information in the kriging algorithm. Among the most common choices for variogram models are the exponential and the spherical models. The curves in Figure 5.23 are best represented by a combination of these two. The fitted model variogram used in the kriging and shown in Figure 5.23 is one-half exponential model with a characteristic length of 11 *km*, and one-half spherical model with a characteristic length of 19 *km* (Equation 5.18).

$$\frac{2\gamma(h)}{C(\underline{0})} = \begin{cases} 0.5\left(1-e^{-h/11}\right)+0.5\left(3\frac{h/2}{19}+\frac{h^3/2}{19^3}\right), & h \le 19km \\ 0.5\left(1-e^{-h/11}\right)+0.5, & h > 19km \end{cases} \qquad 5.18$$

A final decision when interpolating data is what domain to include in the interpolation for each point. Though the weights given to the various gauges drops of quickly with distance from the interpolation point, it is nonetheless computationally beneficial to limit the number of stations used in each interpolation. Based on Figure 5.23, a search radius of 120 *km* appears reasonable, as covariance has reached its minimum by that separation distance.

The inverse-squared distance method and ordinary kriging with no trend using Equation 5.18 were applied to the precipitation data set. The performance statistics for these two methods, calculated at the excluded stations, are shown in Figure 5.24.

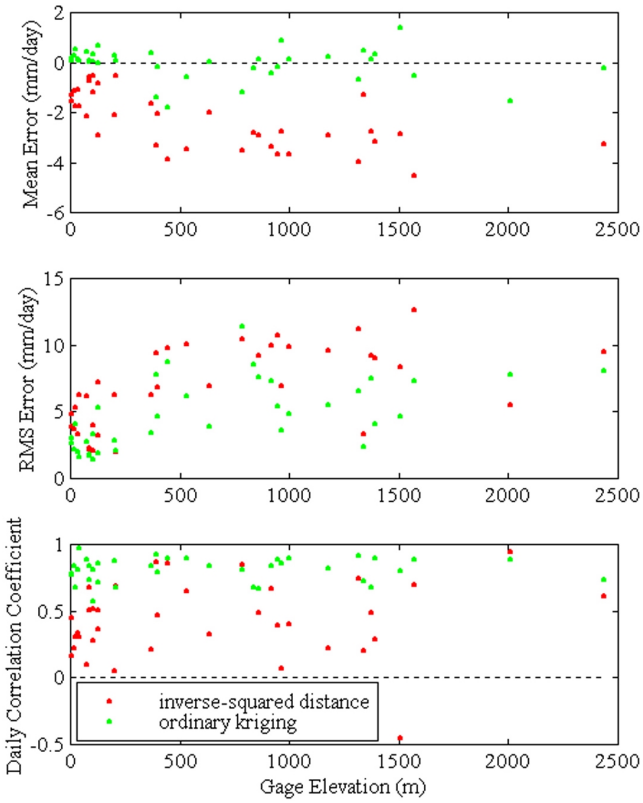

Figure 5.24 Performance statistics for the inverse-square and ordinary kriging interpolation methods as applied to precipitation data.

In all three statistics, ordinary kriging clearly outperforms the simpler inverse-squared method. The mean error shows that the built-in unbiased constraint gives kriging a decided edge over inverse-squared which consistently underestimates precipitation. The RMS error and the correlation coefficient both show kriging performing better. It appears, therefore, that the extra effort involved in the kriging method is merited.

5.5.1.4 Kriging With Trends

The clear elevational trend in the RMS error of both methods, especially below 500 *m*, highlights the need to account for spatial non-stationarity in the data. Describing the "trend" in precipitation is the challenge. First, only linear trends are considered here. Kriging with second-order trends was attempted, but such methods tended to dramatically increase errors at higher elevations and were excluded from consideration.

The difficulties in developing reliable trend estimates are threefold. First, only relatively large areas contain enough gauges to get a good picture of the trend. Second, precipitation is a highly spatially variable process, and trends in that process vary significantly in space. These first two difficulties are at odds. Finally, precipitation and the trends associated with it also vary temporally a great deal. The spread in trends with elevation, for example, is evident in Figure 5.22.

As a compromise among these problems, the watershed can be broken into five regions (Figure 5.25), each with relatively distinct topography but large enough that they contain a fair number of gauges.

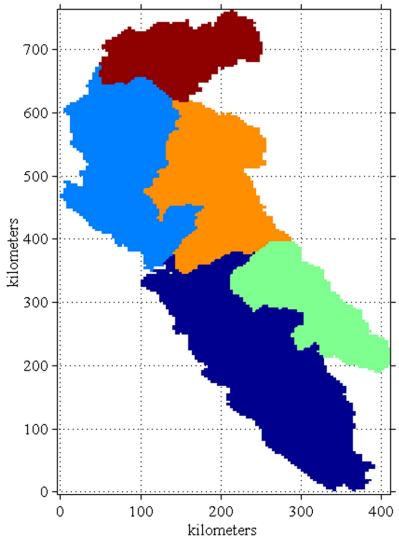

Figure 5.25 Five regions used in regionally-based kriging methods.

Next, in each of these regions, regressions of monthly precipitation averages on gauge elevation yield monthly climatological precipitation "lapse rates" (Figure 5.26).

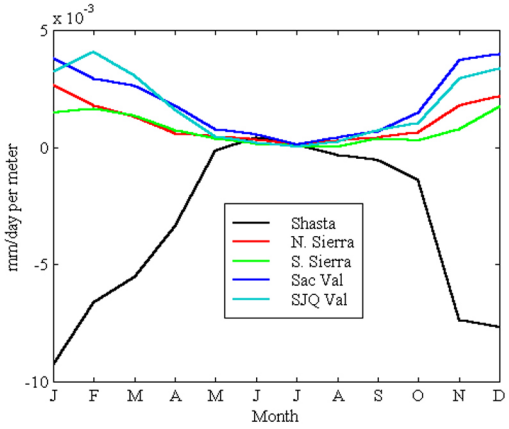

Figure 5.26 Monthly regional precipitation "lapse rate" climatologies.

This figure gives some idea of the spatial and temporal variation in precipitation elevational trends. The main features include the seasonal cycle in trends, with higher increases of precipitation with elevation during the wetter months from

November through March. The other very prominent feature is the marked difference of the Shasta basin from the other regions. As shown in Section 5.2, this region is topographically distinct from the other regions. The inverted precipitation "lapse rate" curve in Figure 5.26 for this basin may be a result of several factors. One is the presence of a relatively low-lying, arid region in the northeast extremity of the watershed, the Modoc Plateau. This area has little orographic forcing and a slight rainshadow effect, so it sees relatively little precipitation, which can be seen in Figure 5.21.

Another possible, and more substantial, reason for the negative elevational trend is the different topography of this volcanic region. Throughout most of the watershed, elevation and slope are positively correlated (r~0.6 for the entire watershed, using the 4 *km* resolution elevation and slope data). However, in the Shasta basin elevation and slope are slightly anti-correlated (r~-0.2). This difference in orography may be partly responsible for the negative elevational trend in precipitation. Slope, after all, is what forces orographic uplift, not elevation. The correlation between precipitation and elevation may be an artifact of the correlation of elevation and slope, combined with a correlation between slope and precipitation. The odd behavior in the Shasta basin seems to support this idea, as lapse rates based on slope instead of elevation (not shown) are positive in this and all other basins. Indeed, the watershed average correlation between measured precipitation and slope (r~0.58) is slightly higher than that between precipitation and elevation (r~0.51) during the wet

season. This suggests the possibility of using slope instead of elevation as the independent variable for determining trends in the precipitation field.

While large regions and monthly climatologies were used to determine the trend estimates of Figure 5.26, it is possible that considering smaller spatial and temporal scales may offer improved performance. Using only stations within a given "search radius", as was done for the interpolations evaluated in Figure 5.24, may limit the trend calculations to localized precipitation patterns. This may improve or degrade the quality of the interpolation. Further limiting the stations to only those in a similar topographic region (Figure 5.25) may generate a more specific characterization of the orographic nature of the precipitation in that region. Finally, calculating trends at a daily time scale may limit the information to individual precipitation events.

With the above considerations in mind, four differing methods of removing trends from the precipitation data were evaluated. The first involved using the regional monthly climatological lapse rates of Figure 5.26 to determine the trends, then kriging the anomalies within a 120 *km* search radius. Next, trends were calculated for each day and for each interpolated point using a 120 *km* search radius, and the anomalies were kriged using a 120 *km* search radius. The third method was identical to the second, but based the trends on the local (16 km^2 average, Figure 5.5) slope instead of elevation. The final method was identical to the second, but limiting both the trend calculation and the kriging to those stations within a 120km search radius *and* within the same topographic region as determined by Figure 5.25.

It should be noted that the variograms of Figure 5.23 were re-calculated after detrending in each case, and the results were never significantly different from those original variograms. Hence, the variogram model given by Equation 5.18 was used throughout.

The performance statistics for all four kriging-with-a-trend methods are shown in Figure 5.27, along with the original results from kriging with no trend. The most important feature of these statistics is that all methods of incorporating trends offer no significant improvement over kriging without a trend, even at the higher elevations. In fact, all trend-based methods appear to perform slightly worse than the no-trend method. Perhaps the deviations from the climatological patterns are so great that the trends in Figure 5.26 are useful only as climatologies, offering no real predictive information at the daily scale. Further, perhaps the daily precipitation values are at too fine a time scale to see any real trends emerge. Certainly other studies have found useful trends at monthly and shorter time scales (Chua and Bras 1982; Goovaerts 2000), but the spatial scale was much smaller in those studies than here. For the scale addressed here, there may be some intermediate temporal and spatial level at which useful trends can be detected. However, searching this out is beyond the scope of the present interpolation study, and developments in the next chapter will offer additional insight into this problem.

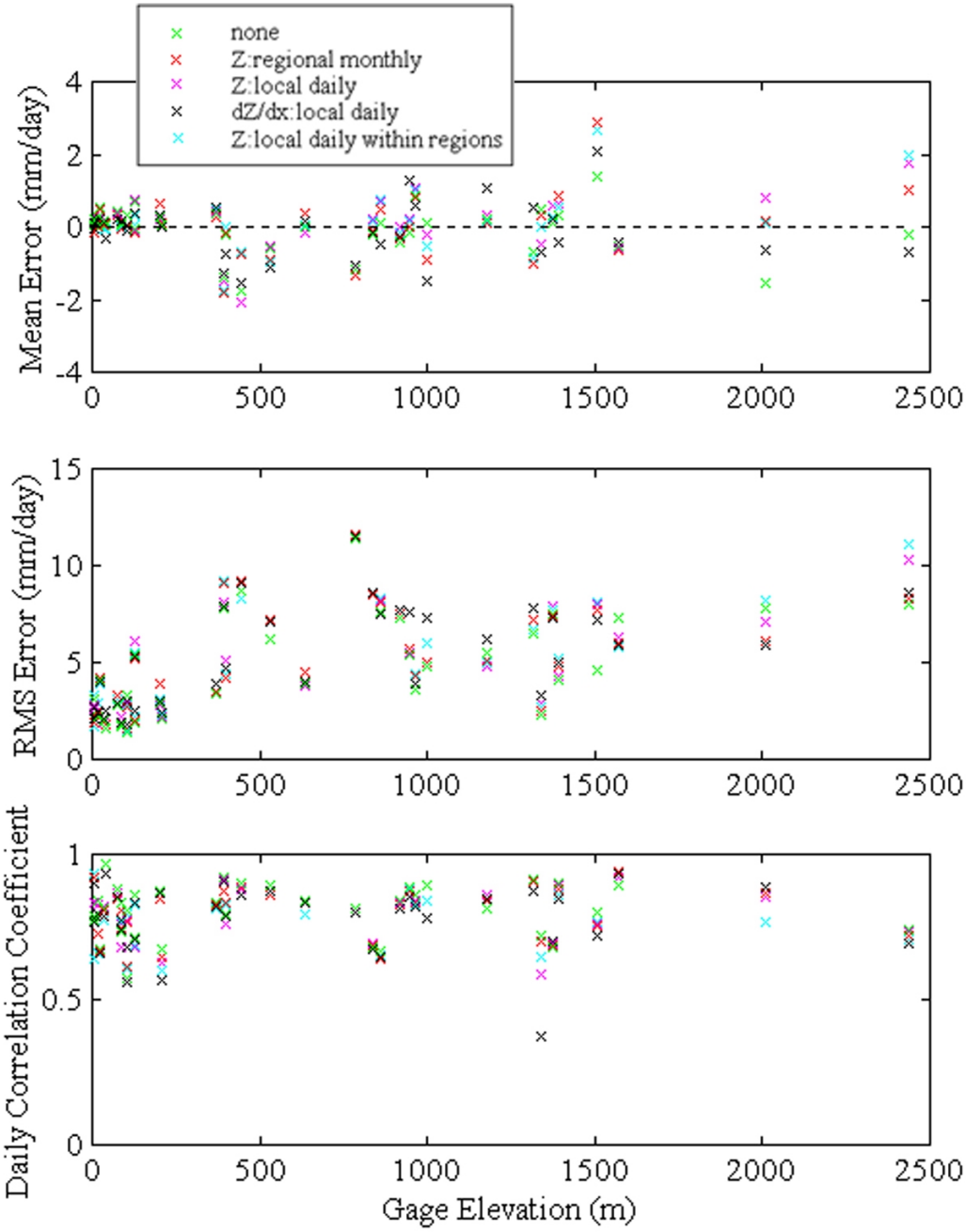

Figure 5.27 Errors of interpolated precipitation, using ordinary kriging with various trends, versus elevation. Trend methods are given in the legend.

Certainly the trend methods may offer more realistic estimates above the highest gauge, but there is no way as of yet to evaluate high elevation performance with this data. For now, the only conclusion that can be drawn is that ordinary kriging without a trend appears to offer the best precipitation estimates below 2500 *m*. The mean precipitation field determined in this manner is shown in Figure 5.28.

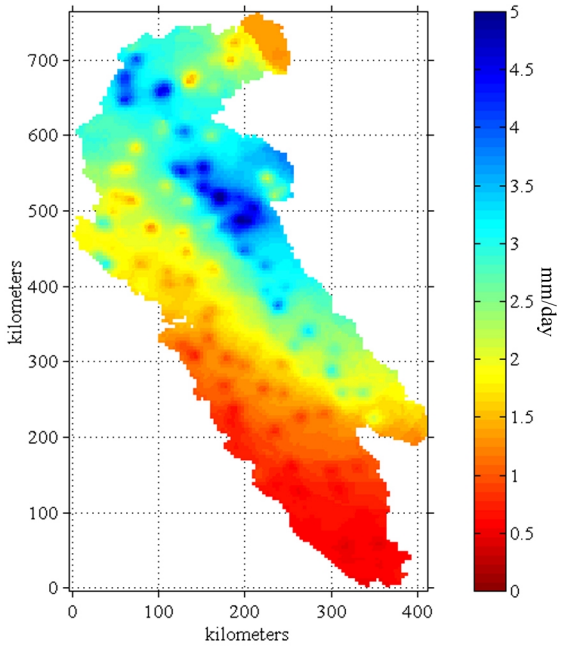

Figure 5.28 Mean precipitation field generated using ordinary kriging with no trend. Accuracy above 2500 *m* is not directly testable, and is questionable.

5.5.2 Temperature

After precipitation, the most important meteorological quantity driving the watershed is temperature. Temperature controls the accumulation and ablation of the snowpack, and determines evapotranspiration demand. Temperature is also much less

variable than precipitation, and hence easier to interpolate. Much of the treatment of temperature to follow will parallel the treatment of precipitation in the previous section.

5.5.2.1 Data

The temperature data were also obtained from the EarthInfo/NCDC database. The data consist of maximum and minimum daily temperature (T_{max} and T_{min}) at each sensor location. There are fewer available sensors for temperature than there are for precipitation (Figure 5.29).

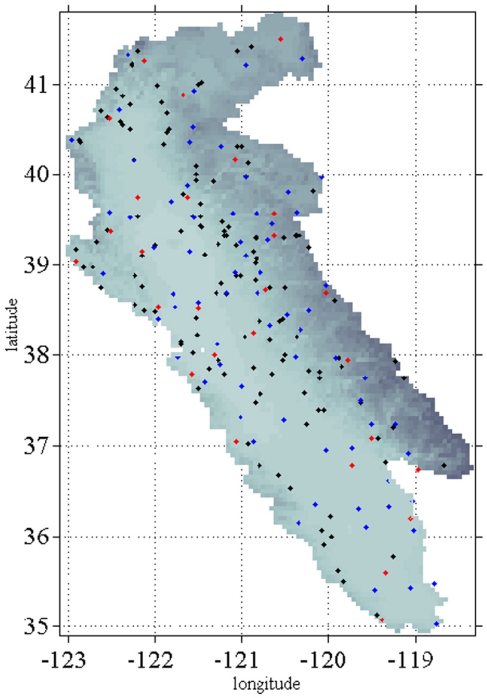

Figure 5.29 Locations of the 233 temperature sensors used in this study. The 97 stations whose period of record included the entire period of study (WY 65-87) are shown in blue and red. The 27 stations in red were excluded for use in error analysis.

Again, there is a low-elevation bias in the station distribution, but this should be less of a problem due to the more reliably linear dependence of temperature on elevation. The decrease of temperature with altitude is a well-understood phenomenon. This linear relationship is clearly evident in Figure 5.30.

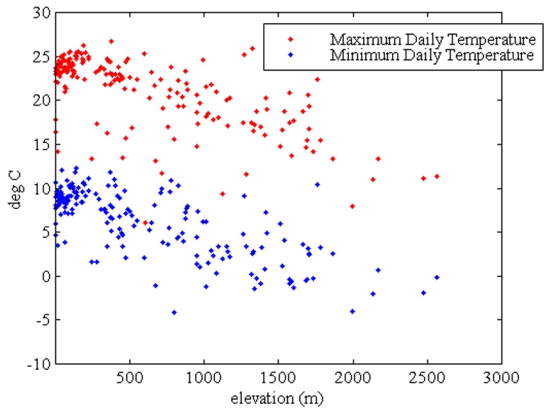

Figure 5.30 Mean maximum and minimum daily temperature versus sensor altitude.

Clearly, the temperature field is non-stationary, and kriging methods will need to incorporate the elevational dependence. It is expected that the trend methods will fare better with temperature than they did with precipitation.

5.5.2.2 Temperature Interpolation with Trends

To characterize the spatial and temporal variability in the temperature lapse rate, monthly climatologies for the regions of Figure 5.25 were calculated for T_{max} and T_{min}, analogous to the precipitation "lapse rates" in Figure 5.26. The temperature lapse rates are shown in Figure 5.31.

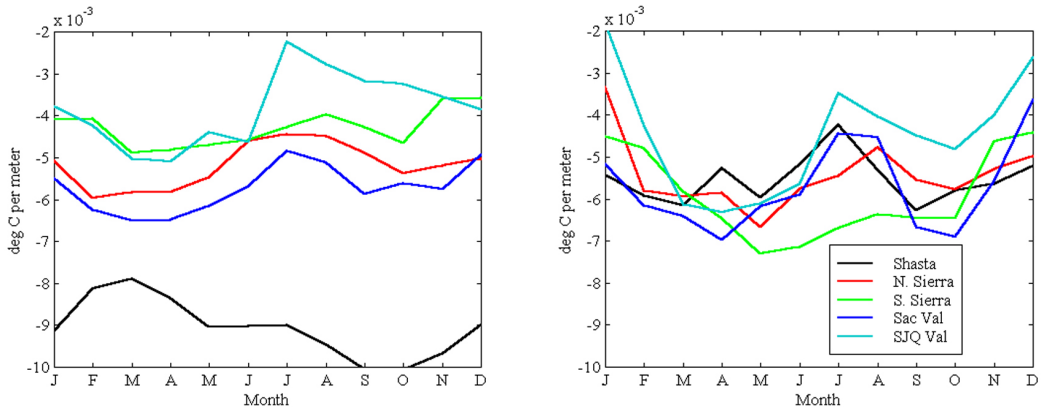

Figure 5.31 Monthly regional temperature lapse rate climatologies. Minimum daily temperature lapse rates are on the left, and maximum daily temperature lapse rates are on the right.

The theoretical moist adiabatic lapse rate is 6-7°*C* per 1000 *m*. This is roughly the observed lapse rate for T_{max} in most months and regions, but T_{min} shows quite different variability. This makes sense, since T_{min} is much more dependent on the local topography (*e.g.*, cold air settles in the valleys at night). The Shasta basin again shows distinct behavior, this time with large lapse rates, roughly equal to the dry adiabatic value of 9-10°*C* per 1000 *m*. As with precipitation, this is likely the result of the distinct topography of the region.

The variogram structure for the temperature fields (Figure 5.32) was very similar to that of precipitation. In fact, the same variogram model (Equation 5.18) fits the sample variograms for temperature equally well. Again, the assumption of isotropy appears reasonable.

The same methods of kriging with no trend and kriging with different trends used with precipitation were applied to T_{max} and T_{min}, with the exception of the slope-based method. There is no evidence that slope plays a significant role in determining temperature fields. Again, the variogram (Figure 5.32) was relatively unaffected by

the removal of the trends, and the same model was used throughout. The performance statistics are summarized in Figure 5.33.

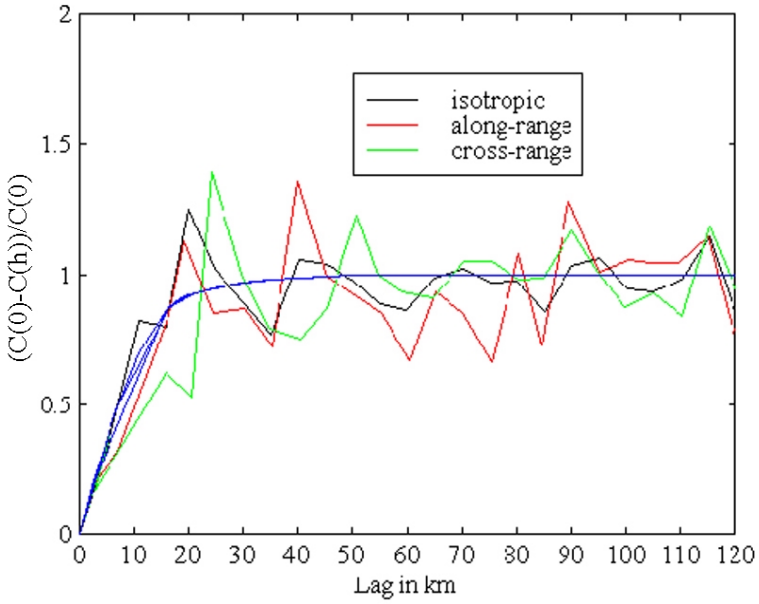

Figure 5.32 Sample variograms for the daily watershed T_{max} data, normalized by the stationary variance, C(0)=47 °C^2, with a fitted variogram model.

Unlike precipitation, kriging temperature with no trend gives worse results than any of the trend-based methods, particularly above 1500 *m*. Faring only slightly better is the method using daily local trend fits and kriging, limited to the given topographic region ("local daily within regions"). The "local daily" and "regional monthly" methods are basically indistinguishable in quality, with very good performance in all statistics, although there is still some degradation at higher altitudes. This could be a problem, since the highest altitudes are where temperature has its most significant impact, on snow.

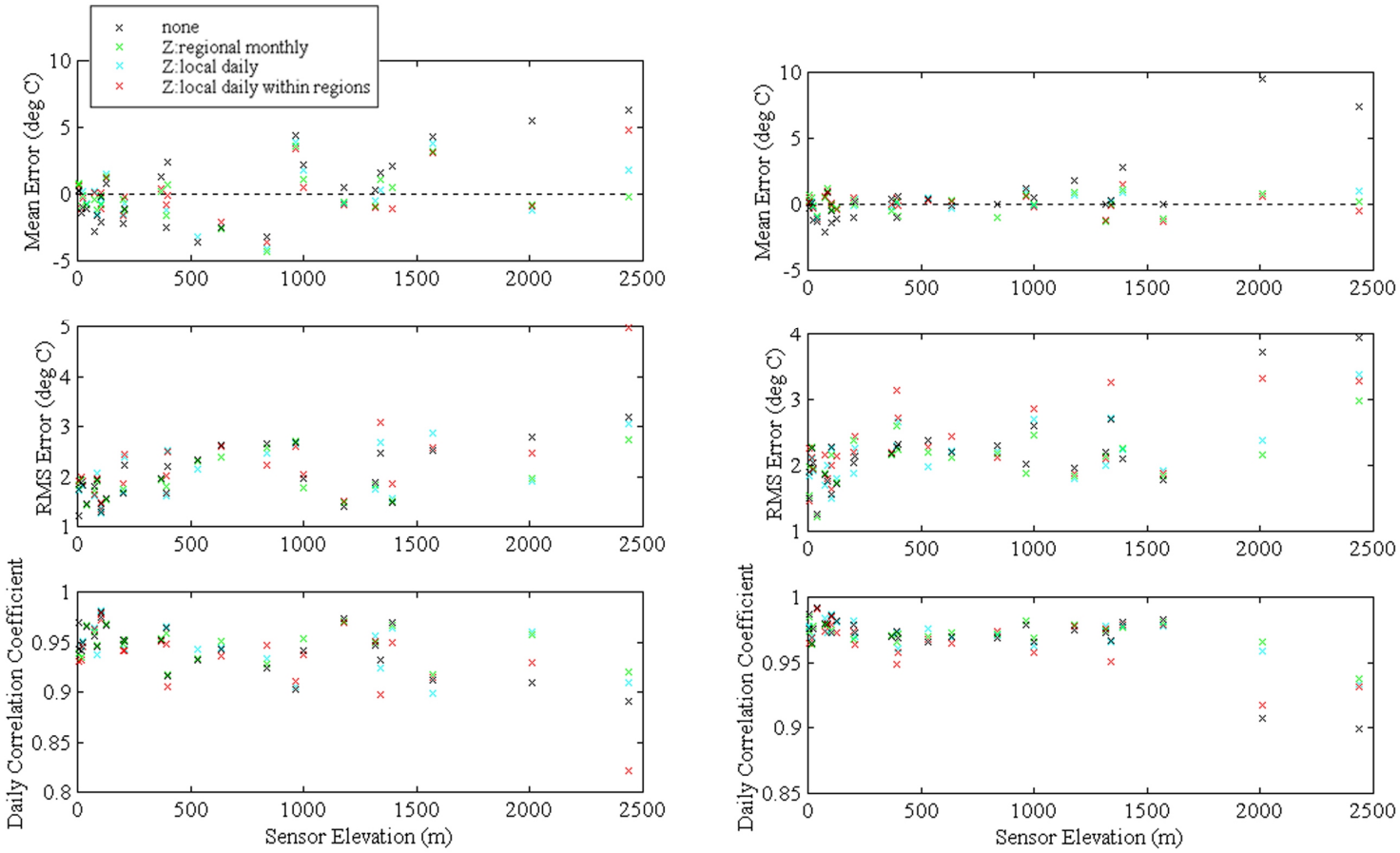

Figure 5.33 Errors of interpolated temperature, using ordinary kriging with various trends, versus elevation. Results for daily minimum temperature are on the left, and results for daily maximum temperature are on the right. Trend methods are given in the legend.

For now, both temperature methods will be used as alternate representations of the watershed's temperature forcing. In the next chapter, additional insight into their relative merits will be offered. The mean T_{max} and T_{min} fields for the "local daily" method are shown in Figure 5.34.

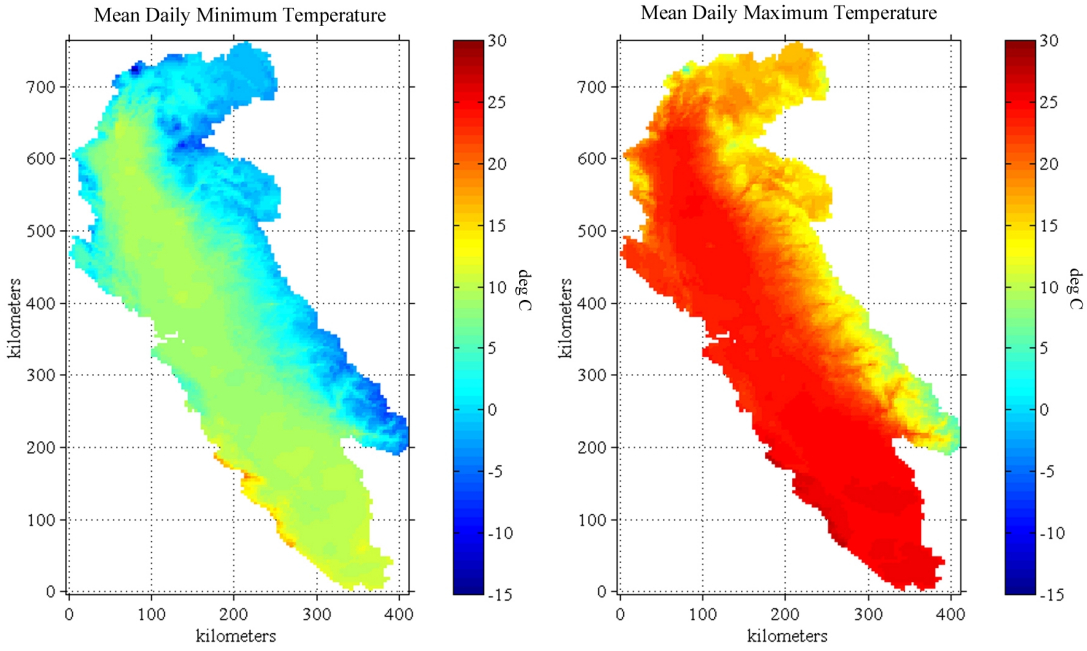

Figure 5.34 Mean temperature field generated using kriging with a local daily trend. Accuracy at higher elevations is uncertain.

5.5.3 Wind Speed and Relative Humidity

Additional data needed to characterize the watershed's meteorology for the current study are wind speed and relative humidity. These are important quantities affecting the rates of soil water evapotranspiration and snow sublimation. Since both of these effects vary strongly with the Sun's diurnal cycle, it is useful to represent this cycle in the data.

Hourly observations of relative humidity and wind speed were available from the EarthInfo/NCDC data base. These data are quite sparse in both space and time, with only 9 stations in the watershed. While this is not ideal for either wind speed or relative humidity, few other options exist short of developing a fully-distributed atmospheric boundary layer model. In the case of wind speed, however, it was decided to supplement the ground-level data with upper air sounding data from Oakland, California.

Wind speed varies strongly with elevation, and the sparse ground data would not capture this important variability at higher elevations. The sounding data, however, offers twice daily (midnight and noon) wind speed data at many elevations. This data was processed to generate monthly climatologies for each time of day and each elevation. The two daily soundings were interpolated to yield 4 daily values in an attempt to better capture the diurnal cycle. The resulting climatologies were distributed over the watershed, using the DEM data to map the corresponding elevational data. The climatologies for the ground-level data were applied to elevations from 0-750 *m* (using nearest-neighbor mapping), while the lowest 6 levels of the sounding data (which correspond roughly to heights of 1 *km*, 1.5 *km*, 2 *km*, …3.5 *km*) were applied to 750-1250 *m*, 1250-1750 *m*, and so on through the highest interval, 3250-3800 *m* (the highest elevation on the 16 km^2 grid is 3794 *m*). The mean total climatology of all the wind speed data is shown in Figure 5.35

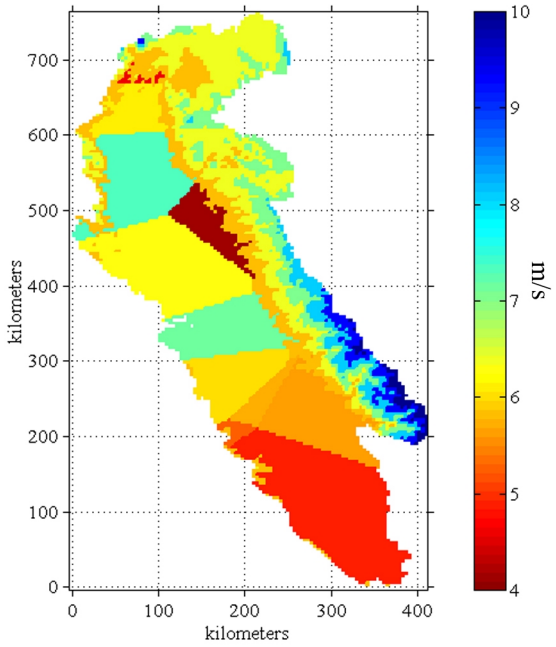

Figure 5.35 Mean wind speed estimates based on ground station data and upper air sounding data.

The sounding data also offered measurements of relative humidity; however it was decided preferable to simply interpolate the ground measurements over the watershed, since the temperature variations near the surface strongly drive the relative humidity. This is evident in the mean diurnal cycle of hourly relative humidity data (Figure 5.36). The sounding data agreed quite well with the daytime ground sensor data, but at nighttime, discrepancies were the norm.

The RH data was similarly processed to yield monthly climatologies of relative humidity at each station, with four data points per day. This data was interpolated to the data grid using nearest-neighbor mapping.

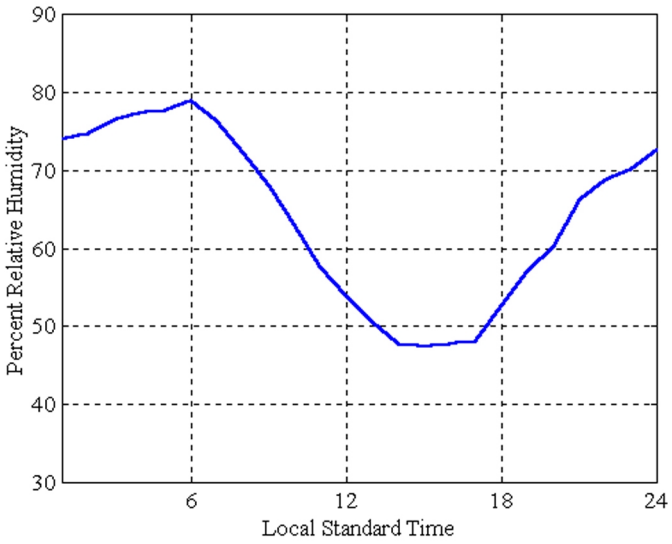

Figure 5.36 Mean diurnal cycle of hourly relative humidity (RH) record from all California stations. Late afternoon/evening shows low RH; nighttime/early morning shows high RH.

5.6 Summary

In this chapter, data characterizing the topography, hydrologic behavior of the soils, landcover, stream network, aquifers, and meteorology of the San Francisco Bay-Delta watershed were assembled, processed, aggregated and interpolated onto a data grid in an appropriate map projection. This database represents a significant contribution to our understanding of the Bay-Delta watershed.

In particular, extensive numerical simulations of vertical diffusion of soil moisture were performed to characterize the percolation process throughout the watershed. Since percolation is the soil moisture process which limits all others, this data tells a great deal about the watershed's hydrology. In addition, the methods developed and used here to parameterize percolation constitute a new and effective

means of representing the sub-basin heterogeneity of hydrologic soil properties and may be easily applied to other watersheds.

Also, an extensive study of the properties of the daily precipitation and temperature fields over the watershed was performed. The results offer new insight into the behavior of these fields as they vary from basin to basin and with elevation. Many interpolation methods were evaluated, and the successes and failures of each were evaluated to arrive at the optimal methods.

Besides offering new insight into the hydrologic behavior of the Bay-Delta watershed, the assembled database lays the foundation of a hydrologic modeling capability for the watershed. Such a capability will permit the investigation of the watershed's role in shaping the Bay-Delta estuary's response to forcing by the weather/climate system. The next chapter concerns the formulation and development of this model.

6 Modeling the Watershed

6.1 Approaches to Hydrologic Modeling

In hydrologic modeling, the region to be studied and the nature of the studies to be conducted determine, to a large extent, the type of model which needs to be employed. For many situations, there are existing models which are appropriate. In other cases, a suitable model must be developed. Modeling methodologies vary greatly, but the most commonly-used models today can be grouped into three basic categories, lumped conceptual, statistical-dynamical and distributed physical.

The lumped conceptual types generally represent entire catchments with one model element. The aggregate processes governing the movement of water through the soils of the catchment, such as infiltration and baseflow, are parameterized in the lumped conceptual model, the parameters being determined by specific characteristics of the catchment's outflow hydrographs.

The forerunner of many of today's conceptual models is the Stanford Watershed Model (SWM) (Crawford and Linsley 1966). This model represents the aggregate soil water behavior of entire catchments, accounting for one soil zone in the vertical. The model generates flow estimates at each time step. The SWM parameterizes two processes affecting the soil moisture, namely the infiltration of water into the soil and the rate of evapotranspiration from the soil. Prior to this, commonly-used methods such as the U.S. Weather Bureau's Antecedent Precipitation Index model (Betson, Tucker *et al.* 1969), the Army Corps of Engineers' HEC model

(http://www.wrc-hec.usace.army.mil/), and the USDA's SCS model (Soil Conservation Service 1972) did not explicitly simulate soil moisture, instead parameterizing the relationship between precipitation and runoff. Simulating the soil moisture directly is a more physically realistic way to estimate streamflows, yielding more robust estimates under a range of hydrologic conditions and allowing continuous hydrologic simulation.

One of the SWM's descendants is the Sacramento model (SM) (Burnash and Ferral 1983). This model further divides the soils of a catchment into two vertical layers and represents soil moisture in each layer as "tension" and "free" water components. These are intended to represent soil water bound to the soil matrix (extracted only by evapotranspiration) and water free to move under the force of gravity, respectively. The SM additionally parameterizes the percolation of water from the upper to the lower layer, as well as horizontal flow in the upper layer (interflow) and in the lower layer (baseflow). The parameters related to each of these processes are estimated initially from different characteristics of the catchment hydrograph, then fine-tuned using automated computer techniques to fit model output to observed outflows. The SM has been extremely successful (*e.g.*, Bae and Georgakakos 1992) and a version of it is used by the National Weather Service to generate river flow forecasts.

The main disadvantage of lumped conceptual models is their dependence on historical streamflow data for determination of model parameters. This can be a problem either when such records are unavailable, or when available records represent

only a limited and temporary hydrologic regime for the catchment. It is desirable, then, to develop models based only on the physical characteristics of the watershed itself. Although the data required to characterize the physical characteristics of the watershed are inevitably extensive, it may at least be feasible to collect it, whereas long streamflow records may be non-existent. Further, basing a model on a watershed's physical properties rather than its flow history should ideally (*i.e.*, with low input and parameter error) result in simulations which are robust and accurate regardless of hydrologic regime.

The difficulty in developing a physically-based hydrologic model of even a moderately-sized watershed lies in the complexity of hydrologic processes involved. The movement of water through the soil depends on local variations in soil properties, topography, landcover, meteorology, and other factors. Each of these factors can exhibit a great deal of heterogeneity within a catchment, resulting in the complex hydrologic variability which ultimately determines catchment outflow.

One way of representing this heterogeneity is to attempt to relate the catchment's aggregate hydrologic processes to the distribution functions of the various physical characteristics of the catchment, resulting in a statistical-dynamical model. Several attempts have been made to relate the parameters of lumped conceptual models to physical properties of the catchment, (*e.g.*, Ross 1970; James 1972) with limited success. More successful models have been developed using the distribution function approach to represent heterogeneity (*e.g.*, Wood, Sivapalan *et al.* 1988; Avissar and Rind 1992; Liang, Wood *et al.* 1996). These models typically base runoff

on the distribution of a single index, and most were developed for coupled use with atmospheric and general circulation models. The drawbacks of this approach are that much of the heterogeneity affecting hydrologic processes is ignored, and that horizontal movement of soil water is typically not represented in these models.

As was seen in the previous chapter, a great deal of data is now available to physically characterize watersheds, especially in the U.S. Also, computer technology offers ever-increasing speed and storage capabilities. These developments have led to the growing popularity of the physically-based, distributed modeling approach. The term "distributed" implies that instead of representing the aggregate behavior of a catchment, the catchment is subdivided into many small areas, each of which is assumed homogeneous. In each of these areas, hydrologic processes are simulated based on the average physical properties and according to known laws of hydrology. While a lumped conceptual model might have a model element with an area of 100-1000 km^2, and some of the distribution function models represent areas of 10,000 km^2 or more, a distributed model typically has elements on the order of 0.1-1.0 km^2. Many distributed models are in operation (*e.g.*, Leavesley, Lichty *et al.* 1983; Beven, Kirkby *et al.* 1984), and are typically intended to generate runoff estimates at time scales from hours to weeks.

6.2 Modeling Requirements for Hydroclimate Studies

The present study is aimed at simulating hydrologic variability over a 140,000 km^2 watershed under a wide range of historical and hypothetical hydroclimate

regimes. Capturing spatial variability , at least to the scale of individual river basins, is important for characterizing the hydrologic differences across the Bay-Delta watershed. Representing temporal variability at time scales of a week and longer is needed to understand changes in flow magnitude and timing related to climate variability. The abilities to simulate very long periods, up to a century, and to perform ensemble runs are also essential to the goals of this study.

Fully-distributed models are typically too computationally demanding for such lengthy runs over this large an area. However, the wide range of hydroclimate regimes to be simulated demands a physically-based approach. Model elements need to be small enough that areally-averaged meteorological quantities generate reasonable estimates of snowmelt (a lumped approach was attempted initially, but ruled out on this basis). If homogeneity of each model element is to be assumed, the element size must also be small enough that the neglected heterogeneity has little effect at the intended time scales. The assumption of homogeneity is desirable because it greatly simplifies the model formulation.

6.3 Bay-Delta Watershed Model

6.3.1 Overview

As a result of the above considerations, a physically-based, quasi-distributed approach was chosen for modeling the hydroclimate variability of the Bay-Delta watershed. Model elements in the Bay-Delta watershed model (BDWM) have an area of 16 km^2, corresponding to the data grid shown in Figure 5.2. While not small enough

to qualify as a high-resolution fully distributed model, this size should suffice for representing meteorological variability, and should allow the assumption of homogeneity while maintaining enough accuracy for hydroclimate studies.

Much of the physical basis of the model was described in the previous chapter. There, the data was processed in such a way as to prepare it for incorporation into the BDWM model formulation. The structure of each model element is similar to the conceptual structure of the Sacramento model, though it is more closely derived from the Rainfall-Runoff-Routing model by Georgakakos *et al.* (Georgakakos and Baumer 1996). The main differences from the Sacramento formulation are the merging of tension and free water elements, and that the model parameters are based on the watershed's physical characteristics.

Like the SM, the BDWM has 2 vertical layers for each element, here chosen based on permeability profiles as described in Chapter 5. The soil moisture processes simulated in each element are as shown in Figure 6.1.

The resulting equations for soil moisture in the upper (subscript 1) and lower (subscript 2) layers are:

$$\begin{aligned} \frac{d\Theta_1}{dt} &= Q_{in} - Q_{SR} - Q_{ET_1} - Q_{IF} - Q_{PC} \\ \frac{d\Theta_2}{dt} &= Q_{PC} - Q_{ET_2} - Q_{BF} - Q_{GL} \end{aligned} \qquad 6.1$$

and the water actually flowing into the stream network is given by:

$$Q_{chan} = Q_{SR} + Q_{IF} + Q_{BF} \qquad 6.2$$

where Q_{ET_1} is evapotranspiration from the upper layer, Q_{ET_2} is evapotranspiration (mainly transpiration) from the lower layer, and all other variables are defined as in Figure 6.1.

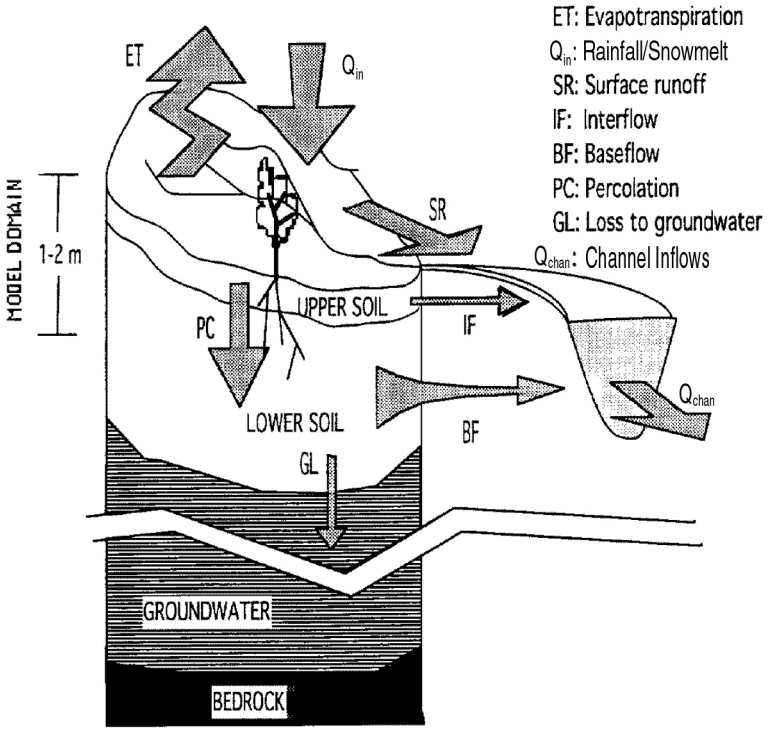

Figure 6.1 BDWM soil moisture element schematic (from Mullusky and Georgakakos 1993).

In addition to the soil moisture component which simulates the above processes, the model contains a snow component which simulates snow accumulation and ablation processes for each model element. The output from this component determines Q_{in}, the water input to the soil moisture component. There is also a river routing component which takes the sum of Q_{chan} over all elements in each of the 15 river basins (Figure 3.2) as input and simulates the effect of the basin's river channels in determining the total basin outflow.

The model's time step is one day, though some components of the water budget (snow, potential ET) are initially calculated each day at 6-hour steps to resolve the diurnal cycle, then averaged to the daily scale. For each day, the BDWM takes as input precipitation, daily maximum temperature and daily minimum temperature. Possible outputs include all simulated components of the water budget, including snowpack liquid water equivalent, sublimation, all quantities in Equations 6.1, and stream network inflows and outflows. Though the output is given at the daily scale, it is not expected that simulated flows will be accurate at that scale due to the finite resolution of the model and the expected uncertainties of its inputs and parameters. The daily time step is used because it is commensurate with available input data and allows some parameterization of diurnal processes, offering more accurate estimates of longer-term flow variability.

For each day and each model element, snow accumulation and melt are calculated, then the remaining quantities illustrated in Figure 6.1 are calculated to yield a pair of coupled differential equations, Equations 6.1. The equations are solved using a 4^{th}-order Runge-Kutta method (Press 1986) to yield changes in soil moisture and flows into the stream network, Q_{chan}. These are then routed through each basin's channel network by means of another pair of differential equations (described later), also solved using 4^{th}-order Runge-Kutta, to yield daily outflow estimates for each river basin, and total outflow for the Bay-Delta watershed.

The BDWM algorithm will be presented again later in more detail, but first the methods for determining each of the individual components of the water budget

are presented. An important matter of notation is that in the next two sections on snow and evapotranspiration, the variable Q will represent energy fluxes unless otherwise indicated, whereas in the rest of the dissertation, Q represents flows.

6.3.2 Snow

6.3.2.1 Choice of Snow Model

One of the most important hydrologic processes, both in terms of its impact on the annual hydrograph and its sensitivity to climate variability, is snowpack accumulation/ablation. The strong effect of snowpack is particularly evident in the high Sierra hydrographs of Figure 3.5. In California, the mean total annual snow water storage is approximately 40 km^3 (Kahrl, California Office of Planning and Research *et al.* 1979).

Simulation of snowpack is a science unto itself. The processes involved in snowpack accumulation, evolution and ablation are quite complex and are the subject of ongoing research. Many models have been developed (Anderson 1973; Anderson 1976; Morris 1982; Leavesley, Lichty *et al.* 1983; Kondo and Yamazaki 1990), but these often require calibration, extensive input data, or are intended for snowpack process research only. The Utah Energy Balance Snow Accumulation and Melt Model (UEB) was developed relatively recently with the intent of providing "a parsimonious, physically-based model that could be driven by readily available inputs and applied anywhere with no (or minimal) calibration" (Tarboton and Luce 1996, http://www.engineering.usu.edu/dtarb/snow.html). These qualities make the UEB

model particularly well-suited for the present study. It has the further advantage that one of its test sites was the Central Sierra Snow Lab, the primary snow laboratory in the Bay-Delta watershed. The model was demonstrated to perform well at this site. Finally, the model was designed to be distributed over a grid, which is precisely the intended application here.

6.3.2.2 UEB Model Overview

The UEB model has three state variables, U, the snowpack energy (kJ/m^2) relative to ice at 0°C, W, the snowpack liquid water equivalent (meters), and τ, the age of the snow surface which is used in albedo calculations. U and W obey the following equations:

$$\begin{aligned} \frac{dU}{dt} &= Q_{sn} + Q_{li} + Q_p + Q_g - Q_{le} + Q_h + Q_e - Q_m \\ \frac{dW}{dt} &= P_r + P_s - M_r - E \end{aligned} \qquad 6.3$$

where the terms in the energy balance equation are (all in $kJ/m^2/hour$):

Q_{sn}: net shortwave radiation,

Q_{li}: incoming longwave radiation,

Q_p: advected heat from precipitation,

Q_g: ground heat flux,

Q_{le}: outgoing longwave radiation,

Q_h: sensible heat flux,

Q_e: latent heat flux due to sublimation/condensation,

Q_m: advected heat removed by meltwater,

and the terms in the mass balance equation are (all in *m/hour* of water equivalence):

P_r: rainfall rate,

P_s: snowfall rate,

M_r: meltwater outflow from the snowpack, and

E: sublimation from the snowpack.

An illustration of the energy balance processes is shown in Figure 6.2, followed by a schematic of the UEB model's physics and parameterizations in Figure 6.3.

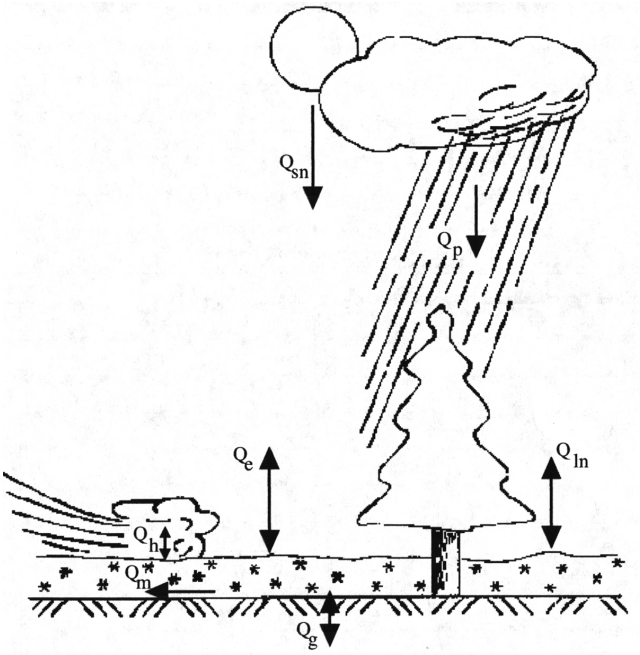

Figure 6.2 Energy fluxes involved in snowmelt and snowpack ablation (from Tarboton and Luce 1996).

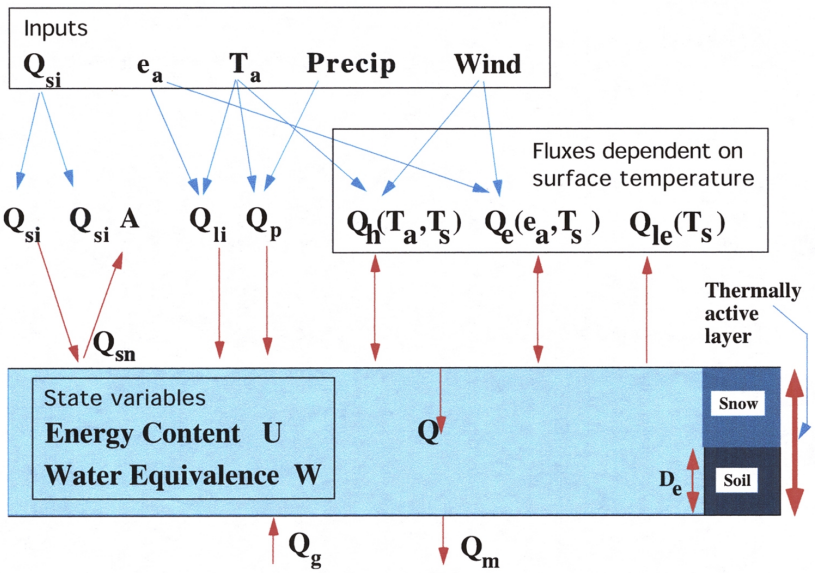

Figure 6.3 UEB snow model physics and parameterizations (from Tarboten and Luce, 1996).

Note that Figure 6.3 indicates that the model represents energy as the total energy in the snowpack, plus the energy in a portion (upper 40 *cm*) of the soil. This provides a simple approximation to the effect of ground temperature on snow. Q_g then represents the vertical flux of heat within the soil at a depth of 40 *cm*, and is taken to be zero in the absence of observations.

The other quantities in the model are determined based on the inputs, the values of the state variables, and configuration parameters using procedures to be described in more detail shortly. The configuration parameters include slope, aspect, latitude and forest canopy density, all derived and summarized for the model grid in Section 5.2. The model calculates all quantities at a time step sufficient to resolve the diurnal cycle; the largest such step, 6 hours, is used here. Since precipitation and

temperature are given as daily values, they must be interpolated to the diurnal cycle. Precipitation is distributed evenly over the day, while temperature is approximated as:

$$T(t) = \left(\frac{T_{\max} + T_{\min}}{2} \right) - \left(\frac{T_{\max} - T_{\min}}{2} \right) \cos\left(\frac{\pi t}{12} \right) \qquad 6.4$$

where $T_{\max}$ and $T_{\min}$ are the daily maximum and minimum temperatures, and t is the time in hours, with midnight being zero. This approximation applied to the 6 hour time step provides the highest average temperature between noon and 6pm, which is appropriate since temperature lags insolation by about 3 hours.

With the interpolated inputs, the UEB model calculates all components of the soil moisture budget and updates the state variables by solving the differential equations, Equations 6.3. This is very similar to the approach taken in the soil moisture component of the BDWM, except that instead of Runge-Kutta, the UEB model uses an Euler predictor-corrector solution (Gerald 1978). The outputs can include all state variables, as well as any of the values calculated at the diurnal cycle. This is particularly useful because radiation values determined by the UEB model are subsequently used to estimate evapotranspiration in the BDWM model.

In Appendix B, a discussion paralleling that of Tarboten and Luce (Tarboton and Luce 1996) details the methods used to determine the individual terms in Equations 6.3. Particular attention is given to the radiation calculations, since these are used again by the soil moisture component as mentioned.

6.3.2.3 Incorporation of UEB into BDWM

The fact that the UEB model is designed to function primarily under snowpack conditions means some adjustments were needed in order to use it in the BDWM model, which is intended to simulate a range of hydrologic conditions, including bare soil. In particular, the UEB model tends to simulate sublimation effects even when no snowpack is present (W=0). This would lead to a false reduction of rainfall amounts before they reach the soil. To remedy this, a judicious use of UEB outputs is required. In cases where W>0, the melt outflow from the model is used as Q_{in}, the surface water input to the soil moisture component. When W=0, the UEB output was ignored and the original precipitation input was used as Q_{in}.

Thus the original inputs are processed through the UEB component, yielding daily inputs to the soil moisture component which include the effects of snowpack. Other outputs of the UEB model which are used by the soil moisture component of the BDWM are net solar radiation, Q_{sn}, and incoming longwave radiation, Q_{li}. These quantities are used in the calculation of reference crop evapotranspiration, discussed in the next section. This will begin the description of the individual terms in the basic equation (Equation 6.1) for the soil moisture component.

6.3.3 Evapotranspiration

Evapotranspiration (ET) is the combined effect of evaporation, or the loss of moisture by vaporization directly from plant canopies or the soil, and transpiration, the movement of soil water into the atmosphere through plants. In California, ET accounts

for the fate of nearly 75% of the annual average 200 km^3 of precipitation (Kahrl, California Office of Planning and Research *et al.* 1979). There are several different methods for estimating ET, ranging from the rigorous, theoretical, and data-intensive to the empirical but more practical. The following discussion draws from Shuttleworth (Shuttleworth 1993).

6.3.3.1 The Penman-Monteith Method

One of the most physically-based approaches treats ET as a diffusion of water vapor driven by radiation and acting against two basic resistances, stomatal resistance (r_s) and aerodynamic resistance (r_a). Stomatal resistance represents the degree to which plants hold their water by keeping their stomata, small apertures in the leaf surfaces, closed. Plants open their stomata when they need to, releasing water vapor to the atmosphere and decreasing the effective stomatal resistance. The more leaf area plants have, the lower the effective stomatal resistance of the plant canopy, r_s. The aerodynamic resistance depends on wind speed V_f and plant canopy height, and represents the inverse of the atmosphere's competence in transporting water vapor away from the surface through turbulent diffusion, enhancing the vapor pressure deficit which allows more ET to occur.

Solving the equations representing the diffusion of water vapor including the effect of these resistances gives the physically-based Penman-Monteith Equation for ET in *mm/day* (Monteith 1965):

$$E = \frac{1}{\lambda}\left[\frac{\Delta A + \rho_a c_p D / r_a}{\Delta + \gamma\left(1 + r_s / r_a\right)}\right] \qquad 6.5$$

Several terms in this equation require explanation. First, c_p is the specific heat of moist air (1.013 *kJ/kg/°C*). Next, ρ_a is the density of air, given approximately (in kg/m^3) as a function of temperature and pressure:

$$\rho_a = 3.486\frac{P}{275 + T} \qquad 6.6$$

λ, the latent heat of vaporization of water is given by (in *MJ/kg*):

$$\lambda = 2.501 - 0.002361T \qquad 6.7$$

The vapor pressure deficit, *D* (in *kPa*), is given by:

$$D = e_s(T)(1 - RH) \qquad 6.8$$

where the relative humidity climatological values derived in Section 5.5.3 are used, and e_s, the vapor pressure (in *kPa*) is given as a function of temperature by:

$$e_s = 0.6108e^{\left(\frac{17.27T}{237.3+T}\right)} \qquad 6.9$$

Next, Δ is the rate of change of vapor pressure, e_s, with temperature (in *kPa/°C*):

$$\Delta(T) = \frac{4098\,e_s(T)}{\left(273.3 + T\right)^2} \qquad 6.10$$

γ, known as the psychrometric constant, has units of *kPa/°C*, and is given as a function of atmospheric pressure and latent heat of vaporization of water by:

$$\gamma = 0.0016286\frac{P}{\lambda} \qquad 6.11$$

Pressure as a function of altitude in meters is approximately

$$P(Z) = 101.3\left(\frac{293 - 0.0065Z}{193}\right)^{5.256} \qquad 6.12$$

for a stable atmosphere.

Finally, the energy available for evaporation, A, is the sum of some of the radiation fluxes discussed in the previous section:

$$A = \left(Q_{sn} + Q_{li} - Q_{le}\right) \qquad 6.13$$

with units of MJ/m^2 per 6 hours. The net solar radiation, Q_{sn}, and the incoming longwave radiation, Q_{li}, were determined over 6-hour time increments in the UEB model calculations. As mentioned, the longwave radiation emitted from the ground, Q_{le}, is not a reliable output of the UEB model. For ET calculations, Q_{le} is calculated based on the air temperature as:

$$Q_{le} = \varepsilon_g \sigma T_a^{\,4} \qquad 6.14$$

where the emissivity of the ground is taken as ε_g=0.99, and the daily temperature values interpolated to the diurnal cycle are used. The assumption implicit in this calculation is that the soil surface is effectively at air temperature. This will be a particularly bad assumption when snow is on the ground. For reasons which will be discussed later, this does not present a problem.

6.3.3.2 Reference Crop ET

Though Equation 6.5 provides a rigorous, physically-based approximation to ET, it requires detailed information about plant physiology and the effect of plant

canopies on the surrounding wind currents. Such information is not, in practice, available. The most common solution to this dilemma is to calculate a *reference crop* ET, E_{rc}, in which Equation 6.5 is computed using values of r_a and r_s which correspond to a specific, idealized reference crop: short (12 *cm*), actively growing grass. For the reference crop, the resistance values are (both in *s/m*):

$$\begin{aligned} r_s &= 69 \\ r_a &= \frac{208}{V_f} \end{aligned} \qquad 6.15$$

The effect of deviations from these specific values of the resistances in other plants are then parameterized in an empirically-determined multiplicative factor, the *crop coefficient*, K_c:

$$E = K_c E_{rc} \qquad 6.16$$

Substituting Equations 6.6, 6.15 and 6.11 into 6.5, and defining

$$\gamma^* = \gamma\left(1 + 0.33 V_w\right) \qquad 6.17$$

results in the equation for reference crop ET:

$$E_{rc} = F_1 A + F_2 D \qquad 6.18$$

where F_1 and F_2 are functions of temperature T, wind speed V_w, and elevation Z, and are given by:

$$\begin{aligned} F_1 &= \frac{\Delta}{\Delta + \gamma^*} \\ F_2 &= \left(\frac{\gamma}{\Delta + \gamma^*}\right)\frac{900 V_w}{T + 275} \end{aligned} \qquad 6.19$$

Equation 6.18 offers a rigorous, physically-based estimate of reference crop ET. The largest errors are introduced in the parameterization of variations due to different plants, Equation 6.16. This is an inevitable sacrifice in light of available data to characterize the various flora of the Bay-Delta watershed. Empirical crop coefficients are available for several types of land cover, however, and the combination of these coefficients, the meteorological input data and Equations 6.16 and 6.18 should provide a satisfactory representation of the magnitude and variability (heterogeneity) of ET throughout the watershed.

In any case, the most notable deficiency in this treatment is not the empirical treatment of plant effects, but is instead the limited treatment of atmospheric effects. In fact, the lack of understanding about the atmospheric boundary layer is the limiting factor in most treatments of ET (Brutsaert 1988). Until the BDWM can be coupled with a suitable atmospheric model, however, the present circumstances must suffice.

6.3.3.3 Crop Coefficients

To provide values of K_c for each model element which represent the seasonal cycle in plant canopy effects, monthly crop coefficients for four classes of landcover were compiled (Saxton and McGuinness 1982; Maidment 1993). These annual K_c curves are shown in Figure 6.4.

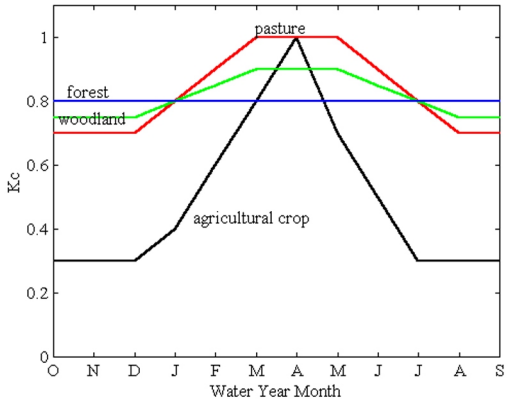

Figure 6.4 Crop coefficients for 4 major landcover classifications.

These are very broad categories, and significant variation would in fact be present within each of them (particularly agricultural crops), but the intent here is only to capture broad variations in ET due to landcover variability. The four categories were mapped to the model grid using the categories of landcover shown in Figure 5.16 as follows:

1) agricultural crop: all “cropland” categories and “irrigated land”

2) pasture: “grassland” category

3) woodland: “open woodland grazed”

4) forest: all “forest” categories

The tiny fraction of the watershed categorized as desert and urban areas were assigned high crop coefficients (K_c=1.3), to allow whatever moisture is in the soils of those areas to evaporate.

6.3.3.4 Forest Canopy Interception

Plants, especially trees, have an additional effect on ET, as the plant canopy intercepts precipitation and holds it until it melts and falls to the ground (in the case of snow) or evaporates (rain). Estimates of the total rainfall evaporated in this manner from forests with complete coverage (canopy density = 1) range from 10% to 30%, depending on the interception capacity of the canopy, the particular character and frequency of storms, and consequently on the local climate (Shuttleworth 1993). The BDWM's estimate of rainfall losses due interception evaporation is 25% of the daily rainfall (where rainfall is the liquid portion of the daily precipitation as calculated by the UEB snow component, Section 9.3), times the forest canopy density (Section 5.4, Figure 5.17). While there is a good deal of uncertainty in this estimate, it should provide a reasonable representation of the magnitude and especially the heterogeneity of interception effects as they depend on landcover.

6.3.3.5 ET Implementation

Using the above reference crop formulation with the 6-hourly inputs of temperature and radiation from the snow model component, ET is estimated for all model elements for the two 6-hour intervals from 6am-noon and noon-6pm, since these essentially comprise the period of the day when ET takes place. The sum of the two 6-hour ET values for each model element is taken as the ET demand placed on the soil matrix in that element for that day. If snow is present on the soil surface of the

element, the ET demand is set to zero, since evaporation from the soil matrix will not occur through snow, and transpiration is typically very small in snowy conditions.

When snow is not present, to satisfy the ET soil matrix demand, water is first removed from the element's upper layer soil moisture. In general, the soil moisture content acts to limit ET from the soil. Here, this attenuating effect is treated as linearly proportional to the relative soil moisture content:

$$ET_1 = K_c E_{rc} \frac{\Theta_1}{\Phi_1} \qquad 6.20$$

The remaining ET demand then acts on the lower layer, in the same soil moisture-limited fashion:

$$ET_2 = \left(K_c E_{rc} - ET_1\right) \frac{\Theta_2}{\Phi_2} \qquad 6.21$$

Evapotranspiration is the only process which removes water from the soil matrix, other than water entering the stream network. The remaining components of the soil moisture budget involve mass-conserving water movement over and through the soil.

6.3.4 Surface Runoff

The BDWM's treatment of surface runoff is simple and intuitive, following a "bucket model" approach. All rain and snowmelt in excess of the upper soil layer's available storage capacity becomes runoff:

$$Q_{SR} = \begin{cases} Q_{in} - \left(\Phi_1 - \Theta_1\right) & \text{for } Q_{in} \geq \Phi_1 - \Theta_1, \\ 0 & \text{otherwise} \end{cases} \qquad 6.22$$

This assumes homogeneity of soils within each 16 km^2 model element. In this quasi-distributed approach, the heterogeneity of each river basin is represented at and above this resolution.

6.3.5 Percolation

The representation of percolation used in the BDWM has already been developed in detail in Section 5.3.5.2. It is derived from experiments originally by Holtan (Holtan 1961), and is characterized by 3 parameters, C_p, m_p and f_c. Units of C_p and f_c are mm/day, and m_p is dimensionless. These parameters were derived and summarized for the watershed in Sections 5.3.5 and 5.3.7 (Figure 5.15). Additionally, the percolation process is limited by the relative soil moisture content of the upper layer, $\frac{\Theta_1}{\Phi_1}$:

$$Q_{PC} = \left[C_p \left(1 - \frac{\Theta_2}{\Phi_2} \right)^{m_p} + f_c \right] \left(\frac{\Theta_1}{\Phi_1} \right) \qquad 6.23$$

with the constraint: $0 \leq Q_{PC} \leq \Phi_2 - \Theta_2$

so percolation does not exceed the lower layer's available soil moisture capacity.

6.3.6 Interflow, Baseflow and Groundwater Seepage

The theoretical basis for the treatment of the subsurface horizontal flows (interflow in the upper layer and baseflow in the lower layer) in the BDWM is the homogeneous form of the Buckingham-Darcy Equation (Equation 5.5) using the hydraulic conductivity parameterization in Equation 5.4. The resulting equation is:

$$Q_{horiz} = -K_{sat}\left(\frac{\theta}{\varphi}\right)^{2b+3}\overline{\left(\frac{dz}{dx}\right)} \qquad 6.24$$

where $\overline{\left(\frac{dz}{dx}\right)}$ is the tangent of the average slope for the model element (Figure 5.5). Aggregate values K_{sat} (in *mm/day*) and $m_k \equiv 2b+3$ (dimensionless) were determined for the upper and lower layers of each model element in Sections 5.3.4 and 5.3.7, and summarized in Figure 5.13 and Figure 5.14.

It is also true that $Q_{horiz} = \Phi\upsilon$, where Φ is porosity and υ is the *seepage velocity*, or the actual velocity (in *mm*/*day*) with which the horizontally moving water moves through the soil matrix. The maximum distance water will travel to reach the stream network in a day, here called the *contributing distance*, is therefore:

$$\triangle x = \frac{Q_{horiz}}{\Phi} \quad \text{in } mm \qquad 6.25$$

The ratio of length of stream bed in an element to the element's area is here referred to as the *stream bed density*, α_{SB}. It is related to the stream network density, $\mathcal{D}$, as follows:

$$\alpha_{SB} = \frac{2\mathcal{D}}{10^6} \quad \text{in } mm^{-1} \qquad 6.26$$

where $\mathcal{D}$ is the total stream length divided by the catchment area in km^{-1}, presented for the model grid in Section 5.4 (Figure 5.18). The factor 2 accounts for both sides of a stream through which water reaches the stream, and the factor 10^6 converts from km^{-1} to mm^{-1}.

Multiplying the contributing distance by the stream bed density gives the element's fractional area which produces horizontal contributions to stream flow in a

day, and multiplying this by the moisture content of the element gives total streamflow contributions due to horizontal subsurface flow in a day:

$$Q_{subsurface} = \alpha_{SB}\Theta_{\Delta}x = \alpha_{SB}K_{sat}\left(\frac{\Theta}{\Phi}\right)^{m_k+1}\overline{\left(\frac{dz}{dx}\right)} \qquad 6.27$$

The resulting expressions for subsurface contributions in the BDWM are then:

$$Q_{IF} = \alpha_{SB}K_{sat1}\left(\frac{\Theta_1}{\Phi_1}\right)^{m_{k1}+1}\overline{\left(\frac{dz}{dx}\right)} \qquad 6.28$$

and

$$Q_{BF+GL} = \alpha_{SB}K_{sat2}\left(\frac{\Theta_2}{\Phi_2}\right)^{m_{k2}+1}\overline{\left(\frac{dz}{dx}\right)} \qquad 6.29$$

In the lower layer, however, not all of the water in Equation 6.29 will reach the streambed. A fraction of it will be lost by seepage into deeper aquifers. Some of this water will be returned to the stream network on much longer time scales, and some will remain in confined aquifers unless extracted by artificial means. The effects of these deeper aquifers are the domain of deep groundwater models, a subject very interesting in its own right but not addressed here. Groundwater seepage is regarded as a loss in the BDWM, and the fraction of baseflow lost to this process is based on the fractional area not underlain by aquifers, data presented in Section 5.4 (Figure 5.19). The formulae for baseflow entering the streams, Q_{BF}, and water lost to groundwater seepage, Q_{GL}, are:

$$Q_{BF} = Q_{BF+GL}\ \beta_{\text{no aquifer}} \qquad 6.30$$

$$Q_{GL} = Q_{BF+GL}\left(1-\beta_{\text{no aquifer}}\right) \qquad 6.31$$

Future versions of the BDWM may account for long-term streamflow contributions from aquifers, as this area has relevance to climate studies. For now, this completes the formulation of soil moisture processes in the BDWM.

6.3.7 Stream Network Routing

Equation 6.2 gave the total contributions to the stream network as the sum of horizontal surface and subsurface flows. That equation is restated here:

$$Q_{chan} = Q_{SR} + Q_{IF} + Q_{BF} \qquad 6.32$$

The last process in the generation of river basin outflow is the routing of flows through the stream network. This process differs from all others described in this chapter in that the flows being routed are aggregate flows at the level of the river basins shown in Figure 3.2, and the results represent daily outflow estimates for each of these 15 basins.

The river channels within a basin act to delay and smooth out contributions from surface and subsurface flows. Peak flows are thus reduced, and storm flows are extended days after the storm has ended. There are many methods available for simulation of these effects, which, similarly to hydrologic models, can be categorized as lumped and distributed. The distributed methods typically require detailed data on channel characteristics such as cross-sectional area at many locations throughout the network. These methods are designed for much greater accuracy than required by the present study.

Lumped routing methods have for some time been the most popular in common practice (*e.g.*, McCarthy 1938). These typically represent the effects of rivers by dividing a network into reaches, with the sequence of reaches progressing from the headwaters to the basin outflow. Each reach then has a storage *S*, representing the water contained in that reach at a given time. The manner in which water is transferred from each reach to the reach downstream of it at each time step differentiates the various lumped methods.

The method employed here is derived from Georgakakos and Bras (Georgakakos and Bras 1982), and divides each river basin into an upper and a lower reach. The coupled equations for storage in the two reaches of a given river basin are:

$$\frac{dS_1}{dt} = \sum Q_{chan} - \alpha_{chan} S_1 + \sum_j Q_{out}^j$$
$$\frac{dS_2}{dt} = \alpha_{chan} S_1 - \alpha_{chan} S_2 \qquad 6.33$$

where the subscripts 1 and 2 denote the upper and lower reaches, respectively, and α_{chan} is the *storage transfer coefficient*, with units of *days*$^{-1}$. The sum $\sum_j Q_{out}^j$ denotes all outflows from upstream basins. This sum is zero for mountain headwater basins. The sum $\sum Q_{chan}$ denotes the sum of flow contributions (Equation 6.32) over all elements in a given river basin. The total routing system for the entire Bay-Delta watershed is therefore comprised of 15 sets of Equations 6.33, with 30 storage elements.

The coefficient α_{chan} represents the inverse of the characteristic storage time in each of the reaches. Autocorrelation calculations using observed inflows and outflows

from each of the river basins showed peak correlations at 1-2 days for all basins. The value of α_{chan} used here is 1 day^{-1} for all basins. A more rigorous development of this aspect of the watershed's hydrology may some day be undertaken, but this formulation is quite sufficient for the purposes of this study.

The outflow from each of the 15 river basins in *mm/day* is given by the outflow from the basin's lower reach:

$$Q_{out} = \alpha_{chan} S_2 \qquad 6.34$$

One final note on flow routing—in some applications where only the local basin's behavior is being studied, the term $\sum_j Q_{out}^j$ representing inflows from upstream basins will be omitted from the routing equations (Equations 6.33). In such cases, this modification will be noted.

6.3.8 Summary of Model Components

The BDWM takes daily inputs of precipitation and maximum and minimum temperature which have been interpolated to the model grid. The UEB snow component interpolates these inputs to a 6 hour diurnal cycle and generates snow melt estimates. The combination of rainfall and snowmelt serves as input to the soil moisture component of the BDWM, whose state variables are soil moisture content in the upper and lower layers of each model element. Using the same diurnal radiation and temperature estimates as the UEB model (with the exception of longwave outgoing radiation), the soil moisture component estimates evapotranspiration based

on soil moisture and land cover properties. Estimates of surface runoff, percolation, interflow, baseflow and groundwater seepage are also generated based on soil and topographic properties, stream density, aquifer distribution, and basic hydrologic theory.

All aspects of the soil moisture budget thus estimated for a given day, soil moisture is updated using Equations 6.1 with a 4^{th}-order Runge-Kutta procedure. An adaptive time step is employed such that the amount of rain/snowmelt processed in a given time step does not exceed 2 *mm*. This avoids instabilities which may arise due to the highly nonlinear behavior of soil moisture (Georgakakos and Baumer 1996). Enough time steps are thereby taken to update the state variables over the daily time step of the BDWM.

Streamflow contributions from surface and subsurface flows are then summed over all model elements in a given river basin, and routed through a river routing model. The final result is the estimate of daily outflow for each of the 15 river basins. The total watershed outflow is then the sum of the two lower valley outflows and the Cosumnes/Mokelumne outflow:

$$Q_{out}^{TOT} = Q_{out}^{SAC3} + Q_{out}^{MOK} + Q_{out}^{SJQ2} \qquad 6.35$$

This quantity represents the BDWM estimate of unimpaired inflows to the estuary, and is thus the linkage point between the estuary and watershed components of the combined U-P/BDWM model.

6.4 Initial Model Performance and Refinements

The interpolated fields of daily precipitation and daily maximum and minimum temperatures presented in Section 5.5 were used to drive the Bay-Delta watershed model over the period WY 1965 - WY 1987. The precipitation field used was generated by kriging with no trend, which gave the smallest errors of all the methods. Two methods of temperature trend estimation yielded indistinguishably good results, the regional monthly and the local daily methods. These were both used with the same precipitation input to generate two separate model runs for comparison. Inputs to the routing component from upstream basins (Equation 6.33) were set to zero, so the model output represents local contributions only. These are compared to the estimates of unimpaired local contributions from Section 3.4 to evaluate model performance.

6.4.1 Results for Water Years 1965-1987

Figure 6.5 shows the mean annual hydrographs simulated with local daily temperature trend data. The most notable feature of these simulations is the poor representation of the snowmelt portion of the hydrograph (April-July) for most Sierra basins. The results using the regional monthly temperature trend data (not shown) were almost identical to Figure 6.5 with the same poor snowmelt generation.

These results suggest two non-exclusive possibilities: interpolated precipitation is too low at higher, snowpack-bearing elevations, and temperature is too high at those elevations during the snowpack accumulation season, December-April.

The rainfall runoff portion of the hydrograph, from December-March, shows much better performance with accurate estimates of the timing and magnitude of rainfall runoff peaks in the mean hydrographs. The most notable exceptions are the Yuba and Cosumnes/Mokelumne basins (valley basin natural flow estimates are corrupted by agricultural signals, so it is difficult to evaluate performance there). The Yuba basin has a major reservoir (New Bullards) whose effects could not be accounted for in the natural flow reconstruction, so it is not unreasonable to expect the higher simulated flows there. The Cosumnes/Mokelumne basin outflows were reconstructed with stations significantly upstream from the basin outflow (Figure 3.3), so it is likely that some flow contributions are missing from the reconstruction.

The final major shortcoming apparent from these results is the failure of the model to represent deep groundwater contributions, most evident during the dry season, August through November. This is most apparent in the Shasta basin, which has volcanic aquifers contributing substantial flow throughout the dry season. The lack of accounting for such flows was discussed in Section 6.3.6 above, and is expected in the present version of the BDWM.

The most important shortcoming of model performance for the present study is the failure to properly represent snowmelt. The possibility has already been suggested that the accumulation and melt of snowpack play a role in propagating large-scale climate signals into the watershed/estuary system (Sections 3.5 and 3.7). A reasonably accurate representation of snowpack is therefore crucial.

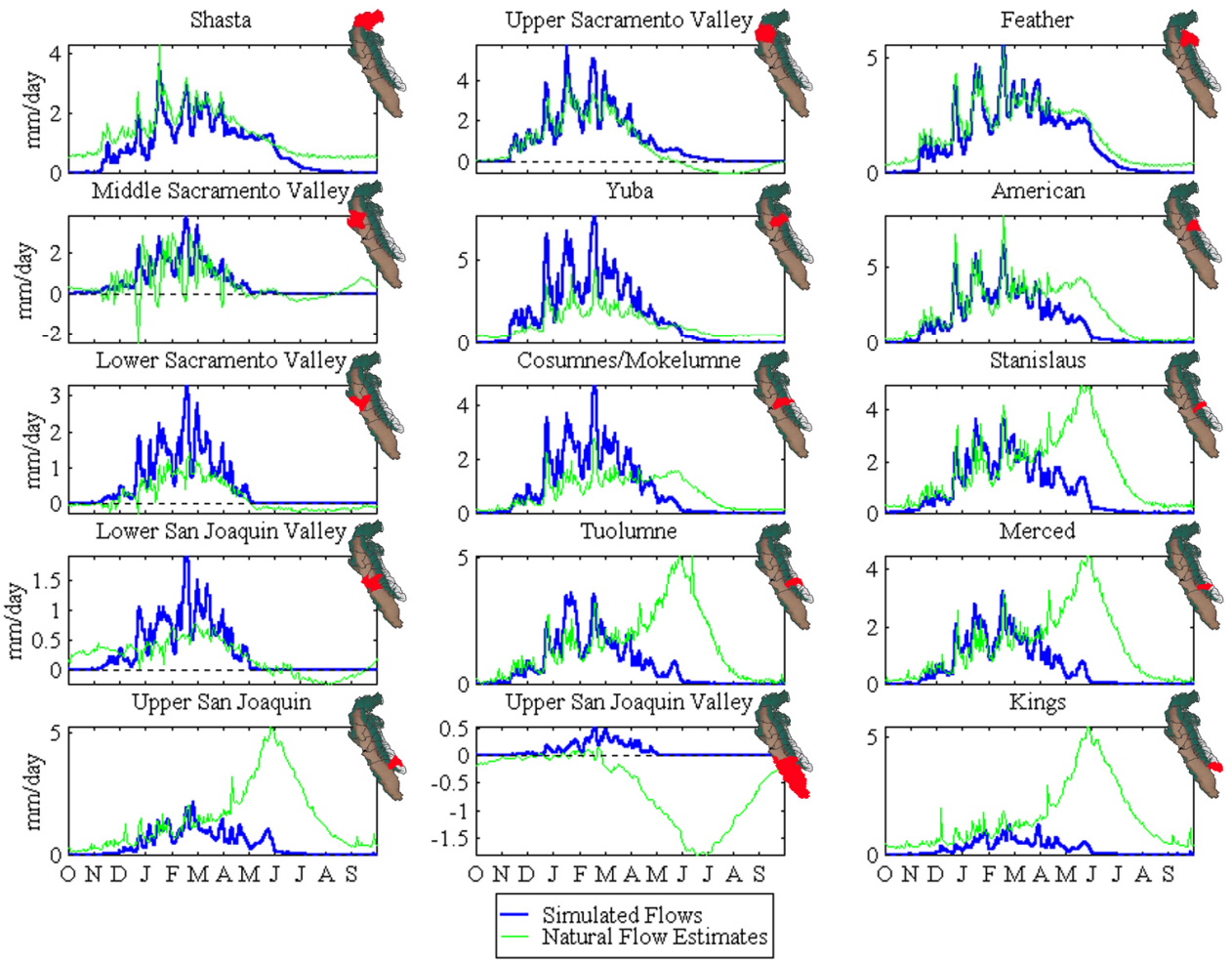

Figure 6.5 Simulated mean annual hydrographs using ordinary kriging precipitation estimates and temperature kriged with a local linear elevation trend.

The fact that the BDWM appears to simulate flow from rainfall runoff quite well suggests that the basic model formulation is sound. It is no surprise that the failure to simulate snowpack is a result of poor temperature and precipitation inputs at the higher elevations of the watershed. The fact that both precipitation and temperature exhibit clear elevational trends was demonstrated in Section 5.5. None of the trend-based methods for precipitation yielded optimal results at the available stations, and the best trend-based results for temperature showed some degradation of accuracy at higher elevations. Further, the paucity of high-elevation stations for both quantities suggests that trends calculated from observed data (Figure 5.26 and Figure 5.31) may be unreliable at higher elevations.

6.4.2 Corrections to High-Elevation Precipitation and Temperature

It is likely that precipitation based on kriging with no trend significantly underestimates high-elevation precipitation, and that this is primarily responsible for the lack of simulated snowpack. Figure 5.27 suggests that significant bias may exist as low as 1.5 *km*. Many scenarios of increasing precipitation above this altitude were tried, however, and while all increased snowmelt runoff from April-July, rainfall runoff during December-March always increased unreasonably as well. Therefore, it was also necessary to correct the high-elevation temperature fields.

Temperatures at lower altitudes are strongly affected by heating from the ground and local processes, while as elevation increases, temperatures are more directly determined by conditions in the free atmosphere. This is particularly

important during the hydrologically important period when snowpack is present at the higher altitudes, as the high albedo of snowpack decreases heating of the atmosphere from below. Comparisons of upper air sounding temperature data from Oakland, California (the same data set used to determine wind speed and relative humidity climatologies in Section 5.5.3) show that though daily temperatures at various altitudes up to 2 *km* in the atmosphere above Oakland and the interpolated temperatures at the corresponding altitudes throughout the watershed are strongly correlated (r>0.90 at all altitudes in all river basins except Shasta, where r>0.80), the watershed temperatures are consistently warmer by about 7°*C*. This suggests that the interpolated temperature field, based on data from primarily low-altitude sensors, would tend to overestimate temperatures in the higher altitudes of the watershed where free-atmosphere conditions have more influence.

Additionally, the free atmosphere itself often exhibits markedly different behavior at higher elevations. The storms which provide California's water typically evolve as cold Arctic air flows off the Asian continent: "…cold polar air masses invading the Pacific Ocean from continental areas are made unstable and increasingly moist by warming from below…. In the modification of the cold polar air masses as they pass southward over the warmer waters of the Pacific Ocean, the air temperatures in the lower layers are raised…" (U.S. Weather Bureau and U.S. Army Corps of Engineers 1942). The air which reaches California is modified in its lower layers by oceanic conditions, whereas the upper altitudes are less altered by the ocean.

These considerations suggest that a combined correction of the higher-elevation precipitation and temperature fields affecting snowpack is needed. The precise distribution of the corrections with elevation and time is difficult to determine. Figure 5.33 demonstrates a degradation of correlation of interpolated temperatures with observations above 2 *km*. Several combinations of adjusted lapse rates for precipitation above 1.5 *km* and temperature above 2 *km* were evaluated, and did lead to more snowmelt. However, increased precipitation with only slightly decreased temperatures typically led to greatly increased rainfall as well as snowmelt runoff, while increased precipitation with still cooler temperatures typically shifted the timing of snowmelt peak later in the year than was observed. It appears that the strong sensitivity of the snowpack to changes in these inputs requires that the corrections be more subtle.

Among the many methods tried for correcting temperature, the most promising was to replace the calculated elevational trends above 2 *km* in the local daily trend method with a dry adiabatic lapse rate of -9.8°*C/km*. The resulting anomaly field was then kriged as usual, and the results above 2 *km* were used in place of the results from the local daily trend method with no correction. This approach generated significantly increased snowpack without introducing errors in the timing of the snowmelt peak, and with minimal increases in rainfall runoff.

To determine corrections to the high-elevation precipitation, a tracer capability was implemented in the BDWM in which a parcel of water entering the stream network in each basin was “tagged” according to the elevation at which it entered.

This was done for all water entering the streams, which was then traced to the basin outflow. Thus the composition of a river basin's simulated outflow in terms of its elevational source distribution was determined. The elevational compositions of the river basins' mean annual hydrographs (Figure 6.5) were simulated using the corrected temperatures as described in the previous paragraph and are shown in Figure 6.6.

The elevational compositions of the hydrographs show clearly how elevational characteristics of the river basins shape their respective hydrographs. The strong snowmelt peaks of the southern Sierra are sourced entirely from the highest elevations (above 2 *km*) in those basins. It is the elevational distribution of these flows which help estimate the necessary corrections to the precipitation field.

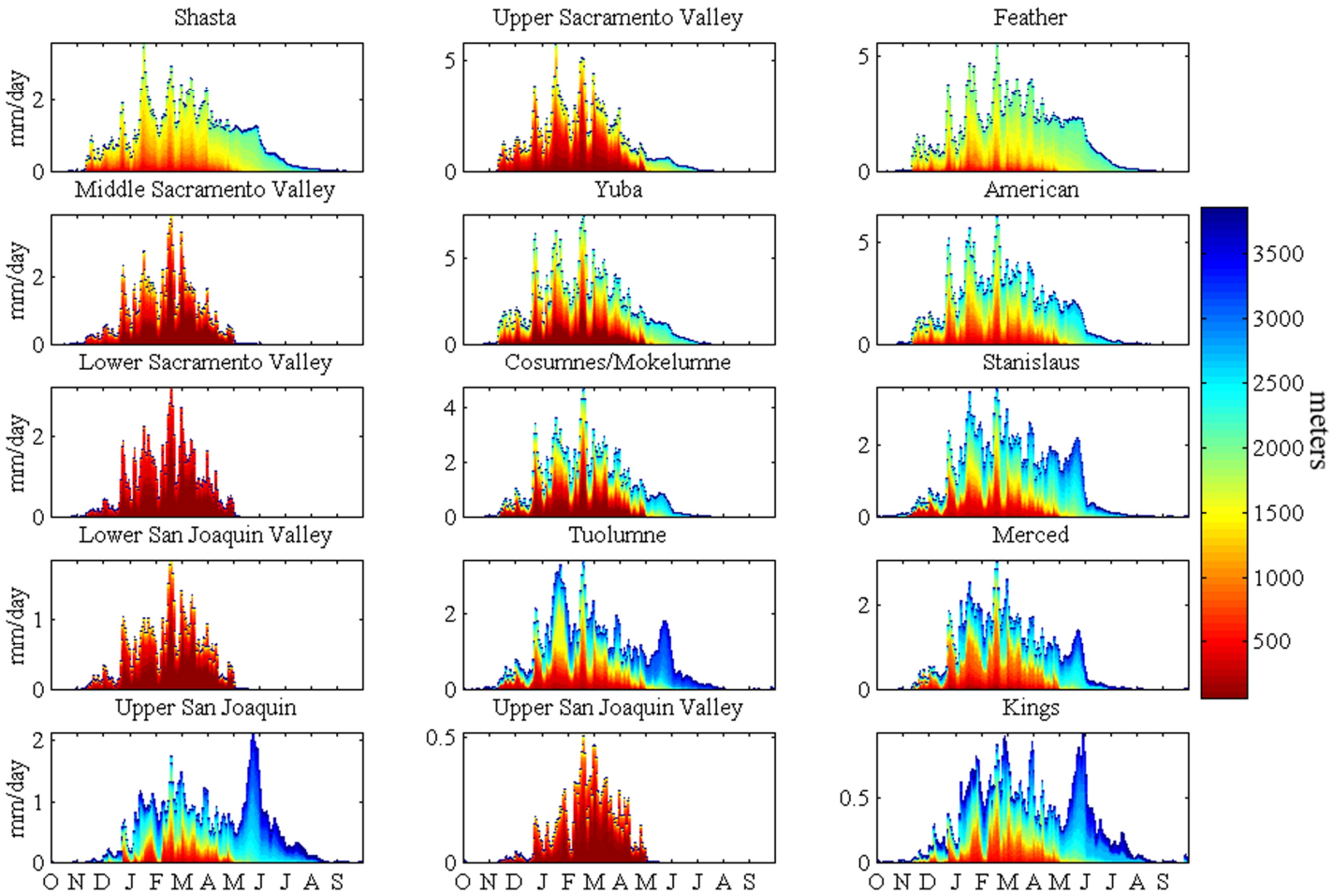

Figure 6.6 Elevational dependence of simulated outflow using temperature fields with adjusted lapse rates above 2 *km*. The color composition of the hydrographs represents the elevation at which water reaching a basin's outflow originally entered its stream network.

The estimates of runoff, categorized by elevational source, were used to estimate multiplicative precipitation correction factors for each elevation band in basins for which precipitation corrections seemed appropriate, based on the differences between the basins' simulated and estimated "actual" annual mean hydrographs. These were the American, Stanislaus, Merced, Upper San Joaquin and Kings river basins. The formula for the corrections in a given basin is:

$$\alpha_P(z) = \frac{1}{\sum_{d=1}^{365} Q_{sim}(d,z)} \sum_{d=1}^{365} \left(\frac{Q_{obs}(d) - \sum_{z=1}^{1500} Q_{sim}(d,z)}{Q_{sim}(d,z) - \sum_{z=1}^{1500} Q_{sim}(d,z)} \right) \qquad 6.36$$

such that

$$P_{new} = \alpha_P P_{old}$$

where P_{new} is the corrected precipitation, and P_{old} the original data generated using ordinary kriging. $Q_{sim}(d,z)$ is the simulated basin outflow on day d which was traced from its origin at altitude z (in meters), and $Q_{obs}(d)$ is the "observed" natural flow estimate for day d. The total simulated flow under 1.5 *km* is subtracted from both "observed" and simulated flows before taking their ratio, as only precipitation above 1.5 *km* is being corrected.

After calculating precipitation corrections, the model was re-run with the corrections. This procedure was iterated, converging quickly on the optimal precipitation corrections for the given temperature field. After a few iterations using the corrected temperature field described previously, the annual mean hydrographs converged to those in Figure 6.7.

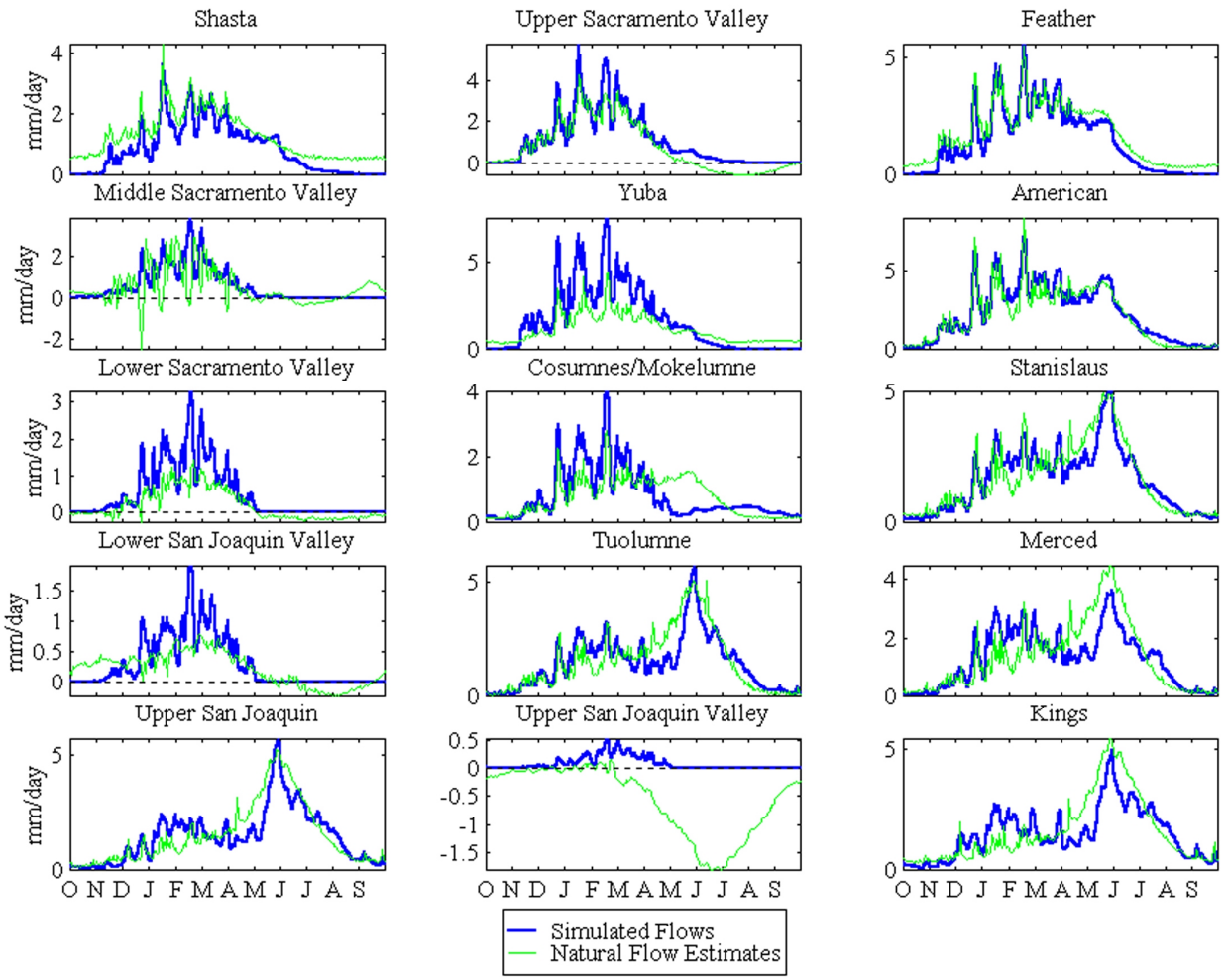

Figure 6.7 Simulated annual mean hydrographs using corrected high-elevation temperatures and precipitation. Compare to Figure 6.5.

With the temperature and precipitation fields corrected at high elevations to provide better representation of snowmelt runoff, model performance is greatly enhanced. With only moderate increases in rainfall runoff, snowmelt runoff is much closer to reconstructed values. The great difference in the hydrographs of Figure 6.5 and Figure 6.7 highlights the importance of these upper elevation regions in shaping the watershed's hydrology and ultimately the Bay's behavior. The correction factors α_P, along with the mean corrected precipitation field are shown in Figure 6.8 (compare to Figure 5.28).

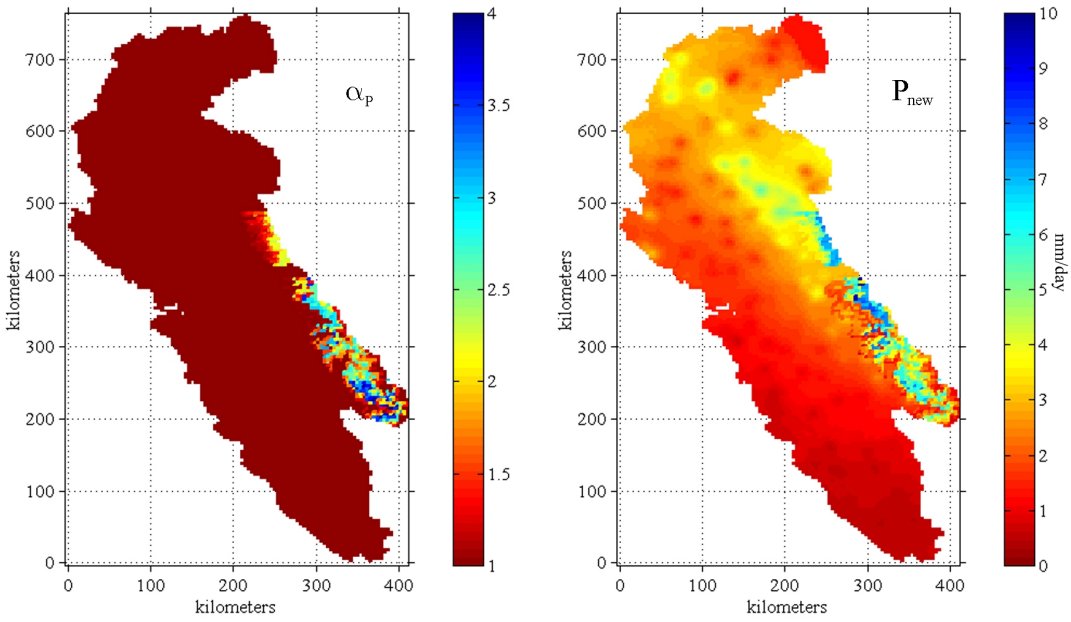

Figure 6.8 Precipitation correction factors and mean corrected precipitation field.

6.4.3 Additional Evaluation of Improved Model Performance

6.4.3.1 Flows

While the model's representation of the mean annual hydrographs is greatly improved, performance over the course of the simulated time series WY 65-87 has not been assessed. Figure 6.9 shows the total outflow from the northern and southern headwater basins as categorized in Figure 3.7. Both simulated and reconstructed natural estimates are shown.

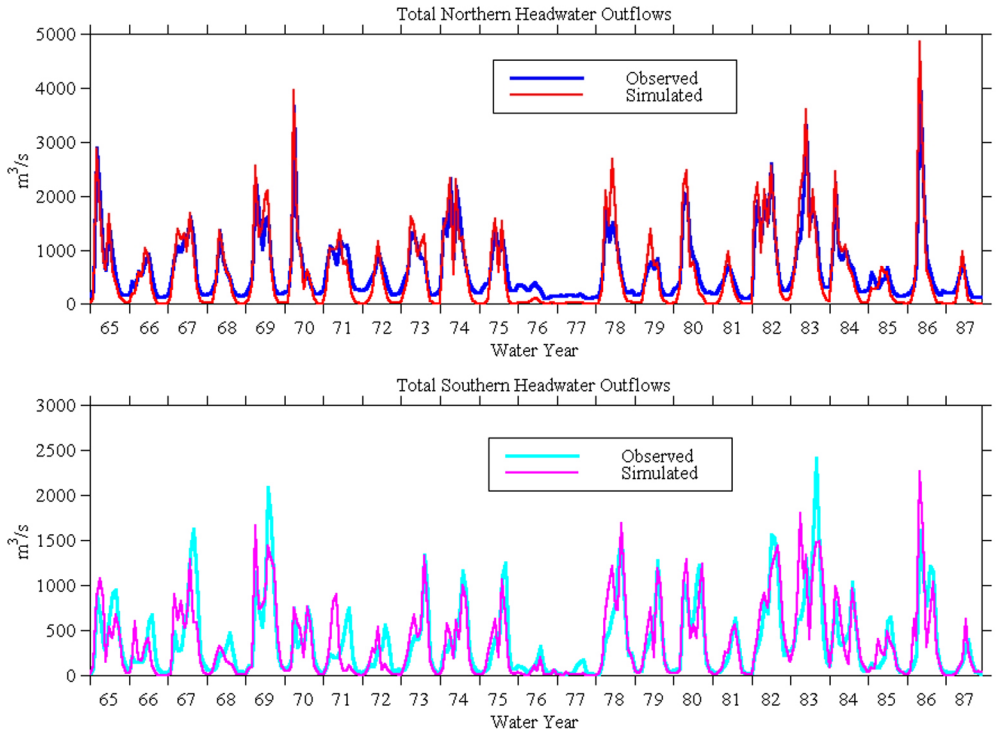

Figure 6.9 Comparison of simulated and "observed" monthly mean flows for the northern and southern headwater basins.

The performance in the northern headwaters appears quite good over the entire record. The lack of simulated dry-season flow sourced from deep groundwater

discussed previously is the most notable exception. Year-to-year variations in flow magnitude and timing in the northern basins appear to be captured quite well by the model. In the southern basins, the magnitude of yearly flows is again captured well. The timing of simulated flows in the south is generally acceptable, though there are several exceptions, especially prior to 1973. It is worth noting that until 1969, the highest meteorological gauge site in the EarthInfo data set for the southern Sierra was at an elevation of about 2.4 *km*. From 1969-1975, the highest site was at 2.6 *km*, and after 1975 the highest site was at about 2.8 *km*. This progressive increase in data coverage at high elevations may be partially responsible for the increased quality of the simulation after the early 70's.

The above discussion qualitatively evaluates model performance during the period used to generate corrections to the precipitation and temperature data, WY 65-87. Performance should also be evaluated using data outside of this period. The simulation was extended to include WY 49-95 (the extended run is discussed further in Chapter 7), and correlations with monthly natural flow estimates obtained from the California Center for Data Exchange (http://cdec.water.ca.gov/) for the periods before and after the period used to correct the inputs were calculated (Table 6.1).

These data show excellent agreement at the monthly time scale in the northern headwaters, with worse performance in the south. The nature of the degraded performance in this region is better understood by generating similar correlations between simulated and observed timing and magnitude of the annual flow hydrographs (Table 6.2). These data indicate excellent performance simulating the

annual flow magnitudes in both regions, as well as simulating annual flow timing in the north. In the San Joaquin headwaters, simulation of flow timing in the latter part of the record is also very good, while correlations are much lower in the early part of the record. This result seems to support the hypothesis that increased high-altitude observations in the last few decades result in significantly improved estimates of precipitation and temperature, which enable the model to more accurately simulate snowpack and its impact on flow timing. This also highlights the critical importance of these high-altitude stations.

Table 6.1 Correlations between simulated and reconstructed natural flows for monthly data in the northern and southern headwater basins.

	Monthly, WY 49-64	Monthly, WY 88-95	Monthly, both periods
Sacramento headwaters	0.96	0.97	0.96
San Joaquin headwaters	0.78	0.70	0.75

Table 6.2 Correlations between simulated and reconstructed natural flow annual magnitude and timing for monthly data in the northern and southern headwater basins.

	Monthly, WY 49-64	Monthly, WY 88-95	Monthly, both periods
Sacramento magnitudes	0.99	0.99	0.98
Sacramento timing	0.94	0.97	0.94
San Joaquin magnitudes	0.98	0.995	0.98
San Joaquin timing	0.74	0.98	0.76

6.4.3.2 Snowpack

The hydrographs of Figure 6.7 give reasonable representations of snowmelt runoff, suggesting that with the high-elevation precipitation and temperature corrections, the mean annual behavior of the snowpack is being adequately represented. However, the results of the previous section reveal some problems in the simulated time series which appear to be due to poorly simulated snowpack. An additional check of model performance is available in the form of snowpack data.

As part of its duties in managing the State's water supply, the California Department of Water Resources collects daily snowpack data at several sites throughout the State. Those sites in the Bay-Delta watershed are shown in Figure 6.10.

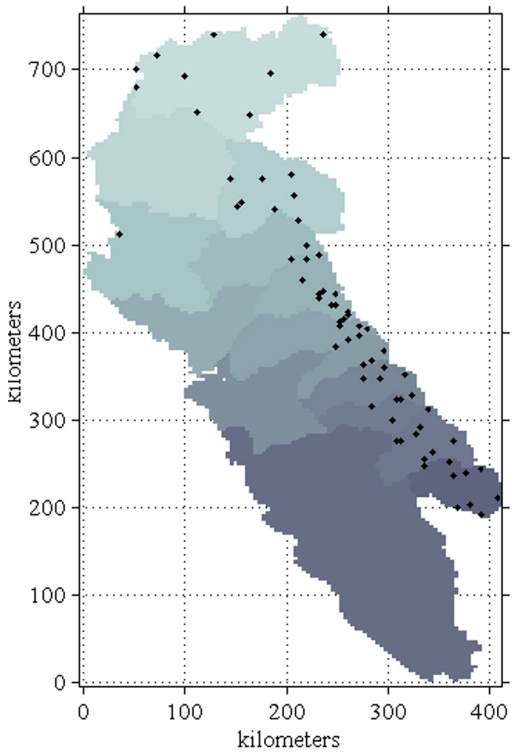

Figure 6.10 Location of DWR snow sensors. Shading represents river basin delineations.

Data at some stations extend back to the early 70's, but most of the stations only have data from the late 70's on. Data describing the daily liquid water depth equivalent (LWE, in *mm*) of snowpack at these 70 sites were compared to simulated snowpack LWE at the model element most closely corresponding to each snow sensor's location. Snowpack exhibits significant variability at scales smaller than the model resolution (due to wind-induced drifting and landcover effects), and it is therefore expected that this will introduce significant sampling error into the analysis. Nonetheless, taken as a whole this data offers an additional means of evaluating model performance.

Three measures of the differences between observed and simulated LWE are shown in Figure 6.11—mean error, RMS error and correlation coefficient. Results are shown from the simulations using the "local daily" and "regional monthly" trend methods with original ordinary kriged (OK) precipitation, as well as the version of "local daily" temperature with a dry adiabatic lapse rate (~-10 *°C/km*) above 2 *km* and corrected OK precipitation as described above. The statistics are plotted versus latitude to show the distribution of error along the mountain ranges.

The corrections to precipitation and temperature clearly provide improved simulation of snowpack over the uncorrected methods. The "local daily" runs outperformed the "regional monthly" runs in RMS error and correlation, though they were more nearly equal in mean error. They both appear to consistently underestimate snowpack in the southern Sierra, a result in agreement with the hydrographs of Figure 6.5.

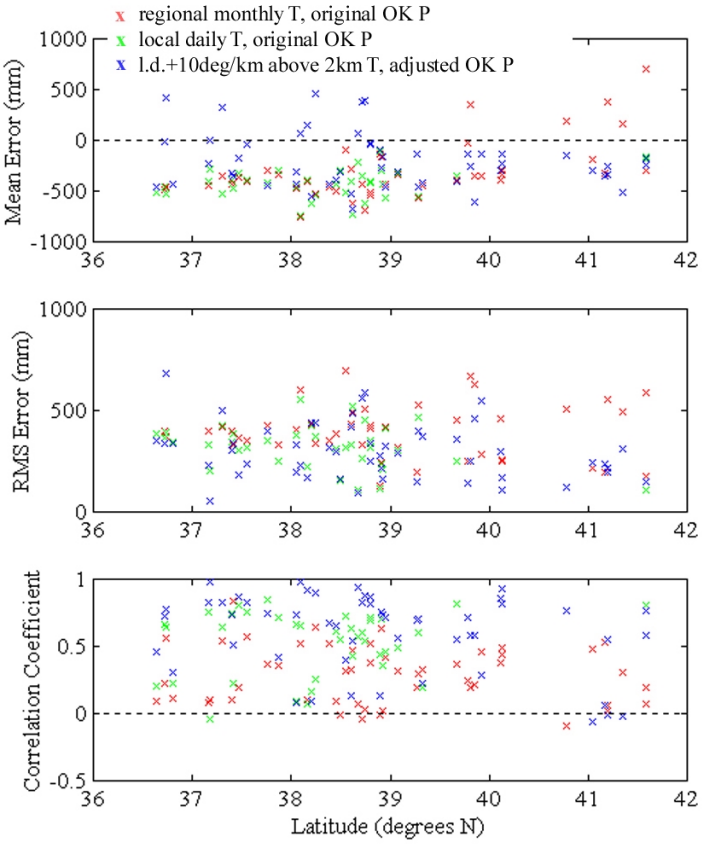

Figure 6.11 Errors of simulated snowpack liquid water equivalence. Simulations used differing temperature (*T*) and precipitation (*P*) inputs, as indicated in the legend.

The simulation using the corrected inputs gave improvement in all measures. Though mean errors still appear large in the southern Sierra, they are not consistently biased positively or negatively, suggesting the model is simulating snowpack more accurately in those basins.

Though the corrected precipitation and temperature fields appear to provide reasonably accurate results, it is difficult to estimate how much the corrections represent reality and to what degree they are simply a calibration. Given the uncertainty inherent in the natural flow reconstructions used for comparison, true

quantitative evaluation of model performance is quite difficult. The fact that simulated snowpack appears to be more accurate is encouraging, but there appears to be enough error present to warrant caution when using model results.

6.4.3.3 A Final Note on Meteorological Inputs

It seems clear at this stage that the greatest gains in the continuing BDWM modeling effort are likely to come from the development of more accurate and robust methods for determining the meteorological inputs, particularly in the higher elevation. This may involve the incorporation of atmospheric models which make use of available data but generate watershed-wide meteorological fields based on the physical processes which create them rather than numerical interpolation.

For now, the BDWM provides sufficient accuracy to address several of the hydroclimate research issues for which it was designed. Before proceeding to these issues, the next section provides a summary of the BDWM.

6.5 Summary of Bay-Delta Watershed Model

The Bay-Delta Watershed Model is a quasi-distributed, physically-based hydrologic model consisting of a snowmelt (UEB) component, a soil moisture component which simulates soil moisture processes in two vertical layers, and a streamflow routing component at the river basin level. The model takes daily precipitation and daily extreme temperatures as inputs for each of 8,648 16 km^2 model elements. In this study, these input fields were determined using kriging of available data, then determining necessary corrections at the data-poor high elevations based on reconstructed unimpaired hydrographs.

The BDWM is also based on preprocessed physical data used to characterize the watershed. Climatologies of some meteorological data were used in the simulation of snowpack and evapotranspiration. Topographic data and data characterizing landcover were used in the simulation of both snowpack and soil moisture processes. Stream and aquifer coverage data were also used in simulation of soil moisture. By far the most extensive preprocessing of data involved data used to characterize the soil matrix itself.

Saturated hydraulic conductivity data and textural classifications were extracted from the STATSGO database, and other relevant soil parameters were assigned by association with texture. Computer simulations of vertical soil moisture movement were then performed, and the results used to parameterize this process throughout the watershed. These parameters, as well as others which describe the horizontal movement of soil water, were aggregated to the 4 *km* model grid using

mass-conserving aggregation methods. The resulting soil parameters are used to simulate the horizontal and vertical movement of soil water in two layers for each model element.

The complete schematic of the inputs, configuration data, model components with state variables, and available outputs are shown in Figure 6.12. It should be noted that potential model outputs include all simulated quantities in this physically-based model. The most significant of these are shown in the schematic.

This model is unique in that it is physically-based, with no other fitting than the corrections to the inputs. This is an essential quality, enabling the model to be used in hydroclimate studies involving flow regimes other than those in the historical record. Further, the model's explicit representation of hydrologic heterogeneity in the watershed make it a unique tool for examining the effects of this heterogeneity on flow properties, a subject of emerging importance in hydrology. Finally, this model represents the first hydrologic model of the entire Bay-Delta watershed, and as such, it offers a significant new tool for research related to this important watershed.

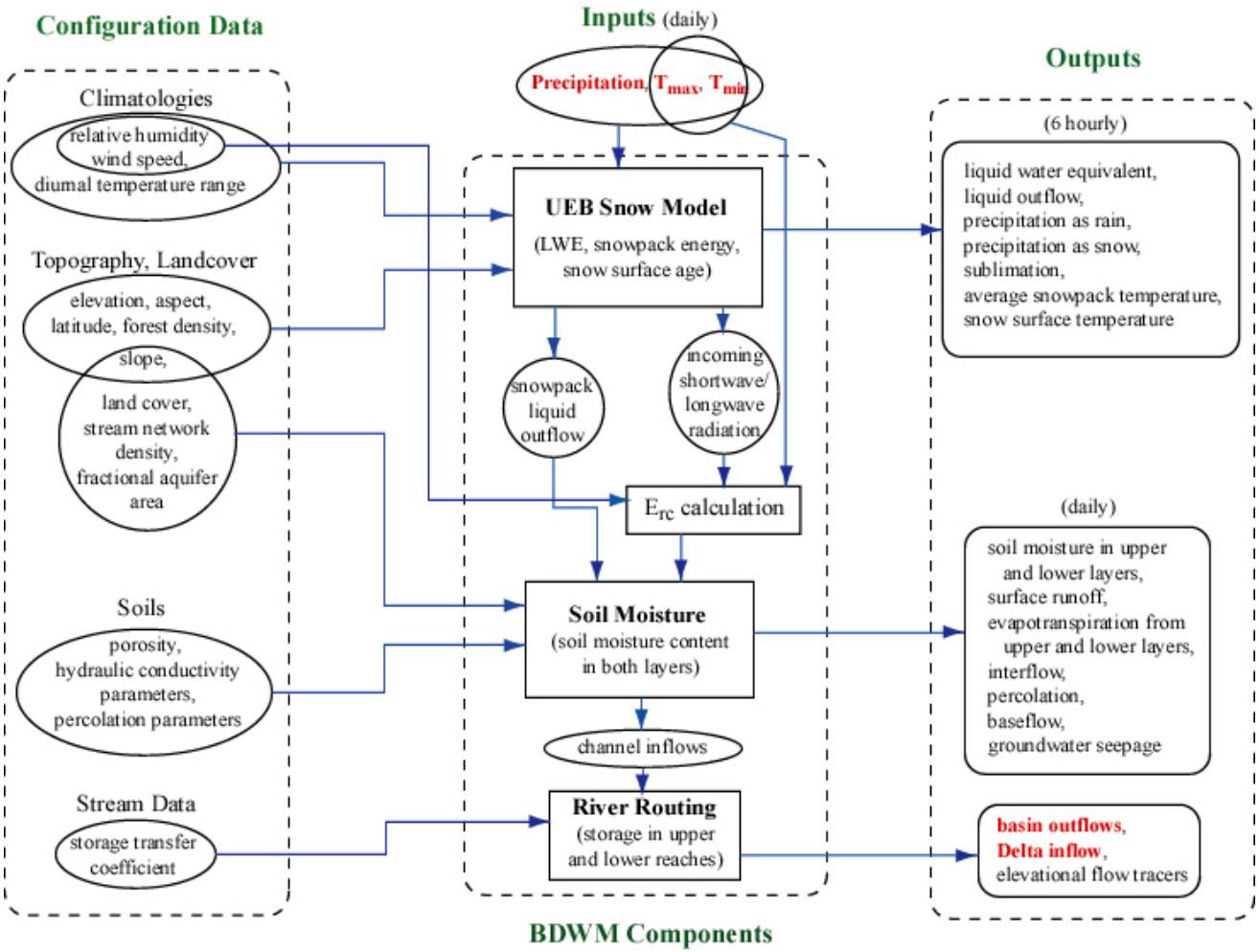

Figure 6.12 BDWM flowchart. Configuration data is in the left column. Model components are in rectangles in the center column, with state variables for each given in parentheses, and with intermediate data in ellipses. Inputs are top center, and major outputs are in the right column.

7 Hydroclimate Variability and Estuarine Response

With working models of both San Francisco Bay-Delta estuary and its watershed in hand, it is now possible to examine the hydrologic behavior of the watershed and its role in propagating climate variability from the atmosphere to the estuary. To address the longest periods of variability possible, the meteorological input data were extended to include water years 1949-1995, using data from EarthInfo/NCDC and the same interpolation methods used in the final version of the BDWM in the previous chapter. Prior to WY 1949, the meteorological observation network was prohibitively sparse. Simulated headwater basin outflows for this period (Figure 7.1) show the strong differences between the basins' hydrology (strongly different flow magnitudes and snow effects), as well as the shared interannual-interdecadal variability shared across the watershed. For example, the prolonged drought of WY 1987-1992 is clearly visible, as are the wet years that preceded and followed it. The information obtained from these simulations will be used in the remainder of this chapter to examine the hydrology underlying such variability, as well as its manifestation in the estuary.

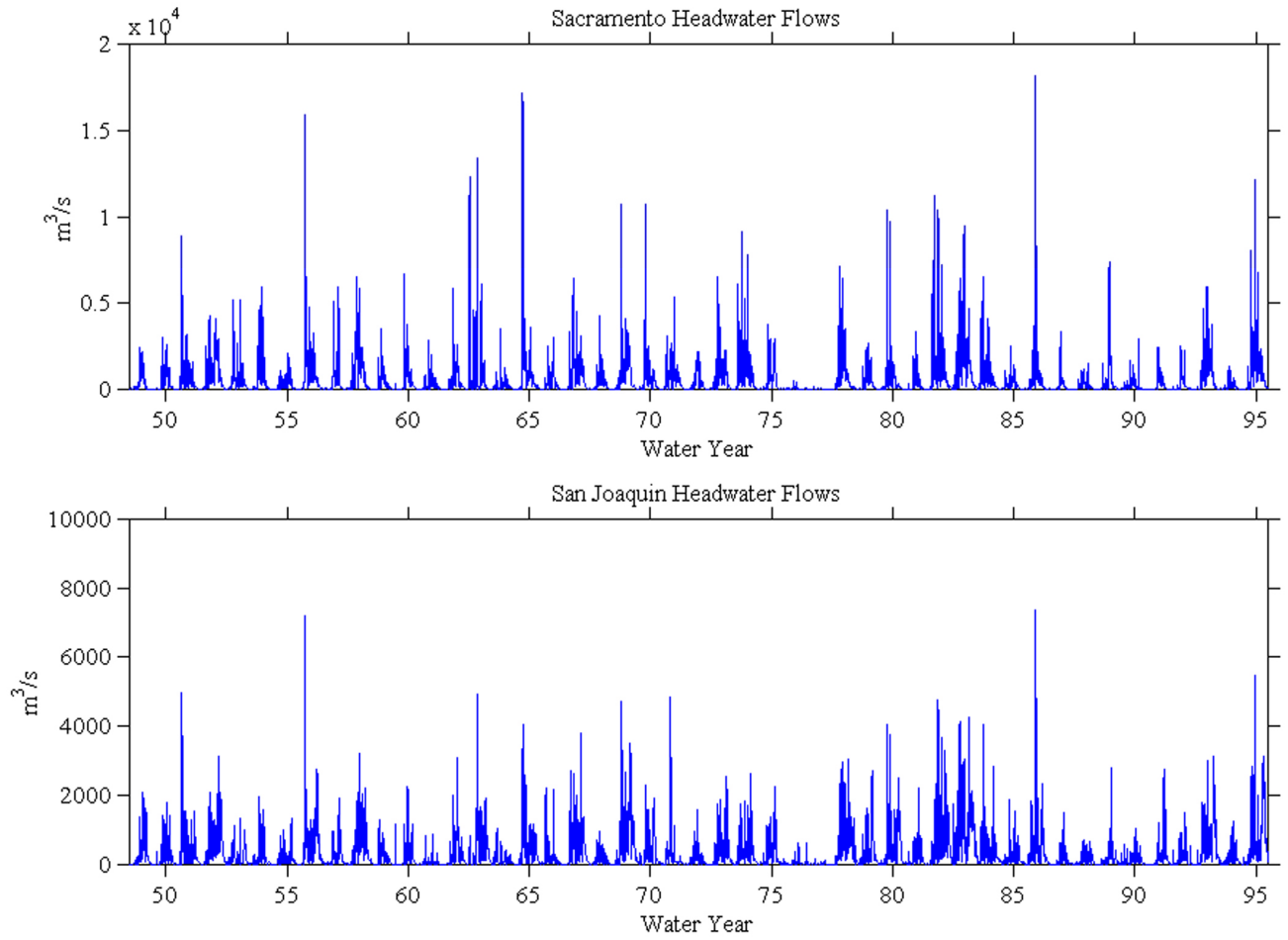

Figure 7.1 Simulated northern and southern headwater local flows, WY 1949-1995. In these simulations, upstream inflows were set to zero so only the sum of flows sourced locally within each region's river basins are shown.

7.1 Components of the Hydrologic Budget

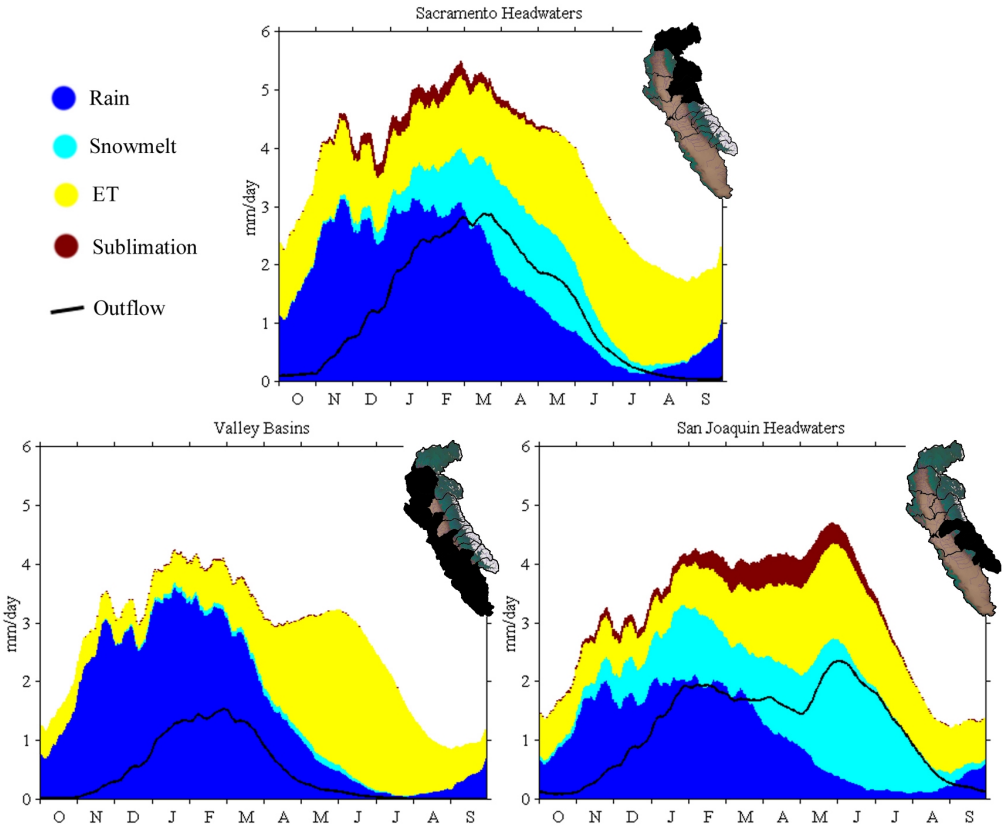

Figure 7.2 Regional breakdown of mean annual (WY 49-95) soil water inputs into rainwater and snowmelt entering the soil, and evapotranspiration (ET) and sublimation losses. The resulting hydrographs are also shown. Groundwater seepage losses are not shown.

7.1.1 Mean Annual Cycles

A wealth of information is available in the model results, offering the opportunity to view the basin flows as the end result of their respective hydrologic components. Water enters and leaves the soil matrix as a result of several processes including rain, snowmelt, sublimation, evapotranspiration and outflow. Each of these

components shows strong variability throughout the year and across the watershed, as shown in 30-day low-pass filtered versions of their simulated mean annual cycles by region (Figure 7.2).

In the valleys, almost no snowmelt or sublimation signal is present, while evaporative losses in the summer are very large compared to the other regions. Further, the deeper valley soils (see Figure 5.12) hold more of the water early in the year than the thinner mountain soils, resulting in much of the rainy-season rainfall being held and lost later in the year to ET, rather than feeding concurrent streamflows.

In the mountains (headwaters), the separation between timing of rainfall and snowmelt inputs is clear, with the northern mountains having a much stronger rainfall signal, and the southern mountains having more snowmelt and consequently higher sublimation. While the thinner mountain soils do not hold as much water as the valley soils, there is still a clear effect, as early season rainfall is absorbed, and soil moisture feeds evaporative demands through summer.

7.1.2 Interannual Variability of Annual Mean Behavior

The year-to year variability in these components of the hydrologic budget is also revealing, as shown by the annual mean values of rainfall plus snowmelt, evapotranspiration plus sublimation, and outflow in the valleys and headwater regions (Figure 7.3). The mean values of these series show the great differences between the high and low elevations of the watershed.

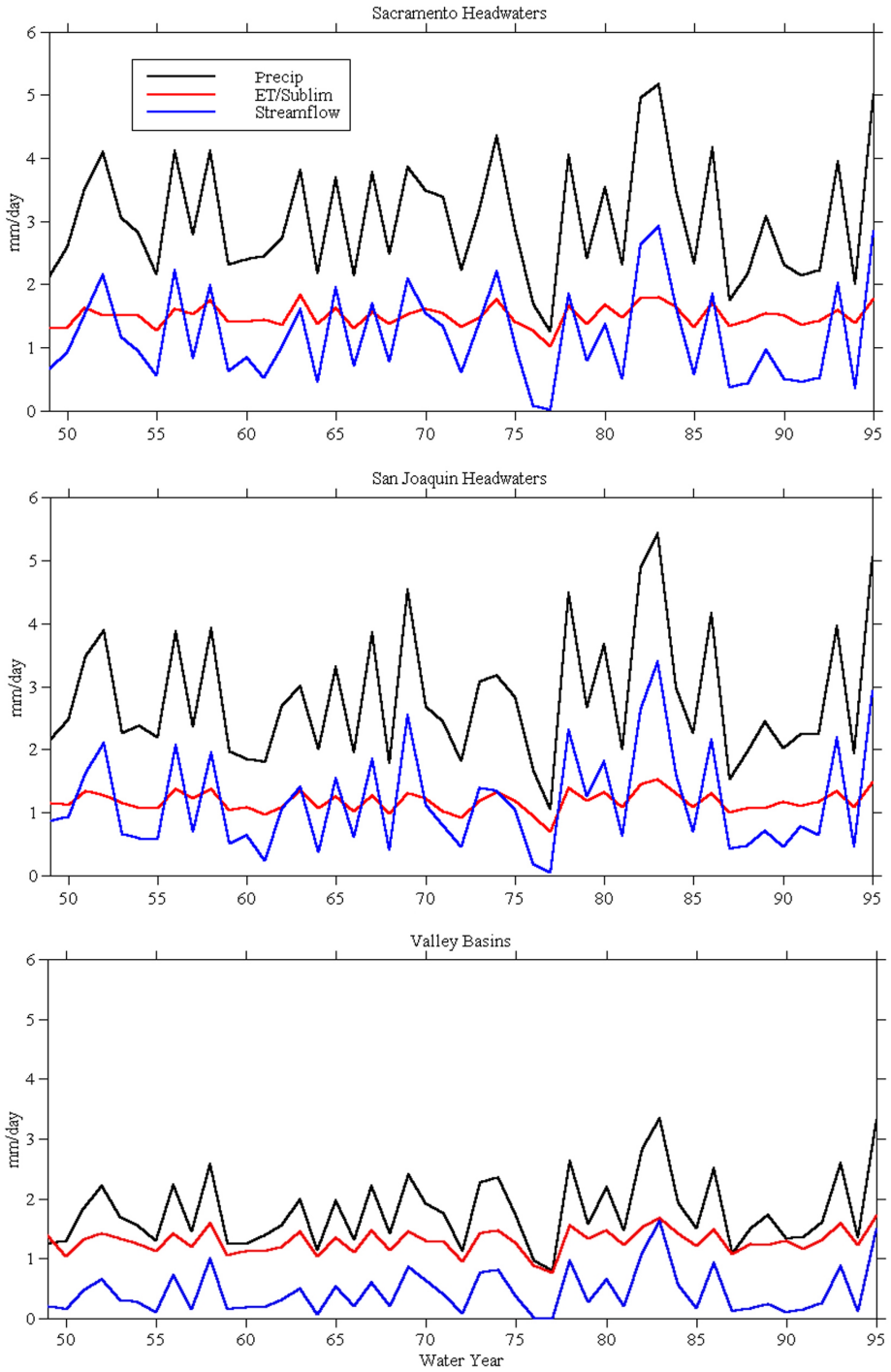

Figure 7.3 Annually- and areally-averaged precipitation, ET/sublimation and outflows for the Sacramento headwater, San Joaquin headwater and valley regions.

The mean precipitation flux is highest in the northern headwaters (3.04 *mm/day*), slightly lower in the south (2.82 *mm/day*), and much lower in the valleys (1.79 *mm/day*). The ratio of ET/sublimation to precipitation, known as the *climate ratio*, is highest for the arid valleys (0.72), followed by the northern headwaters (0.49) and the southern headwaters (0.42). One reason for the smaller ET in the south is the suppression of ET by snow cover, and the failure of increased sublimation to make up the difference. The ratio of outflow to precipitation, known as the *runoff ratio*, is highest in the headwaters (0.42 in the north and 0.39 in the south) and much lower in the valley (0.25). Clearly, the relative distribution of precipitation into ET/sublimation and outflow is a primary distinction between the mountains and the valleys.

The interannual variability of the watershed is very significant for precipitation and streamflow, while ET/sublimation are relatively constant. Annual ET/sublimation remains between 1-2 *mm/day*, while outflow and precipitation cover a range of about 3 and 4 *mm/day*, respectively, with high correlation between the two ($r \geq 0.98$ in all regions). These correlations are equally significant between annual precipitation and reconstructed natural flows (r=0.98 in both headwater regions). Precipitation variability is clearly the main component of the hydrologic budget driving interannual and longer streamflow variability.

7.1.3 Interannual Variability of Mean Annual Cycles

Within a year, the variability of each component of the hydrologic budget changes with the seasons (Figure 7.4). Precipitation shows similar variability in both headwater regions, with smaller variability but similar timing in the valleys. Soil moisture and ET/sublimation show much less variability. In the northern basins, both show greatest variability early in the water year, corresponding to the presence or absence of early storms. Soil moisture consistently approaches maximum in the thin soils of the mountains, limiting variability. The valley soils rarely reach saturation, and soil moisture varies more there as a consequence. ET/sublimation effects show little variability except early in the northern headwaters, corresponding to the months of greatest soil moisture variability, and late in the valleys, when ET demand is highest and there is no snowpack to suppress it, unlike the headwater basins. Where ET/sublimation variability occurs, it is largely driven by variations in soil moisture and hence by precipitation. Hence the variability observed in outflows is driven primarily by precipitation variability. The valley and northern headwater basins show this quite clearly, as they are dominated by rainfall runoff and outflow variability corresponds strongly with precipitation variability. In the southern Sierra, the variability is clearly also a result of snowmelt effects.

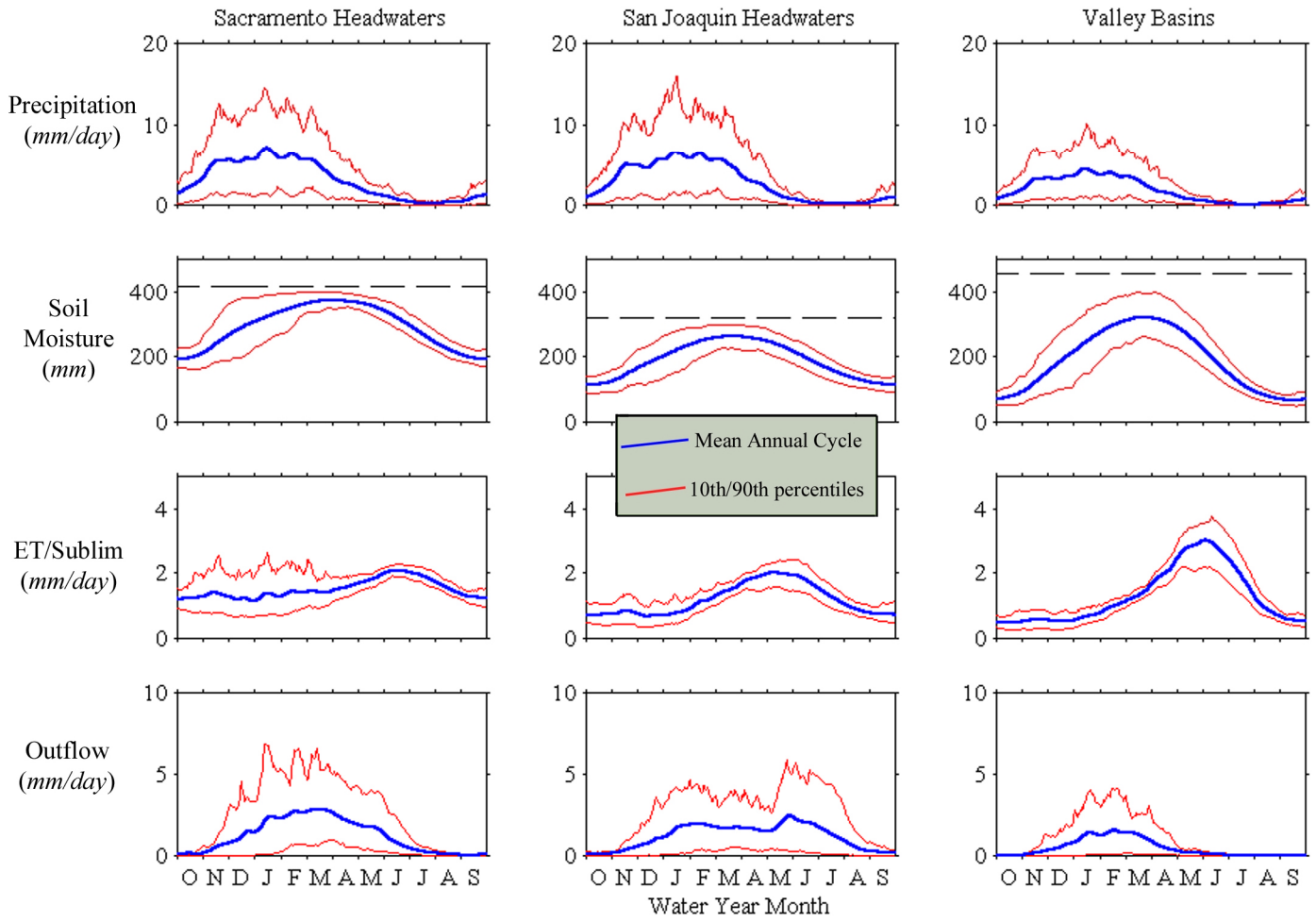

Figure 7.4 Regional distributions of several hydrologic variables within the water year. The distributions are derived from a 47-year simulation of hydrologic variability in the watershed. All time series were low-pass filtered (30-day cutoff) to enhance clarity. The dashed lines for soil moisture represent soil water capacity

7.1.4 Snow Effects

The primary effect of snowmelt is on the timing of flows within a year, rather than on their annual magnitude. Snowmelt acts to delay outflows, an effect which produces the major hydrologic distinction between the different regions of the Bay-Delta watershed. A measure of the effect of this delay on the outflow hydrograph is the average volume of water delayed multiplied by the average length of the delay. Figure 7.5 shows the annual values of this measure, distributed by elevation, for the northern and southern headwater regions.

This figure demonstrates both a strong elevational and regional dependence of snowpack effects, as well as a strong interannual variability. Snowpack delay effects are concentrated near 2 *km* elevation in the northern headwaters, and just below 3 *km* in the southern headwaters. The primary reason for this difference is that the distribution of area as a function of elevation in the north is centered at lower altitudes, whereas the southern mountains are much higher (Figure 7.6). If the plots are normalized by area (not shown), both show the strongest effects around 3 *km*.

The southern headwaters have a much stronger snowpack effect , though both regions show periods of almost no effect, as in the drought of WY 76-77. Both show water delays of over 200 km^3-*days*, though such high values are a much more frequent occurrence in the southern Sierra. The average total effect summed over both regions, and over all elevations, is to delay ~17 km^3 of liquid water equivalent by 70 days. By region, this is 8.7 km^3 for 59 days in the north, and 8.3 km^3 for 80 days in the south.

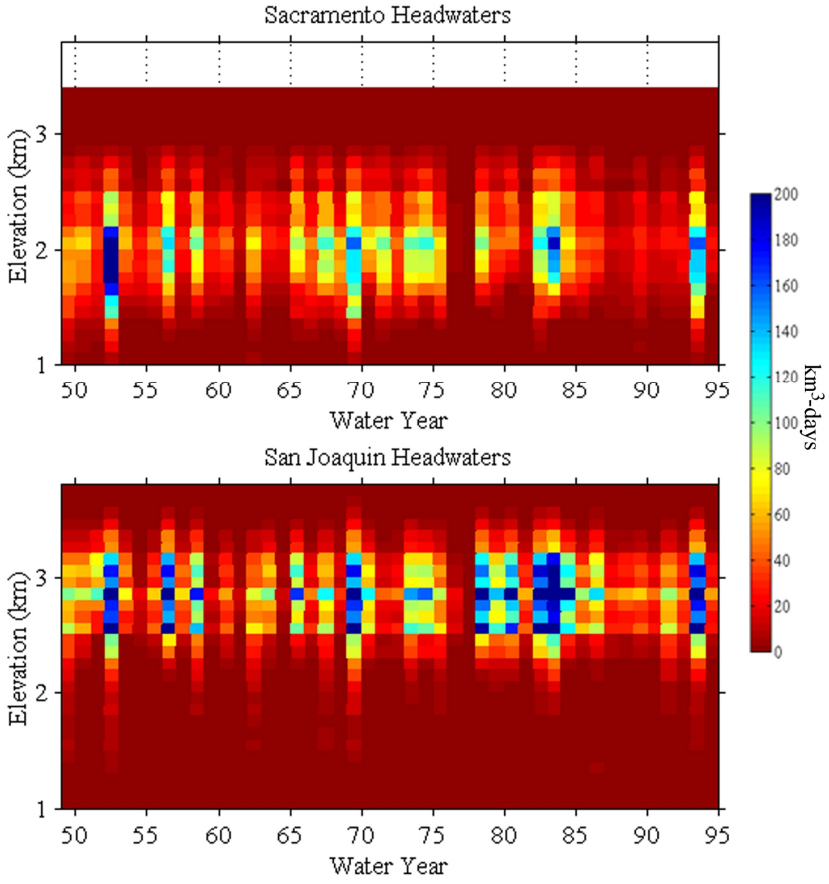

Figure 7.5 Simulated elevational distribution of the snowpack delay effect for WY 49-95 in the northern and southern headwater regions.

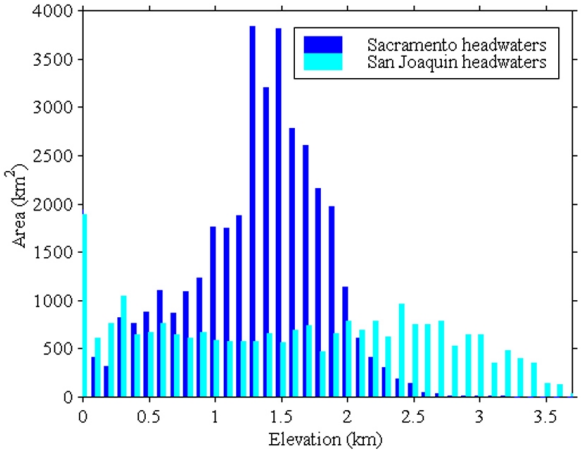

Figure 7.6 Elevational distribution of area by region.

7.2 Extremes of Hydrologic Variability

It was demonstrated in Chapters 2-3 that a particularly useful and revealing means of examining interannual-interdecadal estuarine and flow variability is in terms of the magnitude and the timing of flows into the estuary. The necessary tools are now available to extend this analysis into the watershed in more hydrologic detail. Figure 7.7 and Figure 7.8 show composites of hydrologic quantities for the wettest and driest years of the simulated record (WY 49-95), as well as for years with the earliest and latest average flow dates. Composites are each composed of the 8 most extreme years in each case (Table 7.1), with the extremes determined using total simulated watershed outflow. Table 7.2 and Table 7.3 summarize mean quantities for all composites.

Table 7.1 Years used for composites,
based on total simulated daily outflow.

Driest:	61, 64, 68, 76, 77, 87, 90, 94
Wettest:	56, 58, 69, 78, 82, 83, 93, 95
Earliest:	51, 64, 65, 66, 70, 71, 74, 84
Latest:	49, 52, 57, 75, 76, 79, 91, 93

Figure 7.7 shows the (30-day low-pass filtered) composite annual cycles of the hydrologic budget components for the Sacramento and San Joaquin headwater regions. Figure 7.8 shows composites of the filtered precipitation, the snow-delay effect versus elevation, and simulated Delta inflow and San Pablo Bay salinity. There is a great deal of information in these plots, but several key features may be identified. First, ET and sublimation effects are similar for all composites within a region, though sublimation increases and ET decreases when more snowpack is present. The presence of snow enhances sublimation and suppresses evaporation. As shown in Figure 7.3,

ET and sublimation are inherently less variable than precipitation. While precipitation in wet years increases by 224% compared to dry years in the northern headwaters and 260% in the south, ET/Sublimation increase by only 125% and 141%, respectively (Table 7.2).

Second, while there is little overall shift in the timing of precipitation between wet and dry years, the impact of snowpack increases dramatically, despite slightly higher temperatures during the snow accumulation season. While rainfall (the liquid portion of precipitation) increases by only 217% in the north and 239% in the south, snowmelt increases by 495% in the north and 527% in the south. The plot of snow-delay versus elevation shows this effect is particularly strong in the high southern Sierra. The strong effect of snowpack in wet years in the southern Sierra leads to outflows from southern headwaters being nearly a month later in wet years than dry years, compared to only a week later in the northern headwaters. Thus, wetter years correspond to dramatic increases in upper-elevation snowpack delay of the hydrograph, which keep salinities down well into the summer. Conversely, drier years have much less snowpack, allowing spring-summer salinities to reach high levels as rainfall-driven streamflows subside.

The differences in timing between early- and late-year composites appear to be due to a combination of later rainfall and increased snowpack delay, with the rainfall timing as the dominant effect in the north and a combination of later rainfall and increased snowmelt generating later flows in the south.

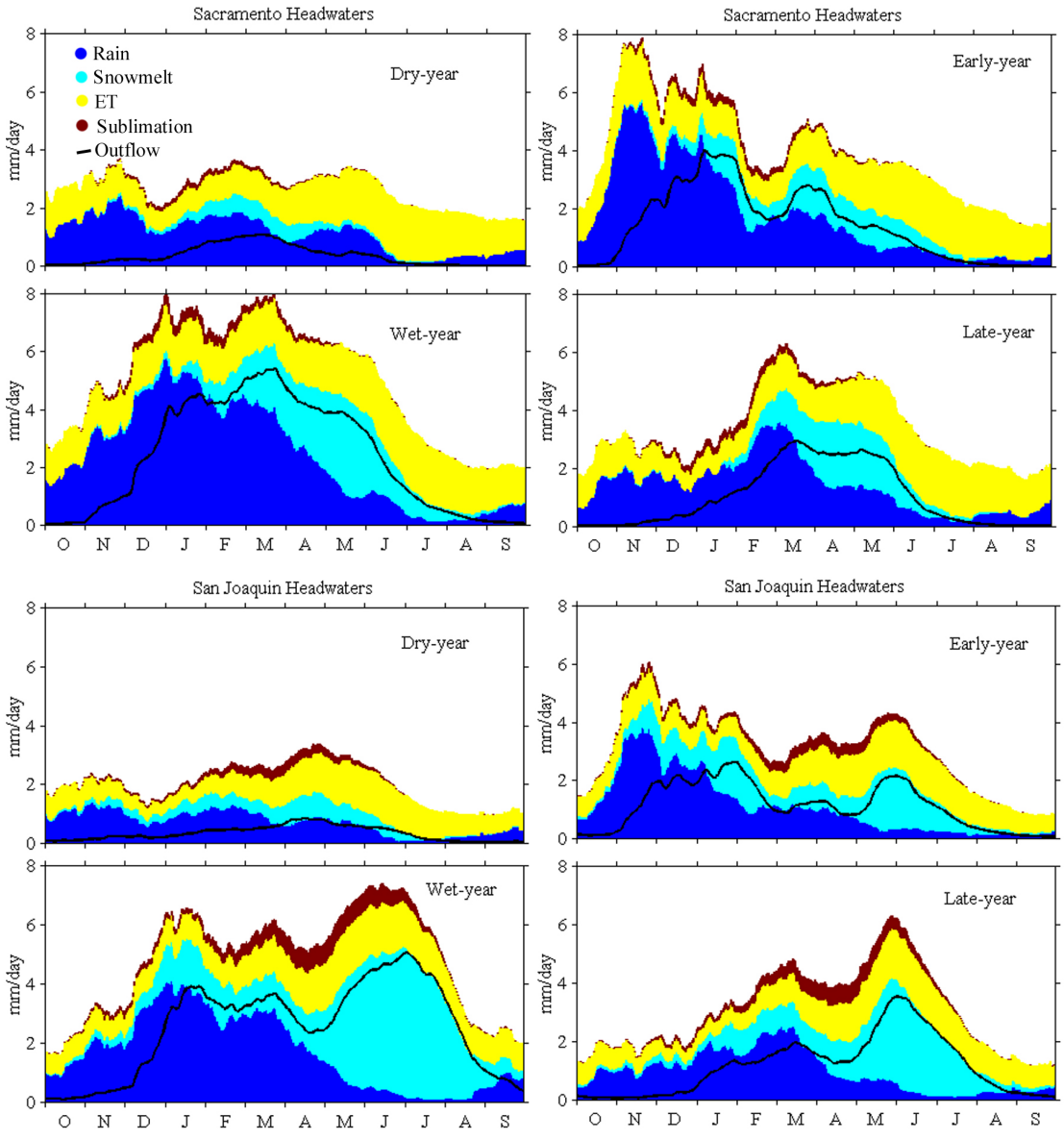

Figure 7.7 Mean annual cycles of the hydrologic budget components for dry/wet (left column) and early/late (right column) water year composites. Composites are based on the 8 extreme years corresponding to each criterion (Table 7.1).

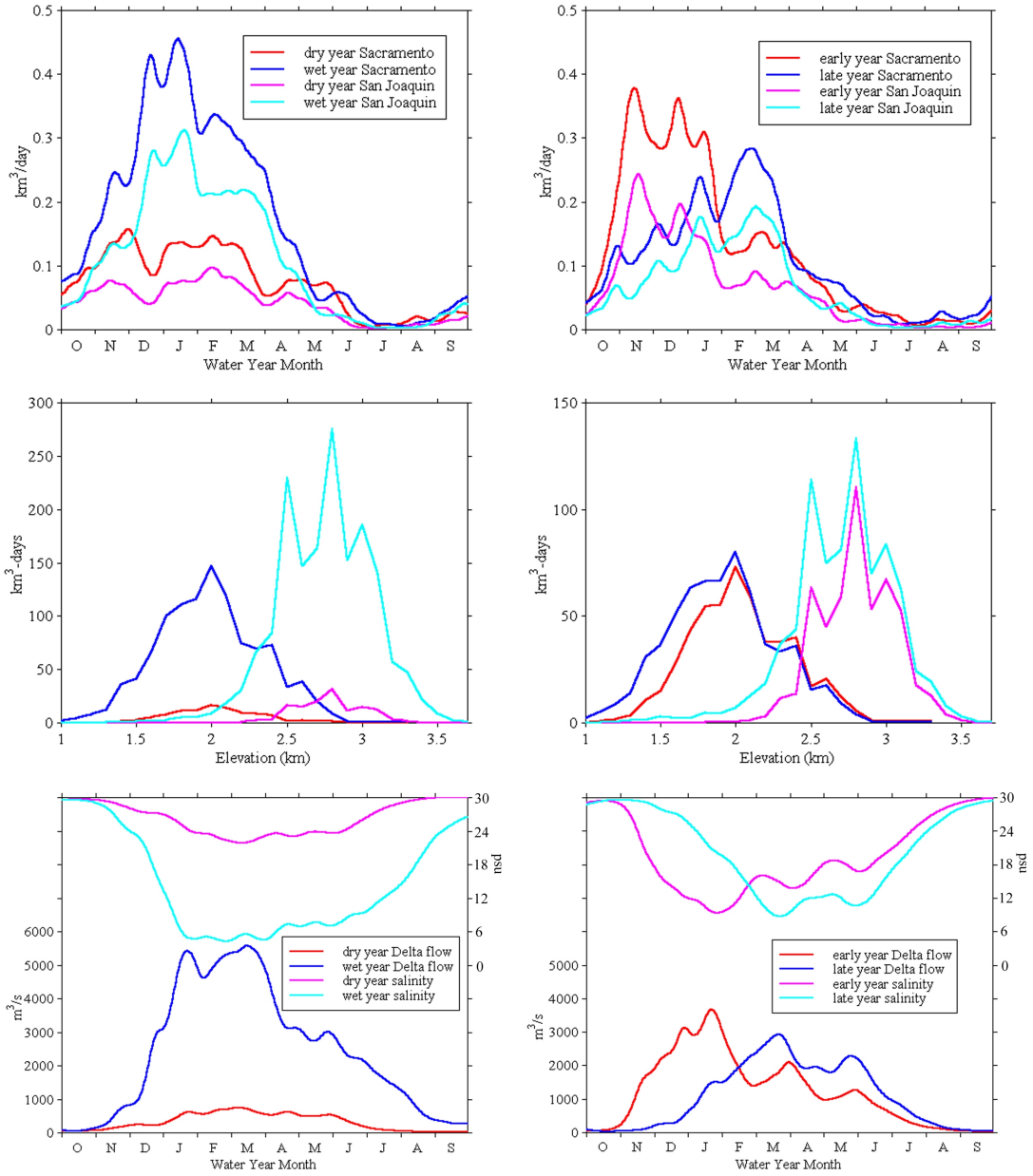

Figure 7.8 Precipitation, snowpack delay, Delta outflow, and salinity mean annual cycles for dry/wet (left column) and early/late (right column) water year composites.

Table 7.2 Composite values of hydrologically important quantities for the northern and southern headwaters, corresponding to the 8 wettest and driest years of the record as measured by simulated total watershed outflow.

Composite Type	Precip (*mm/day*)	Precip timing (date)	T_{max} (Dec-Mar, *°C*)	Snow Delay (km^3-*days*)	Rainfall (*mm/day*)	Snowmelt (*mm/day*)	ET/ Sublimation (*mm/day*)	Outflow Size and Timing (*mm/day*, date)	Salinity (*psu*)
dry-year Sacramento	1.97	2/7	-4.06	105	1.09	0.20	1.35	0.35, 3/10	26.3
wet-year Sacramento	4.41	2/2	-3.31	1090	2.36	0.99	1.69	2.32, 3/18	14.3
dry-year San Joaquin	1.75	2/8	-3.96	139	0.69	0.33	1.00	0.33, 3/31	26.3
wet-year San Joaquin	4.52	2/5	-3.62	1660	1.65	1.74	1.41	2.50, 4/27	14.3

Table 7.3 Composite values of hydrologically important quantities for the northern and southern headwaters, corresponding to the 8 earliest and latest flow years of the record as measured by simulated total watershed outflow.

Composite Type	Precip (*mm/day*)	Precip timing (date)	T_{max} (Dec-Mar, *°C*)	Snow Delay (km^3-*days*)	Rainfall (*mm/day*)	Snowmelt (*mm/day*)	ET/ Sublimation (*mm/day*)	Outflow Size and Timing (*mm/day*, date)	Salinity (*psu*)
early-year Sacramento	3.28	1/15	-3.79	520	1.81	0.60	1.57	1.42, 2/17	19.9
late-year Sacramento	2.76	2/12	-5.00	641	1.39	0.60	1.42	1.01, 4/4	20.5
early-year San Joaquin	2.76	1/ 12	-3.97	520	1.09	0.82	1.20	1.13, 3/9	19.9
late-year San Joaquin	2.73	2/9	-4.98	817	0.94	0.97	1.18	1.15, 5/2	20.5

Whereas precipitation timing was unchanged between wet and dry years, the difference in precipitation timing between early and late years is about one month in both regions (Table 7.3). In the north, this shift is responsible for most of the timing change. Although precipitation is lower in the late years in the north (a reduction of 16%), snowmelt is unchanged (the snow delay even increases slightly), due to cooler (-1.21°*C* cooler on average) temperatures during the snow accumulation season in the late-flow years. Interestingly, the higher precipitation and outflows from the north in early years do not correspond to a large reduction in San Pablo Bay salinity, which is decreased by only 0.6 *psu* in early years compared to late years. In contrast, wet versus dry years produce a 12 *psu* change in annually-averaged salinity. In late years, the broad snowmelt-driven hydrograph keeps salinities nearly as low as the stronger rainfall hydrograph of early years. This suggests that a rainfall runoff peak is not as effective as a broader, more sustained hydrograph in keeping the estuary fresh.

In the southern headwaters, a different situation contributes to the shift in flow timing. Again, precipitation occurs on average a month later in late years, though the annual average is unchanged from wet to dry years. Additionally, the snowmelt peak increases considerably in late years. Though the increase in snow delay is lessened by the later precipitation timing, average snowmelt increases by 18%, largely during late spring-early summer. As in the north, this change appears to be driven by cooler temperatures. In the north, however, the average snowmelt/rainfall ratio is 0.38, while it is 0.89 in the south. In the snowmelt-dominated southern Sierra, the changes in

snowmelt contribution to the overall hydrograph have a much stronger influence on the timing of the annual hydrograph.

7.3 Hydrology, Climate Variability and the Estuary

Having discerned some of the features of hydrologic behavior associated with differences in the magnitude and timing of watershed outflow, it is now pertinent to assess to what degree such differences are linked to global-scale climate processes.

7.3.1 Climate Signals Affecting the Watershed

Two prominent climate signals which have been identified and shown to have impacts in the western United States are the El Niño/Southern Oscillation (ENSO) (Rasmusson and Carpenter 1982; Rasmusson and Wallace 1983; Redmond and Koch 1991; Cayan, Redmond *et al.* 1999) and the North Pacific Oscillation (NPO) (Latif and Barnett 1994; Mantua, Hare *et al.* 1997; Dettinger, Cayan *et al.* 1998). ENSO is associated with sea-surface temperature and sea-level pressure anomalies in the tropical Pacific, though anomalies related to ENSO extend across the globe. ENSO anomalies typically persist 6-18 months, recurring at 3-7 year intervals. The other climate phenomenon addressed here, NPO, is defined as the amplitude of the leading mode of decadal sea-surface temperature variations in the North Pacific. NPO-related anomalies persist 20-30 years. The distribution of SST anomalies associated with opposite phases of the NPO (Figure 7.9) are quite similar to those associated with

ENSO phases, the primary difference between the two signals being their distinct temporal behavior.

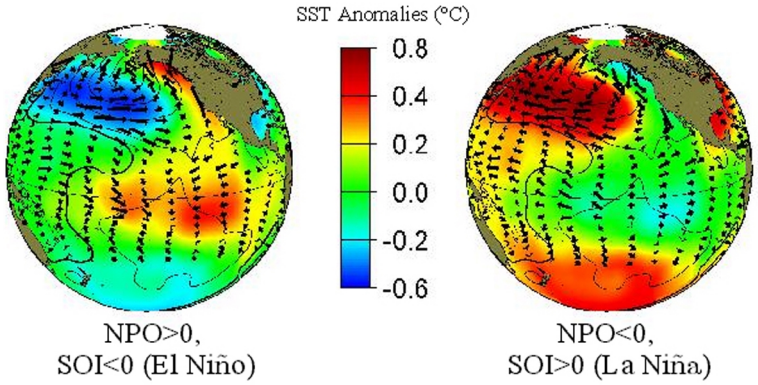

Figure 7.9 SST and surface wind stress anomalies associated with opposite phases of the North Pacific oscillation (adapted from http://tao.atmos.washington.edu/pdo). SST patterns associated with ENSO are similar, and corresponding signs of SOI and the NPO index are indicated.

In this study, the ENSO state is represented by the Southern Oscillation Index (SOI), defined as the standardized difference in sea level pressure anomalies between Tahiti and Darwin, Australia (Ropelewski and Jones 1987). Following Redmond and Koch (Redmond and Koch 1991), annual values of SOI used here (Figure 7.10) correspond to the June-November averages of the previous year, as they found slightly higher correlations between SOI and climate variability at this lag.

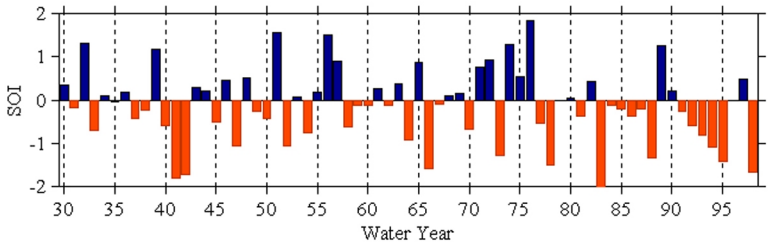

Figure 7.10 The Southern Oscillation index represents the state of ENSO, a primarily tropical Pacific phenomenon. ENSO events are 6-18 month duration at 3-7 year intervals. See Figure 7.9.

Negative values of this index correspond to the warm (El Niño) phase of the tropical Pacific.

NPO is represented by the principal component of the leading EOF of central North Pacific sea surface temperatures (Mantua, Hare *et al.* 1997). When this index is negative, the North Pacific is warmer than average. Annual (water year) averages of this monthly index are used here (Figure 7.11).

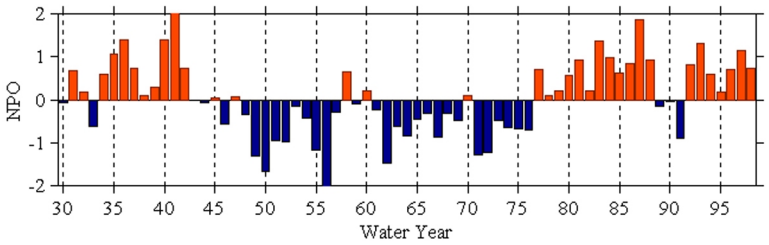

Figure 7.11 The NPO index represents the state of the North Pacific Oscillation, a primarily North Pacific phenomenon. NPO "events" are 20-30 years in duration. See Figure 7.9.

7.3.2 Climate Effects on Regional Flows

To assess associations of the watershed's "natural" behavior with climate, monthly unimpaired (also called "full natural") flow estimates at nine of the major rivers (all headwaters except those of Cosumnes/Mokelumne) for the period WY 1930-1998 were obtained from the California Center for Data Exchange (http://cdec.water.ca.gov/). From these data, annually-averaged total outflow from all nine headwaters, as well as annually-averaged flows partitioned into Sacramento headwaters and San Joaquin headwaters, were calculated. The average timing of flows

in these three regional categories were also calculated for each water year as the date of the center of mass of the water year's hydrograph.

Proceeding with the analysis, Figure 7.12 shows the time series of the annual climate indices with values in excess of one standard deviation from the mean highlighted. These four sets of years were used to generate corresponding composite values of flow timing and magnitude from the corresponding time series described above. These values, along with *t*-test results indicating the significance of the differences (Press 1986), are shown in Table 7.4.

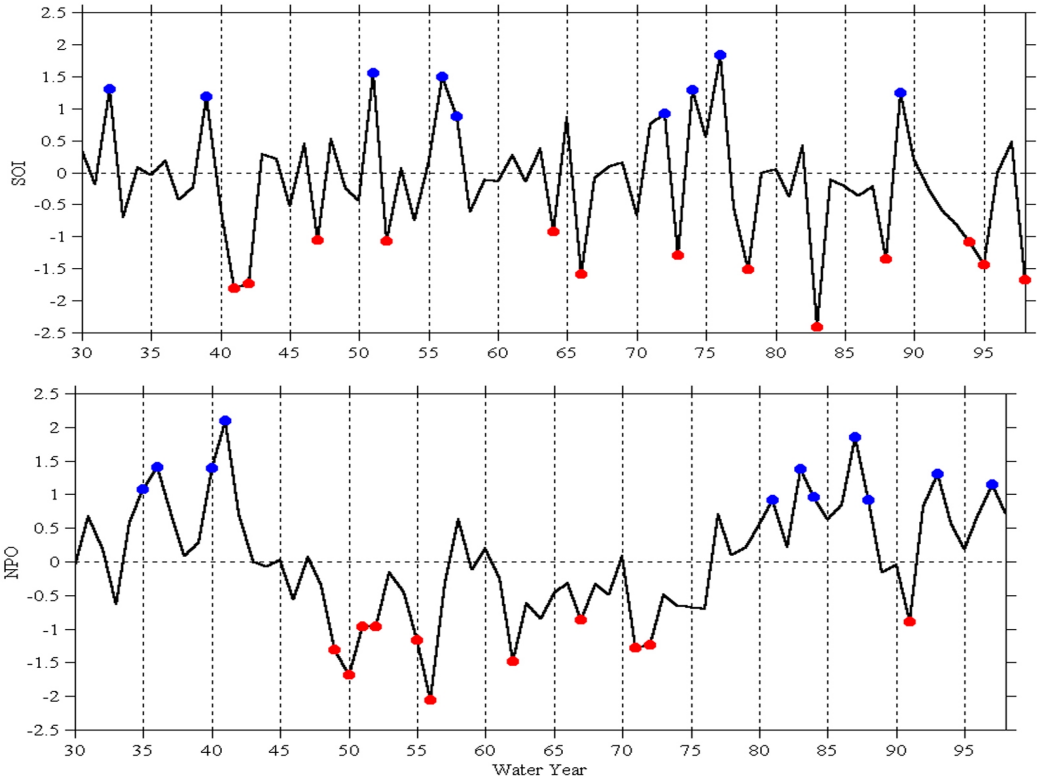

Figure 7.12 Annual values of SOI (top) and NPO (bottom) indices for WY 30-98. Values in excess of one standard deviation from the mean used for compositing are indicated.

Table 7.4 Composite values of unimpaired annual flow magnitude and timing for northern, southern, and all headwaters corresponding to extreme values of ENSO and NPO climate indices.

	El Niño	La Niña	*t*-test	low NPO	high NPO	*t*-test
Sacramento flow magnitude (km^3)	26.6	21.7	64%	22.7	24.8	37%
San Joaquin flow magnitude (km^3)	11.6	8.2	83%	9.4	10.9	49%
All basins flow magnitude (km^3)	38.2	29.8	72%	32.1	35.6	42%
Sacramento flow timing (date)	3/15	3/12	58%	3/4	2/28	71%
San Joaquin flow timing (date)	4/25	4/12	**94%**	4/10	4/4	56%
All basins flow timing (date)	3/28	3/20	83%	3/16	3/7	67%

These results suggest that neither ENSO nor NPO has any strong effect on flow timing or magnitude within the watershed, with the exception of San Joaquin flow timing. Conditions associated with the El Niño phase of ENSO are associated with later flows in the San Joaquin headwaters, conversely for La Niña. It was shown in Section 7.2 that later flows in the San Joaquin headwaters are primarily caused by an increase in the proportion of precipitation falling as snow, suggesting that El Niños may be associated with such an increase. It does appear that El Niños are associated with higher precipitation in the San Joaquin basin (significance 83%). It also appears that El Niños are associated with later outflows from the watershed as a whole (83%).

While these results present an unclear picture of possible links between climate variability and the watershed, it is nonetheless true that El Niños are associated with some of the most extreme events in the hydrologic record (*e.g.*, WY 1983 and WY 1998 were extremely wet El Niño years). When taken in composite, clear hydrologic signals associated with ENSO often fail to emerge. However, though the signals represented in Table 7.4 are weak, they do seem to suggest differing patterns of climate-associated variability in the northern and southern halves of the watershed. Such patterns were also uncovered in Chapter 3, where analysis of flows revealed decadal-scale oscillations in the timing of annual Delta outflow. These oscillations appeared to be the result of an interdecadal shifting of the storm track which changed the relative distribution of flows in the Sacramento versus the San Joaquin headwater regions. Several studies have found such north-south patterns to be associated with both the ENSO and the NPO phenomena (*e.g.*, Kiladis and Diaz 1989; Cayan and Webb 1992; Dettinger, Cayan *et al.* 1998).

7.3.3 North-South Changes and ENSO

To attempt to further uncover these connections between the watershed, estuary, and climate phenomena, Figure 7.13 presents composite values of several quantities related to the north-south changes, as well as to the timing of both watershed outflows and the estuarine salinity cycle. For each quantity, years corresponding to extreme values of the SOI are indicated. Composite values are given

at the right, along with a *t*-test significance of the difference between the values corresponding to opposite SOI extremes. The quantities thus analyzed include the Sacramento-versus-San Joaquin ratios of total precipitation and total headwater outflows, the annual timing of observed Delta outflows to the estuary (derived from DAYFLOW data) and the resultant timing of the annual estuarine salinity cycle (as represented by the mode 2 amplitude from the E-EOF salinity analysis of Chapter 2, shown in Figure 2.4), and the annual watershed-averaged winter (DJF) temperature.

Since ENSO varies at a time scale much shorter than 7 decades, opposite extremes are evenly interspersed throughout the record (Figure 7.13, plot 1 of 6). Composite values of north-south precipitation and headwater outflow ratios both show decreased values for El Niño conditions, corresponding to higher San Joaquin precipitation and outflows relative to those of the Sacramento basin (Figure 7.13, plots 2-3 of 6). This makes sense in the context of known ENSO-related precipitation/streamflow patterns, which show wetter conditions in the southwestern U.S. for El Niños, and drier conditions in the Northwest (*e.g.*, Cayan, Redmond *et al.* 1999). The San Francisco Bay-Delta watershed just happens to straddle the fulcrum of this seesaw, making it a particularly interesting natural laboratory in which to study links between climate and a watershed. Note the amplification of the north-south precipitation signal (*t*-test significance of only 55%) in the outflows (90%) by the watershed (Figure 7.13), an effect which enhances both the strength of climate signals and their impact in the watershed and estuary.

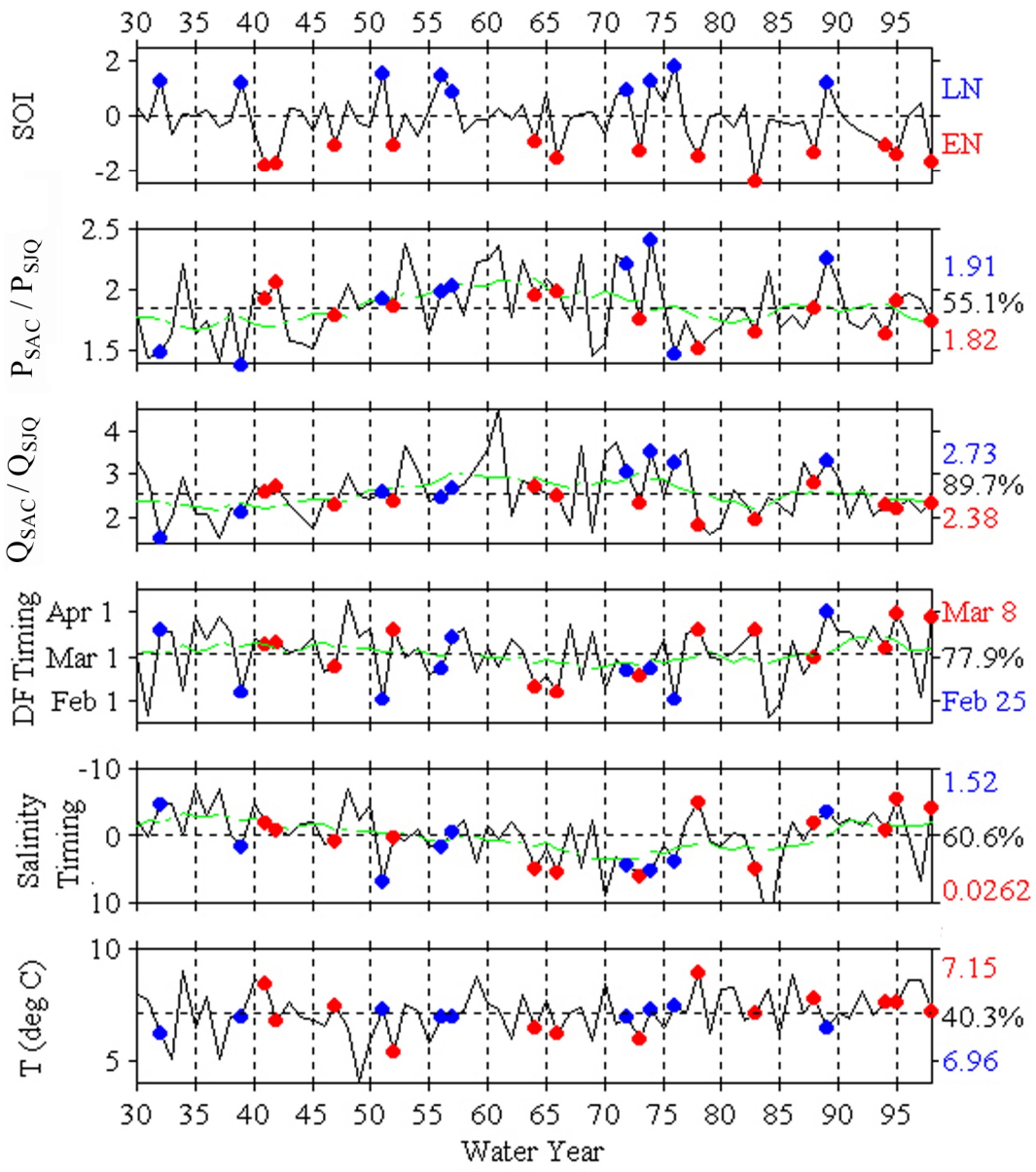

Figure 7.13 SOI, Sacramento vs. San Joaquin precipitation and outflow ratios, Delta outflow and annual salinity cycle timing, and watershed-averaged winter temperature. Composites of years with extreme SOI values are shown to the right of each plot, with *t*-test results for significance of the difference. 10-year low-pass filtered values are shown in light green.

The observed Delta outflow timing, despite significant corruption of natural signals by management, also show an effect associated with ENSO (78% significance) (Figure 7.13, plot 4 of 6). El Niño conditions are associated with later Delta outflows. The timing of the annual salinity cycle also shows an ENSO-related change (Figure 7.13, plot 5 of 6), though the significance of this association (61%) is weaker than the Delta outflow signal. Since there appears to be no significant difference in watershed-averaged winter (DJF) temperatures associated with ENSO extremes (Figure 7.13, plot 6 of 6), a likely explanation for the ENSO-related Delta outflow timing difference is the relative shift of precipitation from the rainfall-dominated Sacramento headwaters to the snowmelt-dominated southern Sierra. The shift in emphasis from rain to snow changes the overall nature of the watershed's annual hydrograph, from an early rainfall hydrograph to a later snowmelt one. As this signal propagates through the system to the estuary, it remains remarkably strong considering the impact of management on Delta outflows.

7.3.4 Interdecadal Changes, NPO and Human Effects

Low-pass filtered versions (with a 10-year cutoff period) of the variability of the north-south ratios and the annual flow and salinity timing (Figure 7.13, green lines) reveal longer-term changes in behavior. The annual salinity cycle exhibits interdecadal changes in timing which were first demonstrated in Chapter 2 (*cf* Figure 2.4). Similar patterns in the north-south ratios suggest a possible causal relationship between

climate variability and long-term timing shifts. It was suggested in Chapter 2 that these timing shifts result from both natural and human-induced effects.

To better diagnose the causes of the interdecadal changes in flow and salinity timing, two additional low-pass filtered time series are examined (Figure 7.14). The first of these is the filtered annual timing of the sum of the nine full natural flow time series obtained from CDEC. This signal reveals naturally-driven changes in flow timing, that is, changes unrelated to management of the water supply. The second new time series represents the effect of management on the annual timing of freshwater inflows to the estuary. This was derived by taking the difference between the annual timing of the unimpaired flow totals and the annual timing of observed Delta outflow, then filtering the difference to obtain a representation of interdecadal changes in human. effects. These effects include reservoirs, agriculture and Delta exports. All low-pass filtering was done using a 12-pole, symmetric low-pass Kaylor filter (Kaylor 1977) with a 10-year cutoff period.

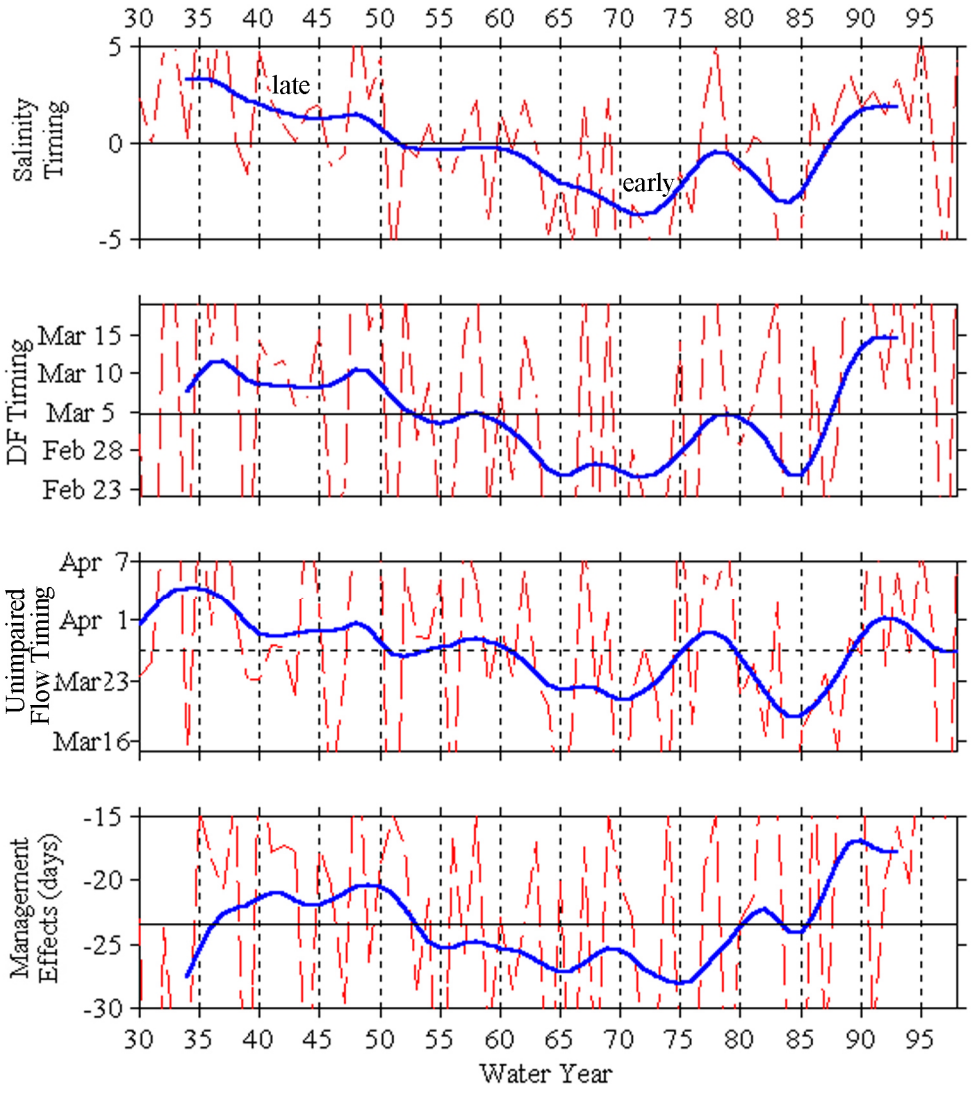

Figure 7.14 Interdecadal changes in annual salinity and Delta outflow timing, unimpaired flow timing, and management effects.

Clearly, both management and natural variability contributed to interdecadal changes in observed estuarine inflows. In particular, both contributed to the trend toward earlier runoff from the late 1930's through the mid-1970's, as well as to its subsequent abatement. To understand the causes of long-term changes in the timing of the estuarine salinity cycle, each of these contributing factors must be understood.

In Chapters 2-3, the net effect of management was shown to be a removal of much of the snowmelt portion of the annual hydrograph, resulting in earlier estuarine inflows. This effect is shown here (in Figure 7.14) as a shift of just over three weeks, on average. From the late 1940's through about 1975, this management effect increased, coinciding with the period of development of California's massive water projects. After 1975, the management effect subsided considerably, possibly due to management changes as well as the extended drought beginning in 1987.

Between 1936 and 1971, the filtered unimpaired flow signal shifted earlier by about 15 days. After 1971, this steady trend broke down, replaced by shorter fluctuations. Several natural forcing factors have been identified which contributed to the timing signal. The first of these is a long-term trend toward earlier runoff of Sierran snowmelt (Figure 7.15), originally identified by Maury Roos (Roos 1987).

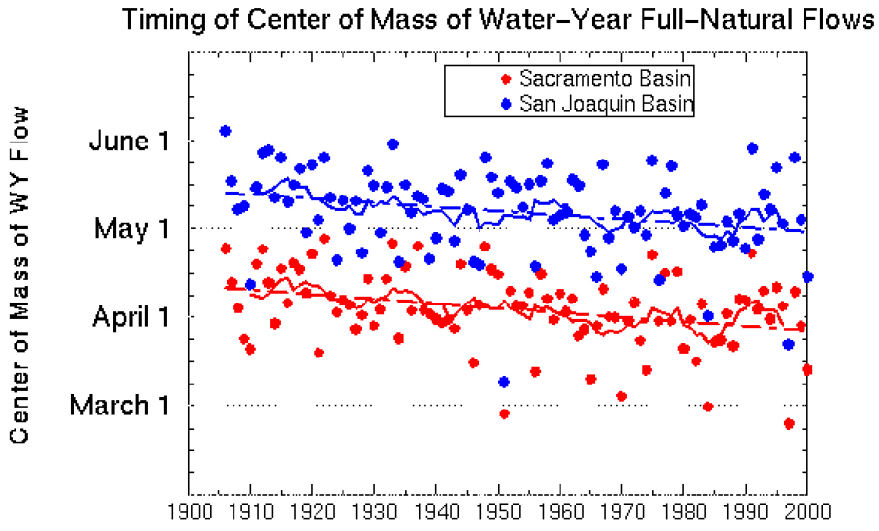

Figure 7.15 Long-term trend toward earlier runoff. Figure courtesy of Mike Dettinger. Annual timing values are shown as dots, 10-year smoothed version as a solid line, and a linear fit as a dashed line.

This trend has since been associated with a spring warming trend (Dettinger and Cayan 1995). This trend has been quite steady over the past century, constituting a timing shift of about a week over that period. Clearly, this signal alone can not explain the observed changes in natural flow timing (Figure 7.14, 3rd plot), though it does contribute to the shift between the 30's and the 70's.

In addition to the timing of snowmelt runoff, two other factors have been identified in this work which affect the timing of unimpaired watershed outflows: the north-south distribution of precipitation and the timing of precipitation. Precipitation timing, particularly in the rainfall-dominated Sacramento basin, was shown in Section 7.2 to strongly affect outflow timing. In Chapter 2, evidence was presented which suggested that climate-driven storm track shifts affect the relative amounts of precipitation falling in the northern and southern halves of the watershed. Since the two halves have distinct hydrologic characteristics which lead to very different outflow timing, this redistribution of precipitation should result in a change of the timing of total watershed outflow. In Section 7.3.3, we saw that such north-south shifts and the consequent changes in outflow timing are indeed associated with the ENSO phenomenon.

Since ENSO and NPO share a similar pattern of SST anomalies (Figure 7.9), they also have similar effects on the storm track. It therefore seems likely that NPO-related storm track shifts contributed to the interdecadal variability of the timing of unimpaired headwater flows (Figure 7.14, 3rd plot). The low-pass filtered versions of the NPO index, the north-south ratios of precipitation and unimpaired flows, and the

total unimpaired flow timing are shown in Figure 7.16. The filtered annual center-of-mass date for Sacramento basin precipitation timing is also shown.

First, there is a clear association between the NPO oscillation and the relative north-south shifting of precipitation and flow. For low NPO, the Sacramento to San Joaquin ratios are high (note flipped axes on ratios), meaning less southern snow. Less precipitation as southern Sierran snow should result in earlier outflow timing. This means unimpaired flow should have come progressively earlier as the NPO caused a shift of precipitation distribution from the early 1930's to about 1960, with a gradual reversal of this change and a return to later flows after 1960.

To determine if NPO is indeed contributing to the unimpaired flow timing changes, the impact of the other two contributing factors—the long-term warming trend and interdecadal changes in precipitation timing—must also be considered. As mentioned, the timing of filtered unimpaired flow shifted earlier by about 15 days between 1936 and 1971. By the 1950's, this shift had already amounted to a week. The century-long trend towards earlier snowmelt runoff due to warming (Figure 7.15) resulted in a timing shift of only 10-12 days over the course of the century . The precipitation timing showed no long-term trends; in fact between the 30's and the late 50's, precipitation timing shifted later by about a week. This suggests that a factor other than the warming trend or the precipitation timing changes must have contributed to unimpaired flow timing changes. The only remaining candidate is the NPO forcing. Further evidence that the NPO-related north-south shifts affected timing can be seen by comparing the response of unimpaired flow timing to the two late

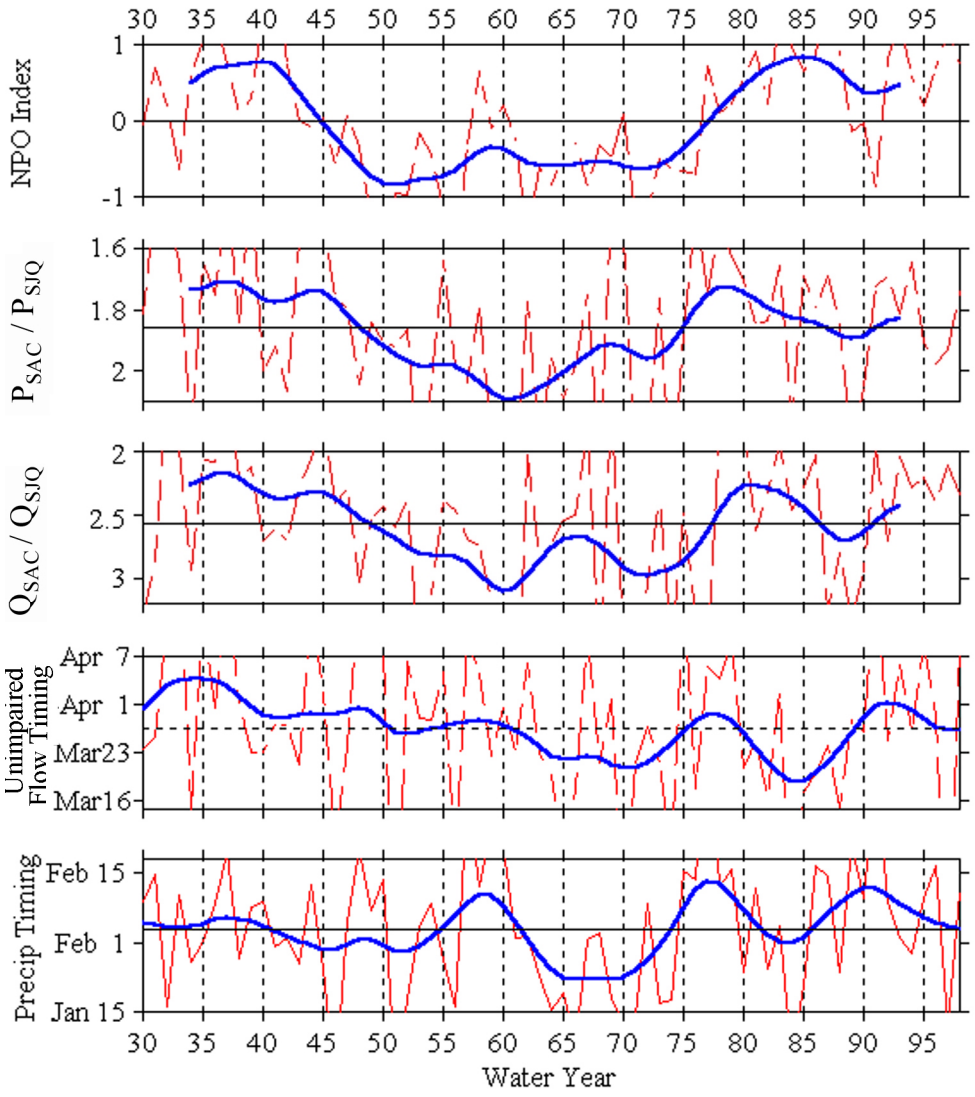

Figure 7.16 NPO, Sacramento vs. San Joaquin precipitation and outflow ratios, and timing of Delta outflow and Sacramento basin precipitation. Annual values are shown in red; 10-year low-pass filtered values in blue.

precipitation peaks centered on 1958 and 1977. The response of flow timing to the first of these peaks was quite muted compared to the second. This makes sense if NPO is playing a role, since in 1958 the NPO effect was to counteract the late precipitation timing, while in 1977 the NPO effect was neutral.

7.3.5 Discussion of Climate Effects

Clearly, known patterns of climate variability such as ENSO and NPO have detectable effects in both the Bay-Delta estuary and watershed. The mechanism by which these signals propagate through the system begins with the oceanic climate signals altering the mean position of the storm track which delivers precipitation to the watershed. Both NPO and ENSO are associated with north-south shifts in the storm track, which alters the distribution of precipitation between the two halves of the watershed. The distinct hydrologic behavior of these two regions means the climate signal then propagates to the watershed outflow, primarily as changes in the timing of the annual hydrograph which drives the estuarine salinity cycle.

While outflow timing shifts are associated with the ENSO phenomenon with a good degree of statistical significance, NPO-related effects are more difficult to verify due to human and other natural influences operating on the system at the interdecadal time scale. Interdecadal variability of salinity and outflow timing are a result of both natural and human-induced variability. Human effects have varied over time with increased development, a correlation with natural variability, and changes in policy. Natural variability is influenced at the interdecadal scale by three main factors: changes in precipitation timing, a long-term trend toward earlier runoff, and NPO-related timing shifts.

It is particularly interesting to note that since 1977, NPO has been in a “phase” which has tended to counteract the effects of the long-term warming trend. Preliminary evidence suggests that NPO may have shifted phase in the last few years.

If this is true, and if the warming trend continues, it is possible that a tendency for very early runoff may characterize the next few decades.

While the combination of human and natural effects described above explain the multi-decadal "trends" in salinity timing first presented in Chapter 2 (Figure 2.4, "timing mode"), one question remains: what is the cause of the long-term trend apparent in the "magnitude" mode of the E-EOF salinity analysis (Figure 2.4, mode 1 amplitude) toward higher mean annual salinities over the period WY 30-98? While it seems clear that increasing diversions of freshwater contributed to this increase, there was no strong (statistically significant) corresponding decrease in Bay inflows over this period (Table 2.2). It was postulated in Chapter 2 that mean annual salinities may have been affected by the timing shifts in Bay inflows, which show strong statistical significance (Table 2.2), through a nonlinear interaction between inflow timing and mean annual salinity. The next section investigates the possibility that this effect enhances the long-term trend in Bay salinity levels.

7.3.6 Can Inflow Timing Affect Mean Salinity?

It was shown in Section 7.2 that despite higher average flows in early-flow years, the weaker, broader, snowmelt-driven hydrograph of late-flow years was equally effective at keeping down annually-averaged salinities in the estuary. This would seem to suggest that two hydrographs of equal volume, differing only in hydrologic character, would generate different annually-averaged salinities.

In order to test the hypothesis that annual salinity is affected by runoff timing, smoothed (30-day low-pass filtered) mean hydrographs were generated separately from Delta outflow estimates for two periods of very different outflow timing – WY 35-45 and WY 65-75. The smoothed hydrographs were adjusted to have the same dry-season flow, so only wet-season timing shifts were apparent. Finally, the two

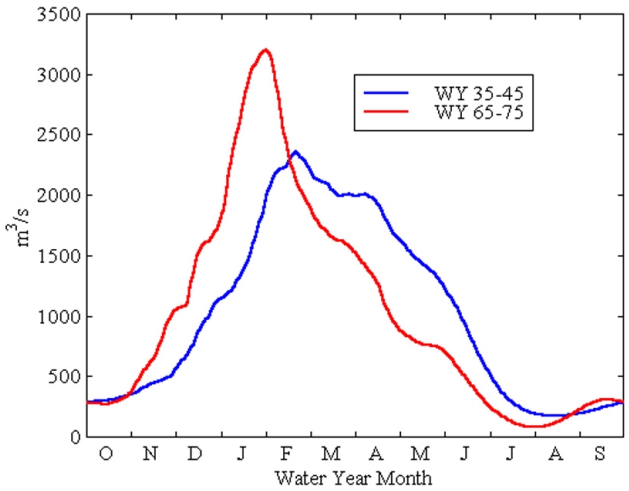

Figure 7.17 Composite mean annual hydrographs for two periods with differing outflow timing. The hydrographs have been adjusted to have the same initial and total flow values.

hydrographs were normalized to have the same total annual flow (the mean flows for the two composites were originally 891 m^3/s and 588 m^3/s, chronologically). The resulting hydrographs are shown in Figure 7.17.

The difference in hydrologic character of the two hydrographs is evident, with the WY 35-65 period characterized by a broad, strong snowmelt delay, while the WY 65-75 period is more influenced by the peaky runoff of rainfall due to the effects of management and natural forcing reducing the snowmelt portion of the hydrograph.

Based on the two adjusted composite hydrographs, and using the 10-year smoothed Delta flow timing from Figure 7.14 to determine the relative mix of these two hydrographs, a 69-year time series (WY 30-98) was generated which reflected only interdecadal shifts in intraannual flow timing and no year-to-year changes in flow magnitude. That is, the annually-averaged flow magnitude in this idealized Delta outflow is the same for all 69 years, and the flow timing corresponds exactly to the 10-year low-pass filtered Delta outflow timing shown in Figure 7.14 (2nd plot, blue line).

This time series was used to drive the UP salinity model, with ocean salinity held to its long-term mean, local precipitation neglected, and using a mean annual cycle of evaporation. Tidal data from Fort Point were used for the period WY 30-98. The annually-averaged Baywide salinity changes resulting from the inflow timing shifts are shown in Figure 7.18.

This figure shows an increase in salinity of over 1 *psu* from 1940-1973 resulting from Bay inflow timing shifts associated with natural and human-induced effects. A clear modulation of this effect by the 19-year tidal cycle is also apparent,

particularly in the late 1980's when annual averages of daily standard deviations in water levels were relatively high.

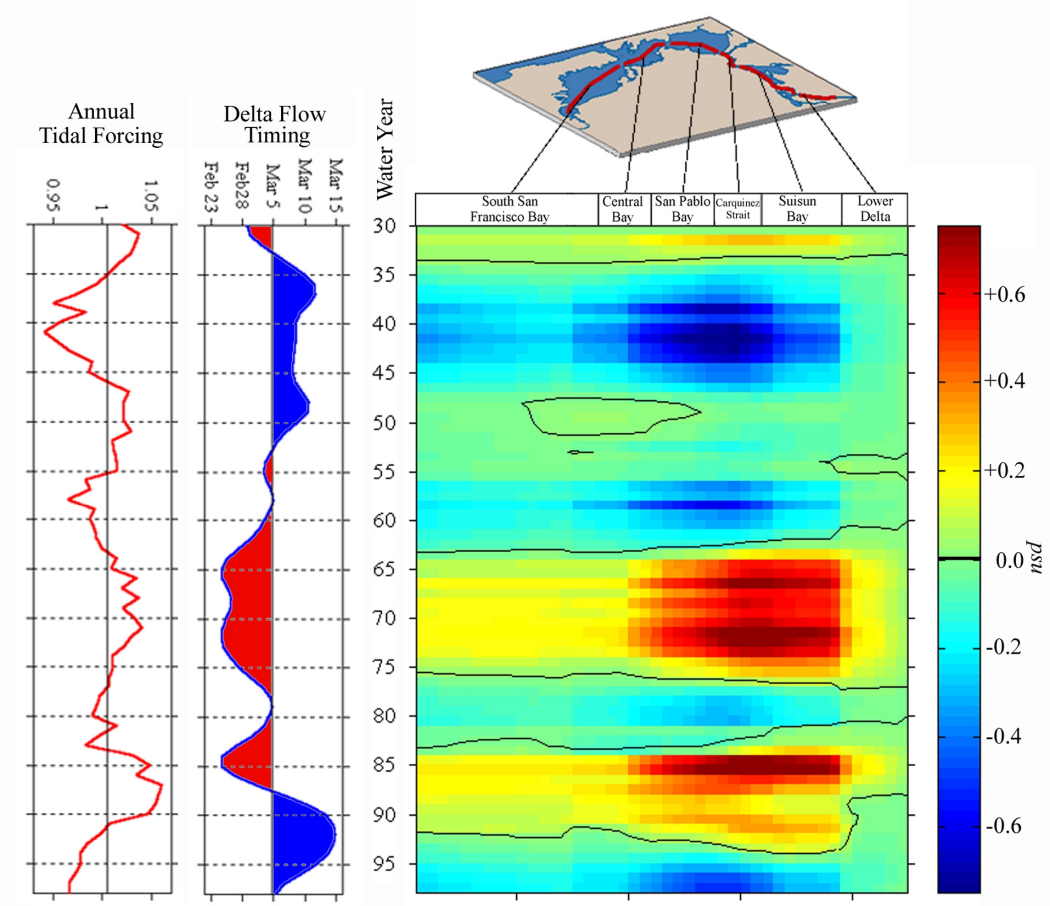

Figure 7.18 Salinity changes resulting from timing shifts in the annual inflow hydrograph. The associated timing shifts and standardized average annual daily standard deviation of tidal forcing are shown on the left.

Clearly, timing shifts alone can be responsible for significant changes in mean salinity levels, without any change in the total annual inflow volume. The salinity changes are even stronger if a shorter average is considered. For example, taking January-July averages instead of annual averages results in salinity changes approximately twice as large. Also, the hydrograph shift in Figure 7.17 represents a

change of the annual mean flow timing (the "center of mass" date of the hydrograph) of only 3 weeks. Larger shifts could have more significant impacts on salinity.

Finally, note the similarity of the Baywide patterns in Figure 7.18 and in the mode 1 spatial loading factors of Figure 2.4. The result that changes in mean salinity may be related to changes in runoff timing suggest a possible connection between the trends in the timing and magnitude of the salinity modes, at least in the early part of the record, from WY 1930-1970.

7.4 Summary and Conclusions

In this chapter, we have begun to complete the circle started in Chapter 2, linking large-scale, long-term variability of the San Francisco Bay-Delta estuary to climate forcing of its watershed. Along the way, year-to-year and decade-to-decade climate variability has been depicted as the natural and inevitable context of the estuarine ecosystem. Human activities, such as reservoir operation and freshwater pumping, have a large impact, but themselves depend strongly on the natural climate variability. Though these human effects can be very significant, they are overwhelmed by the extremes of natural variability (Figure 4.9).

The complex set of factors which determines hydrologic variability in the upstream watershed was also examined in detail, and a synthesis of data was derived to characterize for the first time the hydrologic behavior of the entire Bay-Delta watershed on a physical basis. Using this data, a new modeling approach was

implemented which provides the ability to conduct investigations into fundamental issues of hydrology with the richly diverse Bay-Delta watershed as the laboratory.

The new watershed model, combined with the Uncles-Peterson estuary model, provides a complete modeling system from the Sierra to the Golden Gate. Filling this crucial modeling gap opens up new areas to research, and provides an essential tool for conducting integrated interdisciplinary studies of the estuary/watershed system.

Applying the new modeling capability to the watershed, mechanisms which contribute to hydrologic variability were examined at a level of detail previously unattainable. It was shown how the higher elevations present in the southern half of the Bay-Delta watershed lead to a more snowmelt –dominated hydrograph there, while the northern half of the watershed is characterized by a more peaked rainfall runoff hydrograph.

In a remarkable coincidence, patterns associated with climate variability correspond spatially with these north-south differences in the watershed's hydrologic character. This fact was exploited to understand the degree to which the climate signals propagate through the watershed and into the estuary.

These experiments have also presented new mysteries. Foremost among them, and most critical to improving our understanding of the watershed's variability as well as the model's performance, is the nature of high-altitude meteorological variability. The details of the upstream variability have been shown to have an enormous impact on basin freshwater outflows to the estuary, yet are marked by considerable uncertainty. Besides improving the upper altitude observational network, one

possibility for improvement is the coupling of this model to orographic atmospheric models over the watershed, which should provide much more detailed estimates of temperature and precipitation than are obtainable by statistical means alone.

Another pressing question regards the effects of global warming on hydrologic and estuarine processes. The results presented here suggest that an overall increase in temperatures would reduce snow effects, leading to an earlier, peaked rainfall runoff hydrograph, which in turn might raise mean salinities in the estuary. The new combined model will permit in-depth investigations into the implications of such changes for water resource management and ecosystem restoration efforts.

The combined estuary/watershed model is also suitable for use in streamflow/salinity forecast studies. The numerical efficiency of the model, combined with its minimal data requirements, make it ideal for generating ensembles of simulations representing the range of likely conditions in the estuary and watershed. This would allow the generation of probabilistic forecasts of estuarine and hydrologic quantities weeks to months in advance, allowing the predictability of the estuary/watershed system to be studied.

Finally, the Uncles-Peterson Bay-Delta estuarine model has recently been extended to include simulation capabilities for various passive and active tracers. This permits investigations into processes critical to the biology and chemistry of the estuarine ecosystem. Similar extensions are feasible for the watershed model, potentially expanding the range of possible research enormously.

8 Appendix A: Flow Gauge Information

The following information was obtained from http://waterdata.usgs.gov/nwis-w/CA.

Gauge Designation from Figure 3.3	USGS Gauge #	Name	Longitude (decimal degrees)	Latitude (decimal degrees)	Drainage Area (km^2)	Datum (m above NGVD)
1	11221500	Kings R Bl Pine Flat Dam	-119.3	36.8	4001.6	169.8
2	11251000	San Joaquin R Bl Friant	-119.7	37.0	4340.8	89.6
3	11261500	San Joaquin R A Fremont Ford Br Nr Stev	-120.9	37.3	19722.9	N/A
4	11270900	Merced R Bl Merced Falls Dam Nr Snell	-120.3	37.5	2748.0	N/A
5	11272500	Merced R Nr Stevinson	-120.9	37.4	3297.1	22.3
6	11274000	San Joaquin R Nr Newman	-121.0	37.4	24656.8	N/A
7	11289650	Tuolumne R Bl Lagrange Dam Nr Lagrange	-120.4	37.7	3983.4	N/A
8	11290000	Tuolumne R A Modesto	-121.0	37.6	4879.6	15.2
9	11302000	Stanislaus R Bl Goodwin Dam Nr Knights Ferry	-120.6	37.9	2553.7	N/A
10	11303500	San Joaquin R Nr Vernalis	-121.3	37.7	35058.2	7.6
11	11319500	Mokelumne R Nr Mokelumne Hill	-120.7	38.3	1409.0	178.3
12	11329500	Dry C Nr Galt	-121.2	38.2	839.2	16.1
13	11335000	Cosumnes R A Michigan Bar	-121.0	38.5	1388.2	51.2
14	11370500	Sacramento R A Keswick	-122.4	40.6	16752.1	146.2
15	11389000	Sacramento R A Butte City	-122.0	39.5	31274.3	-0.9
16	11407150	Feather R Nr Gridley	-121.6	39.4	9520.8	N/A
17	11421000	Yuba R Nr Marysville	-121.5	39.2	3468.0	-0.9
18	11424000	Bear R Nr Wheatland	-121.4	39.0	756.3	21.9
19	11425500	Sacramento R A Verona	-121.6	38.8	55040.1	-0.9
20	11426000	Sac Weir Spill To Yolo Bypass Nr Sac	-121.6	38.6	N/A	N/A
21	11446500	American R A Fair Oaks	-121.2	38.6	4889.9	21.8
22	11447650.0	Sacramento R A Freeport	-121.5	38.5	N/A	N/A
23	11452500	Cache C A Yolo	-121.8	38.7	2950.0	15.9
24	11453000	Yolo Bypass Nr Woodland	-121.6	38.7	N/A	15.9
25	11454000	Putah C Nr Winters	-122.1	38.5	1486.7	49.0

Table 8.1 Details of NWIS gauge stations used in this study.

9 Appendix B: UEB Snow Model Calculations

9.1 Shortwave Radiation

Note that though incoming solar radiation, Q_{si}, is shown in Figure 6.3 as an input to the UEB model, it is not among the inputs generated in Section 5.5. When this data is not available, the UEB model estimates it. The model's formulation for net shortwave radiation is:

$$Q_{sn} = Q_{si}(1-A) = T_f I_0 \alpha_{hri}(1-A) \qquad 9.1$$

where A is the albedo, a function of solar illumination angle (adjusted for local slope and aspect) and snow surface age, and Q_{si} is the incoming solar radiation, a function of a transmission factor T_f, the solar constant I_0=4914 $kJ/m^2/hour$, and α_{hri}, a multiplication factor to account for the relative effects of the solar angle and the local slope. This factor is given as:

$$\alpha_{hri} = \frac{1}{\cos(\frac{dz}{dx})\Delta t} \int_{t}^{t+\Delta t} \cos(\Psi(t))dt \qquad 9.2$$

where $\frac{dz}{dx}$ represents the local slope, Δt =6 hours in the present UEB configuration, and $\Psi(t)$ is the Sun's angle above the horizon.

The transmission factor T_f is estimated using the formulation developed by Bristow and Campbell (Bristow and Campbell 1984), wherein the diurnal temperature range ΔT is used as a proxy for cloud cover (more cloud cover leads to cooler

daytime temperatures and a smaller $\vartriangle T$), and thus for transmissivity. The Bristow-Campbell formulae are:

$$T_f = a\left[1 - e^{-b(\vartriangle T)^c}\right] \quad \text{with} \quad a = 0.8,\ c = 2.4, \text{ and} \qquad 9.3$$
$$b = 0.036e^{-0.154\overline{\vartriangle T}}$$

The values for *a* and *c* were determined empirically by Bristow and Campbell for their study site, but Tarboten *et al.* found them to apply satisfactorily at the Central Sierra Snow Lab as well.

9.2 Longwave Radiation

In the UEB model, outgoing longwave radiation is given by:

$$Q_{le} = \varepsilon_s \sigma T_s^4 \qquad 9.4$$

where ε_s is the emissivity (~0.99 for snow), σ is the Stefan Boltzmann constant, and T_s is the snow's surface temperature, the determination of which will be addressed later.

It is important to note that the UEB model is designed for the simulation of snowpack processes, and Q_{le} is valid as a representation of outgoing longwave radiation only when snow is present.

The calculated incoming longwave radiation, however, is valid in general, and is given by 9.4 using the emissivity for air, ε_a, in place of that for snow, and using air temperature, T_a, in place of snow surface temperature. The UEB model uses a

parameterization of emissivity under clear-sky conditions by Satterlund (Satterlund 1979):

$$\varepsilon_{acls} = 1.08\left[1 - e^{-\left(\frac{e_a}{100}\right)^{T_a/2016}}\right] \qquad 9.5$$

where this clear-sky emissivity is a function of air temperature in degrees C, T_a, and vapor pressure in Pa, e_a. Total air emissivity also depends on cloud cover, since clouds are a more effective emitter of longwave radiation than clear air (with an emissivity of ~1). Cloud cover is estimated from Equation 9.3 as:

$$\beta_{CF} = 1 - \frac{T_f}{a} \qquad 9.6$$

This is based on the idea that as cloud cover fraction approaches 0, the transmission factor T_f will approach its maximum value, a, and that the converse is also true. The emissivity of air is then calculated as a weighted sum of cloudy and clear sky emissivities:

$$\varepsilon_a = \beta_{CF} + (1 - \beta_{CF})\varepsilon_{acls} \qquad 9.7$$

The incoming longwave radiation is then given by:

$$Q_{li} = \varepsilon_a \sigma T_a^4 \qquad 9.8$$

9.3 Other Heat Fluxes

The incoming precipitation is partitioned into rain (P_r) and snow (P_s) according to air temperature (U.S. Army Corps of Engineers 1956). If $T_a > 3°C$, all

precipitation is liquid; if $T_a < -1°C$, all precipitation is snow. Between the two temperatures, the ratio of rain to snow is determined by linear interpolation between these two values. The temperature assigned to the rain and snow determine the energy advected to the snowpack: "The temperature of rain is taken as the greater of the air temperature and freezing point and the temperature of snow is the lesser of air temperature and freezing point. The advected heat, Q_p, is the energy required to convert this precipitation to the reference state ($0°C$ ice phase)" (Tarboton and Luce 1996).

The remaining heat fluxes are the sensible and latent heat fluxes, Q_h and Q_e. These fluxes are proportional to gradients in temperature and vapor pressure, respectively. They are given by:

$$Q_h = K_h \rho_a C_p \left(T_a - T_s\right) \qquad 9.9$$

$$Q_e = -h_v M_e = -h_v K_e \rho_a \left(q_s - q\right) \qquad 9.10$$

where ρ_a is the density of air, C_p is the specific heat capacity of air, h_v is the latent heat of sublimation, q is the specific humidity of the air, and q_s is the specific humidity near the surface. K_h and K_e are the constants of proportionality known as the turbulent transfer coefficients. These represent the effectiveness of air turbulence in generating flux near the surface, and they depend on wind speed and height above the surface:

$$K_h = K_e = \frac{k^2 V_w}{\left[\ln\left(\frac{z}{z_0}\right)\right]^2} \qquad 9.11$$

where k=0.4, V_w is the wind speed from the climatology developed in Section 5.5.3, and z and z_0 are, respectively, the height corresponding to the measurement height of V_w, and the height at which the boundary layer wind speed profile becomes zero due to frictional resistance from the ground. In this study, z_0 =0.005 m and z =2.0 m.

Typically, turbulent transfers such as these are modified by temperature gradients near the ground, and such effects are incorporated into the formulation by using the Richardson number, the ratio of the buoyancy-inducing temperature gradients to the turbulence-inducing velocity gradient. The designers of the UEB model found this method induced numerical instabilities in the model, and therefore decided not to include these effects.

Expressing specific humidity in terms of vapor pressure, Equation 9.10 becomes:

$$Q_e = K_e \frac{h_v 0.622}{R_d T_a}\left(e_a - e_s(T_s)\right) \qquad 9.12$$

where R_d is the dry gas constant (287 *J/kg/K*), e_a is the vapor pressure of the air, determined from the climatological relative humidity and the air temperature, and $e_s(T_s)$ is the (saturated) surface vapor pressure, a function of the snow surface temperature.

The amount of sublimated water corresponding the vapor flux is then:

$$E = -\frac{Q_e}{\rho_w h_v} \qquad 9.13$$

9.4 Snowpack and Snow Surface Temperatures

Many of the calculations shown so far have involved the snowpack surface temperature T_s. This temperature is determined as the temperature at which all heat fluxes across the snowpack surface balance. The only flux in this balance which has not yet been given is the flux of heat into the snowpack, *Q*. This is calculated using the temperature gradient within the snowpack as:

$$Q = K_s \rho_s C_s \left(T_s - T\right) \qquad 9.14$$

where K_s is the thermal diffusivity of snow divided by the effective depth of the temperature gradient, assigned as 0.02 *m/hour*, ρ_s is the density of snow (450 kg/m^3), and C_s is the heat capacity of snow (2.09 *kJ/kg/C*). *T* is the average snowpack/upper soil layer temperature, calculated as a function of the state variables, *U* and *W*, the heat of fusion of water, the heat capacity of soil, and the heat capacity of snow. T_s is then determined by iterative methods as the value which satisfies the balance:

$$Q = Q_{sn} + Q_{li} + Q_h(T_s) + Q_e(T_s) + Q_p - Q_{le}(T_s) \qquad 9.15$$

If the resulting T_s is greater than freezing, then enough snow is converted to liquid water to make up the difference.

9.5 Liquid Water Output

The liquid fraction, L_f, of the snowpack water equivalent is determined as:

$$L_f = \frac{U}{\rho_w h_f W} \qquad 9.16$$

The liquid outflow from the snowpack, M_r, is derived from the snowpack equivalent of Darcy's law, Equation 5.1, with L_f playing the role of soil moisture. The melted water is assumed to be at $0°C$, so the advected heat is:

$$Q_m = \rho_w h_f M_r \qquad 9.17$$

This completes the description of all terms in Equations 6.3.

9.6 Forest Density

The final ingredient in the UEB model is forests. Forests reduce winds and radiation fluxes, among other effects. Their effect on snowpack in a given model element is determined by the forest density data introduced in Section 5.4, representing average canopy closure over the element. The UEB model avoids the complex treatment of forest canopies found in some other models, simply representing the forest effect as attenuation of wind speed and radiative fluxes. Wind speed is reduced by a factor of $(1-0.8FC)$, where FC is the forest canopy closure, varying from 0 to 1 for complete coverage. Radiative fluxes Q_{sn}, Q_{li} and Q_{le} are reduced by $(1-FC)$.

References

Aguado, E., D. Cayan, L. Riddle and M. Roos (1992). "Climatic Fluctuations and the Timing of West Coast Streamflow." Journal of Climate **5**(12): 1468-1483.

Ahrens, C. D. (1994). Meteorology today : an introduction to weather, climate, and the environment. Minneapolis/St. Paul, West Pub.

Anderson, E. A. (1973). National Weather Service River Forecast System-Snow Accumulation and Ablation Model, U.S. Dept of Commerce.

Anderson, E. A. (1976). A Point Energy and Mass Balance Model of a Snow Cover, U.S. Department of Commerce.

Atwater, B. F., S. G. Conard, J. N. Dowden, C. W. Hedel, R. L. MacDonald and W. Savage (1979). History, landforms, and vegetation of the estuary's tidal marshes. San Francisco Bay-the urbanized estuary. T. J. Conomos, AAAS, Pacific Division**:** 347-386.

Avissar, R. and D. Rind (1992). "Conceptual aspects of a statistical-dynamical approach to represent landscape subgrid-scale heterogeneities in atmospheric models." Journal of Geophysical Research, D, Atmospheres **97**(3): 2729-2742.

Bae, D. H. and K. P. Georgakakos (1992). Hydrologic modeling for flow forecasting and climate studies in large drainage basins, Iowa Inst. of Hydraulic Research and Dept. of Civil and Envirnmental Eng., University of Iowa.

Bay Institute (1998). From the Sierra to the Sea: the ecological history of the San Francisco Bay-Delta watershed. San Rafael, CA, The Bay Institute.

Betson, R. P., R. L. Tucker and F. M. Haller (1969). "Using analytical methods to develop a surface-runoff model." Water Resources Research **5**(1): 103-111.

Beven, K. J., M. J. Kirkby, N. Schofield and A. F. Tagg (1984). "Testing a physically-based flood forecasting model (TOPMODEL) for three U.K. catchments." Journal of Hydrology **69**(1-4): 119-143.

Bristow, K. L. and G. S. Campbell (1984). "On the Relationship Between Incoming Solar Radiation and the Daily Maximum and Minimum Temperature." Agricultural and Forest Meteorology **31**(159-166).

Brooks, R. H. and A. T. Corey (1964). Hydraulic properties of porous media. Fort Collins, Colorado State University.

Brutsaert, W. (1988). The formulation of evaporation from land surfaces. Recent advances in the modeling of hydrologic systems. D. S. Bowles and P. E. O'Connell, Kluwer Academic.

Burnash, R. J. C. and R. L. Ferral (1983). "Evapotranspiration and soil moisture processes in the Sacramento model." Eos, Transactions, American Geophysical Union **64**(45): 711.

California Department of Water Resources (1998). Water Conditions in California, California Department of Water Resources. **3**.

California Department of Water Resources (1999). DAYFLOW Data, California Department of Water Resources. **1999**.

Campbell, G. S. (1974). "A simple method for determining unsaturated conductivity from moisture retention data." Soil Science **117**(6): 311-314.

Cayan, D. (1999). The Spring Runoff Pulse from the Sierra-Nevada. 14th Conference on Hydrology, Dallas, Texas, American Meteorological Society.

Cayan, D. R. (1996). "Interannual Climate Variability and Snowpack in the Western United States." Journal of Climate **9**(5): 928-948.

Cayan, D. R. and D. H. Peterson (1993). "Spring Climate and Salinity in the San Francisco Bay Estuary." Water Resources Research **29**(2): 293-303.

Cayan, D. R., K. T. Redmond and L. G. Riddle (1999). "ENSO and hydrologic extremes in the western United States." Journal of Climate **12**(9): 2881-2893.

Cayan, D. R., L. G. Riddle and E. Aguado (1993). "The Influence of Precipitation and Temperature On Seasonal Streamflow in California." Water Resources Research **29**(4): 1127-1140.

Cayan, D. R. and R. H. Webb (1992). El Niño /Southern Oscillation and streamflow in the western United States. El Niño -Historical and Paleoclimatic Aspects of the Southern Oscillation. H. F. Diaz and V. Markgraf, Cambridge University Press**:** 29-68.

Cheng, R. T. and J. W. Gartner (1984). Tides, tidal and residual currents in San Francisco Bay, California--results of measurements, 1979-1980. Part I: description of data, U.S. Geological Survey, Water Resources Division.

Chua, S.-H. and R. L. Bras (1982). "Optimal estimators of mean areal precipitation in regions of orographic influence." Journal of Hydrology **57**(1-2): 23-48.

Clapp, R. B. and G. M. Hornberger (1978). "Empirical equations for some soil hydraulic properties." Water Resources Research **14**(4): 601-604.

Cloern, J. E. and F. H. Nichols (1985). Temporal dynamics of an estuary : San Francisco Bay. Dordrecht ; Boston
Hingham, MA, W. Junk ;
Distributors for the U.S. and Canada Kluwer Boston.

Conomos, T. J., American Society of Limnology and Oceanography and American Association for the Advancement of Science. Pacific Division (1979). San Francisco Bay : the urbanized estuary : investigations into the Natural History of San Francisco Bay and Delta with reference to the influence of man : fifty-eighth annual meeting of the Pacific Division American Association for the Advancement of Science held at San Francisco State University, San Francisco, California, June 12-16, 1977. San Francisco, Calif., The Division.

Conomos, T. J., R. E. Smith and J. W. Gartner (1985). Environmental setting of San Francisco Bay. Temporal Dynamics of an Estuary: San Francisco Bay. J. E. Cloern and F. H. Nichols, Developments in Hydrobiology, Dr. W. Junk Publishers**:** 1-12.

Cosby, B. J., G. M. Hornberger, R. B. Clapp and T. R. Ginn (1984). " A statistical exploration of the relationships of soil moisture characteristics to the physical properties of soils." Water Resources Research **20**(6): 682-690.

Crawford, N. H. and R. K. Linsley (1966). Digital simulation in hydrology: Stanford Watershed Model IV. Stanford, CA, Department of Civil Engineering, Stanford University.

Deetz, C. H. (1934). Elements of map projection with applications to map and chart construction (4th ed.), U.S. Coast and Geodetic Survey.

Dettinger, M. D. (2000). "Variability of seasonal Sierra Nevada streamflow and San Francisco Bay salinity." in press.

Dettinger, M. D. and D. R. Cayan (1995). "Large-Scale Atmospheric Forcing of Recent Trends Toward Early Snowmelt Runoff in California." Journal of Climate **8**(3): 606-623.

Dettinger, M. D., D. R. Cayan, H. F. Diaz and D. M. Meko (1998). "North-south precipitation patterns in western North America on interannual-to-decadal timescales." Journal of Climate **11**(12): 3095-3111.

Deutsch, C. V. and A. G. Journel (1998). GSLIB: Geostatistical software library and user's guide. New York, Oxford University Press.

Fischer, H. B., E. J. List, R. C. Y. Koh, J. Imberger and N. H. Brooks (1979). Mixing in Inland and coastal waters. New York, Academic Press.

Galloway, D. L., D. R. Jones and S. E. Ingebritsen (1999). Land subsidence in the United States. Reston, VA, U.S. Geological Survey.

Georgakakos, K. and O. W. Baumer (1996). "Measurement and Utilization of On-Site Soil Moisture Data." Journal of Hydrology **184**(1-2): 131-152.

Georgakakos, K. P. and R. L. Bras (1982). "Real-time, statistically linearized, adaptive flood routing." Water Resources Research **18**(3): 513-524.

Gerald, C. F. (1978). Applied Numerical Analysis, 2nd Edition. Reading, MA, Addison Wesley.

Ghosh, R. K. (1980). "Estimation of soil-moisture characteristics from mechanical properties of soils." Soil Science **130**(2): 60-63.

Gleick, P. H. (1986). Regional water availability and global climatic change : the hydrologic consequences of increases in atmospheric CO2 and other trace gases**:** 2 v.

Goovaerts, P. (2000). "Geostatistical approaches for incorporating elevation into the spatial interpolation of rainfall." Journal of Hydrology **228**(1-2): 113-129.

Guetter, A. K. and K. P. Georgakakos (1996). "Large-Scale Properties of Simulated Soil Water Variability." Journal of Geophysical Research-Atmospheres **101**(D3): 7175-7183.

Healy, R. W. (1990). Simulation of solute transport in variably saturated porous media with supplemental information on modifications to the U.S. Geological Survey's computer program VS2D, U. S. Geological Survey**:** 125.

Hedgpeth, J. W. (1979). San Francisco Bay: the unsuspected estuary. San Francisco Bay-the urbanized estuary. T. J. Conomos, AAAS, Pacific Division**:** 9-30.

Herbold, B. (1995). "Comparison of new standards and historical flows." Interagency Ecological Program for the Sacramento-San Joaquin Estuary Newsletter(Summer): 12-14.

Hillel, D. (1980). Fundamentals of soil physics. New York, Academic Press.

Hollibaugh, J. T., Ed. (1996). San Francisco Bay : the ecosystem : further investigations into the natural history of San Francisco Bay and Delta with reference to the influence of man. San Francisco, Calif., Pacific Division of the American Association for the Advancement of Science.

Holtan, H. N. (1961). A concept for infiltration estimates in watershed engineering. Beltsville, MD, Agricultural Research Service, USDA**:** 24.

Ingram, B. L., J. C. Ingle and M. E. Conrad (1996). "A 2000 Yr Record of Sacramento San Joaquin River Inflow to San Francisco Bay Estuary, California." Geology **24**(4): 331-334.

James, L. D. (1972). "Hydrologic modeling, parameter estimation and watershed characteristics." Journal of Hydrology **17**.

Jassby, A. D., W. J. Kimmerer, S. G. Monismith, C. Armor, J. E. Cloern, T. M. Powell, J. R. Schubel and T. J. Vendlinski (1995). "Isohaline Position As a Habitat Indicator For Estuarine Populations." Ecological Applications **5**(1): 272-289.

Journel, A. G. and C. Huijbregts (1978). Mining geostatistics. London ; New York, Academic Press.

Kahrl, W. L., California Office of Planning and Research and California Dept. of Water Resources (1979). The California water atlas. Sacramento/Los Altos, Calif., The Governor's Office of Planning and Research ; distributed by William Kaufmann.

Karl, T. and R. Knight (1998). "Secular trends of precipitation amount, frequency, and intensity in the Unites States." Bull. Amer. Meteor. Soc. **79**: 231-241.

Kaylor, R. E. (1977). Filtering and decimation of digital time series. College Park, MD, University of Maryland**:** 14.

Kendall, M. G. (1938). "A new measure of rank correlation." Biometrika **30**: 81-93.

Kiladis, G. N. and H. F. Diaz (1989). "Global climatic anomalies associated with extremes of the Southern Oscillation." Journal of Climate **2**: 1069-1090.

Knowles, N. (1996). Simulation and Prediction of Salinity Variability in San Francisco Bay. Scripps Institution of Oceanography. La Jolla, CA, University of California, San Diego.

Knowles, N., D. Cayan, L. Ingram, D. H. Peterson and R. J. Uncles (1997). "Diagnosing the Flood of 1997 in San Francisco Bay with Observations and Model Results." Interagency Ecological Program Newsletter **10**(Summer).

Knowles, N., D. Cayan, D. H. Peterson and R. J. Uncles (1995). "Modeling and Predicting Intertidal Variations of the Salinity Field in the Bay/Delta." Interagency Ecological Program Newsletter **8**(Fall).

Knowles, N., D. Cayan, D. H. Peterson and R. J. Uncles (1998). "Simulated Effects of Delta Outflow on the Bay: 1998 Compared to Other Years." Interagency Ecological Program Newsletter **11**(Fall): 29-31.

Knox, J. B. (1991). Global Climate Change and California, University of California Press.

Kondo, J. and T. Yamazaki (1990). "A prediction model for snowmelt, snow surface temperature and freezing depth using a heat balance method." Journal of applied meteorology **29**: 375-384.

Krannich, R. S., S. P. Keenan, M. S. Walker and D. L. Hardesty (1995). "Social Implications of Severe Sustained Drought - Case Studies in California and Colorado." Water Resources Bulletin **31**(5): 851-865.

Lappala, E. G., R. W. Healy and W. E. P. (1987). Documentation of computer program VS2D to solve the equations of fluid flow in variably saturated porous media, U. S. Geological Survey**:** 184.

Latif, M. and T. P. Barnett (1994). "Causes of Decadal Climate Variability Over the North Pacific and North America." Science **266**(5185): 634-637.

Latif, M. and T. P. Barnett (1996). "Decadal Climate Variability Over the North Pacific and North America - Dynamics and Predictability." Journal of Climate **9**(10): 2407-2423.

Leavesley, G. H., R. W. Lichty, B. M. Troutman and L. G. Saindon (1983). Precipitation-Runoff Modeling System: User's Manual, U.S. Geological Survey**:** 207.

Leopold, L. B. (1994). A view of the river. Cambridge, Mass., Harvard University Press.

Lettenmaier, D. P. and T. Y. Gan (1990). "Hydrologic Sensitivities of the Sacramento-San-Joaquin River Basin, California, to Global Warming." Water Resources Research **26**(1): 69-86.

Liang, X., E. F. Wood and D. P. Lettenmaier (1996). "Surface soil moisture parameterization of the VIC-2L model: Evaluation and modifications." Global and Planetary Change **13**: 195-206.

Maidment, D. R. (1993). Handbook of hydrology. New York, McGraw-Hill.

Mantua, N. J., S. R. Hare, Y. Zhang, J. M. Wallace and R. C. Francis (1997). "A Pacific interdecadal climate oscillation with impacts on salmon production." Bulletin of the American Meteorological Society **78**(6): 1069-1079.

Masutani, M. and A. Leetmaa (1999). "Dynamical mechanisms of the 1995 California floods." Journal of Climate **12**(11): 3220-3236.

Matheron, G. and C. Huijbregts (1971). Universal Kriging (An Optimal Method for Estimating and Contouring in Trend Surface Analysis). Decision-Making in the Mineral Industry. Montreal, PQ, Canadian Institute of Mining and Metallurgy. **12:** 159-169.

McCarthy, G. T. (1938). The unit hydrograph and flood routing. New London, CT, U.S. Army Corps of Engineers.

Monteith, J. L. (1965). "Evaporation and the environment." Symp. Soc. Expl. Biol. **19**: 205-234.

Morris, E. M. (1982). Sensitivity of the European Hydrological System snow models. Hydrological Aspects of Alpine and High Mountain Areas, Proceedings of the Exeter Symposium, IAHS.

Mount, J. F. (1995). California rivers and streams : the conflict between fluvial process and land use. Berkeley, University of California Press.

Mullusky, M. G. and K. P. Georgakakos (1993). Sensitivity of large-basin hydrology, forecasts and management to historical climatic forcing. Iowa City, IA, Iowa Inst. of Hydraulic Research and Dept. of Civil and Environmental Eng., University of Iowa**:** 169.

Munk, W. H. and E. R. Anderson (1948). "Note on the theory of the thermocline." Journal of Marine Research **7**: 276-295.

Namias, J. (1979). CALCOFI Atlas No. 27. La Jolla, CA.

Nichols, F. H. (1985). "Increased benthic grazing: An alternative explanation for low phytoplankton biomass during the 1976-1977 drought." Estuarine Coastal Shelf Sci. **21**: 379-388.

Nichols, F. H., J. K. Thompson and L. E. Schemel (1990). "Remarkable Invasion of San-Francisco Bay (California, Usa) By the Asian Clam Potamocorbula-Amurensis .2. Displacement of a Former Community." Marine Ecology-Progress Series **66**(1-2): 95-101.

Norris, R. M. and R. W. Webb (1990). Geology of California, 2nd ed., Wiley.

Null, J., , 55. (1995). Climate of San Francisco. Monterey, CA, National Oceanic and Atmospheric Agency, National Weather Service.

Olea, R. A. (1991). Geostatistical glossary and multilingual dictionary. New York, Oxford University Press.

Peterson, D., D. Cayan, J. Dileo, M. Noble and M. Dettinger (1995). "The Role of Climate in Estuarine Variability." American Scientist **83**(1): 58-67.

Peterson, D. H., R. E. Smith, M. D. Dettinger, D. R. Cayan and L. Riddle (2000). "An organized signal in snowmelt runoff over the western United States." Journal of the American Water Resources Association **36**(2): 421-432.

Press, W. H. (1986). Numerical recipes : the art of scientific computing. Cambridge Cambridgeshire ; New York, Cambridge University Press.

Rasmusson, E. M. and T. H. Carpenter (1982). "Variations in tropical sea surface temperature and surface wind fields associated with the Southern Oscillation/El Niño." Monthly Weather Review **110**: 354-384.

Rasmusson, E. M. and J. M. Wallace (1983). "Meteorological aspects of the El Niño/Southern Oscillation." Science **222**: 1195-1202.

Redmond, K. T. and R. W. Koch (1991). "Surface Climate and Streamflow Variability in the Western United-States and Their Relationship to Large-Scale Circulation Indices." Water Resources Research **27**(9): 2381-2399.

Richard, L. A. (1931). "Capillary conduction of liquids through porous mediums." Physics **1**: 318-333.

Roos, M. (1987). Possible changes in California snowmelt patterns. Fourth Pacific Climate Workshop, Pacific Grove, CA.

Roos, M. (1989). Possible climate change and its impact on water supply in California. Oceans '89 Conference, Inst. of Electr. and Electron. Eng., Seattle, WA.

Roos, M. (1991). A trend of decreasing snowmelt runoff in northern California. 59th Western Snow Conference, Juneau, AK.

Ropelewski, C. F. and P. D. Jones (1987). "An extension of the Tahiti-Darwin Southern Oscillation index." Monthly Weather Review **115**: 2161-2165.

Ross, G. A. (1970). The Stanford Watershed Model: the correlation of parameter values selected by a computerized procedure with measurable physical characteristics of the watershed. Lexington, KY, Water Resources Institute, University of Kentucky.

San Francisco Bay Area Wetlands Ecosystem Goals Project (1999). Baylands Ecosystem Habitat Goals. A report of habitat recommendations prepared by the San Francisco Bay Area Wetlands Ecosystem Goals Project, U.S. Environmental Protection Agency, San Francisco, CA/S.F. Bay Regional Water Quality Control Board, Oakland, CA**:** 169.

Satterlund, D. R. (1979). "An Improved Equation for Estimating Long-wave Radiation From the Atmosphere." Water Resources Research **15**: 1643-1650.

Saxton, K. E. and J. L. McGuinness (1982). Evapotranspiration. Hydrologic modeling of small watersheds. C. T. Haan, H. P. Johnson and D. L. Brakensiek. St. Joseph, MI, Am. Soc. Agric. Eng.**:** 229-273.

Schimmelmann, A., M. Zhao, C. C. Harvey and C. B. Lange (1998). "A large California flood and correlative global climatic events 400 years ago." Quaternary Research **49**(1): 51-61.

Schonher, T. and S. E. Nicholson (1989). "The Relationship Between California Rainfall and Enso Events." Journal of Climate **2**(11): 1258-1269.

Shuttleworth, W. J. (1993). Evaporation. Handbook of Hydrology. D. R. Maidment, McGraw-Hill.

Smith, L. H. (1987). A review of circulation and mixing studies of San Francisco Bay, California, U. S. Geological Survey**:** 38.

Smith, L. H. and R. T. Cheng (1987). "Tidal and Tidally averaged circulation characteristics of Suisun Bay, California." Water Resources Research **23**: 143-155.

Snyder, J. P. (1987). Map projections--a working manual. Washington, U.S. G.P.O. : For sale by the Supt. of Docs.

Soil Conservation Service (1972). National Engineering Handbook. Washington, D.C., USDA.

Stine, S. (1994). "Extreme and Persistent Drought in California and Patagonia During Mediaeval Time." Nature **369**(6481): 546-549.

Tarboten, D. G., R. C. Bras and I. Rodriguez-Iturbe (1988). "The fractal nature of river networks." Water Resources Research **24**(8): 1317-1322.

Tarboton, D. G. and C. H. Luce (1996). Utah Energy Balance Snow Accumulation and Melt Model (UEB): Computer model technical description and users guide, Utah Water Research Laboratory and USDA Forest Service Intermountain Research Station.

Tokanaga, E. (1978). Consideration on the composition of drainage networks and their evolution, Tokyo Metropolitan University.

Trenberth, K. E. and D. A. Paolino (1980). "The northern hemisphere sea-level pressure data set: trends, errors and discontinuities." Monthly Weather Review **108**: 855-872.

U.S. Army Corps of Engineers (1956). Snow Hydrology, Summary report of the Snow Investigations. Portland, OR, U.S. Army Corps of Engineers, North Pacific Division.

U.S. Geological Survey (1967). National Atlas of the United States.

U.S. Geological Survey (1987). Hydrologic Unit Map, State of California- 1978 (north half and south half). Reston, VA, USGS and U.S. Water Resources Council.

U.S. Geological Survey (1998). Water Resources Data, California, Water Year 1997, vols. 3-4. Sacramento, CA, U.S. Geological Survey, Water Resources Division**:** 340.

U.S. Weather Bureau and U.S. Army Corps of Engineers (1942). Maximum possible precipitation over the Sacramento basin of California. Vicksburg, MI, U.S. Weather Bureau, Hydrometeorological Section and the
U.S. Army Corps of Engineers**:** 225.

Uncles, R. J. (1991). M4 tides in a macrotidal, vertically mixed estuary: the Bristol Channel and Severn. Tidal Hydrodynamics. B. Parker, Wiley**:** 341-356.

Uncles, R. J. and I. R. Joint (1983). "Vertical mixing and its effects on phytoplankton growth in a turbid estuary." Canadian J. Fisheries and Aquatic Sci. **40**: 221-228.

Uncles, R. J. and D. H. Peterson (1995). "A Computer Model of Long-Term Salinity in San Francisco Bay - Sensitivity to Mixing and Inflows." Environment International **21**(5): 647-656.

Uncles, R. J. and D. H. Peterson (1996). "The Long-Term Salinity Field in San Francisco Bay." Continental Shelf Research **16**(15): 2005-2039.

US Environmental Protection Agency (1995). "Water quality standards for surface waters of the Sacramento and San Joaquin Rivers, and San Francisco Bay and Delta, California; Final Rule." Federal Register, Part II: 4463-4709.

Van Genuchten, M. T. and D. R. Nielsen (1985). "On describing and predicting the hydraulic properties of unsaturated soils." Annales Geophysicae **3**(5): 615-627.

Weare, B. C. and J. S. Nasstrom (1982). "Examples of Extended Empirical Orthogonal Function Analysis." Monthly Weather Review **110**: 481-485.

Wells, L. E., M. Goman and R. Byrne (1997). Long term variability of fresh water flow into the San Francisco estuary using paleoclimatic methods. Berkeley, CA, University of California Water Resources Center, UC Berkeley.

Wilkinson, R. and T. Rounds (1998). Climate change and Variability in California. Santa Barbara, California, National Center for Ecological Analysis and Synthesis.

Wood, E. F., M. Sivapalan, D. Thongs, K. Beven and L. Band (1988). "A DEM based model for catchment storm response using catchment morphology." Eos, Transactions, American Geophysical Union **69**(44): 1224.

Zhu, Z. and D. L. Evans (1994). "U.S. Forest Types and Predicted Percent Forest Cover from AVHRR Data." Photogrammetric Engineering & Remote Sensing **60**(5): 525-531.